Identification and Predictive Modeling of High Propensity of Defects and Field Failure in Copper-aluminum Wire Bond Interconnect under Exposure to High Temperature and Humidity

by

Yihua Luo

A dissertation submitted to the Graduate Faculty of
Auburn University
in partial fulfillment of the
requirements for the Degree of
Doctor of Philosophy

Auburn, Alabama
August 4, 2018

Keywords: Copper-aluminum Wire bond, Accelerated Life Testing, Galvanic Corrosion, Butler-Volmer Equation, Nernst-Planck Equation Multiphysics Simulation

Copyright 2017 by Yihua Luo

Approved by

Dr. Pradeep Lall, Chair, John and Anne MacFarlane Professor of Mechanical Engineering and Director, NSF Center for Advanced Vehicle Electronics
Dr. Jeffrey Suhling, Quina Distinguished Professor and Chair of Mechanical Engineering
Dr. George Flowers, Professor of Mechanical Engineering
Dr. Virginia Davis, Professor of Chemical Engineering
Dr.Ujjwal Guin, Assistant Professor of Electrical and Computer Engineering

Abstract

Copper wire bonding is finding applications in almost all areas of modern microelectronic industry. As a recently developed wire bonding technology, it helps microelectronic manufacturers to reduce the cost of their products by replacing the costlier gold wire with copper wire. In addition, as an alternative to Au wire bond interconnect, Cu wire bond interconnect possesses other desirable characteristics such as superior mechanical, thermal and electrical properties, lower intermetallic growth rate between ball bond and pad, all of which makes it more suitable as a future wire bonding material.

Currently, the main issue of using copper wire bond is the concern of corrosion-related failure of wire bond under exposure to high temperature and high humidity operational conditions. It has been reported by previous studies that under high humidity operational conditions, Cu wire bond fails much faster than Au wire bond. To the author's best knowledge, due to complex nature of micro galvanic corrosion, the exact failure mechanism is still unknown and there is a lack of understanding of what transpires in the electronic packages that causes the failure of Cu wire bond.

This dissertation aims to help identify the failure mechanism of copper wire bond and provides more insight into how to improve the reliability of Cu-Al wire bond under harsh environmental conditions. Also, in the dissertation, several approaches for suitable lifetime predictions of Cu-Al wire bond will be presented including a novel Multiphysics FEM simulation, an acceleration factor model, a Kalman-filter based prognostics and health management framework. Those tools will

greatly reduce the time and effort needed to develop suitable Cu-Al wire bond products and estimate the lifespan of those products. Finally, those simulation results are validated by experimental results.

Acknowledgments

First and foremost, My sincerest thanks to my parents, Taiming Luo and Zhaolan Liu. I wouldn't be who I am today if not for their support and encouragement throughout my life. This work is dedicated to them.

A special thanks to Dr.Pradeep Lall, Dr. Jeffery Suhling, Dr. George Flowers, Dr. Virginia Davis and Dr. Guin for being my dissertation chair, dissertation committees & dissertation reader, supporting me in the completion of my dissertation. I would also like to thank the staffs of the department of mechanical engineering for the assistance they provided when needed. I would also like to thank my fellow researches for their contribution to the completion of my dissertation in one way or another.

Table of Contents

Abstract II

Acknowledgements IV

List of Tables .... *viii*

List of Figures xii

Chapter 1 Overview 1

1.1 Wire bonding 1

1.2 Copper wire bond 4

1.3 Epoxy molding compound 8

1.4 Research Objective 10

Chapter 2 Literature Review 35

2.1 Cu-Al Intermetallic Layer Corrosion 12

2.2 Electrochemical characteristics of Cu-Al IMCs 17

2.3 Chlorine diffusion in epoxy molding compounds 21

2.4 Levenberg-Marquardt prognostication 24

Chapter 3 Extended Kalman Filter-based PHM of Cu-Al wire bond reliability under 50

3.1 Resistance Spectroscopy 30

3.2 Extended Kalman Filter 36

3.3 Test vehicle, Test Conditions & Test Results 45

Chapter 4 Chlorine transport in EMCs 71

4.1 Chlorine in Epoxy Molding Compounds ... 56

4.2 Test Vehicle & Test Approaches ... 59

4.3 Experimental & Simulation Results ... 76

4.4 Built-in Chlorine Contaminant Tests ... 83

Chapter 5 De-bonding simulation of Cu-Al WB Intermetallic Compound Layers ... 102

5.1 Cu-Al IMC Microstructure Evolution & Wire Bond Intergranular Cracking ... 93

5.2 Modeling of Cu-Al Wire Bond IMCs De-bonding ... 97

5.3 IMCs De-Bonding Simulation Results and Analysis ... 108

Chapter 6 COMSOL Cu Wire Bond Corrosion Modeling ... 125

6.1 Test Vehicle & Experimental Approaches ... 120

6.1 Test Vehicle & Experimental Approaches ... 120

Chapter 7 Electrochemical Polarization Based Cu-Al IMC Corrosion Modeling ... 153

7.1 Micro-galvanic Corrosion ... 151

7.2 Corrosion Modeling Approach ... 154

7.3 Simulation Results & Analysis ... 164

7.4 Acceleration Factor Model ... 179

Chapter 8: Reliability Assessment of Cu-Al WB under High Voltage Bias ... 189

8.1 Test Setup & Test Procedures ... 192

8.2 Diffusion-Migration Cell Experiments ... 199

Chapter 9: MATLAB Multiphysics FE Simulation of Cu-Al WB Corrosion ... 206

9.1 Overview of Cu-Al WB Corrosion Modeling ... 210

9.2 Mathematic Model for Cu-Al WB Corrosion 215

9.3 Model Implementation 219

9.4 Construction of Model Inputs 237

9.5 Corrosion Simulation 296

Chapter 10 Summary and Conclusions 275

References 276

List of Tables

Table 1: Result of Icorr (μA/cm2) for Cu-Al IMCs at 100ppm NaCl solution[Lee 2014] 20

Table 2: Specifications of the test vehicle 45

Table 3: Comparison between Models with Regular and Irregular Grains 107

Table 4: Basic Mechanical Properties of Cu-Al IMCs 107

Table 5: Basic Mechanical Properties of Cu-Al IMCs 107

Table 6: Electrode Potential Difference between Copper and Aluminum in KCl solutions with different pH values and Different Values of Ion Concentration 137

Table 7: Tafel Parameters 139

Table 8: Initial Conditions 145

Table 9: Model Inputs 163

Table 10: Corrosion Decrease as IMCs Grow 173

Table 11: Lifespan Prediction as a Function of Cl contamination Level 175

Table 12: Lifespan Prediction as a Function of pH Level 175

Table 13: Lifespan Prediction as a Function of Temperature 175

Table 14: Dimensions of Test Vehicle 176

Table 15: Built-in Contaminant Test 177

Table 16: Comparison of Activation Energy for Al Corrosion 178

Table 17: Comparison of experimental & simulation results 179

Table 18: Result of Multi-linear Regression 180

Table 19: Result of ANOVA Test 181

Table 20: Model Summary 181

Table 21: Model Comparison 185

Table 22: Dimensions of QFN Package 192

Table 23: Summary of D and μ measurements 206

Table 24: Simulation Parameters for a PDE subjected to Butler-Volmer B.C. 224

Table 25: Simulation Parameters for a transport cell 227

Table 26: Simulation Parameters for NP equation coupled with BV B.C. 231

Table 27: Chlorine Release Rate Measurement 238

Table 28: Summary of D and μ Measurements 239

Table 29: Polarization Test Matrix 241

Table 30: Tafel Parameters Estimation of Polarization Tests 242

Table 31: Tafel Extrapolation of Cu at 6.2pH, 15ppm and 250C 243

Table 32: Tafel Extrapolation of Cu at 6.2pH, 15ppm and 450C 244

Table 33: Tafel Extrapolation of Cu at 6.2pH, 15ppm and 650C 245

Table 34: Tafel Extrapolation of Cu at 6.2pH, 15ppm and 850C 246

Table 35: Tafel Extrapolation of Cu at 6.2pH, 0.01M and 250C 247

Table 36: Tafel Extrapolation of Cu at 6.2pH, 0.01M and 450C 248

Table 37: Tafel Extrapolation of Cu at 6.2pH, 0.01M and 650C 249

Table 38: Tafel Extrapolation of Cu at 6.2pH, 0.01M and 850C 250

Table 39: Tafel Extrapolation of Cu at 6.2pH, 0.05M and 250C 251

Table 40: Tafel Extrapolation of Cu at 6.2pH, 0.05M and 450C 252

Table 41: Tafel Extrapolation of Cu at 6.2pH, 0.05M and 650C 253

Table 42: Tafel Extrapolation of Cu at 6.2pH, 0.05M and 850C 254

Table 43: Tafel Extrapolation of Cu at 6.2pH, 0.1M and 250C 255

Table 44: Tafel Extrapolation of Cu at 6.2pH, 0.1M and 450C 256

Table 45: Tafel Extrapolation of Cu at 6.2pH, 0.1M and 650C 257

Table 46: Tafel Extrapolation of Cu at 6.2pH, 0.1M and 850C 258

Table 47: Tafel Extrapolation of Cu at 6.2pH, 0.3M and 250C 259

Table 48: Tafel Extrapolation of Cu at 6.2pH, 0.3M and 450C 260

Table 49: Tafel Extrapolation of Cu at 6.2pH, 0.3M and 650C 261

Table 50: Tafel Extrapolation of Cu at 6.2pH, 0.3M and 850C 262

Table 51: Tafel Extrapolation of Cu at 6.2pH, 0.5M and 250C 263

Table 52: Tafel Extrapolation of Cu at 6.2pH, 0.5M and 450C 264

Table 53: Tafel Extrapolation of Cu at 6.2pH, 0.5M and 650C 265

Table 54: Tafel Extrapolation of Cu at 6.2pH, 0.5M and 850C 266

Table 55: Tafel Extrapolation of IMC at 6.2pH, 15ppm and 250C.. 267

Table 56: Tafel Extrapolation of IMC at 6.2pH, 15ppm and 450C.. 268

Table 57: Tafel Extrapolation of IMC at 6.2pH, 15ppm and 650C.. 269

Table 58: Tafel Extrapolation of IMC at 6.2pH, 15ppm and 850C.. 270

Table 59: Tafel Extrapolation of IMC at 6.2pH, 0.01M and 250C 271

Table 60: Tafel Extrapolation of IMC at 6.2pH, 0.01M and 450C 272

Table 61: Tafel Extrapolation of IMC at 6.2pH, 0.01M and 650C 273

Table 62: Tafel Extrapolation of IMC at 6.2pH, 0.01M and 850C 274

Table 63: Tafel Extrapolation of IMC at 6.2pH, 0.05M and 250C 275

Table 64: Tafel Extrapolation of IMC at 6.2pH, 0.05M and 450C 276

Table 65: Tafel Extrapolation of IMC at 6.2pH, 0.05M and 650C 277

Table 66: Tafel Extrapolation of IMC at 6.2pH, 0.05M and 850C 278

Table 67: Tafel Extrapolation of IMC at 6.2pH, 0.1M and 250C 279

Table 68: Tafel Extrapolation of IMC at 6.2pH, 0.1M and 450C 280

Table 69: Tafel Extrapolation of IMC at 6.2pH, 0.1M and 650C 281

Table 70: Tafel Extrapolation of IMC at 6.2pH, 0.1M and 850C 282

Table 71: Tafel Extrapolation of IMC at 6.2pH, 0.3M and 250C 283

Table 72: Tafel Extrapolation of IMC at 6.2pH, 0.3M and 450C 284

Table 73: Tafel Extrapolation of IMC at 6.2pH, 0.3M and 650C 285

Table 74: Tafel Extrapolation of IMC at 6.2pH, 0.3M and 850C 286

Table 75: Tafel Extrapolation of IMC at 6.2pH, 0.5M and 250C 287

Table 76: Tafel Extrapolation of IMC at 6.2pH, 0.5M and 450C 288

Table 77: Tafel Extrapolation of IMC at 6.2pH, 0.5M and 650C 289

Table 78: Tafel Extrapolation of IMC at 6.2pH, 0.5M and 850C 290

Table 79: Simulation Inputs 298

List of Figures

Figure 1: Fine-pitch wire bonding [Bogatin 1997] 1

Figure 2: Ball bonding procedure [Suhling 2013] 3

Figure 3: Ball bonding procedure [Suhling 2013] 4

Figure 4: Example of Al splash [Schueller 2013]... 5

Figure 5: Corrosion at Cu-Al wire bond ball bond-pad interface 8

Figure 6: Epoxy molding compound 9

Figure 7: Images of Cu-Al WB after humidity treatment (left: top of Al pad, right: bottom of Cu ball bond) [Boettcher 2010] 14

Figure 8: Result of EDX line scan across the ball bond-pad region of a failed Cu-Al WB [Boettcher 2010] 14

Figure 9: SEM images of Cu-Al WB central regions after exposed to 350°C for various amount of time [Lu 2011] 16

Figure 10: Assembly of a working electrode for electrochemical tests [Lee 2014] 18

Figure 11: Schematic plot of a three-electrode electrochemical testing system [Lee 2014] 19

Figure 12: Result of OCP of Cu-Al IMCs [Lee 2014].. 20

Figure 13: TOF-SIMS analysis of the fractured surface of an EMC sample after exposure to a basic NaCl solution [Lantz 2003] 23

Figure 14: Discoloration of EMC samples after a 60-day exposure to a NaCl solution at elevated temperature [Lantz 2003] 24
Figure 15: Prognostication of thermally aged Cu-Al wire bond interconnect 26
Figure 16: Example of Cu-Al wire bond RULs prognostication using LM algorithm 27
Figure 17: Example result of "planar analysis" on the Cu-Al WB interfacial area after prolonged exposure to a temperature/humidity environmental condition 28
Figure 18: Example of application of life-span prediction model on Cu-Al packages with varying EMCs 29
Figure 19: Schematic plot of RS setup 32
Figure 20: Lock-in Signals 33
Figure 21: Probe station 36
Figure 22: SRS830 Lock-In Amplifier 36
Figure 23: Example of resistance of Cu-Al WB used as a failure leading indicator 38
Figure 24: EKF operation diagram 45
Figure 25: 32-pin chip-scale package 46
Figure 26: Temperature humidity chamber used for harsh environmental aging test 47
Figure 27: Experimental result of change of Cu-Al WB resistance over 500 thermal cycling loops and EFK filtering performance 48
Figure 28: Experimental result of change of Cu-Al WB resistance over 240 hours under 200°C isothermal aging condition and EFK filtering performance 49

Figure 29: Experimental result of change of Cu-Al WB resistance over 8 weeks under 85RH/85°C temperature humidity aging condition and EFK filtering performance.................................... 50
Figure 30: PHM result of Cu-Al wire bond under thermal cycling condition for 500 loops 51
Figure 31: PHM result of Cu-Al wire bond under 200C for 240 hours.................................... 52
Figure 32: PHM result of Cu-Al wire bond under 85RH/85°C for 8weeks 53
Figure 33: Performance of prognostic horizon of the result of Cu-Al wire bond under thermal cycling condition for 500 loops 54
Figure 34: Performance of prognostic horizon of the result of Cu-Al wire bond under 200C for 240 hours.. 55
Figure 35: Performance of prognostic horizon of the result of Cu-Al wire bond under 85RH/85°C for 8weeks... 55
Figure 36: SEM image of bond pads and pitting corrosion [Wolff 2010]................................ 58
Figure 37: MicroCT image of 32pin chip scale Cu-Al wire bond package............................... 60
Figure 38: Schematic of ICP-MS main processes [Workley 1996]... 62
Figure 39: 3D model of chlorine transfer in EMCs [unit in micrometer].................................. 64
Figure 40: Electric double layer according to Stern's model 66
Figure 41: Debye Length in terms of bulk concentration of ion in EMC, εr=4, T=298K, ppm to mol/m3 ratio is 76.92 to 1 67
Figure 42: Absolute value of Ez/Ex for the area between the two wire bonds, εr=4, V=3.3Volt, height=70μm, thickness=2μm.. 68
Figure 43: Simplified two-dimensional model based on original three-dimensional one 69

Figure 44: Simplified model with the height reduced to 40μm and the site of interest P is highlighted by red 70
Figure 45: comparison of original electric field between 2-D model 71
Figure 46: schematic picture of concentration profile across the EMC after 60 days of aging in 0.15M NaCl........ 73
Figure 47: Flow chart of calculation of chlorine diffusivity in EMC samples 74
Figure 48: comparison among the results of multiphysics simulation, the empirical equation and the experiment results 75
Figure 49: Concentration change with respect to time at site of interest P, V=3Volt, D=7*10-16m2/s, T=298K, Cbulk=41ppm, C∞=4100ppm 77
Figure 50: variation of electric potential profile in the vicinity of the electrode-EMC interfaces, V=3Volt, D=7*10-16m2/s, T=298K, Cbulk=41ppm, C∞=4100ppm 78
Figure 51: Change of saturation time at P vs. different diffusivities under potential bias, V=3.0Volt, T=298K........ 79
Figure 52: maximum local concentration increase as a function of electric potential, D=7*10-16m2/s, T=298K, Cbulk=41ppm, C∞=4100ppm 80
Figure 53: saturation time vs. electric potential, D=7*10-16m2/s, T=298K, Cbulk=41ppm, C∞=4100ppm........ 81
Figure 54:Diffusion coefficient of Chloride ion as a function of temperature 83
Figure 55: Change of time to maximum concentration at P vs. different temperature........ 83
Figure 56:time to failure plot monitored by RS 84

Figure 57: Optical microscopic sample image with built-in chloride contaminant 86

Figure 58: 16 pairs of wire bond has been labeled in order to measure and track change of resistances 87

Figure 59: Optical microscopic image of sample #1 and its corresponding Cu-Al wire bond resistance monitoring 88

Figure 60: Optical microscopic image of sample #2 and its corresponding Cu-Al wire bond resistance monitoring 89

Figure 61: 2D COMSOL model for built-in contaminant experiment sample#1 90

Figure 62: 2D COMSOL model for built-in contaminant experiment sample#2 91

Figure 63: time to maximum concentration in built-in contaminant experiment sample#1and sample#2 under room temperature condition and 1300C/100RH 92

Figure 64: Cu-Al Wire Bond at As-bonded Stage 95

Figure 65: Cu-Al Wire Bond after Thermal Treatment 96

Figure 66: Crack Initiation and Propagation 97

Figure 67: Procedures for Generating IMC Grain-like Structures 99

Figure 68: Procedures for Generating IMC Grain-like Structures 99

Figure 69: Cohesive Elements at Undeformed State 102

Figure 70: Cohesive Elements at Deformed State 103

Figure 71: Normal Traction-separation Relationship 104

Figure 72: Tangential Traction-separation Relationship 104

Figure 73: Cu-Al Ball Bond Geometry with Regular Hexagon-shaped IMC grains 105

Figure 74: Cu-Al Ball Bond Geometry with Irregular Hexagon-shaped IMC grains 105

Figure 75: Discretization of Model with Regular Hexagon-Shaped IMC Grains 106

Figure 76: Discretization of Model with Irregular Hexagon-Shaped IMC Grains 106

Figure 77: Regular Grain Shape vs. Irregular Grain Shape 109

Figure 78: Micro-crack Pattern in Regular Shape IMC 110

Figure 79: Micro-crack Pattern in Irregular Shape IMC 110

Figure 80: Micro-crack Pattern and σ22 in Model with Irregular Grain Shape 111

Figure 81: Weibull Distributed Grain Interfacial Strength 113

Figure 82: Uniform Grain vs. Weibull Distributed 113

Figure 83: Normal Displacement and Normal Stress Contour 114

Figure 84: Models with Different IMC Thicknesses 115

Figure 85: Models with Different IMC Thicknesses 116

Figure 86: Models with Multiple IMC Layers 117

Figure 87: Micro-crack Pattern in Model with Multiple IMCs 117

Figure 88: Molding compound sample F 120

Figure 89: Diffusion Cell Setup 122

Figure 90: PH meter 123

Figure 91: Calibration Plot 124

Figure 92: Calculation of Diffusion Coefficient at RT 125

Figure 93: Diffusion Coefficient as a Function of T 125

Figure 94: Comparison of Diffusion Coefficient Values under different PH values at room temperature 126
Figure 95: Schematic of ICP-MS main processes 127
Figure 96: Schematic Picture of Concentration Profile 128
Figure 97: Comparison among Results of Multiphysics Simulation, Empirical Equation and Experiment results 129
Figure 98: SEM Image of Cross-section of EMC Sample B after a 3-week immersion in 1M KCl Solution at 850C 131
Figure 99: EDS Mapping Image of Figure 98 132
Figure 100: SEM Image and EDS Spot Analysis of Filler Material A 133
Figure 101: SEM Image and EDS Spot Analysis of Filler Material B 133
Figure 102: Overlap between Chlorine Mapping & x-section of EMC Sample B 134
Figure 103: SEM Image of Cross-section of EMC Sample F after a 96-hour immersion in 1M KCl Solution at 1500C 135
Figure 104: Weight Loss Test under 2000C 136
Figure 105: Polarization Curves of Aluminum under Different Values of Chloride Ion Concentration at pH=7 138
Figure 106: Polarization Curves of Aluminum under Different pH Values at 0.5M Concentration of KCl 139
Figure 107: Schematic Plot of Galvanic Corrosion 141
Figure 108: Model Geometry (unit in μm) 142

Figure 109: Aluminum Pad/EMC Interface 144

Figure 110: Copper ball bond/EMC Interface 144

Figure 111: Time=5*106(Second) 147

Figure 112: Time=107(Second) 147

Figure 113: Comparison of Average Corrosion Current Density 148

Figure 114: Hydroxide Ion Flux 149

Figure 115: PH contour at time=3(hours) 150

Figure 116: pH contour at time=24(hours) 150

Figure 117: Schematic Plot of V-I Curve 152

Figure 118: Schematic Plot of Cu-Al Galvanic Corrosion 153

Figure 119: Cu-Al Interfacial Corrosion 154

Figure 120: Micro-Galvanic Corrosion Configuration 156

Figure 121: IMC Sample Preparation 158

Figure 122: Polarization Curves for Large-scale Cu-Al Corrosion Cell 158

Figure 123: COMSOL 3D Corrosion Model 159

Figure 124: Simulation Result 160

Figure 125: Plots of Locating Linear Regions 162

Figure 126: Tafel Extrapolation of Cu under 0.5M Chlorine Concentration and 7pH 162

Figure 127: Tafel Extrapolation of Al under 0.5M Chlorine Concentration and 7pH 163

Figure 128: Corrosion under 0.5M Chlorine Concentration and 7pH 164

Figure 129: Electrochemical Polarization Curves of Al 165

Figure 130: Electrochemical Polarization Curves of Cu 165

Figure 131: Effect of Chlorine Concentration 166

Figure 132: Effect of Chlorine Concentration 166

Figure 133: Effect of pH (Al) 167

Figure 134: Effect of pH (Cu) 168

Figure 135: Effect of pH (Cu-Al Corrosion Cell) 168

Figure 136: Polarization Experiment Setup 170

Figure 137: Polarization Curves of Al 171

Figure 138: Polarization Curves of Cu 171

Figure 139: Simulation Results under Different Temperatures 172

Figure 140: Polarization Curves of Cu-Al IMCs 173

Figure 141: Result with Different CuAl Lengths 173

Figure 142: Micro-CT Reconstruction of Package 176

Figure 143: Ln (k) vs 1/T 178

Figure 144: Regression Model Modification 183

Figure 145: Change of AF with Respect to Each Predictor 183

Figure 146: Validation of Regression Model 184

Figure 147: Image of BGA337 186

Figure 148: IMC Growth under Isothermal Aging 187

Figure 149: Measurements of IMC Thickness 187

Figure 150: Change of Thickness vs Aging Duration 189

Figure 151: Box Plot of Ball Shear Strengths 189
Figure 152: Oxygen Mapping 190
Figure 153: Test Vehicle 193
Figure 154: Schematic Plot of High Voltage Test Setup 194
Figure 155: Setup of PWM Controller 194
Figure 156: Setup of Gate Driver 194
Figure 157: Schematic Plots of the Functionality of Gate Driver 195
Figure 158: High Voltage Test Setup 196
Figure 159: Voltage Waveform Passing through Cu-Al WB 197
Figure 160: High Voltage/Temperature Test Setup 198
Figure 161: Effect of temperature/voltage bias on Cu-Al WB interconnect 199
Figure 162: Diffusion Cell 201
Figure 163: Migration Cell 202
Figure 164: Migration Cell in a Thermal Chamber 203
Figure 165: COMSOL Electric Field Modeling 204
Figure 166: Location Where Electric Potential Gradient is Extracted 205
Figure 167: Electric Potential across Z-direction 206
Figure 168: Cu-Al WB Corrosion Model 207
Figure 169: Close-up View of Model Geometry 207
Figure 170: Effect of Voltage Bias on WB Corrosion at 130°C/100RH 208
Figure 171: Schematic plot of chlorine release during EMC degradation process 210

Figure 172: Flowchart of Cu-Al WB Corrosion Simulation 212

Figure 173: Factors Involved in Cu-Al WB Galvanic Corrosion 213

Figure 174: Schematic Plot of Micro-Galvanic Corrosion Cell 213

Figure 175: SEM Image of Crack Progression at Cu-Al WB interface 213

Figure 176: Initial Geometry of Corrosion Model 214

Figure 177: Geometry of Corrosion Model with a Developed Crack 215

Figure 178: A System of Coupled Non-linear PDEs 216

Figure 179: Gauss–Seidel Iterative Scheme 217

Figure 180: Cu-Al WB Corrosion Front Tracking 219

Figure 181: Initial Simulation Domain and Important Boundaries 220

Figure 182: Linear Triangular Element in xy-plane & ξη-plane 222

Figure 183: Newton-Galerkin method 224

Figure 184: Test Simulation Results (electric field distribution with/without polarization) 225

Figure 185: Case Study 1 227

Figure 186: Concentration contour at different durations 228

Figure 187: Case study 2 230

Figure 188: Electric field 230

Figure 189: Chlorine concentration field 231

Figure 190: Corrosion front 232

Figure 191: General procedures of corrosion front tracking 233

Figure 192: Schematic of corrosion front nodal displacements 235

Figure 193: Detailed procedures of corrosion front tracking 236

Figure 194: geometrical progression of Cu-Al WB micro-corrosion cell 236

Figure 195: Schematic Approach to Calculating Chlorine Release Rate of Different EMCs .. 238

Figure 196: Electrochemical Polarization Test Samples 240

Figure 197: Electrochemical Polarization Test Setup 240

Figure 198: Schematic Plot of Measuring Tafel Parameters 241

Figure 199: Repeated Measurement at one of the 24 test conditions for Cu-Al IMC 242

Figure 200: Electrochemical Polarization Test Results of Cu at 6.2pH, 15ppm and 250C 243

Figure 201: Electrochemical Polarization Test Results of Cu at 6.2pH, 15ppm and 450C 244

Figure 202: Electrochemical Polarization Test Results of Cu at 6.2pH, 15ppm and 650C 245

Figure 203: Electrochemical Polarization Test Results of Cu at 6.2pH, 15ppm and 850C 246

Figure 204: Electrochemical Polarization Test Results of Cu at 6.2pH, 0.01M and 250C 247

Figure 205: Electrochemical Polarization Test Results of Cu at 6.2pH, 0.01M and 450C 248

Figure 206: Electrochemical Polarization Test Results of Cu at 6.2pH, 0.01M and 650C 249

Figure 207: Electrochemical Polarization Test Results of Cu at 6.2pH, 0.01M and 850C 250

Figure 208: Electrochemical Polarization Test Results of Cu at 6.2pH, 0.05M and 250C 251

Figure 209: Electrochemical Polarization Test Results of Cu at 6.2pH, 0.05M and 450C 252

Figure 210: Electrochemical Polarization Test Results of Cu at 6.2pH, 0.05M and 650C 253

Figure 211: Electrochemical Polarization Test Results of Cu at 6.2pH, 0.05M and 850C 254

Figure 212: Electrochemical Polarization Test Results of Cu at 6.2pH, 0.1M and 250C 255

Figure 213: Electrochemical Polarization Test Results of Cu at 6.2pH, 0.1M and 450C 256

Figure 214: Electrochemical Polarization Test Results of Cu at 6.2pH, 0.1M and 650C 257

Figure 215: Electrochemical Polarization Test Results of Cu at 6.2pH, 0.1M and 650C 258

Figure 216: Electrochemical Polarization Test Results of Cu at 6.2pH, 0.1M and 850C 259

Figure 217: Electrochemical Polarization Test Results of Cu at 6.2pH, 0.3M and 450C 260

Figure 218: Electrochemical Polarization Test Results of Cu at 6.2pH, 0.3M and 650C 261

Figure 219: Electrochemical Polarization Test Results of Cu at 6.2pH, 0.3M and 850C 262

Figure 220: Electrochemical Polarization Test Results of Cu at 6.2pH, 0.5M and 250C 263

Figure 221: Electrochemical Polarization Test Results of Cu at 6.2pH, 0.5M and 450C 264

Figure 222: Electrochemical Polarization Test Results of Cu at 6.2pH, 0.5M and 650C 265

Figure 223: Electrochemical Polarization Test Results of Cu at 6.2pH, 0.5M and 650C 266

Figure 224: Electrochemical Polarization Test Results of Cu at 6.2pH, 0.5M and 850C 267

Figure 225: Electrochemical Polarization Test Results of IMC at 6.2pH, 15ppm and 450C... 268

Figure 226: Electrochemical Polarization Test Results of IMC at 6.2pH, 15ppm and 650C... 269

Figure 227: Electrochemical Polarization Test Results of IMC at 6.2pH, 15ppm and 850C... 270

Figure 228: Electrochemical Polarization Test Results of IMC at 6.2pH, 0.01M and 250C ... 271

Figure 229: Electrochemical Polarization Test Results of IMC at 6.2pH, 0.01M and 450C ... 272

Figure 230: Electrochemical Polarization Test Results of IMC at 6.2pH, 0.01M and 650C ... 273

Figure 231: Electrochemical Polarization Test Results of IMC at 6.2pH, 0.01M and 850C ... 274

Figure 232: Electrochemical Polarization Test Results of IMC at 6.2pH, 0.05M and 250C ... 275

Figure 233: Electrochemical Polarization Test Results of IMC at 6.2pH, 0.05M and 450C ... 276

Figure 234: Electrochemical Polarization Test Results of IMC at 6.2pH, 0.05M and 650C ... 277

Figure 235: Electrochemical Polarization Test Results of IMC at 6.2pH, 0.05M and 850C ... 278

Figure 236: Electrochemical Polarization Test Results of IMC at 6.2pH, 0.1M and 250C 279

Figure 237: Electrochemical Polarization Test Results of IMC at 6.2pH, 0.1M and 450C 280

Figure 238: Electrochemical Polarization Test Results of IMC at 6.2pH, 0.1M and 650C 281

Figure 239: Electrochemical Polarization Test Results of IMC at 6.2pH, 0.1M and 850C 282

Figure 240: Electrochemical Polarization Test Results of IMC at 6.2pH, 0.3M and 250C 283

Figure 241: Electrochemical Polarization Test Results of IMC at 6.2pH, 0.3M and 450C 284

Figure 242: Electrochemical Polarization Test Results of IMC at 6.2pH, 0.3M and 650C 285

Figure 243: Electrochemical Polarization Test Results of IMC at 6.2pH, 0.3M and 850C 286

Figure 244: Electrochemical Polarization Test Results of IMC at 6.2pH, 0.5M and 250C 287

Figure 245: Electrochemical Polarization Test Results of IMC at 6.2pH, 0.5M and 450C 288

Figure 246: Electrochemical Polarization Test Results of IMC at 6.2pH, 0.5M and 650C 289

Figure 247: Electrochemical Polarization Test Results of IMC at 6.2pH, 0.5M and 850C 290

Figure 248: Cu-Al IMC Alpha as a Function of Temperature 291

Figure 249: Cu-Al IMC Beta as a Function of Temperature 291

Figure 250: Cu-Al IMC OCP as a Function of Temperature 292

Figure 251: Cu-Al IMC OCP as a Function of Concentration 292

Figure 252: Cu-Al IMC Icorr as a Function of Temperature 293

Figure 253: Cu-Al IMC Icorr as a Function of Concentration 293

Figure 254: Cu Alpha as a Function of Temperature 294

Figure 255: Cu Beta as a Function of Temperature 294

Figure 256: Cu OCP as a Function of Temperature 295

Figure 257: Cu OCP as a Function of Concentration 295

Figure 258: Cu Icorr as a Function of Temperature 296

Figure 259: Cu Icorr as a Function of Concentration 296

Figure 260: Cl Diffusivity as a Function of Temperature 297

Figure 261: Cl Ionic Mobility as a Function of Temperature 298

Figure 262: Cl Release Rate as a Function of Temperature 298

Figure 263: Crack Initiation and Crack Propagation 299

Figure 264: Cu-Al IMC Crack Length vs Aging Duration at 1300C/100RH/1V Simulation Conditions 300

Chapter 1 Introduction

1.1 Wire bonding

Wire bonding is a technique which forms connections between an integrated circuit (IC) and a metal lead frame during the process of microelectronics packaging. Figure 1 illustrates a typical chip-level connection created using wire bonding. It provides an electric path both from and to a substrate for signal transmission and power distribution. It is the working horse technique in the manufacturing industry to make fine-pitch microelectronics. Compared to other existing chip-connection approaches such as flip chip technique or tape automated bonding (TAB), wire bonding forms connections one at a time. In addition, wiring changes can easily be done without retooling, and chip preparation is much less complicated, which makes wire bonding the most flexible chip-connection technique among other techniques.

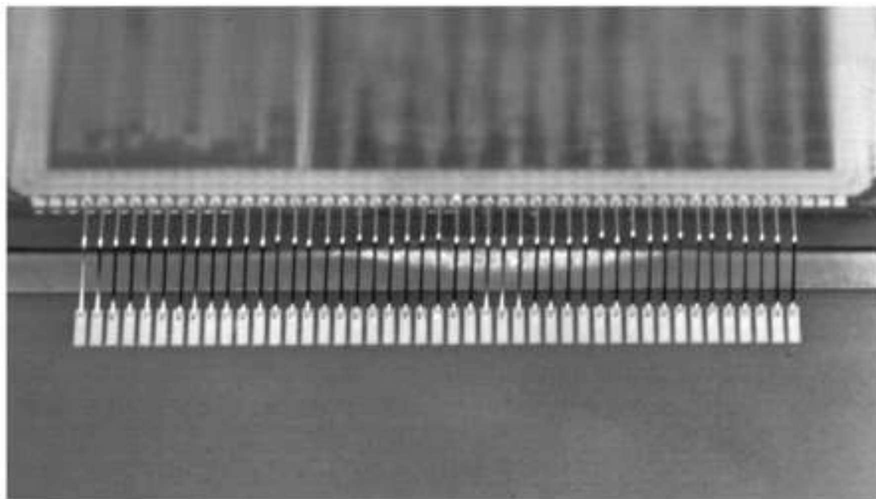

Figure 1: Fine-pitch wire bonding [Bogatin 1997]

A combination of heat, pressure and ultrasonic energy are used to bond a wire and two bond pads made of different metallic materials to form a wire bond connection. Such technique is called thermosonic bonding. During the wire bonding process, ultrasonic and heat energy are applied to soften the wire, and pad metallization, while pressure is applied to form a metallurgical bond. There are two types of wire bonds, bond–wedge bonding and wedge-wedge bonding. Currently, most of wire bonds are ball-wedges bonds due to its faster speed in electronic packages [Ginsberg 1989]. The procedure of forming a ball bond is illustrated in Figure 2. In step a, the bonding tool descends to the bond pad location. In step b, a free air ball (FAB) is created by the use of electrical flame-off (EFO). Thermosonic force is used to form the first bond in step c. The last three steps illustrate how the second bond is formed. A wire bonding machine is shown in Figure 3.

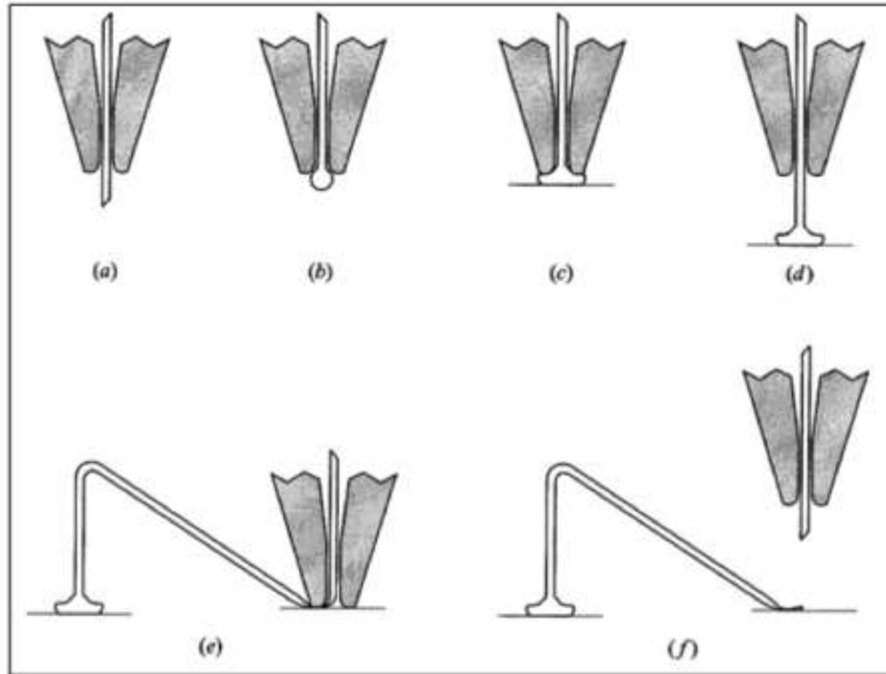

Figure 2: Ball bonding procedure [Suhling 2013]

Figure 3: Ball bonding procedure [Suhling 2013]

1.2 Copper wire bond

Before the emergence of copper wire bond as the main chip-level interconnection, gold wire bond was widely used in microelectronic packages. Unlike copper wire bond, the behavior of gold wire bond has been studied extensively over the years [Sylvester 2013]. The advantages of using gold wire bond cover gas free when forming wire bonds, similar radii and electronegativity between gold and the aluminum (pad material) which makes it easy to form a metallic bond, compatible hardness to aluminum which results in minimum Al splash and underneath stress during wire bond process, difficult to be ionized in humid environment, requires less stringent

epoxy molding compound encapsulants. Therefore, it is a well-established production, operation and testing guidelines for gold wire bonds.

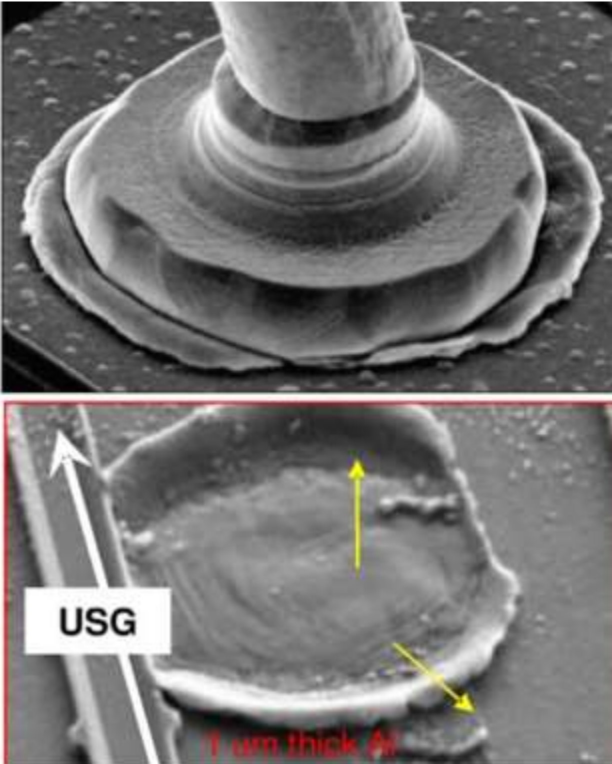

Figure 4: Example of Al splash [Schueller 2013]

The rise of copper wire bond as an alternative to gold wire bond is mainly driven by cost-related issues with gold. As of the end of 2016, gold price had reached 1250 dollars per ounce, which is five times higher than the gold price at the beginning of this century. In order to reduce the cost of their products, microelectronics manufacturers like Taxes Instruments and Freescale starts to transition from gold wire bonding to other wire bonding techniques such as copper wire

bonding, palladium coated Cu wire bonding and silver wire bonding. Among those new wire bonding techniques, copper wire bond got the most attentions as Cu wire bonding cost the least and is considered acceptable in terms of manufacturing and reliability [Pecht 2014]. Being used as a bonding material, copper has some superior material properties than gold. For example, higher mechanical strength, lower yield strength, high electrical conductivity, high thermal conductivity and slower Cu-Al IMCs (intermetallic compounds) growth. Stronger mechanical strength allows cooper wire bond to be more reliable under mechanical stress such as shocking and vibration. High thermal and electrical conductivity make it more suitable for fine-pitch applications and high power applications. Lower intermetallic compounds (IMCs) growth rate results in a reduced likelihood of having kirkendall voids or other type of weak IMCs occurred in the wire bonds. Despite of those upsides associated with copper wire bond. It has its share of shortcomings such as easily being oxidized, etc. During the formation of a copper free air ball (FAB), Cu oxidation inhibits the formation of a spherical ball, which in turn affects the reliability of the first bond. Cu oxidation will weaken the bond between Cu and Al, making wire bond prone to corrosion. Therefore, the use of inert gas (forming gas) is required during bond. Also, copper is much harder than Al. Forming a metallic bond between Cu and Al is not as easy as forming a metallic bond between Au and Al. As a result, excessive thermosonic energy are require to soften the ball during the bonding process, which will often lead to undesirable Al splash and excessive damage to the package substrate underneath the pad. Figure 4 shows an example of Al splash during copper wire bonding. The processing window for copper wire bonding is much narrower than that of gold wire bonding. Therefore, it is harder to maintain a consistent wire bond quality in practical

manufacturing. Finally, the most noticeable downside of using copper wire bond is the fact that it is susceptible to corrosion-related failure under exposure to high temperature and/or high humidity operational conditions especially when the contamination of epoxy molding compound used to encapsulate packages are high. Figure 5 illustrates a typical SEM image of copper wire bond failure due to excessive corrosion occurred at the copper ball bond-aluminum pad interface. The red zone highlighted in the figure displays the presence of oxygen element, which is commonly spotted when packages are tested under high humidity operational conditions for extended period of time. Another common element found in the case of Cu wire bond corrosion-related failure is chloride ion. These two elements are involved in the corrosion leading to the failure of Cu wire bonds. Suffice it to say that as of now, there are still a lot of challenges for Cu wire bonding to become the leading chip-level interconnection technology, among which the most critical one is to understand the failure mechanism of Cu wire bond under prolonged exposure to harsh operational conditions. Only with a deep understanding of Cu wire bond failure mechanism will researchers and manufacturers be able to come up with engineering solutions to improve the reliability of it. Therefore, produce a more dependable yet cost-effective product.

Figure 5: Corrosion at Cu-Al wire bond ball bond-pad interface

1.3 Epoxy molding compound

Epoxy molding compounds (EMC) are widely used to encapsulate microelectronics. The reliability performance of copper wire bond in electronic packages are closed related to EMCs. They are solid epoxy polymers that are heated to a liquid and then injected over a circuit for protection. Figure 6 shows a typical microscopic image of epoxy molding compound. As it can be seen from the figure, EMCs contain several different components. The bulk component is the epoxy which is a thermosetting polymer formed using a resin and a hardener. During the transfer molding of a semiconductor package, accelerators are applied into the mix to enhance the cross-linking process. The round and bar-shaped particles in EMCs are fillers. Round silica particles are the most commonly used material. The use of filler reduces the overall cost, increase the hardness of the package and at the same time lower the coefficient of thermal expansion and increase the

thermal conductivity of EMCs. However, the addition of fillers also increases the dielectric constant of EMCs and it lowers the tensile strength and the ability of EMCs to flow during the molding process. Other additives present in EMCs are flame retardants, toughening particles, colorants and release agents.

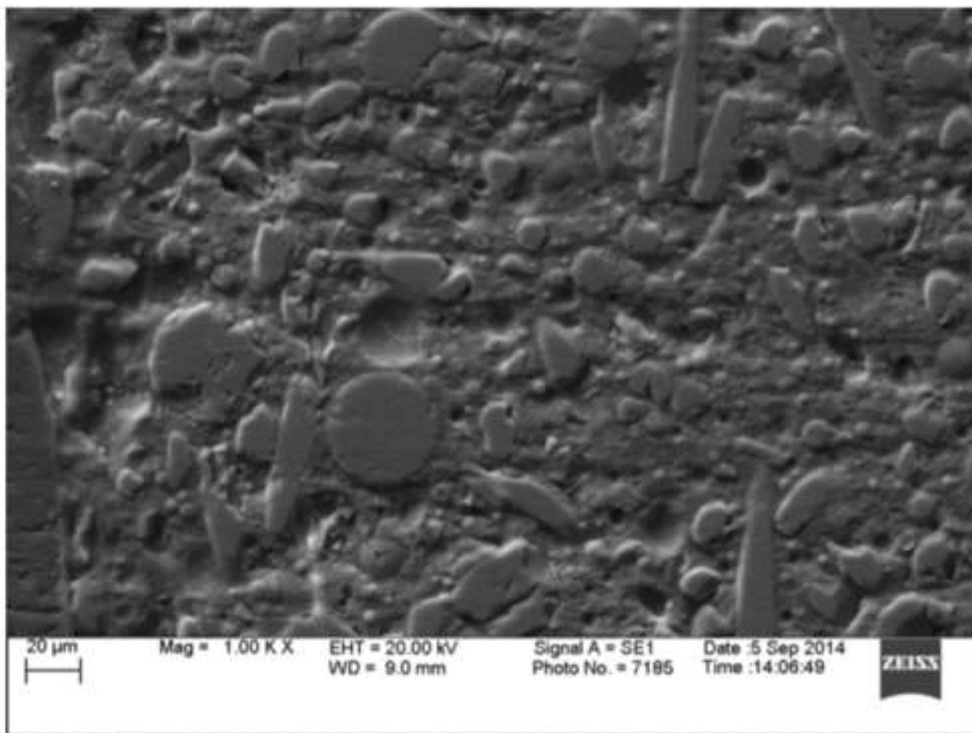

Figure 6: Epoxy molding compound

Unlike structural materials, low molecular weight substances are able to transport in polymeric materials such as EMCs freely at ambient temperatures [Barrie 1968]. Typical electronic molding compounds contains different amount of ionic contaminants including chloride ion. Common sources of chloride ion could be as a result of the chemical synthesis of the subcomponents of the

resin. It could also come from the process of metallization etching, from the decomposition of die-attach material or form the use of flame retardant. EMCs are also hydrophilic. They absorb moistures in humid environments. Study has shown that absorption of moisture will lead to the degradation of EMCs when exposed to harsh environmental stress such as high temperature, high humidity [Lu 2000]. The effect of moisture absorption of EMCs is threefold. First, it causes the mechanical and chemical degradation of EMCs, resulting in a lower material strength of EMCs and generating more freely-transport contaminant such as chlorine in the molding compound. Second, the moisture makes the ionic species in molding compound more mobile, its accelerate the process of transport process of different ionic contaminants. Finally, it involves in a series of corrosion processes known to cause the failure of Cu-Al wire bond. The rate at which EMCs absorb moisture under humid environmental conditions and the rate at which ionic species transport in EMCs has a direct effect on the reliability performance of copper wire bond interconnects. Therefore, understand the moisture absorption behavior and ionic transport behavior of EMCs will help us understand the corrosion of Cu wire bond better.

1.4 Research Objective

Currently, the corrosion-related Cu wire bond failure is one of the major concerns that prevent the mass production of copper wire bond. Studies on fundamental understanding of wire bond corrosion and techniques that could help assess the accumulated damage in the Cu-Al wire bond, prognostic and health management methodologies that could be used to predict the remaining useful life (RUL) is either lacking or not fully-developed. The study presented in this dissertation

aims to fill the gap by doing the following tasks. First, provide a detailed and thorough study of the corrosion mechanisms of Cu-Al wire bond under harsh environmental conditions. Second, build different tools that could be used to assess the damage progression of Cu-Al wire bond and predict the failure of Cu-Al wire bond in advance so that proper maintenance work can be done before catastrophic failure of microelectronics occurs. Finally, several finite element-based predictive multiphysics corrosion frameworks are introduced to help provide more insight into the Cu-Al wire bond corrosion problems and at the same time offer RUL estimations based on the inputs obtained from the operational environment, the Cu-Al wire bond and the epoxy molding compound.

Chapter 2 Literature Review

In this chapter, previous studies on reliability performance of Cu-Al wire bond will be discussed as well as methodologies used to quantify the progression damage in Cu-Al wire bond. Those studies and research methodologies lay the foundations for the understanding of Cu-Al wire bond failure mechanism and provide some insights into the modeling and solving the corrosion-related reliability issue of Cu-Al wire bond. Contributions as well as shortages of those studies will be discussed at the end of each discussion.

2.1 Cu-Al Intermetallic Layer Corrosion

The idea of Cu-Al wire bond intermetallic corrosion has been proposed, studied over the years. Among those research studies of the reliability performance of Cu-Al wire bond exposed to high temperature and humidity conditions, one of the most accepted idea is a theory so called "thick oxide" failure mode [Boettcher 2010]. The "thick oxide" mode is characterized by a lifted copper ball bond after prolonged exposure of Cu-Al wire bond to humidity operational conditions as shown in Figure 7. From the image on the left, discoloration of bond site can be clearly seen overlapped by the unique pattern from the ball bond. From the image on the right, the silver-colored area in the center of the ball bond shows the remaining aluminum bonded to the copper ball bond. Results of EDX analysis as shown in Figure 8 shows what happened to the Cu-Al wire

bond. There is a significant increase of oxygen signal in the Cu-Al ball bond pad interfacial area whilst aluminum signal go down by a little bit and copper signal is also present. The author attributes this type of Cu-Al wire bond failure to the formation of an oxide layer developed at the Cu-Al ball bond pad interfacial area. This oxide layer causes the gradual loss of adhesion between copper ball bond and aluminum pad and eventually lead to the complete separation between the ball bond and pad. There are other important findings beside the formation of oxide layer at the Cu-Al wire bond interfacial region. One of them is that the oxide intensity is at its highest level at the peripheral region of Cu-Al wire bond and lowest at the center of Cu-Al wire bond. This indicates that oxidation initiates from the edge of the ball bond pad interfacial area and proceeds towards the center of it. Another important finding is that Cl signal is always present at the site of failed Cu-Al wire bond interfaces. This suggest the involvement of chlorine in the corrosion process.

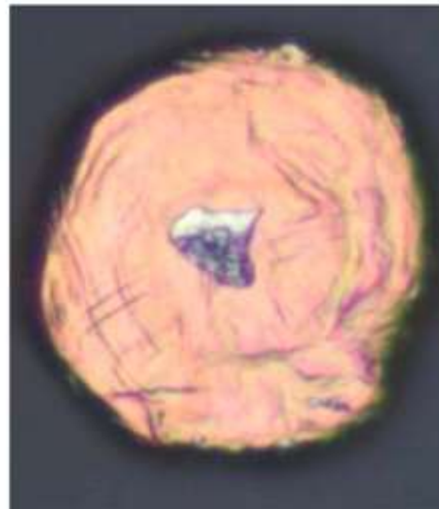

Figure 7: Images of Cu-Al WB after humidity treatment (left: top of Al pad, right: bottom of Cu ball bond) [Boettcher 2010]

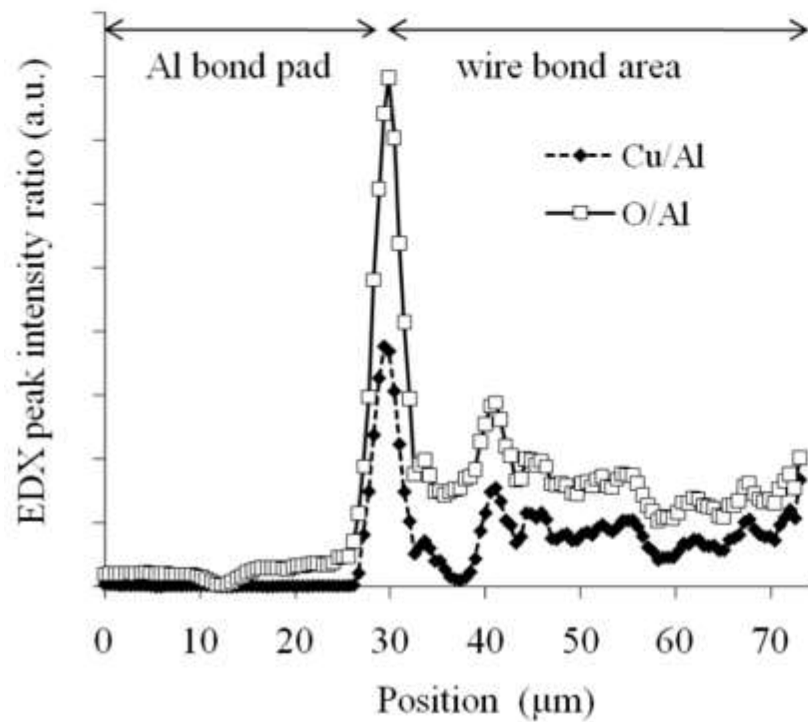

Figure 8: Result of EDX line scan across the ball bond-pad region of a failed Cu-Al WB [Boettcher 2010]

Another important study concerning Cu-Al wire bond reliability performance is the investigation of evolution of IMC microstructures. IMCs forms right after the wire bonding process. The thickness of IMC at the as-bonded stage is extremely thin (around 30 nm) and it

usually consists of $CuAl_2$ as the sole component. Thermal treatment of Cu-Al wire bond such as annealing will result in the growth as well as phase transformation of wire bond. Lu et al. has shown studies on microstructure evolution of Cu-Al IMCs [Lu 2011], wire bonds are aging at high temperature isothermal operational conditions for different amount of times and SEM and EDX analysis are performed on those Cu-Al wire bond samples as shown in Figure 9. As it can be seen from the images, the original $CuAl_2$ layer is thin and discontinues. After 5 minutes of age at 350 degrees Celsius, a new Cu-Al IMC layer is already developed due to the interdiffusion of copper atoms and aluminum atoms at the Cu-Al ball bond pad interface. After three hours of aging, Cu_9Al_4 is developed as near the copper ball bond region. The phase transformation eventually consumes all the remaining aluminum pad and the final product is Cu_9Al_4. The author also demonstrated corrosion of Cu_9Al_4 IMC layer under high temperature and result in the failure of Cu-Al wire bonds.

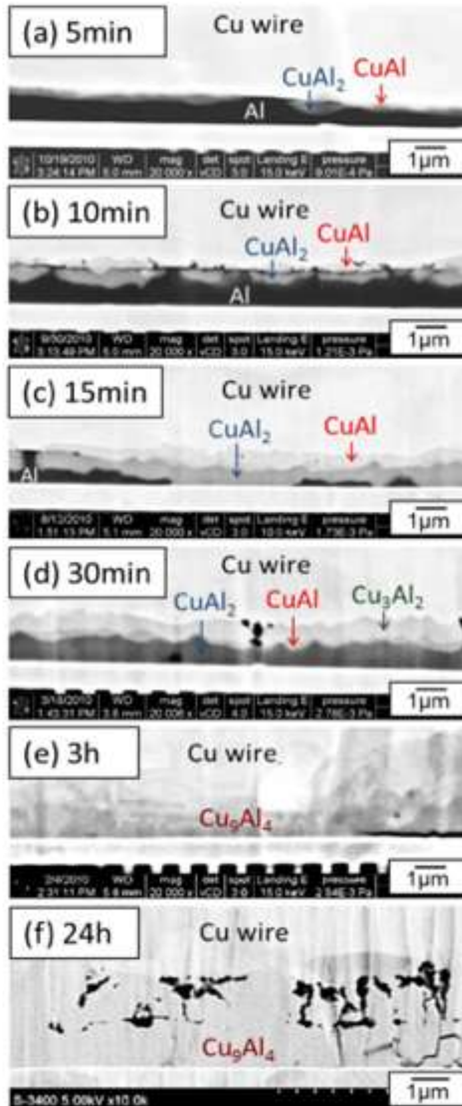

Figure 9: SEM images of Cu-Al WB central regions after exposed to 350°C for various amount of time [Lu 2011]

Both the idea of "Thick oxide" failure mode of Cu-Al wire bond and study of the evolution of Cu-Al IMCs under high temperature helps find out the most susceptible part of Cu-Al wire bond

exposed under harsh environmental conditions. It also points out corrosion as the culprit for wire bond failure and the role of chlorine involved in the corrosion process. However, it does not consider and explain the role of operational environmental conditions and EMCs on the reliability of Cu-Al wire bond. There are lots of factors which have an effect on the reliability performance of Cu-Al wire bond such as pH level, package type, temperature, humidity level, Cl contamination level, etc. It does not provide any technique or methodology to quantify the progression of Cu-Al wire bond failure. Nevertheless, they are excellent studies on Cu-Al wire bond which offer many insightful ideas and results.

2.2 Electrochemical characteristics of Cu-Al IMCs

Since corrosion at Cu-Al ball bond pad is the main reason to cause Cu-Al wire bond failures, quite a few studies [Lee 2012, Lee 2014] on Cu wire bond tried to explore the electrochemical properties of different chemical components which present at the most corrosion-susceptible region of Cu-Al wire bond. Electrochemical characteristics of Cu-Al IMCs are closely related to the corrosion behavior of Cu-Al wire bond interface. Each chemical component of Cu-Al IMCs forms a unique electrochemical potential with the environment it is surrounded by. The study conducted by Lee et al. regarding Cu-Al IMCs component such as CuAl, $CuAl_2$ and Cu_9Al_4 and palladium doped Cu-Al IMCs are successfully synthesized using an argon arc melting device. Those IMC ingots are then diced into small chucks and then assembled as shown in Figure 10. An electrical wire is soldered onto the Cu-Al IMC sample. After that, the entire sample are molded using epoxy. Then, the epoxy encapsulant was grinded to expose IMC sample surface. Finally,

surface treatment of IMC sample is followed by grinding process to remove unwanted residues on the sample surface.

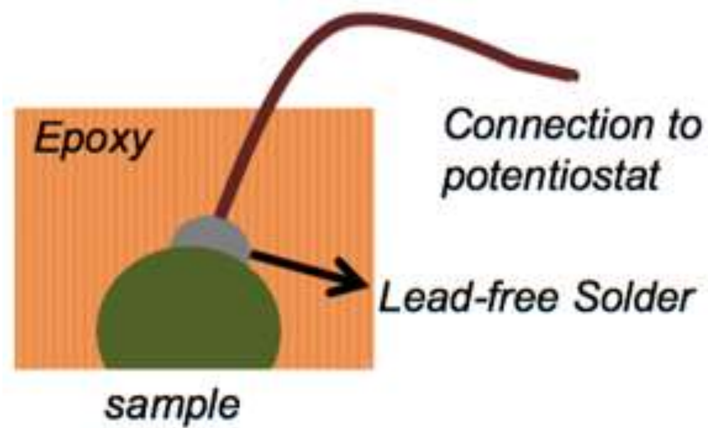

Figure 10: Assembly of a working electrode for electrochemical tests [Lee 2014]

After preparation of a test sample, a three-electrode testing system shown in Figure 11 is used to explore different electrochemical parameters of Cu-Al IMC samples at environmental conditions with varying chlorine concentrations and pH values.

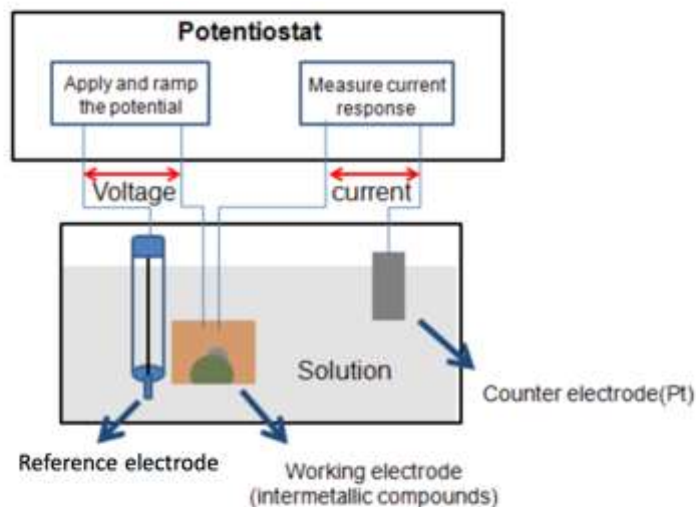

Figure 11: Schematic plot of a three-electrode electrochemical testing system [Lee 2014]

The purpose of these series of tests is to find out the effect of palladium doping, nickel doping and changing solution environment on the nobility ranking and corrosion rate ranking of Cu-Al IMCs. Part of the author's findings are shown in Figure 12 and Table 1. By comparing open circuit potential (OCP) gap among different Cu-Al IMCs, the author concluded that the addition of Pd and Ni in Cu-Al IMCs decreases OCP gap between Cu and Cu-rich IMCs, which suggests a less likelihood of galvanic corrosion between Cu and Cu-rich IMC layer. By comparing corrosion current density of different Cu-Al IMCs under different pH levels, the author finds out that the most corrosion prone Cu-Al IMC layers are different under different pH levels. Cu-rich IMCs show the highest corrosion rate in neutral and acidic solution.

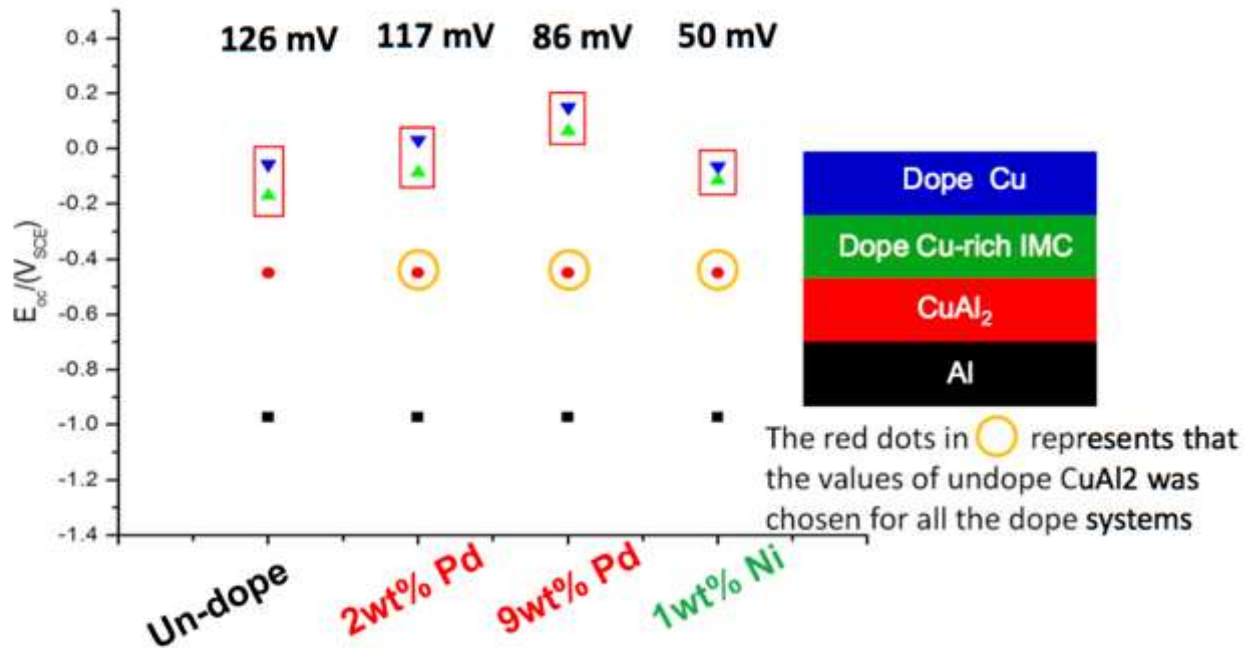

Figure 12: Result of OCP of Cu-Al IMCs [Lee 2014]

Table 1: Result of Icorr (μA/cm2) for Cu-Al IMCs at 100ppm NaCl solution[Lee 2014]

Sample	pH= 4	pH=7	pH=9
Cu	11.56	1.403	1.328
Cu9Al4	7.375	3.711	3.732
CuAl2	2.218	0.936	2.123
Al	0.855	0.290	0.328

Lee takes an electrochemical approach to study the reliability performance of Cu-Al wire bond. The result of work shows the effect of palladium doping, nickel doping and environmental factors (chlorine concentration and solution pH) on the corrosion behavior of different Cu-Al IMCs. It provides a thermodynamics-based evaluation and prediction of corrosion resistance of Cu-Al

IMCs. However, mere analysis of thermodynamics characteristics of Cu-Al IMCs is not enough to predict reaction kinetics of copper wire bond corrosion. Nevertheless, it lays the foundation for further corrosion kinetics study and exploration of electrochemical behavior of Cu-Al IMCs in this dissertation.

2.3 Chlorine diffusion in epoxy molding compounds

Epoxy molding compounds are widely used to encapsulate microelectronics. It offers package components such as Cu wire bond with mechanical and environmental protections [Pecht 1995]. The reliability performance of Cu wire bond under harsh environmental conditions is closely related to the reliability performance of EMCs. Over the years, several studies [Lu 2001, Teverovsky 2006, Seki 2010] on effect of temperature and humidity on EMCs are published. The degradation of EMCs is characterized the decreasing in their mechanical strength as well as the release of freely moved ionic contaminant such as chlorine and bromine. Oxygen and moisture ingress along with the local accumulation of chlorine eventually results in corrosion-related failure of Cu wire bonds. Therefore, understanding the transport behavior of chlorine in different EMCs becomes very crucial as the rate at which chlorine accumulate at the site of Cu-Al wire bond interface affects the lifespan of a Cu-Al wire bond. Lantz came up with several approaches [Lantz 2003, Lantz 2008] to the quantification of diffusion coefficient of ionic species in different EMCs. One of the approaches is the secondary ion mass spectroscopy. It is used to measure the concentration of ions in EMCs, as a function of the depth of penetration into EMCs. According to

the result of diffusion coefficient measurements, values of sodium diffusivity varies from $3*10^{-12}$ cm^2/s to $6*10^{-15}$ cm^2/s in EMCs at room temperature. The result indicates that diffusion coefficient of ionic species varies tremendously from one EMC to another. Some of the results are shown in Figure 13 and Figure 14. The plot in Figure 13 shows that prior to the exposure to sodium chloride solutions, the sodium and chloride ion concentrations were already there in epoxy molding compounds. The level of initial ionic concentration across the EMC sample is relatively low and constant. After the exposure to the 0.15M NaCl solution for 60 days at 85°C, Ionic concentration at the interfacial area of solution/IMC increase by a lot. The concentration level then gradually decreases as the distance from the exposed surface becomes larger. Figure 14 shows the image of tested sample. Discoloration in the cross section area of the EMC sample offers another proof of ionic transport in EMCs. In terms of the mode of ionic transport, the author speculates it to either be a bulling diffusion through the matrix or a interfacial diffusion thru the interfaces of matrix and the filler particles. In the later chapter, experimental results will show the exact ionic transport mode in EMCs.

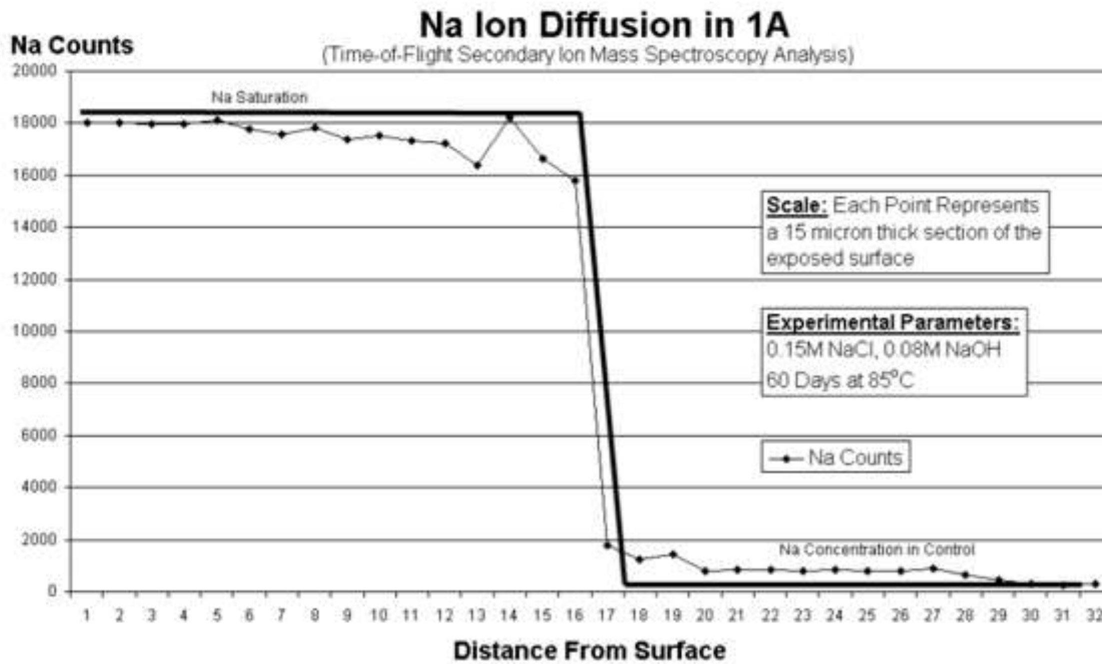

Figure 13: TOF-SIMS analysis of the fractured surface of an EMC sample after exposure to a basic NaCl solution [Lantz 2003]

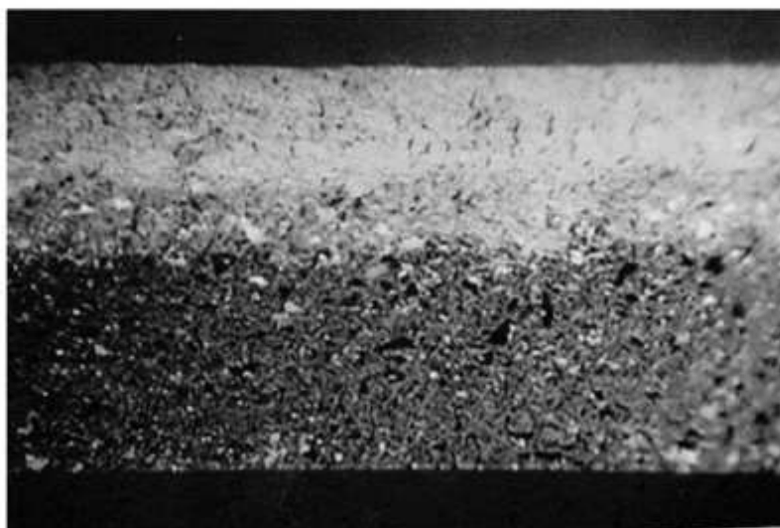

Figure 14: Discoloration of EMC samples after a 60-day exposure to a NaCl solution at elevated temperature [Lantz 2003]

Previous studies on EMCs done by Lu et al. provide the basic understanding of degradation mechanism of EMCs under harsh environmental conditions. The study done by Lantz introduces the basic transport behavior of ionic species in EMCs and provide ideas and methodologies on measuring the diffusion coefficient of chlorine in EMCs. However, as insightful as those studies, there are still of lots of crucial aspects of EMCs need to be explored. For instance, the transport mode of ionic contamination is one of them. Understanding the exact transport mode could enable researches and manufacturers come up with better ways of synthesis of EMCs. Therefore, improve the reliability performance of copper wire bond. Also, the ionic migration behavior in EMCs is still waiting to be explored. High voltage application of Cu wire bonds creates a significant electrostatic field in EMCs. Behavior of ionic transport will be influence by electrostatic field. Thus, how ionic species such as chloride ion migrates under the influence of voltage bias will have an effect on the reliability performance of Cu-Al wire bond. Another important factor needs to be paid closely attention to is the diffusion coefficient of chlorine at high temperature level and high humidity level. Only by acquiring the accurate value of diffusion coefficient and ionic mobility of chlorine at the level where electronics are operated will researches be able to model the behavior of ionic transport and make reasonable predictions on the reliability of Cu-Al wire bonds.

2.4 Levenberg-Marquardt prognostication

Previously, several leading indicator-based PHMs (health management methodologies) for remaining useful life computation of Cu-Al wire bond has been proposed by different researchers [Lall 2014, Rongen 2014]. Lall studied the microstructure evolution of Cu-Al wire bond Intermetallics under prolonged exposure to isothermal aging and then developed a methodology to keep track of the accrued prior damage of Cu-Al wire bond interconnect under harsh operational conditions based on the change in Cu-Al IMCs thickness using Levenberg-Marquardt Algorithm. Figure 15 illustrates how this approach works. Given a population of Cu-Al wire bond interconnects with unknown prior damage due to thermal aging, In order to prognosticate the remaining useful life of those wire bond interconnects, samples will be drawn randomly from the population at a constant interval Δt so that IMC thicknesses of each sample taken at the specific time interval can all be measured. After that, LM algorithm is used along with the IMC thickness measurements to solve for the unknown prior damage in Cu-Al wire bond and prognosticate the RULs of them. Figure 16 gives an example of PHM result using this approach. IMC thickness is normalized and then plotted against thermal aging duration and prediction error.

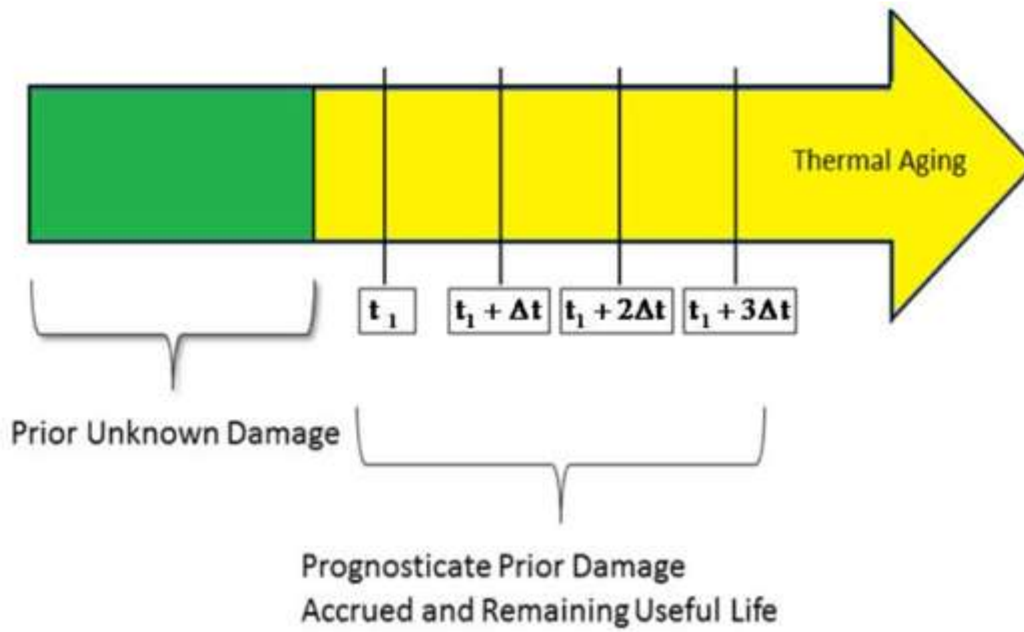

Figure 15: Prognostication of thermally aged Cu-Al wire bond interconnect

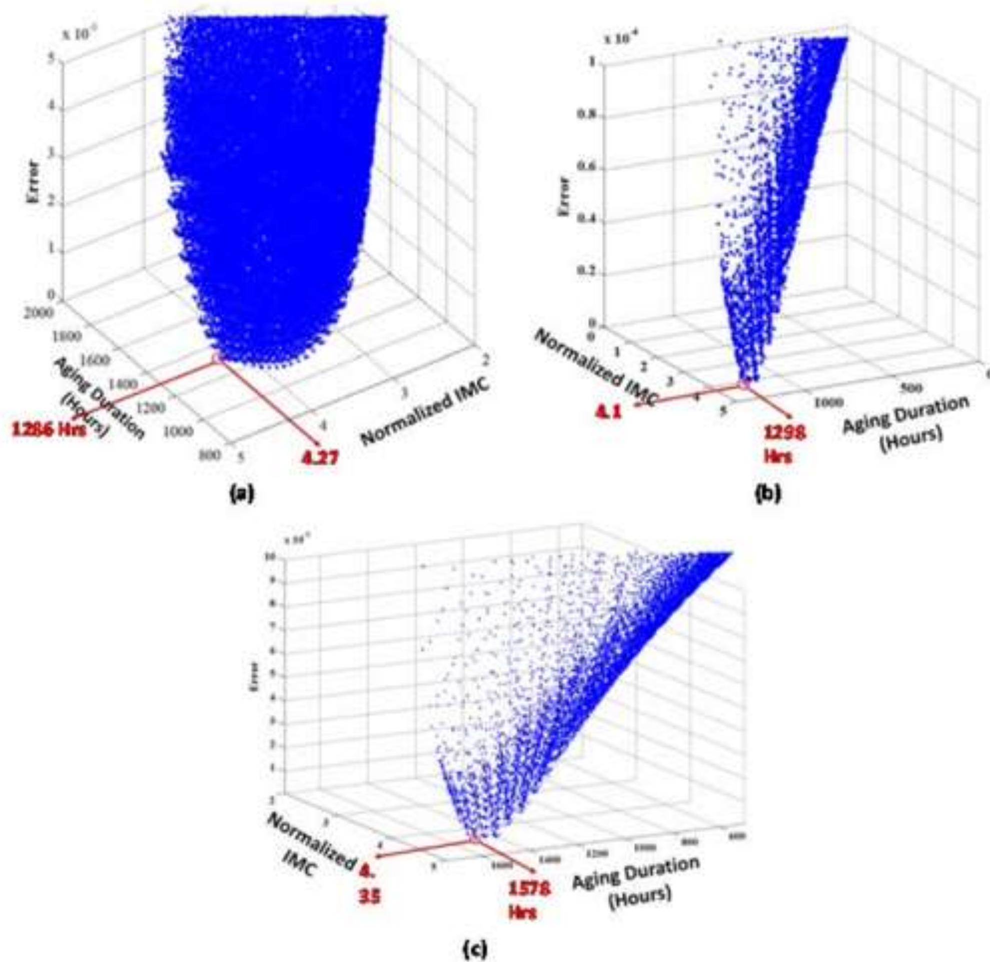

Figure 16: Example of Cu-Al wire bond RULs prognostication using LM algorithm

Rongen investigated the corrosion mechanism of Cu-Al wire bond under harsh environmental conditions and proposed three major corrosion mechanisms, which are corrosion along the Cu-ball bond to IMC interface, bulk IMC corrosion and Al bond pad corrosion. The author then developed the “planar analysis” [Halloran 2013] to monitor the change of degraded area of Cu-Al wire bond interfacial area as a function of aging duration as shown in Figure 17. The degraded Cu-Al WB

interfacial area can be visualized as two concentric circles. In inner circle is the intact area whilst the rest of the remaining area is the degraded area. These two areas are separated by the corrosion front circle. The growth of crack length of a degraded Cu-Al wire bond can be measured as a function of aging duration as shown in Figure 18. A degradation model has been built based on the crack growth sample data. Using this approach, lifetime of Cu-Al wire bond operated under accelerated stress conditions can be predicted.

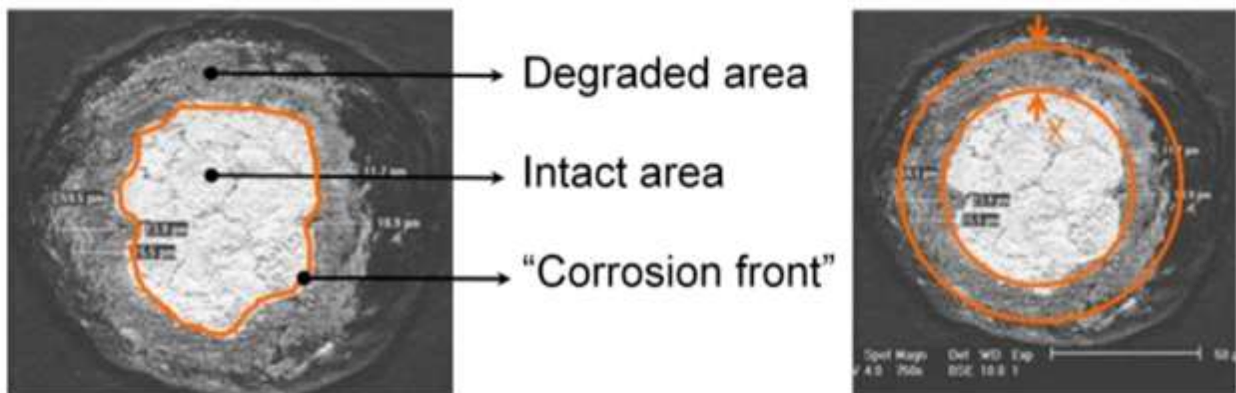

Figure 17: Example result of "planar analysis" on the Cu-Al WB interfacial area after prolonged exposure to a temperature/humidity environmental condition

The idea of taking advantage of failure leading indicators to keep track of the corrosion progression in Cu-Al wire bond is very useful. Both these two approaches presented above use a failure leading indicator to assess the damage progression in Cu-Al wire bond under harsh environmental conditions. In Lall's approach, the idea is that a Cu-Al wire bond system-state is used along with the use of LM algorithm to keep track of the state change of wire bond whilst

Rongen modified the existing reliability model for microelectronics and fitted it with measurements of Cu-Al wire bond interfacial crack length. In this dissertation, the utilization of prognostic health management (PHM) methodologies will be further explored to help assess the damage progression in Cu-Al wire bond interconnect and predict the RULs of wire bonds under exposure to highly accelerated test conditions.

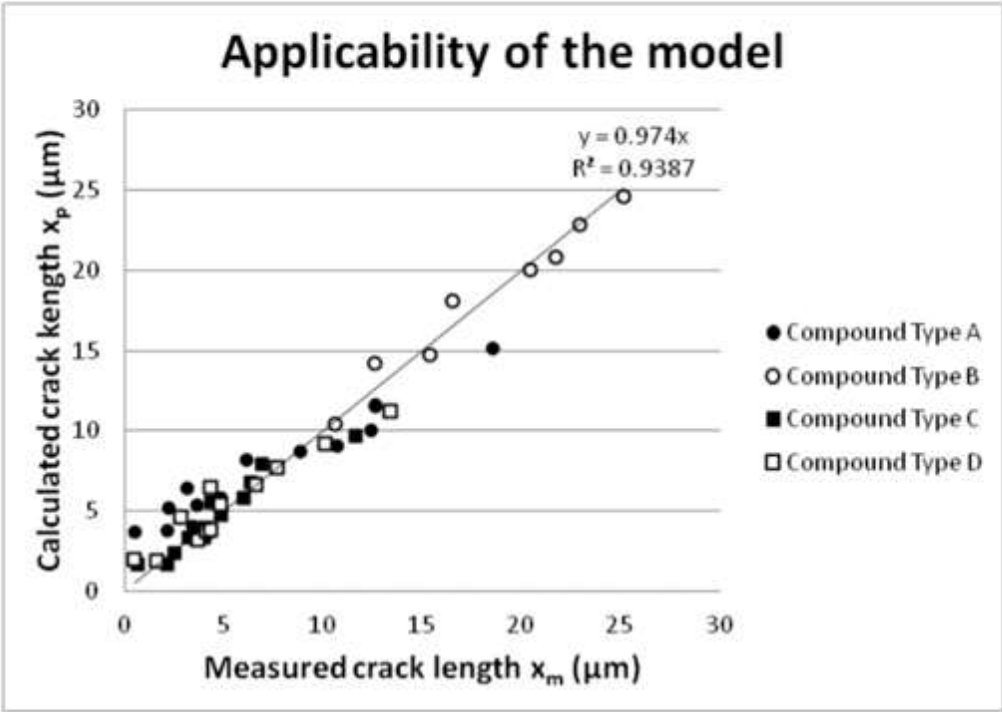

Figure 18: Example of application of life-span prediction model on Cu-Al packages with varying EMCs

Chapter 3 Extended Kalman Filter-based PHM of Cu-Al wire bond reliability under highly accelerated stress test

In this chapter, a leading indicator has been developed to monitor the progression effect of prolonged isothermal aging and temperature/humidity aging on Cu-Al wire bond and prognosticate remaining useful life based on use of resistance spectroscopy in combination with the use of extended Kalman filter (EKF). The Cu-Al wire bond resistance has been measured using a modified Wheatstone bridge along with a probe station and a lock-in amplifier. Prognostic health management technique is implemented for assessment of the remaining useful life of Cu-Al wire bond testing samples.

3.1 Resistance Spectroscopy

The method of monitoring resistance of Cu-Al wire bonds to assess their reliability performance has been used in the industry for quite a period of time [Lall 2013]. As wire bond samples age in accelerated testing environmental conditions, their electrical resistance tend to grow as the aging processes proceed. The change of resistance can be directly related to the ball shear

strength and wire pull strength [Pecht 2014] of aged wire bond. The increase of wire bond resistance indicates the corrosion progression at wire bond interfacial area. The increase of resistance also means the increase of power generated by wire bonds providing the same amount of current density in high power application. As a result, a 20 percentage resistance increase of wire bond has been used by industry is a failure threshold. Despite being used as a standard failure leading indicator, the lack of accurate measurements of wire bond resistance often leads to inaccurate assessment of wire bond reliability performance. The original resistance of a Cu-Al wire bond pair is around 0.1 ohms as measured using resistance spectroscopy [Lall 2013]. The change of resistance during the aging process could be as low as hundreds of micro-ohms. Such small measuring signals can easily be obscured by noise sources hundreds of times larger than their magnitudes. Therefore, it is necessary to develop a more sophisticated approach which enable the researchers to measure the data of electrical resistance of Cu-Al wire bond samples more accurately.

A new resistance measurement approach, resistance spectroscopy (RS), is proposed to solve the measurement accuracy issue. The RS system consists of a SRS830 Lock-In Amplifier, a modified Wheatstone bridge and a probe station as shown schematically in Figure 19. Lock-in amplifiers is designed to detect and measure very small AC signals as low as a few nanovolts. It utilizes a technique known as phase-sensitive detection (PSD) so that it is able to separate a component of the signal from the rest at a specific reference frequency and phase. The PSD can detect the signal at high frequencies with a bandwidth as narrow as 0.01 Hz. Noise signals which are at frequencies other than the reference frequency are rejected and do not affect the

measurement. Therefore, accurate measurement of Cu-Al wire bond resistance is possible. Phase sensitive detection (PSD) is a process of extracting and amplifying a signal with a known carrier wave from an extremely noisy data acquisition environment. It is essentially a homodyne detector followed by a steep low pass filter. It converts the signal's phase and amplitude to a DC voltage signal.

A frequency reference is required in order to operate the lock-in amplifier. Normally, an experiment is excited at a fixed frequency from the internal oscillator inside the lock-in amplifier.

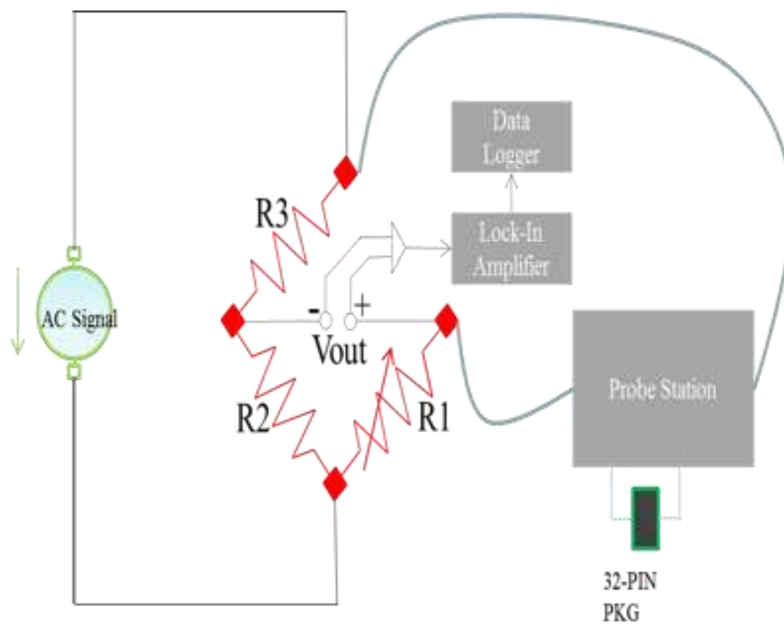

Figure 19: Schematic plot of RS setup

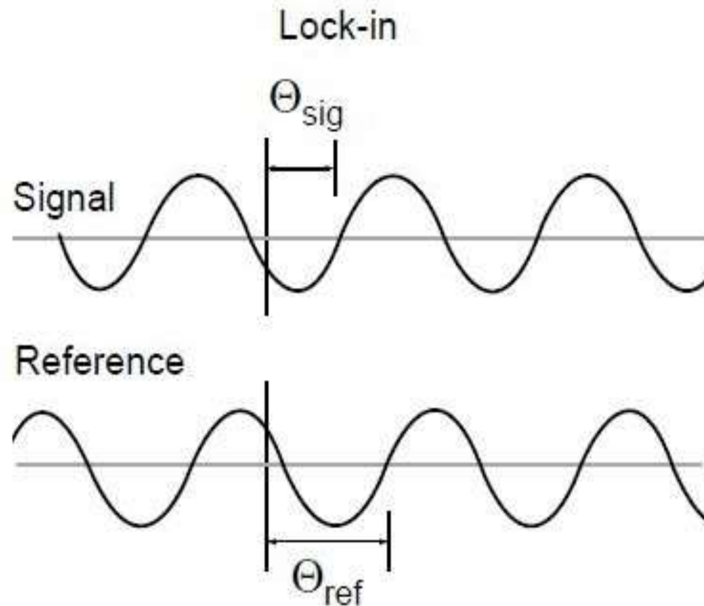

Figure 20: Lock-in Signals

After that, the lock-in amplifier detects the response from the experiment at the designated reference frequency. This could be the synchronized signal output from a function generator. Figure 20 illustrates the relationship between the reference signal and its response signal. In this case, an internal reference signal is generated by a phase-locked-loop locked to the external reference using the lock-in amplifiers SRS830. The reference signal can be represented by $V_L\sin(\omega_L t+\theta_{ref})$, where ω_L stands for the reference signal frequency, V_L represents the reference signal amplitude. θ_{ref} is the phase of the reference signal. Similarly, the response signal can be represented by $V_{sig}\sin(\omega_r t+\theta_{sig})$, where ω_r stands for the response signal frequency, V_{sig} represents the response signal amplitude. θ_{ref} is the phase of the response signal. Once both signals are generated, they are amplified and multiplied with each other by the lock-in reference using a phase-

sensitive detector. The output of the phase sensitive detection is the product of two sine wave shown in Equation (1)

$$V_{psd} = V_{sig} V_L \sin(\omega_r t + \theta_{sig}) \sin(\omega_L t + \theta_{ref}) \quad (1)$$

then use the product-to-sum identities, the equation mentioned above can be separated into two part shown in Equation (2)

$$V_{psd} = 0.5 V_{sig} V_L \cos[(\omega_r - \omega_L)t + \theta_{sig} - \theta_{ref}]$$
$$-0.5 V_{sig} V_L \cos[(\omega_r + \omega_L)t + \theta_{sig} + \theta_{ref}] \quad (2)$$

The output consists of two AC signals, one at the sum frequency (ωL+ωr) and the other at the difference frequency (ω_L-ω_r). In the following step, the output is passed through a low pass filter, thus the latter part which contains the sum of the frequency will be removed and the PLL system locks the internal reference oscillator to this external reference, leading to a reference sine wave at ωr with a fixed phase shift of θ_{ref}. Since the PLL actively tracks the external reference (ω_r=ω_L), changes in the external reference frequency do not affect the measurement. As a result, the former part of the output will turn to be a DC signal and the final output signal is shown in Equation (3)

$$V_{psd} = 0.5 V_{sig} V_L cos(\theta_{sig} - \theta_{ref}) \quad (3)$$

The output signal can be rewritten as shown in Equation (4)

$$V_{psd} \propto V_{sig} cos\theta \quad (4)$$

where θ is defined as the phase difference between the response signal and the reference signal. This signal is extremely useful as it is time invariant and it is proportional to the signal amplitude. Base on the procedures above, in order to eliminate the phase dependency, lock-in amplifier shifts

the reference signal by 90 degrees, multiplies it with the correspond signal and then pass the resultant signal though the low pass filter again, which creates the second PSD output as shown in Equation (5)

$$V_{psd} = 0.5V_{sig}V_L sin(\theta_{sig} - \theta_{ref}) \propto V_{sig} sin\theta \tag{5}$$

The two output PSD and PSD2 can be represented by X and Y, namely X=V_{sig}cosθ and Y=V_{sig}sinθ.They are considered as a vector relative to the lock-in reference oscillator in which X can be thought of as an in-phase component, whereas Y stands for the a quadrature component. When the phase difference is set to be zero (θ=0), X measures the actual signal.

A modified Wheatstone bridge has been used together with the lock-in amplifier to measure the resistance of the single wire bond inside the 32-pin chip scale daisy-chain package; the setup is shown in Figure 19. Two static resistors and one variable resistor which can be utilized to balance the modified Wheatstone bridge, a change in resistance of Cu-Al wire bond will lead to the change in magnitude of the output signal. The mathematic equation of modified Wheatstone bridge can be represented as shown in Equation (6)

$$\frac{V_{out}}{V_{sig}} = \frac{R_3R_1 - R_{PKG}R_2}{(R_2 + R_3)(R_1 + R_{PKG})} \tag{6}$$

where the resistance of Cu-Al WB pairs is represented using R_{PKG}. Figure 21 and Figure 22 displays the setup of probe station and lock-in amplifier, respectively.

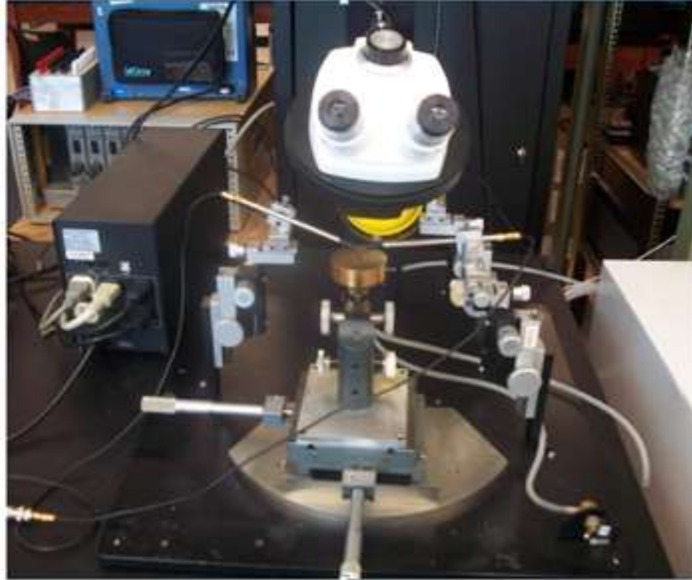

Figure 21: Probe station

Figure 22: SRS830 Lock-In Amplifier

3.2 Extended Kalman Filter

The Kalman filter (KF) is a recursive estimator which generates a statistically optimal estimate of the instantaneous state of a linear dynamic system's output that is obscured by noise [Zarchan 2000, Ribeiro 2004]. In the case of tracking the damage progression in Cu-Al wire bond due to prolonged exposure to aging at elevated temperature and/or humidity operational conditions, it is believed that the mathematic model for the progression of the Cu-Al wire bond damage is nonlinearly based. The extended Kalman filter (EKF) is a nonlinear version of the Kalman filter and it is more robust thanks to the implementation of linear approximations over small ranges of state space and the assumption of linearity over the range of estimation errors. Formerly, the Extended Kalman Filter has been applied in the field of navigation system and global position system (GPS). Here it will be applied in the field of predicting the RULs of Cu-Al wire bonds aged under different harsh environmental conditions. Figure 23 gives an example of monitoring resistance of WB using RS system. Notice the abrupt resistance change of the test sample several minutes before its failure

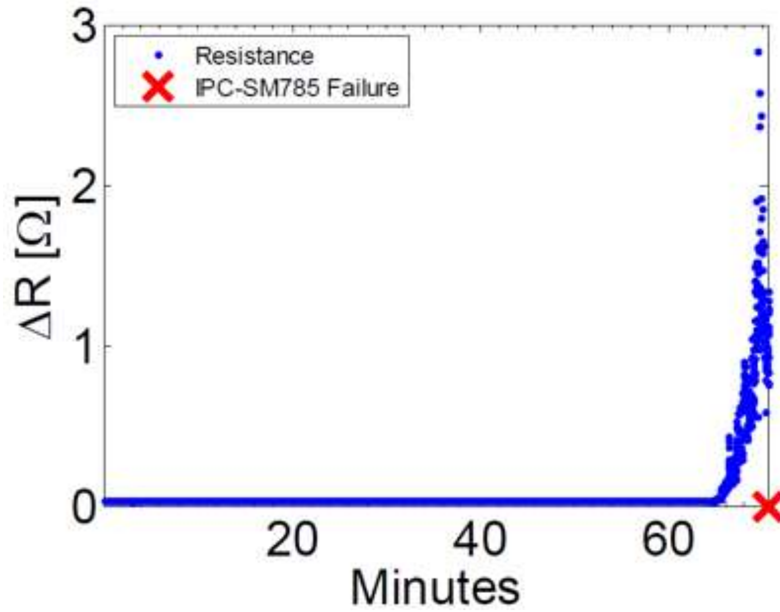

Figure 23: Example of resistance of Cu-Al WB used as a failure leading indicator

State space form has been utilized to put any set of linear differential equations into the form of the first-order matrix differential equation. In EKF, System state has been described in state space form using the measurement of the feature vector change, the first derivative of feature vector change and the exponential decay weight parameter change. In order to track the data of resistance provided by Resistance Spectroscopy (RS) setup, a nonlinear equation shown in Equation (7),

$$x = ae^{bt} \tag{7}$$

has been introduced to define as the first state representation of the state-space form. Where a and b are constant parameters, t denotes time, e stands for Euler's constant and x represents resistance. The resistance of the Cu-Al wire bond is available directly through the experiment. Also, the first and second derivatives are conducive to extrapolate the state of the feature vector into the future.

According to the state space notation above, the derivative of resistance with respect to time and the parameter b have been put into the first-order matrix to construct the state vector. The state vector x_k, can be represented as shown in Equation (8),

$$X = \lfloor x \quad \dot{x} \quad b \rfloor \tag{8}$$

Where, the first order derivative of x and the second order derivative of x have been represented by using Equation (9) and Equation (10),

$$\dot{x} = b(ae^{bt}) = bx \tag{9}$$

$$\ddot{x} = b^2(ae^{bt}) = b\dot{x} \tag{10}$$

Because of the fact that Simple numerical derivatives computed from the raw feature vector are too noisy to be useful. We need to use the Extend Kalman filter to smooth and estimate the state of all of the desired variables.

The system dynamic matrix F can be obtained from the following matrix states manipulation shown in Equation (11),

$$\begin{bmatrix} \Delta\dot{x} \\ \Delta\ddot{x} \\ \Delta\dot{b} \end{bmatrix} = \begin{bmatrix} \frac{\partial \dot{x}}{\partial x} & \frac{\partial \dot{x}}{\partial \dot{x}} & \frac{\partial \dot{x}}{\partial b} \\ \frac{\partial \ddot{x}}{\partial x} & \frac{\partial \ddot{x}}{\partial \dot{x}} & \frac{\partial \ddot{x}}{\partial b} \\ \frac{\partial \dot{b}}{\partial x} & \frac{\partial \dot{b}}{\partial \dot{x}} & \frac{\partial \dot{b}}{\partial b} \end{bmatrix} \begin{bmatrix} \Delta x \\ \Delta\dot{x} \\ \Delta b \end{bmatrix} + \begin{bmatrix} 0 \\ 0 \\ u_s \end{bmatrix} \tag{11}$$

Where us is a white process noise which is put into the rate change of parameter b in order to predict the future estimation and F is a 3by3 matrix shown above. The state vector and its evolution based on resistance spectroscopy has been taken advantage to prognosticate of system state and remaining useful life.

To apply extended Kalman-filtering techniques, the state vector can be expressed in nonlinear feature-vector form as a set of first-order nonlinear differential equations shown in Equation (12),

$$\dot{X} = FX + w \quad (12)$$

Where X is a vector of system states, F is a nonlinear function of those states which is also considered as a system dynamic matrix F that serves for the evolution of the system and w is a random zero-mean process which helps to describing the process-noise matrix shown in Equation (13),

$$Q = E(ww^T) \quad (13)$$

The extended Kalman Filter formulation requires that the measurements be nonlinearly related to the state vectors according to the Equation (14),

$$z = h(X) + v \quad (14)$$

Where h(X) is a nonlinear function of the states and v denotes a zero-mean random process described by the measurement noise matrix R, which as defined in Equation (15),

$$R = E(vv^T) \quad (15)$$

The discrete form for the systems can be rewrite as shown in Equation (16),

$$z = h(x_k) + v_k \quad (16)$$

Due to the reason that the system dynamics equations and measurement equations are both nonlinear, a first-order estimation is applied in the continuous Riccati equations for the systems dynamics matrix (F) and the measurement matrix (H) so that they can be calculated. In the Extended Kalman Filter, in order to Linearize these equations, Jacobian has been introduced to

solve the problem. Thus, the matrices are related to the nonlinear systems and measurement equations according to Equation (17) and Equation (18),

$$F = \frac{\partial f(x)}{\partial (x)}\bigg|_{x=\hat{x}} \tag{17}$$

$$H = \frac{\partial h(x)}{\partial (x)}\bigg|_{x=\hat{x}} \tag{18}$$

where x hat denotes the Extended Kalman filter approximation of system states at a future time step. The resultant discrete Kalman-filtering equation can be represented by Equation (19),

$$\widehat{x_k} = \Phi_k \, \hat{x}_{k-1} + K_k(Z_k - H\Phi\hat{x}_{k-1}) \tag{19}$$

Where, Φ_k is discrete fundamental matrix, x hat k-1 is the current estimation of the system states and K_k is discrete Kalman Filter gain. The Kalman gain has been calculated and updated at each time-step while the filter is operating, from the Riccati equations. The Ricatti equations are a set of recursive matrix equations given by Equation (20), Equation (21) and Equation (22),

$$M = \phi P \phi^T + Q \tag{20}$$

$$K = MH^T(HMH^T + R)^{-1} \tag{21}$$

$$P = (I - KH)M \tag{22}$$

Where I is the identity matrix, P is a covariance matrix representing errors in the state estimates after an update and M is the covariance matrix representing errors in the state estimates before an update. Q is the discrete process noise matrix, Q and R represent the process noise matrix and measurement noise matrix respectively.

The following passage will concentrate on the derivation of all the other matrices required for progressing the Extended Kalman Filter (EKF). First of all, system dynamics matrix can be derived from Equation (11) shown in Equation (23),

$$F = \begin{bmatrix} b & 1 & x \\ b^2 & b & 2bx \\ 0 & 0 & 0 \end{bmatrix} \tag{23}$$

the fundamental matrix has been derived from the Taylor series expansion of the system dynamics matrix shown in Equation (24), Equation (25) and Equation (26),

$$\Phi(t) = e^{Ft} = I + Ft + \frac{(Ft)^2}{2!} + \cdots + \frac{(Ft)^n}{n!} + \cdots \tag{24}$$

$$\Phi(t) = \begin{bmatrix} 1 & 0 & 0 \\ 0 & 1 & 0 \\ 0 & 0 & 1 \end{bmatrix} + \begin{bmatrix} b & 1 & x \\ b^2 & b & 2bx \\ 0 & 0 & 0 \end{bmatrix} t + \begin{bmatrix} b & 1 & x \\ b^2 & b & 2bx \\ 0 & 0 & 0 \end{bmatrix}^T \begin{bmatrix} b & 1 & x \\ b^2 & b & 2bx \\ 0 & 0 & 0 \end{bmatrix} \frac{t^2}{2!} + \cdots \tag{25}$$

$$\Phi(T_s) = \begin{bmatrix} b^2 {T_s}^2 + bT_s + 1 & bT_s + T_s & \frac{3b{T_s}^2 x}{2} + T_s x \\ b^3 {T_s}^2 + b^2 T_s & b^2 {T_s}^2 + bT_s + 1 & \frac{3b^2 {T_s}^2 x}{2} + 2bT_s x \\ 0 & 0 & 1 \end{bmatrix} \tag{26}$$

To proceeding the Riccati Equations, the discrete process-noise matrix Q_k can be found from the continuous process-noise matrix Q and the fundamental matrix according to the Equation (27),

$$Q_k = \int_0^{T_s} \Phi(\tau) Q \Phi(\tau)^T dt \tag{27}$$

where Ts denotes the sampling time, Q is the discrete process noise which can be expressed by using Equation (28),

$$Q = \Phi_s \begin{bmatrix} 0 & 0 & 0 \\ 0 & 0 & 0 \\ 0 & 0 & 1 \end{bmatrix} \tag{28}$$

Where Φs denotes the continuous process-noise spectral density.

So far all the matrices required to solve the matrix Riccati equations have already been defined, the final step is to propagate the extended states from the present step sampling time to the next step sampling time using Euler numerical integration of the nonlinear differential equations shown in Equation (29) to Equation (34),

$$\bar{\dot{x}}_k = \hat{\dot{x}}_{k-1} + T_s \bar{\ddot{x}}_{k-1} \tag{29}$$

$$\bar{x}_k = \hat{x}_{k-1} + T_s \bar{\dot{x}}_{k-1} \tag{30}$$

$$\hat{x}_k = \bar{x}_k + K_{1k} Res_k \tag{31}$$

$$\hat{\dot{x}}_k = \bar{\dot{x}}_k + K_{2k} Res_k \tag{32}$$

$$\hat{\mathrm{b}}_k = \hat{\mathrm{b}}_{k-1} + K_{3k} Res_k \tag{33}$$

$$\bar{\ddot{x}}_k = \hat{\mathrm{b}}_k \hat{\dot{x}}_k \tag{34}$$

where subscript k denotes all projections of the states from preceding estimated to the current time. Res_k stands for the residual which gives the difference between the present measurement and the preceding estimate.

EKF filtering algorithm and block flow diagram are presented below and schematically shown in Figure 24.

(1) initiate the state vector xbar and xtilt at the present time

(2) calculate the projection of component of state vector xbar and xdotbar

(3) initiate the covariance matrix P

(4) calculate the system dynamic matrix F

(5) estimate the fundamental matrix Φ

(6) approximate the discrete process-noise matrix Q

(7) compute the covariance matrix M

(8) calculate the Kalman gain matrix K

(9) measure the resistance of Cu-Al wire bond Z at the present time

(10) update the state vector xtilt

(11) update the projection of component of the state vector xdoubledotbar

(12) update the covariance matrix

(13) iterate to the second step for continuous projection of the future states

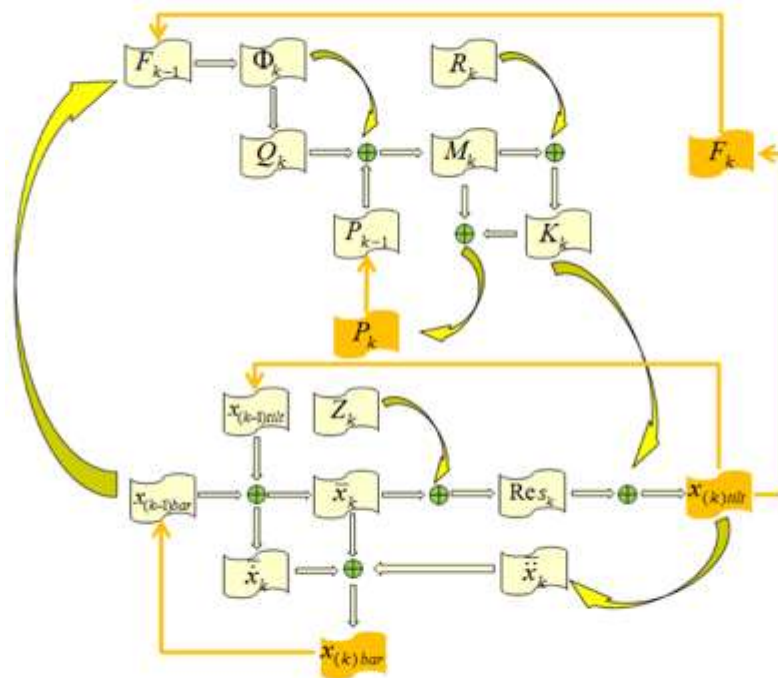

Figure 24: EKF operation diagram

3.3 Test vehicle, Test Conditions & Test Results

The test vehicle used in experimental analysis is a 32-pin chip scale microelectronic package. There are 16 Cu-Al wire bond pairs in the chip. Dimensions and Figures of the package are shown in Table 2 and Figure 25.

Table 2: Specifications of the test vehicle

Sr. Number	Parameter	Dimensions (mm)
1	Width	4.5
2	Length	5.5
3	Height	0.7
4	Length of pin	0.45
5	Width of pin	0.3
6	Pitch	0.5

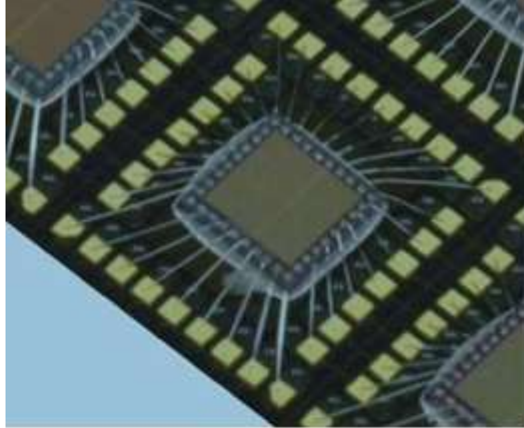

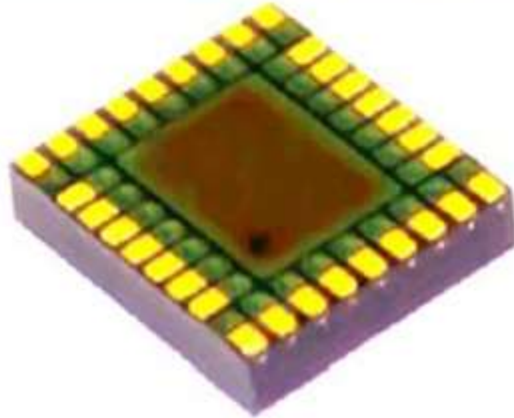

Figure 25: 32-pin chip-scale package

A set of 4 packages has been put into each of the three different type of thermal chamber for prolonged time period to simulate varies harsh working environment it may encounter. Environmental conditions included: 200°C for 10days, 85°C and 85% RH for 8 weeks and -40°C to 125°C for 5 hundred cycles. The resistances of the wire bond are obtained every 24 hours for 200°C environment, every 7 days for 85°C /85RH and every 50 cycles for the thermal cycling environment. Resistance spectroscopy measurements will be taken once every several days

according to time intervals respectively listed above. Figure 26 shows one of the chambers used for accelerated aging test.

Figure 26: Temperature humidity chamber used for harsh environmental aging test

3.4 Experimental results and RUL predictions

In the Extended Kalman Filter based model, the state projections have been constructed by using a nonlinear model. Linearization has been done by taking a Jacobian and evaluating in the neighborhood to estimate the next time step value. Process noise and measurement noise for EFK at the beginning of data tracking has been set to 0.0001 and 0.001 respectively. Figure 27, Figure 28 and Figure 29 show the experimental results and the performance of EKF tracking states.

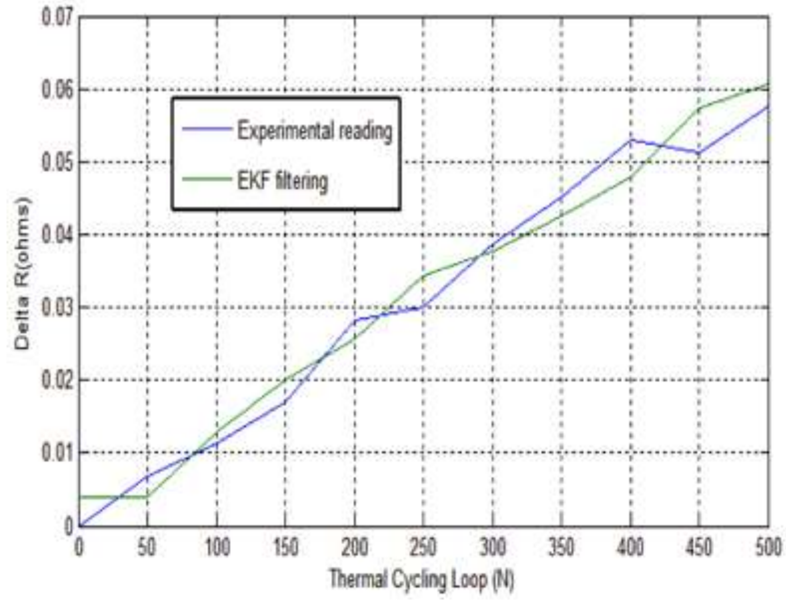

Figure 27: Experimental result of change of Cu-Al WB resistance over 500 thermal cycling loops and EFK filtering performance

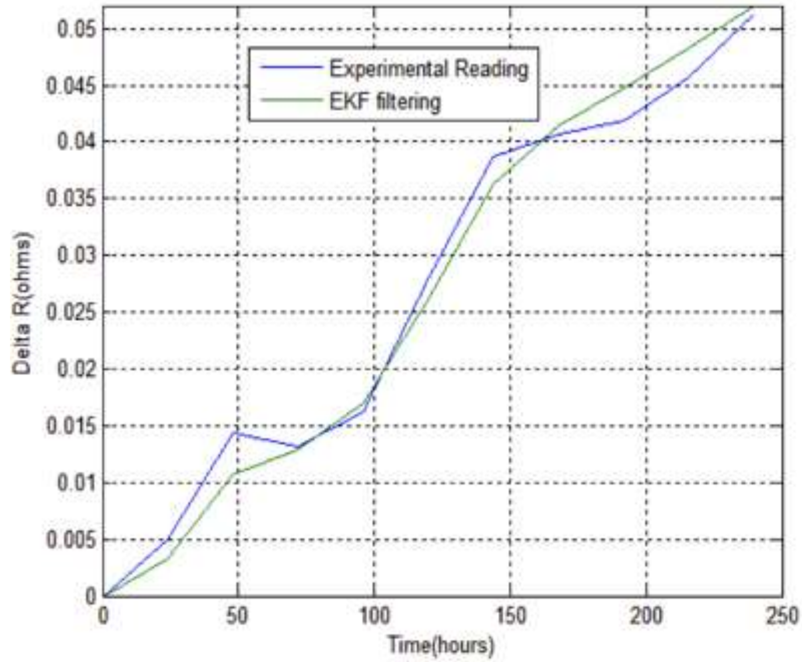

Figure 28: Experimental result of change of Cu-Al WB resistance over 240 hours under 200°C isothermal aging condition and EFK filtering performance

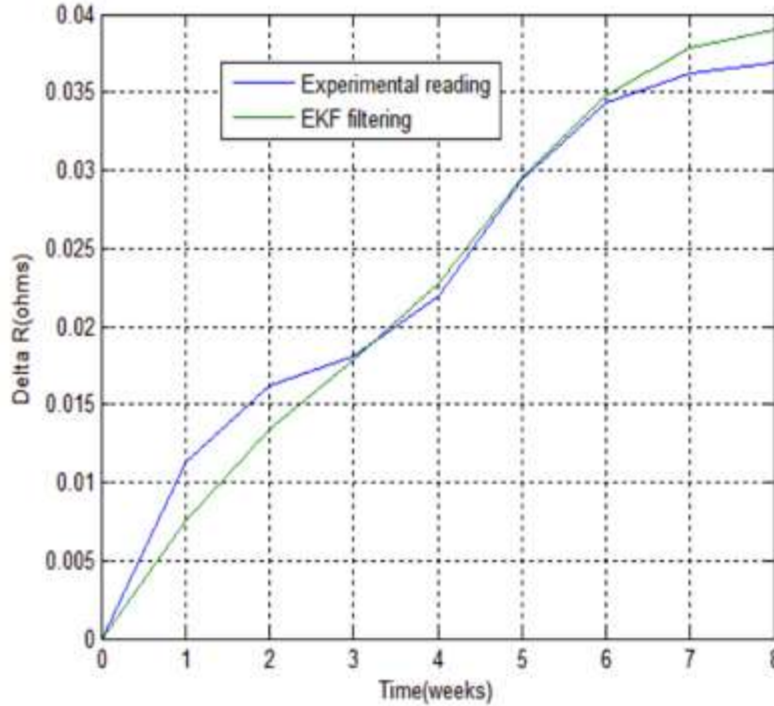

Figure 29: Experimental result of change of Cu-Al WB resistance over 8 weeks under 85RH/85°C temperature humidity aging condition and EFK filtering performance

It can be seen from results above that the resistance of single Cu-Al wire bond pair increases 0.057ohms, 0.094ohms and 0.017ohms under 3 different type of thermal aging condition, respectively. The EKF tracks the datasets very well in all the cases. Also, it is anticipated that the better EKF tracks the experimental reading will lead to better convergence and better performance of RUL closer to actual end of life of the wire bond. Feature state vectors generated from the EFK had been further developed. A nonlinear equation $x=ae^{bt}$ has been utilized to project further performance of every single EKF filtering sample point. The change of measurement of the feature vector, the change of first derivative of feature vector and the change of exponential decay weight parameter give rise to the different traces of different data points. The standard failure threshold

for the resistance of Cu-Al wire bond had been set to prognosticate remaining useful life (RUL) shown in Figure 30, Figure 31and Figure 32.

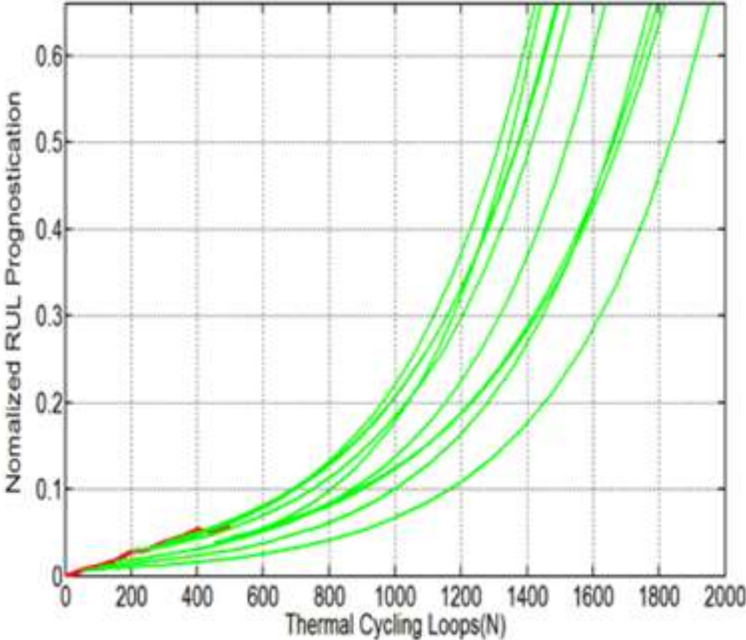

Figure 30: PHM result of Cu-Al wire bond under thermal cycling condition for 500 loops

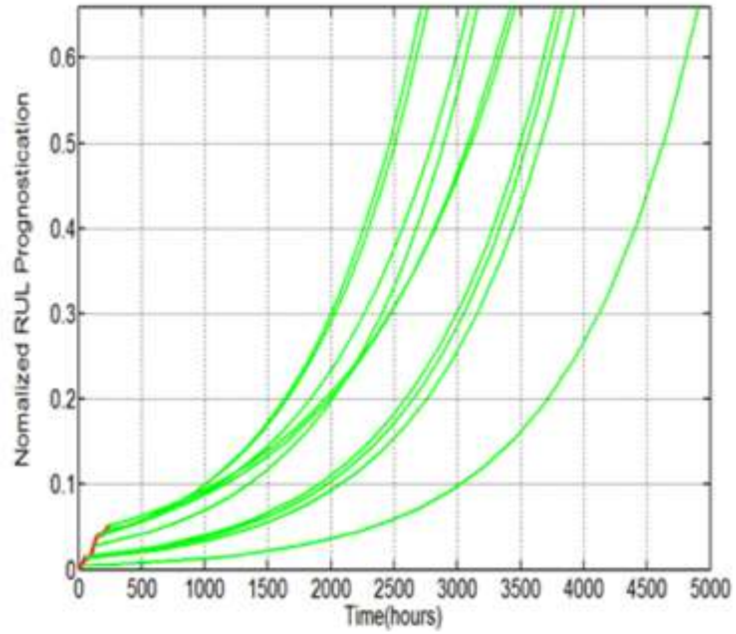

Figure 31: PHM result of Cu-Al wire bond under 200C for 240 hours

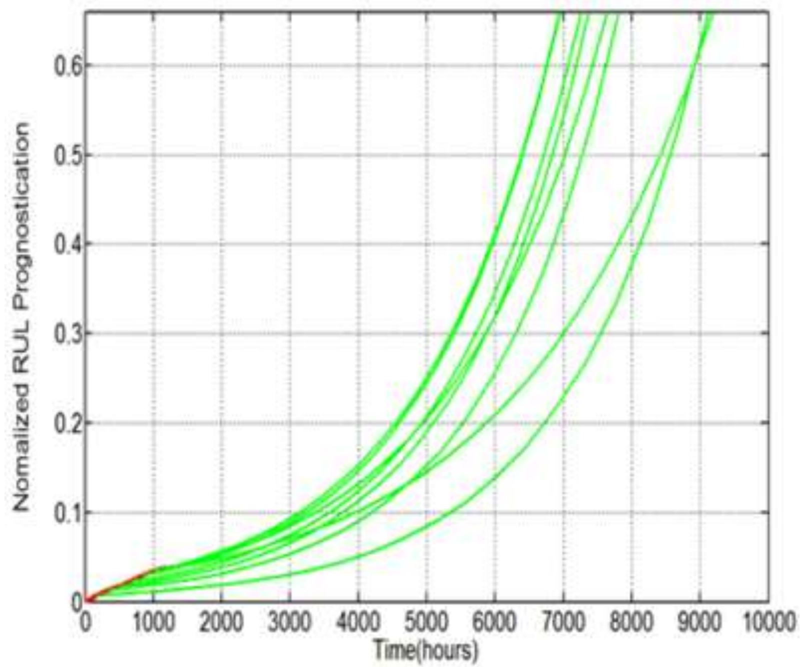

Figure 32: PHM result of Cu-Al wire bond under 85RH/85°C for 8weeks

From the PHM results above, it shows that it will take approximately 1634hours, 3552 hours and 7670 hours to for the Cu-Al wire bond to fail under the thermal cycling aging condition, high temperature isothermal aging condition and thermal/humidity aging condition, respectively.

Prognostic Horizon is defined as the difference between the time when the predictions first meet the specified performance criteria and the time for End of the life. Here the EOF is replace by the peak value of the experimental reading. The performance requirement is specified in terms of ten percent error bound around true EOL. The performances of prognostic horizons are shown in Figure 33, Figure 34 and Figure 35. As it can be seen from the results, in all three cases, life predictions at the beginning of the Cu-Al WB aging stage are not very accurate. This is because the EKF filter hasn't gather enough sample data point to be able to predict the future state of resistance of Cu-Al WBs. As more and more sample points are acquired and processed by the filter, more and more accurate the perditions become.

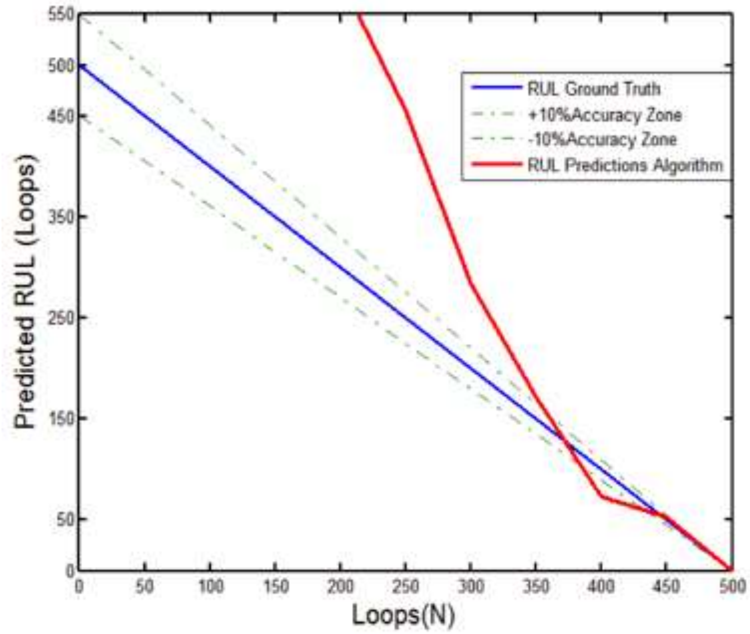

Figure 33: Performance of prognostic horizon of the result of Cu-Al wire bond under thermal cycling condition for 500 loops

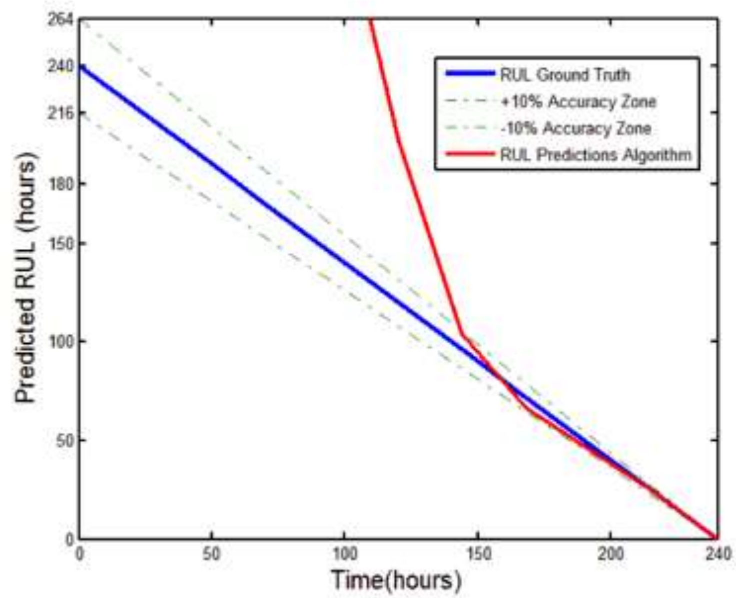

Figure 34: Performance of prognostic horizon of the result of Cu-Al wire bond under 200C for 240 hours

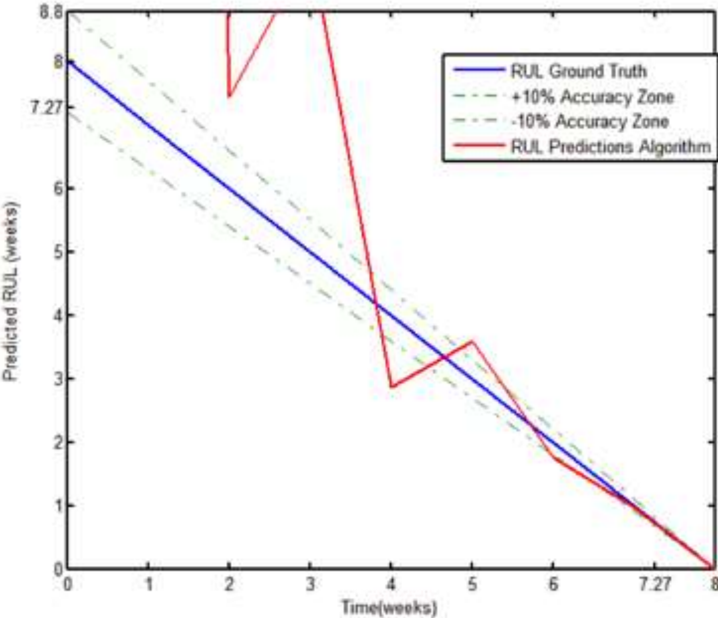

Figure 35: Performance of prognostic horizon of the result of Cu-Al wire bond under 85RH/85°C for 8weeks

Chapter 4 Chlorine transport in EMCs

In this chapter, a multiphysics model for ionic transport in EMCs is established. The contaminant diffusion along with the corrosion kinetics has been modeled. In addition, contaminated samples with known concentration of KCl contaminant have been subjected to the temperature humidity conditions (130°C/100RH). The resistance of the Cu-Al interconnects in the PARR test have been monitored periodically using resistance spectroscopy. The diffusion coefficients of chloride ion at various temperatures in the molding compound have been measured using inductively coupled plasma. Measured diffusion coefficients have been incorporated into the COMSOL multiphysics model. Moisture ingress into the EMC has been quantified through measurements of the weight gain in the EMC. Predictions from the COMSOL multiphysics model have been correlated with experimental data.

4.1 Chlorine in Epoxy Molding Compounds

IC packaging industry has always required that its components have little or no ionic contamination. This is essential to minimize the effect of ion-related corrosion issues within the package. In this paragraph, a detailed description for ion-related corrosion in the microelectronic

package will be presented. First of all, the possible sources of the ion contaminant will be discussed. The packaging of semiconductor chips is prone to contamination from a number of sources. These include the operational environment, the materials used, the processes and the equipment involving in the manufacture of the packages. Small concentration of ions is always present in epoxy molding compounds. Those ions include chloride, sodium, potassium and bromine. One of the reasons for ions ingress in EMCs is because of the chemical synthesis of the subcomponents of the resins. Ethylene oxide and propylene oxide are typical resin components, since they react with alcohol and phenols immediately. Functional groups are attached to these epoxy rings in the presence of NaOH. This will ultimately result in the formation of NaCl. Even though they are purified, there always will be a small concentration of it left in the epoxy molding compounds. In addition, ions liberated from die-attach glue at high temperature or other type of harsh environmental conditions is another possible source of ion contaminant. Besides, the etching of metallization will introduce corrosive ions into electronic packages as well. Contaminant ions from flame-retardants have been identified as one of the primary corrosive ions sources in the encapsulants.

The primary site of corrosion in encapsulated microelectronic devices is the bond pad interface as shown in Figure 36 , which is not protected by a passivation coating and thus makes it most susceptible to be attacked by the corrosive ions such as chloride. Cu wire is one of the most widely used interconnect material in packaging due to its advanced thermal and electrical property over gold wire and Aluminum is the bond pad material.

Figure 36: SEM image of bond pads and pitting corrosion [Wolff 2010]

The corrosion reaction will be presented by a series of subsequent chemical reactions [Soestbergen 2007] shown in Equation 35 to Equation 37,

$$Al \rightarrow Al^{3+} + 3e^{-} \tag{35}$$

$$2Al^{3+} + 3H_2O \rightarrow 2Al(OH)_3 + 3H^{+} \tag{36}$$

The Al ions react with water and form aluminum hydroxide. Dehydration of $Al(OH)_3$ will lead to the formation of alumina (Al_2O_3). The anode attracts negatively charged ions, such as chloride. These ions will attack the protective oxide layer resulting in pitting corrosion. It is considered that pitting corrosion is primarily as a result of the attack of chloride.

$$2\mathrm{Al(OH)_3} + \mathrm{Cl^-} \rightarrow 2\mathrm{Al(OH)_2Cl} + \mathrm{OH^-} \tag{37}$$

Aluminum hydroxide reacts with chloride. After dissolution of the protective oxide film, bare aluminum corrodes according to Equation 38,

$$2Al + \mathrm{Cl^-} \rightarrow AlCl_4^- + 3e^{-} \tag{38}$$

The corrosion product now diffuses into the bulk solution and hydrolyzes yielding $Al(OH)_3$ and Cl-. Therefore, previous chemical reactions will happen again. Pay attention to the fact that a small concentration of chlorine ions can cause a large amount of corrosion since these ions are released during the process of chemical reactions. This incorporates with adsorbed electrolyte on the surface will result in a highly active galvanic cell, which will eventually result in a dramatic increase in the rate at which chloride diffuse to the bond pad.

4.2 Test Vehicle & Test Approaches

The test vehicle used in this chapter is the same 32-pin chip scale Cu-Al wire bond package used in the previous chapter. The specifications and image of package are shown in Figure 37.

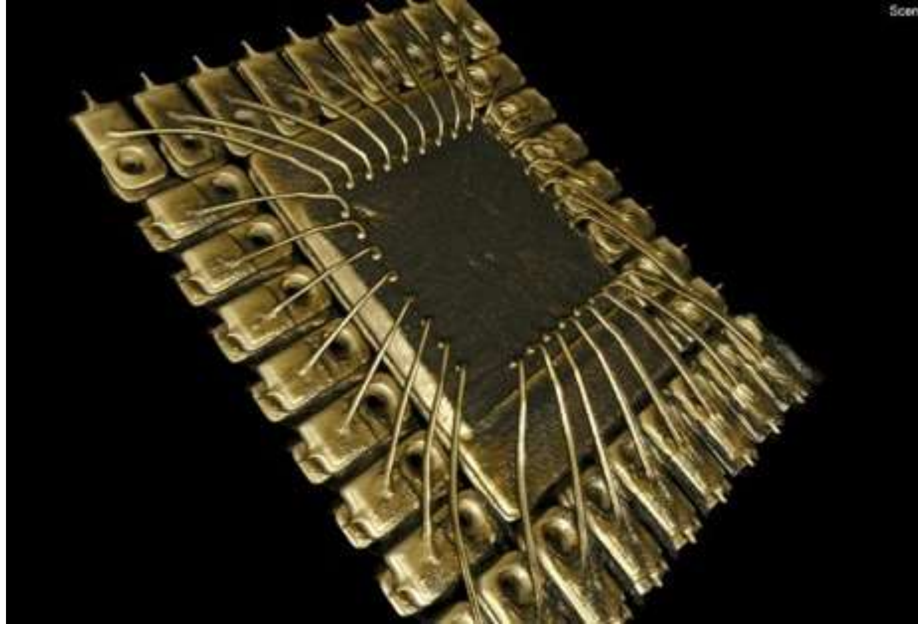

Figure 37: MicroCT image of 32pin chip scale Cu-Al wire bond package

(a) Packages with Built-In Contaminant Test

A set of 12 packages has been put into PARR bomb and the environmental condition of the aging condition is (130°C/100RH). In which half of the samples had been pre-contaminated with a known amount of chloride before being packaged. The resistance of the Cu-Al interconnects in the PARR test have been measured periodically using resistance spectroscopy. The other half of the samples is corresponding samples that are used as baselines. Comparisons will be made between the doped samples and the baselines to study the effect of ion contaminant. The optical microscope picture has been taken before molding the doped packages. Those Images will be used

to study the correlation between the location of the KCL drop inside the chip and the rate at which the Cu-Al wire bond fails.

(b) Diffusion Coefficient Measurement

Inductively coupled plasma is a powerful tool for the determination of concentration of ionic species in a variety of different sample matrices [Simon 2004]. The procedure of this process is illustrated schematically in Figure 38. With this technique, solid samples are ashed by high temperature and then ashes are dissolved into a specific solution. After that, solution is injected into a radiofrequency (RF)-induced argon plasma using one of a variety of nebulizers. The sample mist reaching the plasma is quickly dried, vaporized, and energized through collisional excitation at high temperature. The atomic emission emanating from the plasma is viewed in either a radial configuration, collected with a lens or mirror, and imaged onto the entrance slit of a wavelength selection device. Single element measurements can be performed with a simple monochromatic tube combination, simultaneous multielement determinations are performed for up to 70 elements with the combination of a polychromatic and an array detector. The analytical performance of such systems is competitive with most other inorganic analysis techniques, especially with regards to sample throughput and sensitivity.

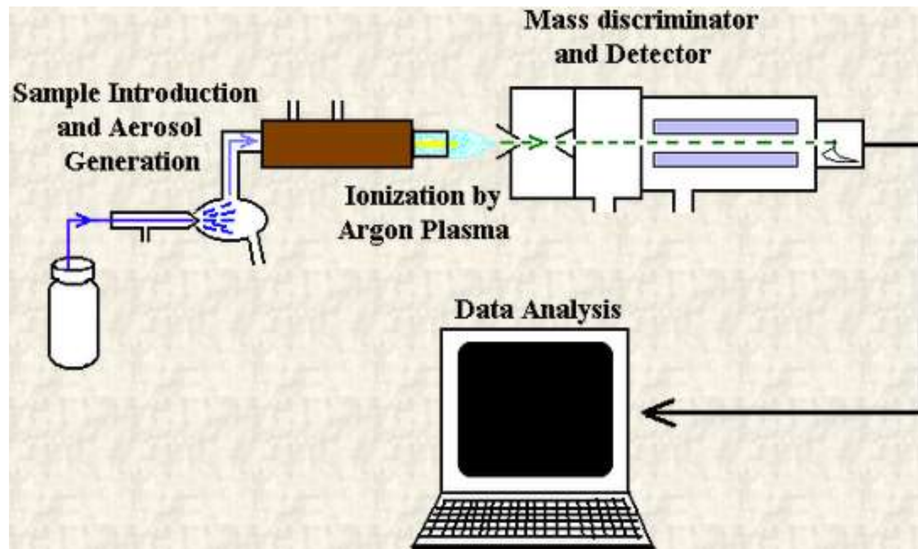

Figure 38: Schematic of ICP-MS main processes [Workley 1996]

(c) Multiphysics Finite Element Model

The primary site of corrosion in encapsulated devices is the bond pad as it is discussed in previous passage. However, the contaminant must transport to the bond pad area in order to react with the bond pad metallization. Thus the ability of the ions to transport in the encapsulant is expected to play an extremely important role in the rate of corrosion and the reliability of encapsulated devices. In this work, a multi-physics finite element model is used to estimate the effect of temperatures and applied electrical bias on the transport behavior of chlorine at the bond pad-molding compound interface.

Theory

The transport of ionic specie i is given by the Nernst Planck Poisson (PNP) equation as shown in Equation 39,

$$N_i = -D_i \nabla c_i - z_i \mu_i F c_i \nabla V \tag{39}$$

Where Ni is the ionic flux (numbers of ions per unit area per unit time), Di is the diffusion coefficient of species i, ci stands for its concentration, zi denotes its valence. F is the universal gas constant and V is the applied electrostatic potential. The mobility of the charged particle i is given by the Einstein-Smoluchowski relation shown in Equation (40),

$$\mu_i = D_i e / k_B T \tag{40}$$

Where kB is Boltzmann constant. T stands for the temperature; e is the elementary charge. The change of ion concentration in time is governed by Equation (41),

$$\frac{\partial c_i}{\partial t} = -\nabla N_i \tag{41}$$

Where t denotes time. Finally, the ion concentration is coupled to the electrical field according to the Poisson's equation shown in Equation (42) and Equation (43),

$$E = -\nabla V \tag{42}$$

$$\nabla . (\varepsilon_0 \varepsilon_r E) = \rho_v = F \sum_i z_i c_i \tag{43}$$

where E stands for the electrical field (V/m), ε0 is the permittivity of vacuum and εr is the relative permittivity. ρv stands for the electrical charge density.

Model

A 3D model shown in is constructed as a start point to simulate the transport of chloride in the epoxy molding compound.

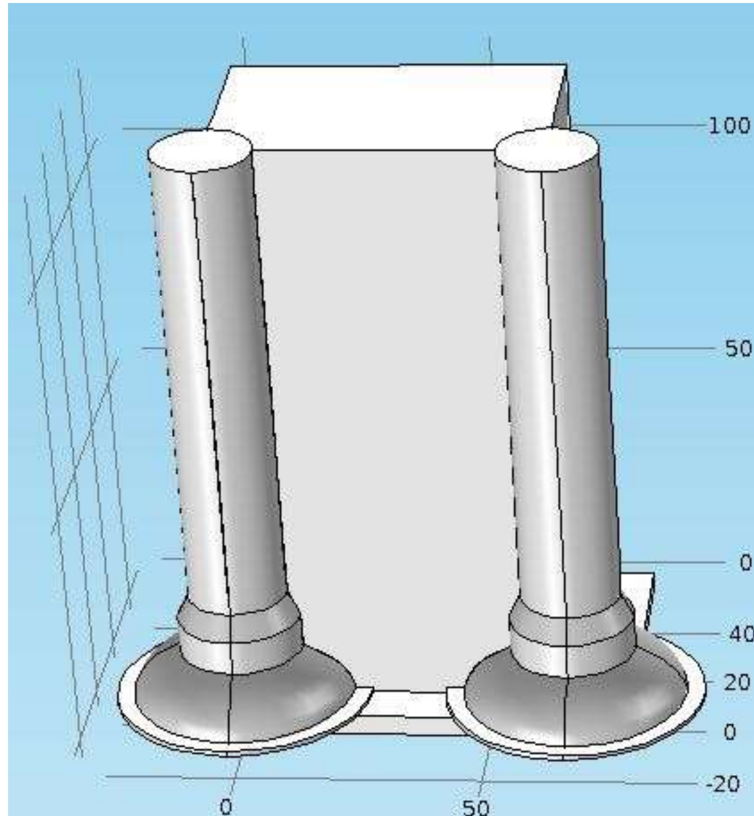

Figure 39: 3D model of chlorine transfer in EMCs [unit in micrometer]

Two bond wires including two bond balls on two pads has been modeled along with the epoxy molding compound encapsulant in between using COMSOL. The relative permittivity of the MC is set to be 4. The bond pads and encapsulant are placed on a 4 m thick interconnect stack. Despite the reason that this stack is made of a metal interconnect structure and a dielectric material, it is modeled as a material with a relative dielectric constant equal to zero. It is hypothesized that the die underneath the interconnect stack results in a zero potential at the bottom of this stack.

Equations above can be used to numerically solve the problem of the ion transport in dilute mixture of point charges, however, for a system of ions in the epoxy molding compound, deviations from the equations above is possible because of the reasons such as non-electrostatic interactions of ions with the polymer matrix. Another effect which needs to be taken into consideration is the fact that the polymer only contains a limited amount of space available for ions to accumulate [Bazant 2007], which leads to a maximum ion concentration. Steric effects can be used to explain the polymer space constraint. Equation (39) is modified in such a way it takes the polymer space constraint into account shown in Equation (44),

$$N_i = -D_i \nabla c_i \left(1 + \frac{\frac{c_i}{c_\infty}}{1 - \frac{c_i}{c_\infty}}\right) - z_i \mu_i F c_i \nabla V \tag{44}$$

Here, c_∞ stands for the maximum concentration of ionic species that is allowed in epoxy molding compound. Equation (44) is added an addition term to meet the constraint. Also, at charged interface which is the primary site of corrosion, electrostatic double layer will be formed as shown schematically in Figure 40.

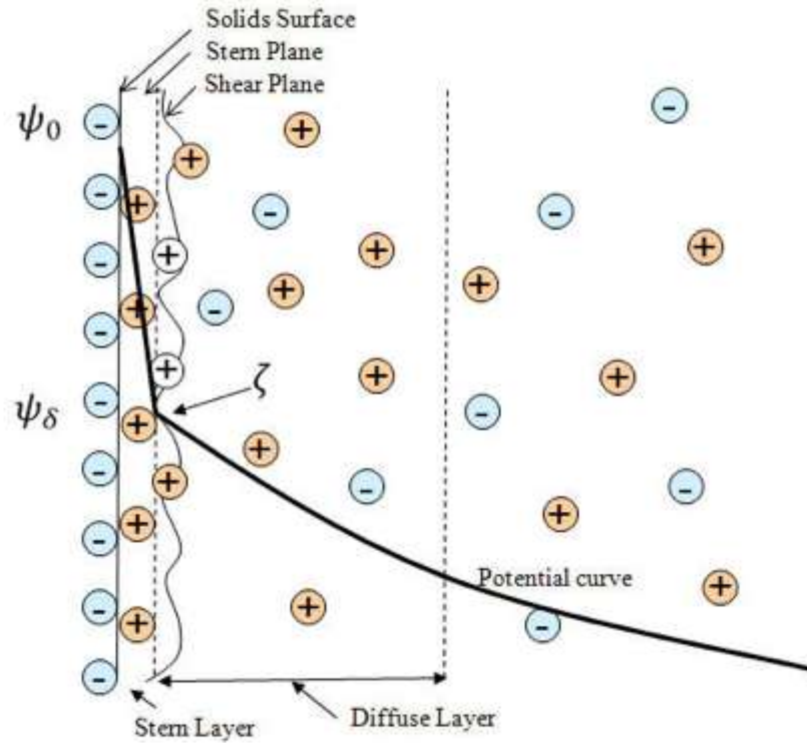

Figure 40: Electric double layer according to Stern's model

The first layer comprises ions adsorbed onto the object due to chemical interactions. The second layer is composed of ions attracted to the surface charge via the Coulomb force, electrically screening the first layer. This second layer is loosely associated with the object. It is made of free ions that move in the fluid under the influence of electric field rather than being firmly anchored. In an electrolyte for a symmetric monovalent ion, the thickness of the electric double layer is in the scale of tens of nanometers, which is the Debye length. And it is given by Equation (45),

$$\kappa^{-1} = \sqrt{\frac{\varepsilon_0 \varepsilon_r RT}{2F^2 C_{bulk}}} \tag{45}$$

Where C_{bulk} denotes the concentration of the bulk solution. Figure 41 shows that in epoxy molding compounds, the Debye length is in the range of 1 to 100 nm.

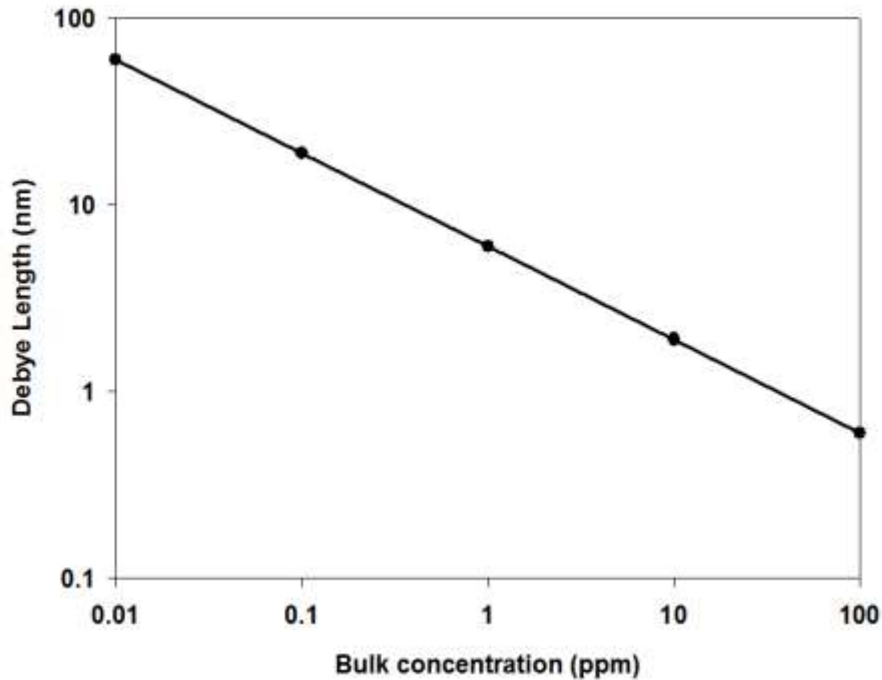

Figure 41: Debye Length in terms of bulk concentration of ion in EMC, εr=4, T=298K, ppm to mol/m3 ratio is 76.92 to 1

Since the length of the electric double layer forms in the vicinity of electrode is in the order of nanometers, an extremely fine mesh is crucial in order to capture the characteristics of EDL, which will tremendously increase the computing time. Thus, it is not likely to solve the large three dimensional models. The model needs to be simplified. In the absence of the effect of Fick's laws [Soestbergen 2007], the electrical field becomes the sole fact that causes the transport of ions. Therefore, at the beginning, Equation (42) and Equation (43) will be solved without the

redistribution of ions and the results of it will be used to simplify the geometry of the model as much as possible in such a way that the initial electrical field stays almost the same as the original 3D model.

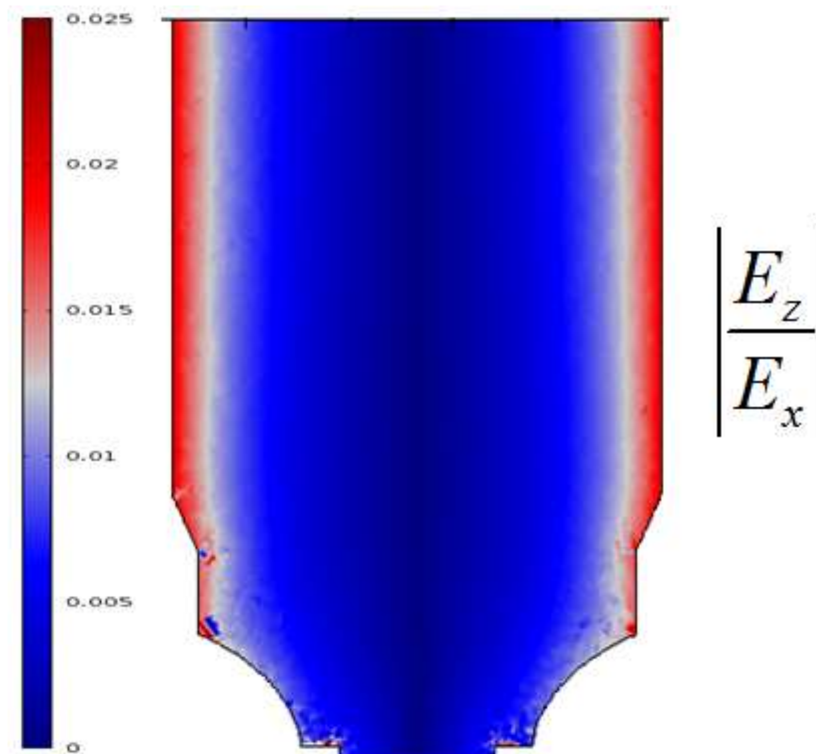

Figure 42: Absolute value of Ez/Ex for the area between the two wire bonds, εr=4, V=3.3Volt, height=70μm, thickness=2μm

An electrical potential of +1.65 Volts and –1.65 Volts is set to the left and right bond wire, respectively. The electrical field ratio of Ez (electrical field perpendicular to the plane) and Ex (electrical field parallel to the plane) is plotted in Figure 42. It can be seen clearly from the plot

that the electrical field perpendicular to the plane is negligible compared to the electrical field parallel to this plane.

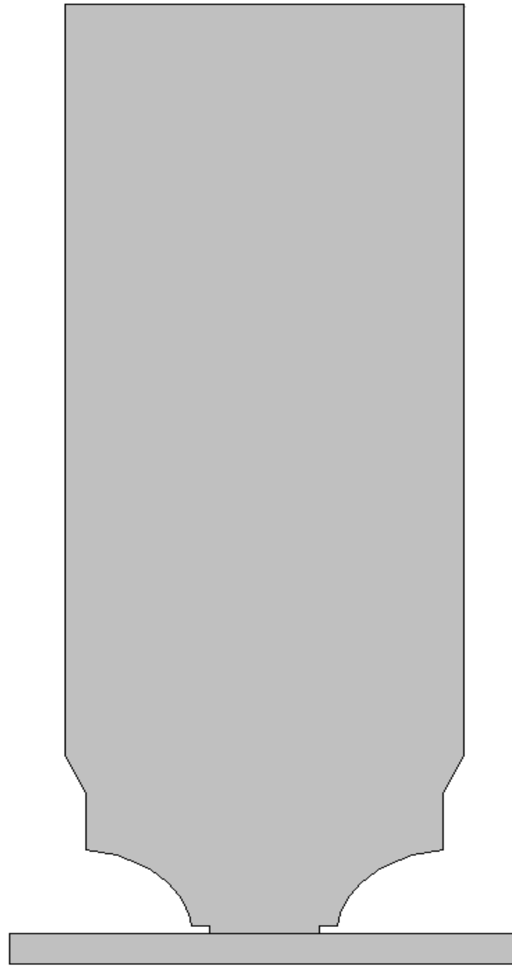

Figure 43: Simplified two-dimensional model based on original three-dimensional one

Therefore, a two-dimensional model has been created accordingly as shown in Figure 43. Since the change of concentration of ions at the bond pad interface are of interest in this simulation, a further step can be taken to continue simplify the geometry of the 2-D model. The height of the

simplified model has been decreased as much as possible and yet still has sufficient accuracy in terms of the original electric field close to the site of interest compares to the unmodified 2-D model as shown in Figure 44.

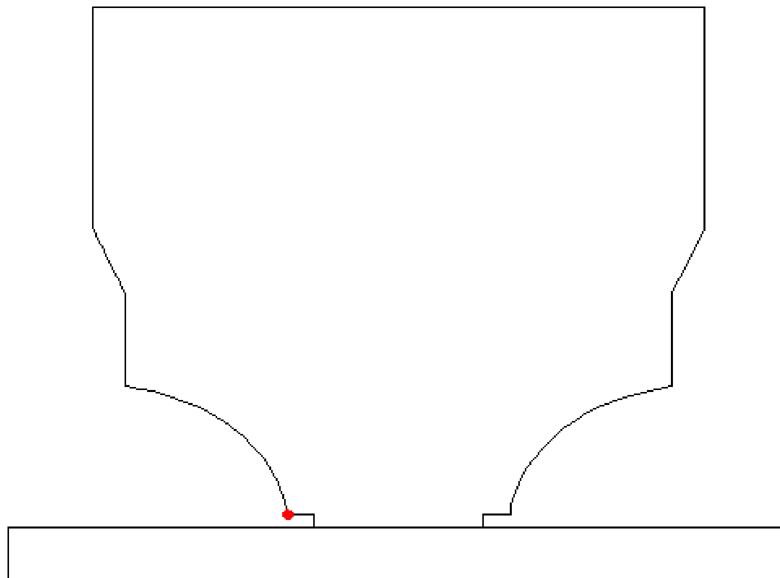

Figure 44: Simplified model with the height reduced to 40μm and the site of interest P is highlighted by red

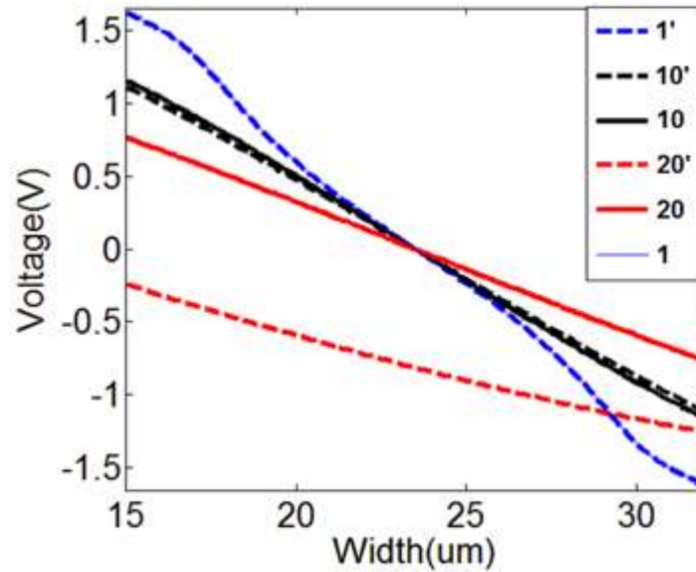

Figure 45: comparison of original electric field between 2-D model

As it can be seen from the Figure 45 ((solid lines) and the simplified 2-D model (dashed lines) within the space between the two wire bonds, 1,10,20 on the top right corner stand for the heights of the electric field with respect to the upper side of interconnect stack in the unit of µm) that the electric field between two models at 1µm seems exactly the same. Also, the electric field of simplified model at 10 µm shifted a little bit (less than 2 percent) with respect to the original two-dimensional model. And even though the electric field comparison at 20µm height is quite different, we can still conclude with sufficient confidence that the simplification is valid because the site of interest is sited at 1µm above the interconnect stack and within the vicinity of 10µm of it, electric field is close enough in terms of the original 2-D model.

Before we go ahead and run the simulations, it is important to find out the diffusion coefficient of chloride ion in the given molding compound material. In this part, a technique will be explicitly

described to experimentally obtain the diffusion coefficient of it under room temperature. First step, to obtain the specimen, Texas Instrument has provided EMC samples of 32 pin package with the size of 26 mm by 26 mm by 0.7 mm. Samples are immersed into a 1M KCl solution beaker at a room temperature with a foil sheet covered on the top to prevent water from evaporating. Samples are taken out periodically from the beaker. After that, they are rinsed thoroughly with distilled water to remove any leftover KCl solution on the surface and are ground and analyzed immediately using inductively coupled plasma. The results are average concentrations of chloride at different aging hours in the EMC samples. In the second step, COMSOL simulations have been used to calculate the change of concentration with respect to time in EMC samples. Before jumping to that step, it is of great importance to estimate the maximum local concentration at this EMC sample. Lantz [Lantz 2003] performed the diffusion cell experiments and found out the maximum diffusion coefficient of chloride ion in several different EMC samples by using TOF-SIMS analysis. Figure 46 gives an example of how chlorine transport in an EMC.

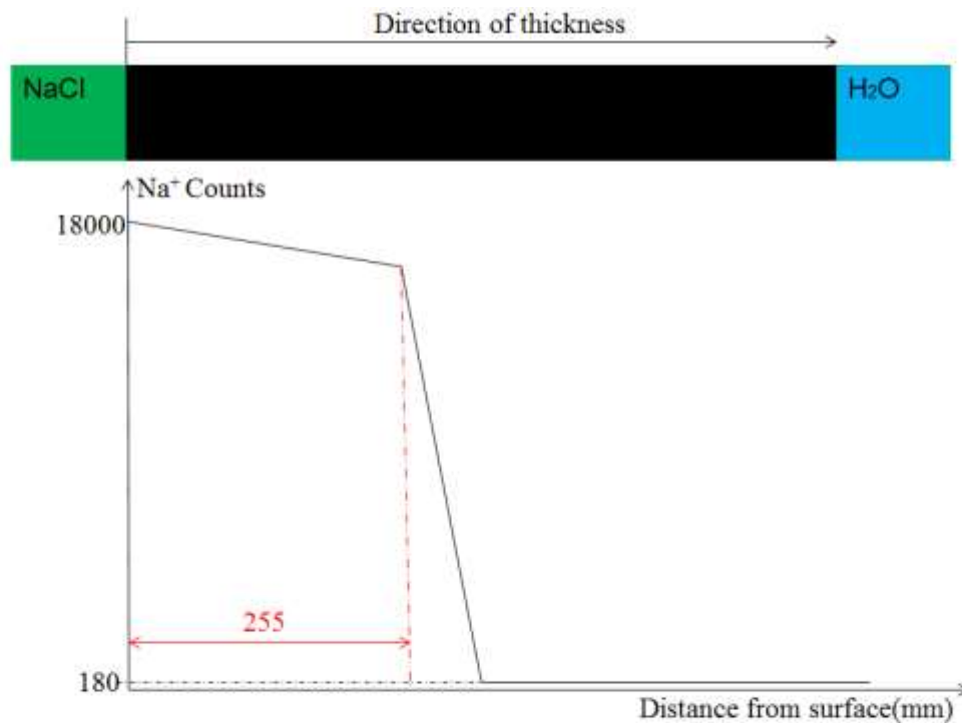

Figure 46: schematic picture of concentration profile across the EMC after 60 days of aging in 0.15M NaCl

The conclusions are that firstly, prior to exposure to NaCl solution, there is a constant Cl ion concentration across the fracture surface of the EMC. Secondly, the maximum concentration is around two orders of magnitude of the initial randomly distributed concentration. In our case, as provided by ICPMS, the initial concentration is 41ppm, thus, the maximum concentration is set to be 4100 ppm. In addition, 1D diffusion model has been used because of the length and the width of the samples are considerably greater than the thickness. Potential gradient is set to be zero because the lack of electrical field. Trial and error is used to figure out the diffusion coefficient of the chloride ion at room temperature. The procedure is schematically shown in Figure 47. In addition, the empirical equations provided by Springer [Springer 1976] shown in Equation 46 is

plotted and compared with the results of simulation in order to cross verify the value of diffusion coefficient.

$$c(t) = c_s[1 - \exp[-7.3(D \cdot \frac{t}{h^2})^{0.75}]] \quad (46)$$

In this equation, c(t) denotes the concentration at time t, Cs stands for the saturation level, h is the thickness of the EMC sample.

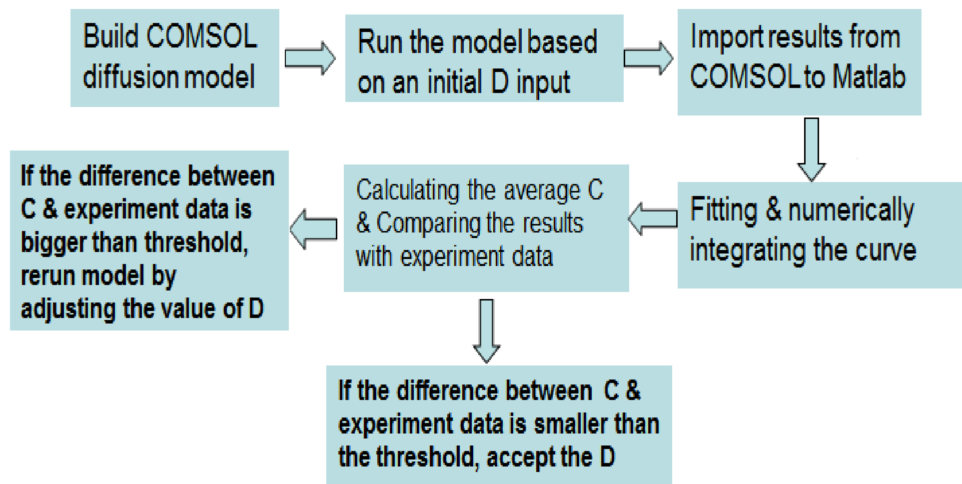

Figure 47: Flow chart of calculation of chlorine diffusivity in EMC samples

The result of diffusion coefficient measurement is shown in Figure 48. it can be readily seen that the simulation results not only match the experiment data but also fit the empirical equation, the maximum error between those two curves are 4.38%. As a result, diffusion coefficient of chloride ion under room temperature is acquired, which is 7*10-16m2/s.

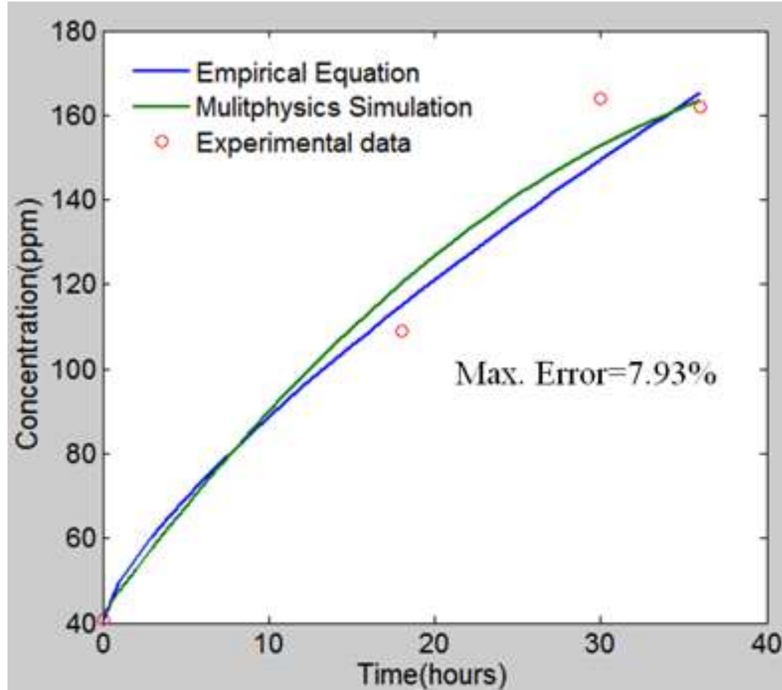

Figure 48: comparison among the results of multiphysics simulation, the empirical equation and the experiment results

Now PNP equations are added to this model to include the transport of ions. All the other boundaries of the model are set to be insulated. One positively charged particle (chloride) and one negatively charged particle (potassium) are present in the molding compound. According to experiment results, the initially randomly distributed ionic concentration of KCl 41 ppm which is the bulk concentration of the contaminant. The maximum concentration is set to be 4100 ppm, the relative permittivity is 4, diffusion coefficients of both charged particles are assumed to be equal. Also, an extremely fine mesh has been applied to the vicinity of electrode-EMC interfaces in the range of nanometer to ensure the accurate simulation of the change of the electric field as suggested by Stern’s model.

4.3 Experimental & Simulation Results

The increase in concentration of chloride ion with respect to time at the site of interest as well as the variation of electric field in the vicinity of the electrode-EMC interfaces has been solved by a time-dependent solver. A typical plot of the increase in concentration versus time is shown in Figure 49. It can be seen that under the effect of a relatively high voltage bias and high diffusivity, the concentration will reach the maximum concentration within a very short time period.

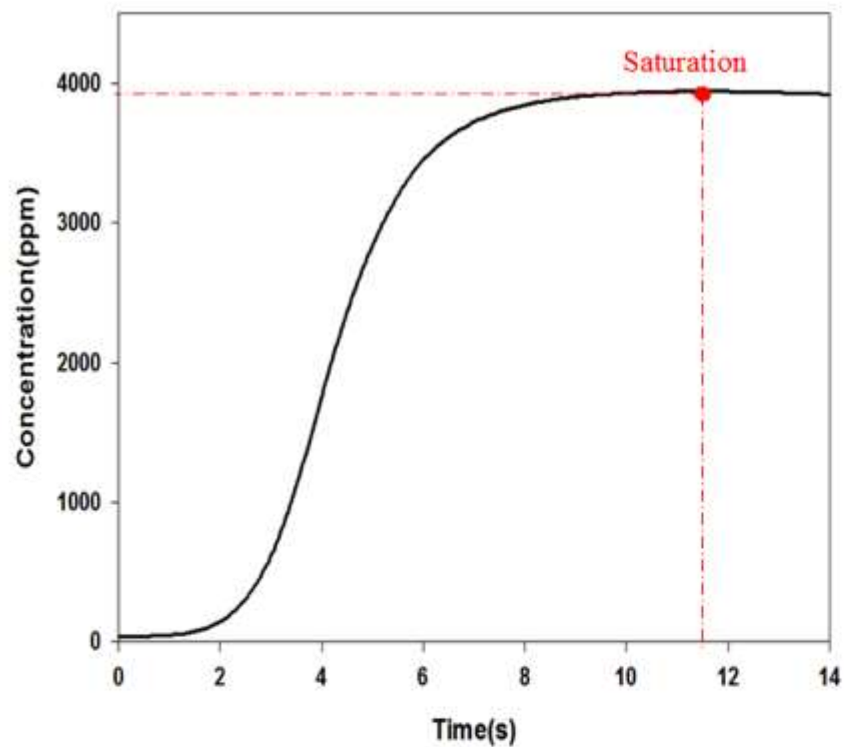

Figure 49: Concentration change with respect to time at site of interest P, V=3Volt, D=7*10-16m2/s, T=298K, Cbulk=41ppm, C∞=4100ppm

The corresponding variation of electric field in the vicinity of the electrode-EMC interfaces under the same simulation condition as the plot above has been plotted in Figure 50.

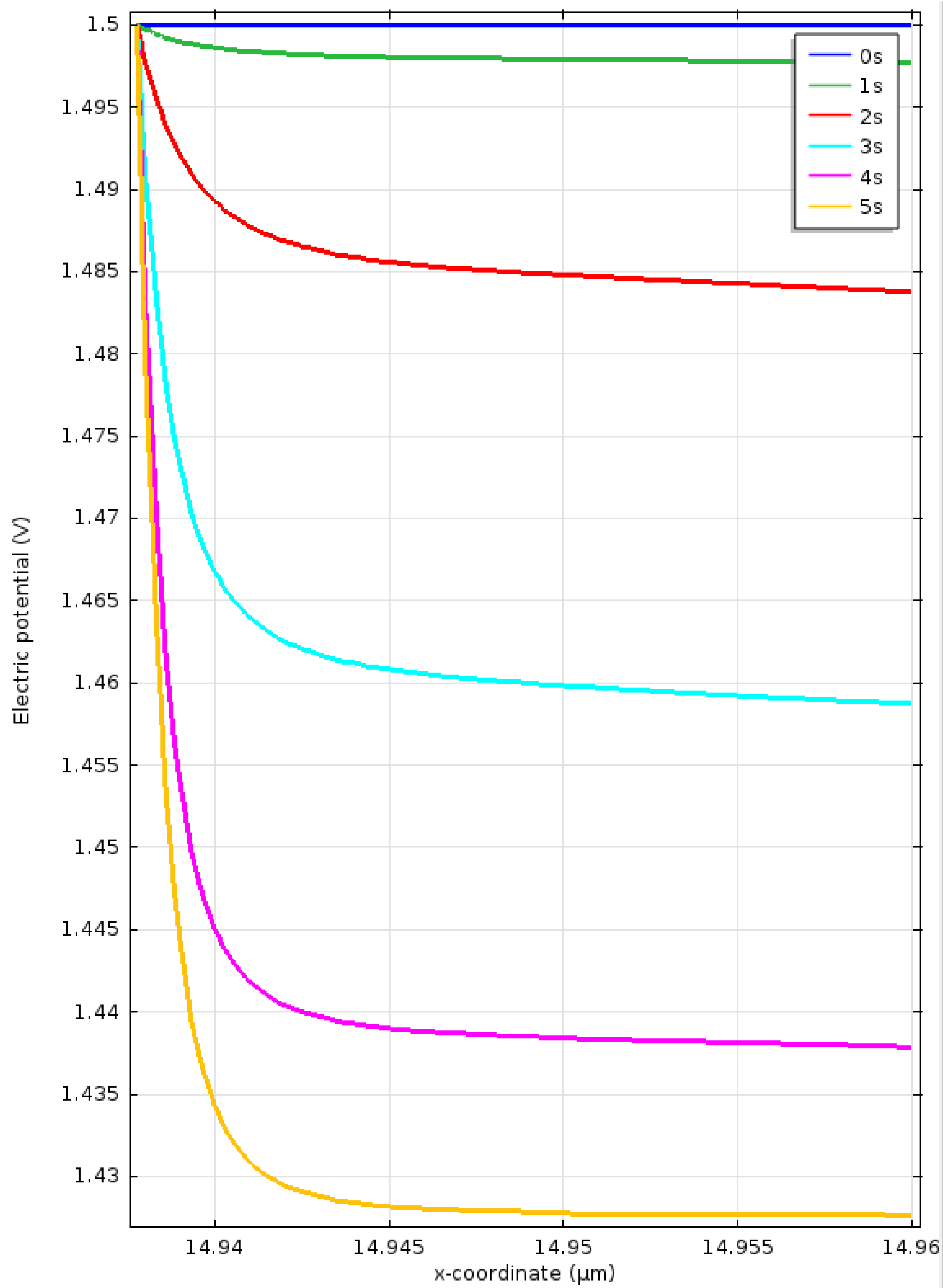

Figure 50: variation of electric potential profile in the vicinity of the electrode-EMC interfaces,

V=3Volt, D=7*10-16m2/s, T=298K, Cbulk=41ppm, C∞=4100ppm

As it can be readily seen in the plot, as time goes on, the electric potential drops within 20nm of the electrode-EMC interface increase, which is consistent with the EDL model predicted by Stern. Stern's model explains the phenomena by assuming the finite size of ions which causes the fact that it is unable to approach the surface closer than a few nanometers. Through a distance known as the Stern Layer, ions can be adsorbed onto the surface up to a point referred to as the slipping plane, where the ions adsorbed meet the bulk liquid. At the slipping plane the potential has decreased to what is known as the zeta potential. Although zeta potential is an intermediate value, it is sometimes considered to be more significant than surface potential as far as electrostatic repulsion is concerned.

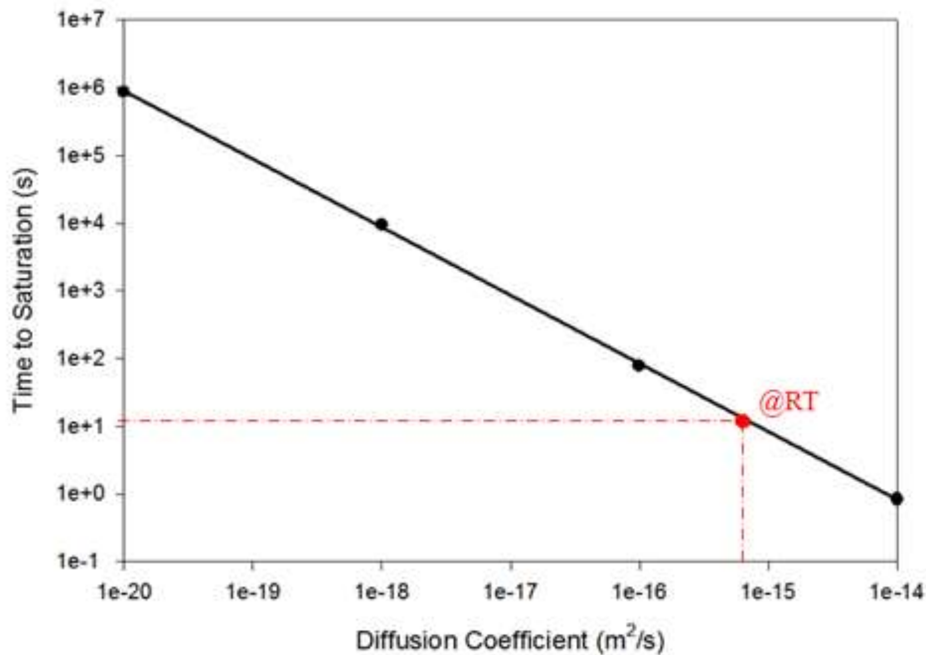

Figure 51: Change of saturation time at P vs. different diffusivities under potential bias, V=3.0Volt, T=298K

Figure 51 shows the change of saturation time with respect to different diffusion coefficients. As it can be seen from the plot. For less mobile ion species under high voltage bias, the time will be hundreds thousands of seconds while for ion species with high mobility, the saturation level will be reached instantaneously. In additional, the change of voltage bias has been applied to the model, the results of the simulation shown in Figure 52 indicate that at a low potential, ion concentration at electrode would not reach the saturation level (4100ppm), thus the result differs from that of a high electric potential. The figure below shows the maximum concentration level at P increase as a function of low electric potentials.

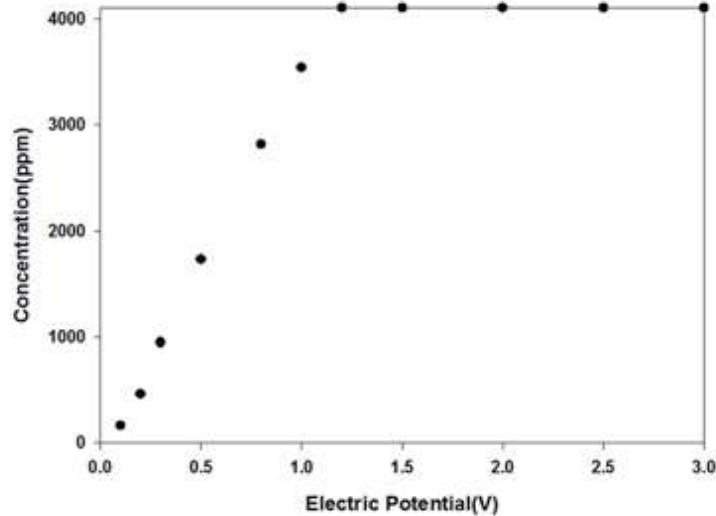

Figure 52: maximum local concentration increase as a function of electric potential, D=7*10-16m2/s, T=298K, Cbulk=41ppm, C∞=4100ppm

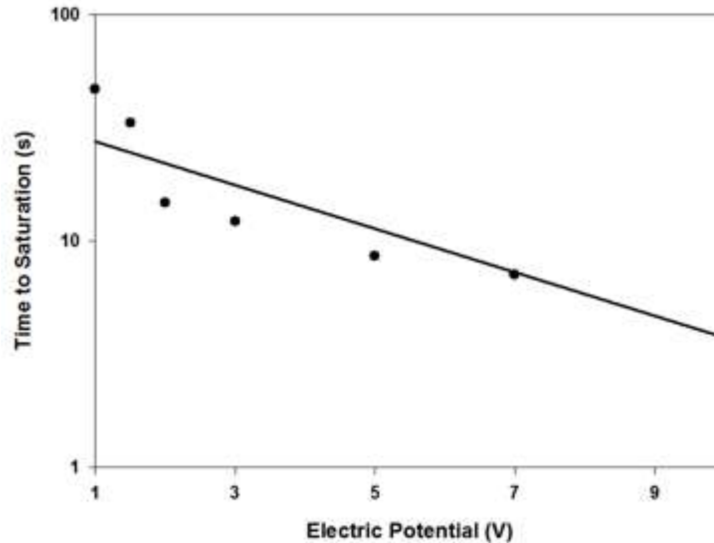

Figure 53: saturation time vs. electric potential, D=7*10-16m2/s, T=298K, Cbulk=41ppm, C∞=4100ppm

As it can be seen from Figure 53, the time to saturation decreases as the electric potential increases under room temperature condition ($D=7*10^{-16}m^2/s$, T=298K). Additionally, for those packages which have defects in the ball bond or Al pad, the maximum concentration at P will dramatically increases because of the presence of water at the bond pad site and the voltage bias will accelerate this process.

In order to take the effect of temperature into consideration, the results of diffusion coefficient of Chloride ion and the Arrhenius equation will be used to obtain the Temperature- Diffusivity profile.

The diffusion coefficient in solids at different temperatures is often found to be well predicted by Arrhenius equation:

$$\mathrm{D} = D_0 e^{-E_a/RT} \tag{46}$$

According to the ICPMS results, we obtained the concentration of Chloride in the EMC samples at different temperatures and different aging durations; it is assumed that, in the absence of the electric field, diffusivity is only governed by Fick's law, thus the empirical equations provided by [Shen 1976] can be used to calculate the diffusivity based on ion concentration results.

$$\mathbf{c}(\boldsymbol{t}) = \boldsymbol{c_s}[\mathbf{1} - \mathbf{exp}[-\mathbf{7.3}(\mathbf{D}.\frac{\mathbf{t}}{\boldsymbol{h}^2})^{\mathbf{0.75}}]] \tag{47}$$

From the results, the diffusion coefficient of chloride ion at 25^0C and 60^0C has been calculated respectively and the values have been plugged into the Arrhenius equation to figure out the unknowns. Finally, the Diffusion-Temperature curve is plotted as shown in Figure 54.

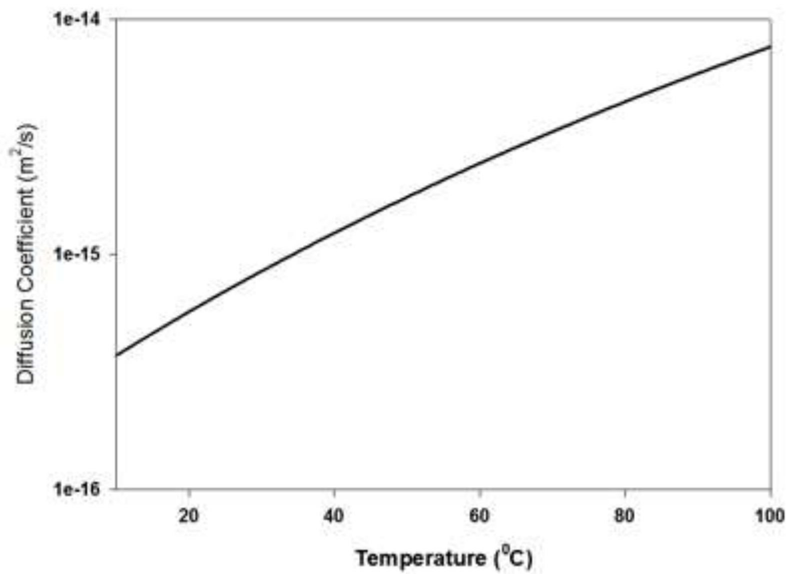

Figure 54:Diffusion coefficient of Chloride ion as a function of temperature

The plot above has been used to generate the time to maximum concentration vs. temperature

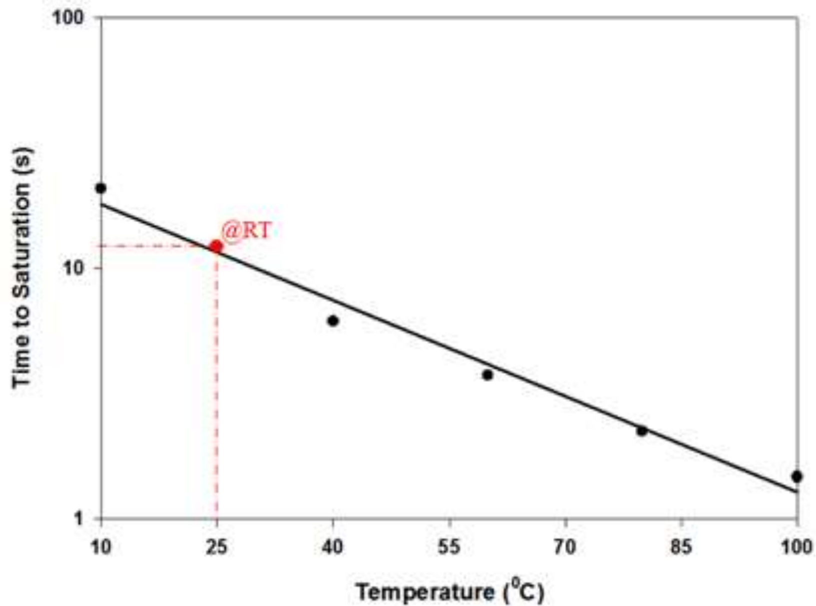

Figure 55: Change of time to maximum concentration at P vs. different temperature

The result of Figure 55 shows the fact that the increase of the temperature accelerates the process of time to maximum concentration.

4.4 Built-in Chlorine Contaminant Tests

In order to study the how the KCl contaminant can affect the reliability of the Cu-Al wire bond based package, the package with built-in contaminant test is performed and the corresponding baseline samples are subjected to the same test condition. The test can be divided into three parts, the first part is to monitor the change of resistance of the interconnect using RS under temperature

humidity aging condition, the second part is to correlate the location of the KCL drop inside the chip and the rate at which the Cu-Al wire bond fails. The final part is to make comparison between samples with built-in contaminant and their corresponding baseline samples.

Resistance Spectroscopy [Lall 2013] has been proved to be an advanced way to measure the change of the resistance accurately. It is hypothesized that change of resistance of the Cu-Al wire bond can be used as a leading indicator to identify progression of damage and impending failure. The plot below gives us an example of how it works.

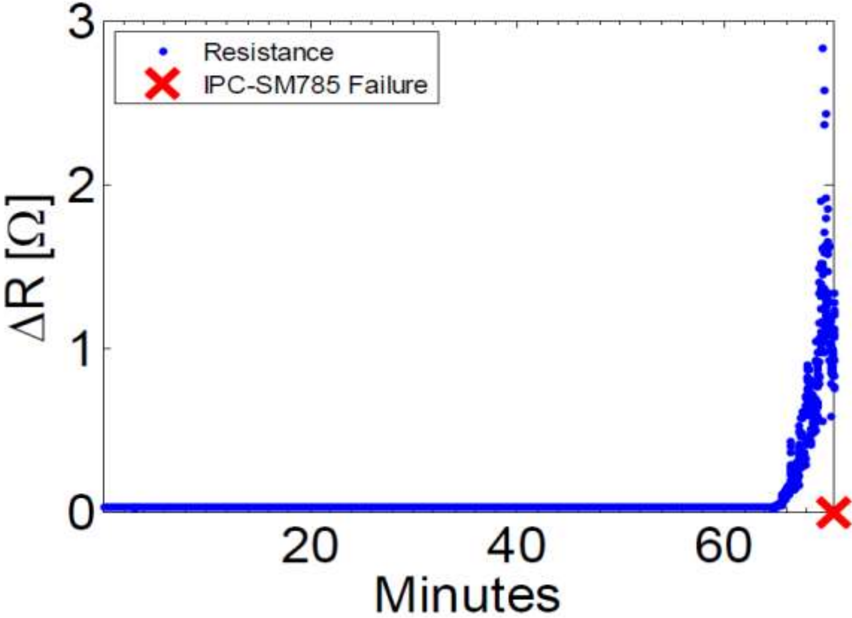

Figure 56:time to failure plot monitored by RS

Figure 56 shows the change of the resistance of a certain type of package interconnect with respect to time under a harsh environmental condition. The Red Cross sign around 70 minutes denotes the amount of time it takes for this type of interconnects to malfunction. It can be readily

seen that the excessive increase of resistance monitored by RS occurred several minutes ahead of the occurrence of actual failure, which show its ability to prognosticate the happening of failure. The RS system consists of a SRS830 Lock-In Amplifier, a modified Wheatstone bridge and a probe station. Accurate measurements are able to be obtained even when the small signal is obscured by noise sources many thousands of times larger. Lock-in amplifiers is designed to detect and measure very small AC signals all the way down to a few Nano-volts. It uses a technique known as phase-sensitive detection so as to single out the component of the signal at a specific reference frequency and phase. In the next step, the resultant signal will go through the modified Wheatstone bridge in which the wire bond of the package has been hooked up to. Two static resistors and one changeable resistor which can be utilized to balance the modified Wheatstone bridge, a change of the resistance of the package will lead to the change in magnitude of the output signal.

In this study, aging condition is set to be temperature humidity 130^0C/100%RH, aging duration is set to be 168 hours, and resistance measurement interval is set to be 24 hours. Failure Threshold, according to the industry standard, is set to be the time when resistance exceeds 20% of the original resistance.

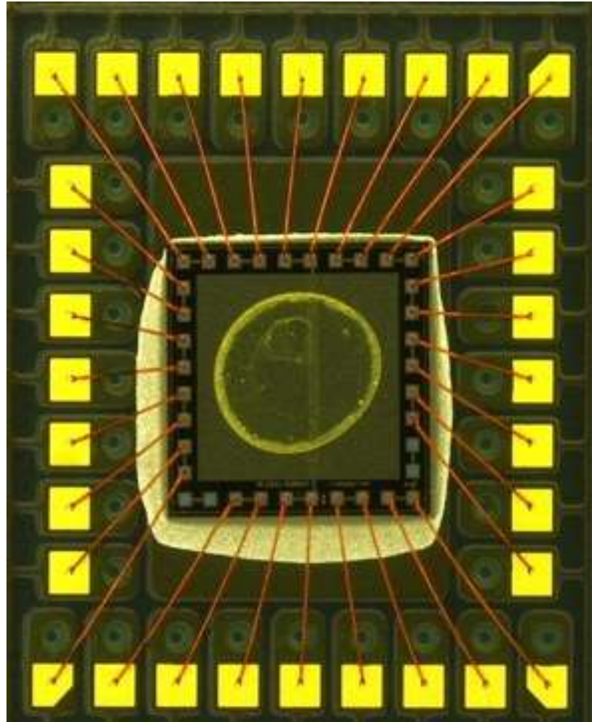

Figure 57: Optical microscopic sample image with built-in chloride contaminant

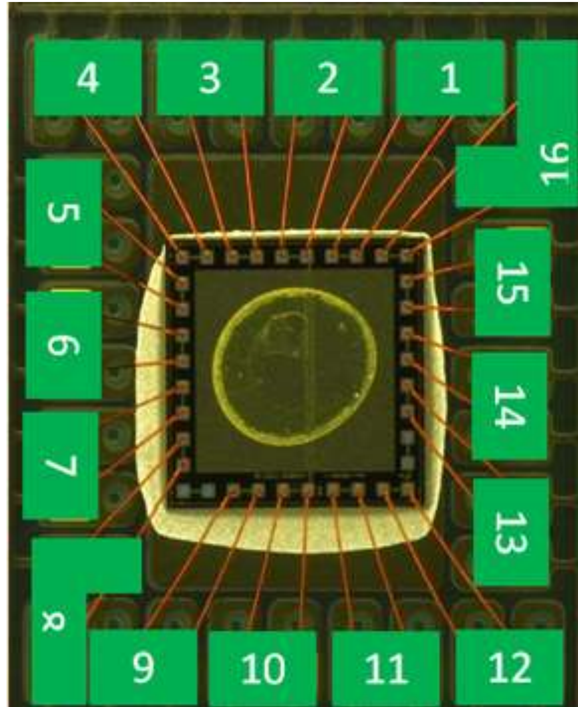

Figure 58: 16 pairs of wire bond has been labeled in order to measure and track change of resistances

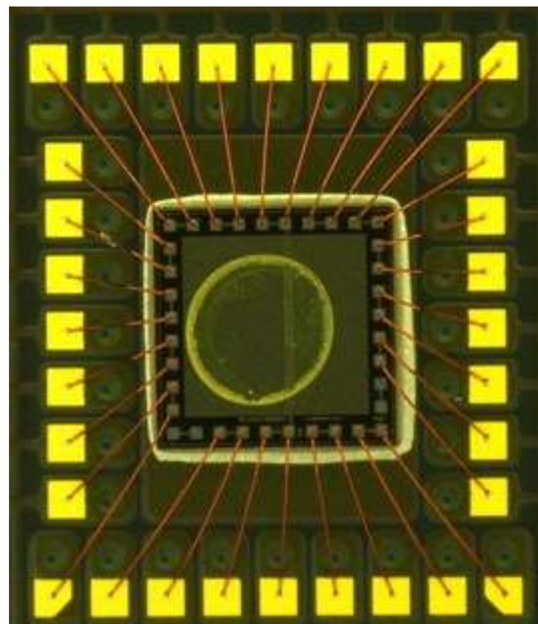

# of PIN	Time zero	24 hr 130C/100 %RH parr bomb	48 hr 130C/100 %RH parr bomb	72hr 130C/100%RH parr bomb	96hr 130C/100 %RH parr bomb	120hr 130C/100 %RH parr bomb
#1	0.3552	0.3625	0.3632	38K	M	M
#2	0.3624	0.3665	0.3596	M	M	M
#3	0.3584	0.3531	0.4825	0.45K	M	M
#4	0.3493	0.3508	0.6983	M	M	M
#5	0.3379	0.3429	M	M	M	M
#6	0.3422	0.9427	13.35	M	M	M
#7	0.3285	0.3313	0.8K	M	M	M
#8	0.3513	0.3487	348.13	0.51K	M	M
#9	0.3533	0.3596	0.3523	0.3624	0.3644	M
#10	0.3462	0.3511	0.3628	0.3584	M	M
#11	0.3742	0.3634	0.3553	0.3521	M	M
#12	0.3629	0.3638	0.3745	0.3678	M	M
#13	0.3585	0.3455	0.3658	0.3695	M	M
#14	0.3365	0.3452	0.3356	0.3328	16K	16K
#15	0.3277	0.3312	0.3188	0.3266	M	M
#16	0.3524	0.3489	0.3529	0.3514	0.3527	M

Figure 59: Optical microscopic image of sample #1 and its corresponding Cu-Al wire bond resistance monitoring

Wire bonds considered to be failed are highlighted with red in spreadsheets and K and M denotes the resistance of wire bond reaches thousand and million-ohm level respectively as shown in Figure 57 and Figure 58. From analyzing the optical microscopic sample image #1 alone shown in Figure 59, one can guess that pin #6 is most likely to be corroded in the first place due to the fact that it is closest to the KCl drop thus is most susceptible one. After that, failure is going to happen on the pins around #6. Because of the distance between them and KCl drop is fairly close compare to the rest of the wire bonds, speculations are all verified by the resistance result of wire bonds that the failure initiated at pin#6 after 24hrs aging duration and then it spreads out to those wire bonds close to #6.

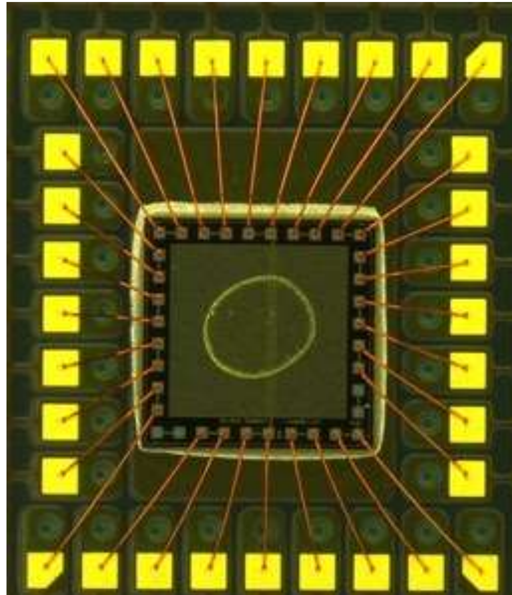

# of PIN	Time zero	24 hr 130C/100 %RH parr bomb	48 hr 130C/100 %RH parr bomb	72hr 130C/100 %RH parr bomb	96hr 130C/100 %RH parr bomb
#1	0.3721	0.3742	0.3623	0.3624	0.3556
#2	0.3588	0.3622	0.3672	0.3597	0.3564
#3	0.3562	0.3485	0.3464	0.3422	0.3442
#4	0.3648	0.3612	0.3688	0.3633	0.5839
#5	0.3413	0.3408	0.3514	0.3467	M
#6	0.3386	0.3356	0.3229	0.3319	M
#7	0.3378	0.342	0.3527	0.3462	M
#8	0.3744	0.3647	0.3632	0.3705	17.05
#9	0.3663	0.3635	0.3659	0.3559	M
#10	0.3574	0.3542	0.3541	0.3435	28.51
#11	0.3563	0.3521	0.3284	0.3541	M
#12	0.3662	0.3633	0.3781	0.3439	0.9026
#13	0.3682	0.3647	0.3562	0.3526	M
#14	0.345	0.3541	0.3447	0.3487	M
#15	0.3375	0.3372	0.3326	0.3335	8.56
#16	0.3629	0.3589	0.3663	0.3688	97.33

Figure 60: Optical microscopic image of sample #2 and its corresponding Cu-Al wire bond resistance monitoring

By comparing between optical microscopic images #1 and #2 shown in Figure 60, one can guess the possible scenario in which it is going to take much more time for the wire bonds to fail in

sample #2 because the KCl dope in #2 is smaller in size and locate at the center of the chip,. Also, the failure of most of the wire bonds might happen simultaneously for the reason that the distance between them and the drop are almost the same, which are also verified by investigating the corresponding resistance spreadsheet. It took 72 more hours for the failure to occur and most of the failure happened at the 96 hours duration.

During the test, none of the wire bond pairs inside baselines reached failure threshold, which indicates that compare to the sole effect of moisture ingress, the resultant effect of built-in contaminant and moisture ingress lead to an extremely high corrosion rate.

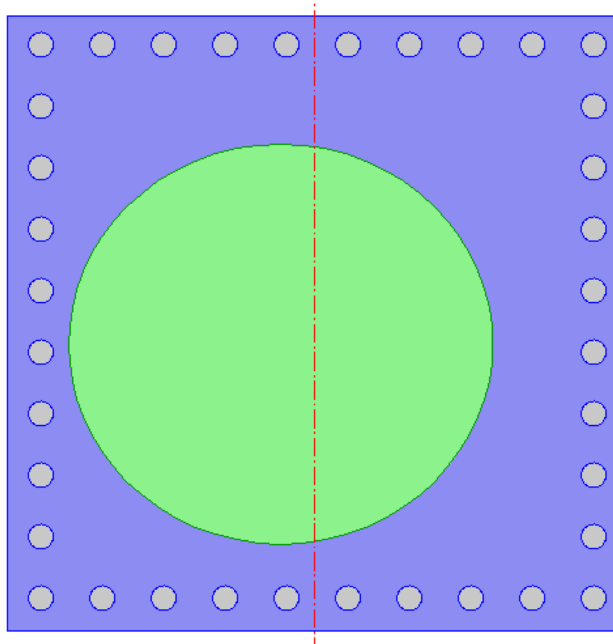

Figure 61: 2D COMSOL model for built-in contaminant experiment sample#1

COMSOL model has been used to simulate the accumulation of chloride ion at the bond pad site. Figure 61is the simulation model of sample #1 the size of it is built accordingly. The size of

chip is 2000 by 2000 micrometers. The radius of the copper aluminum bond pad is 40 micrometers. KCl drop is denoted in the cartoon as a green circle which has an initial concentration of 4100 ppm. Nernst-Planck equations are used to simulate the rate at which contaminants transport with the electrical potential gradient being set to zero. The objective of it is to find out how much does 130^0C/100%RH condition accelerate the diffusion coefficients of chemical species. The diffusion coefficient of chloride ion under room temperature will be used to estimate the time it will take for ion to accumulate at bond pad side in order to compare results under room temperature with the results under harsh environmental conditions.

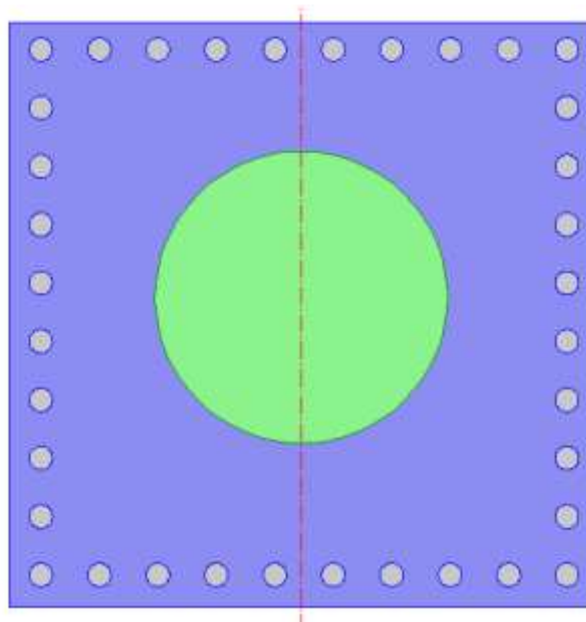

Figure 62: 2D COMSOL model for built-in contaminant experiment sample#2

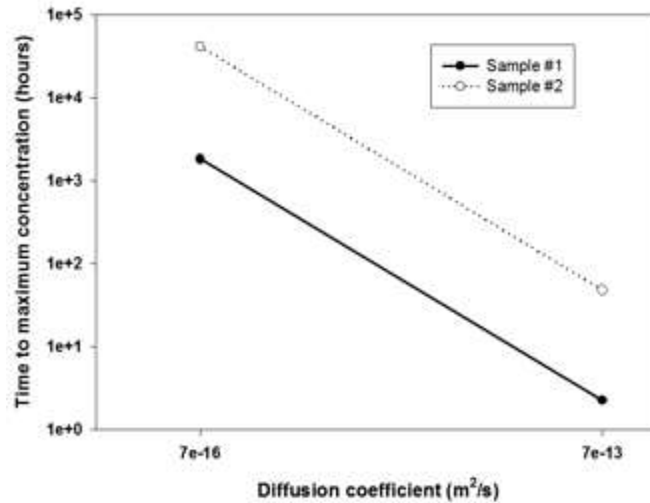

Figure 63: time to maximum concentration in built-in contaminant experiment sample#1and sample#2 under room temperature condition and 1300C/100RH

According to the experiment results, in both cases, the first failures occurred within 24 hours and 96 hours. The trial and error method has been used to find out the corresponding diffusion coefficient of chloride ion under such environmental condition. As we can see from Figure 62 and Figure 63, the result is of the diffusion coefficient is $7*10^{-13}[m^2/s]$ when the time to maximum concentration at bond pad side are 2.28 and 48.2 hours respectively. As for the room temperature condition, it took approximately 1800 hours and 42000 hours for the chloride ion to reach maximum concentration at bond pad side, which is 22 times as much as the time spent in aging condition case. From the COMSOL simulation result, it can be readily seen that the harsh environmental condition of high temperature and high humidity drastically increase the rate at

which chloride ion transport in the epoxy molding compound. The acceleration factor is around 1000.

Chapter 5 De-bonding simulation of Cu-Al WB Intermetallic Compound Layers

In this chapter, an IMC grain-level finite element model has been developed to simulate the interfacial de-bonding behavior in order to study how IMC microstructure characteristics influences the mechanical reliability of Cu-Al wire bond. To start with, Voronoi tessellations are used to construct both regular and irregular IMC grain shapes geometry. Then, intrinsic cohesive zone model is adapted to model interactions between neighboring grain boundaries. After that, both uniform and Weibull distributed grain interfacial strength are modeled. Finally, Cu-Al IMC growth and phase transformation are modeled.

Simulation results indicate Cu-Al IMC microstructure characteristics not only influence bond strength but also have an effect on crack propagation. Regular-shaped IMC grain provides Cu-Al wire bond with more bond strength. Non-uniform grain interfacial strength reduces bond strength. The increase of IMC thickness makes wire bond less reliable. The phase transformation changes the crack propagation mode. Some of the simulation findings are consistent with the experimental observations.

5.1 Cu-Al IMC Microstructure Evolution & Wire Bond Intergranular Cracking

The study of IMC microstructure changes before and after thermal and humidity treatment is the key to understanding how degradation initiates and proceeds. Base off of the IMC thickness growth under high temperature aging, one researcher [Lall 2014] proposes the use of Levenberg-Marquardt algorithm to identify accrued damage in IMC and estimate the remaining useful life. Another researcher [Drozdov 2008, Drozdov 2009] studied IMC microstructure evolution under thermal treatment and reported continuous intermetallic (mainly $CuAl_2$) grains with varying size and morphology. One more researcher [Hang 2008] did a similar study and concluded that the cause of IMC de-bonding is due to the combination of internal stress developed during interdiffusion process and the residual stress developed during wire bonding overwhelming the interfacial bond strength.

Based on results and observations of previous research, an IMC grain-level finite element model is developed in an attempt to simulate de-bonding behavior of IMC and explore effect of different IMC microstructure characteristics on reliability of Cu-Al wire bond.

In this simulation, there are two keys to modeling Cu-Al wire bond IMC, geometric representation of IMC grain microstructure and grain interfacial behavior. The use of Voronoi tessellation proposed by Jose [Ribeiro 2004] and Tian [An 2013] and the use of PPR potential-based cohesive model proposed by Park [Park 2012] are adopted to address these two important issues.

IMC Microstructure Evolution

Extensive studies have been done to investigate Cu-Al IMC evolution after thermal treatment. As shown in Figure 65, there is no visible IMC at the as-bonded stage of Cu-Al wire bond. This is because of the low interdiffusion rate between copper atoms and aluminum atoms causing by misfit in atomic size and electronegativity [Murali 2007]. It is believed that at a high temperature, typically no less than 150^0C, stored energy in the interfacial area during wire bond will be released to facilitate interdiffusion and IMC formation [Kim 2003]. After hours of thermal treatment, IMC growth can be observed as shown in Figure 65. Sample wire bond has been aged for 810 hours under 175^0C. The thickness of IMC is 0.9μm measured by taking the average thickness across the entire interfacial IMC region. Three different types of IMCs are present at the interfacial region. $CuAl_2$ is confirmed to still be the dominant part of IMC along with sporadically distributed irregular grain-like CuAl and Cu_9Al_4 particles.

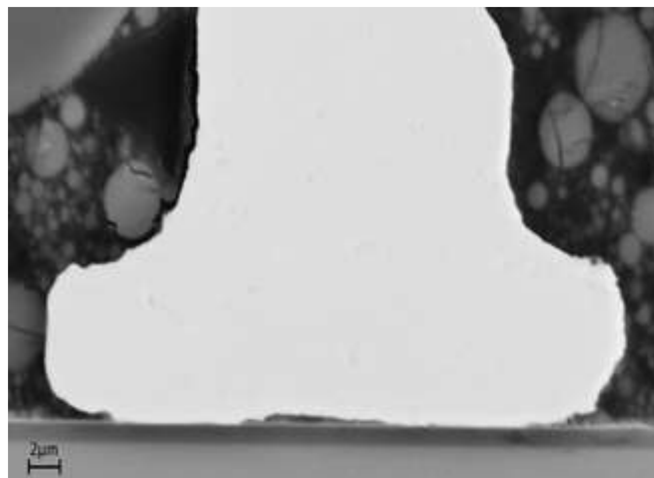

Figure 64: Cu-Al Wire Bond at As-bonded Stage

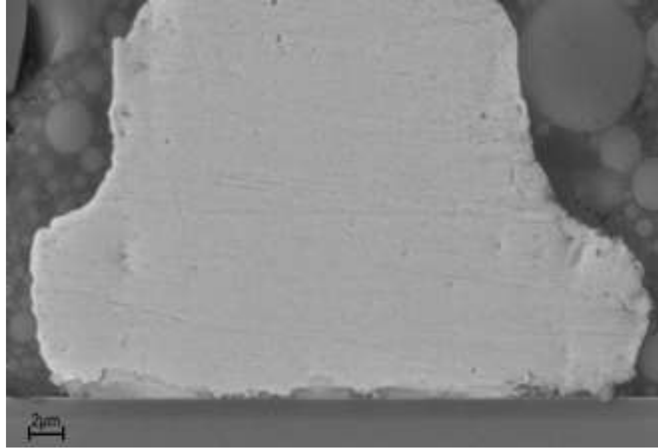

Figure 65: Cu-Al Wire Bond after Thermal Treatment

Cu-Al Wire Bond Intergranular Cracking

In Cu-Al wire bond, crack initiates from bond periphery once intermetallic compound layers are well-developed. Then, crack grows towards center of the ball bond as shown in Figure 66. The reason for crack initiation at periphery region is because during wire bonding process, maximum deformation occurs at the periphery of ball bond [Jung 2003] and crack propagation is related to intrinsic IMC growth stresses and thermos-mechanical degradation of IMC.

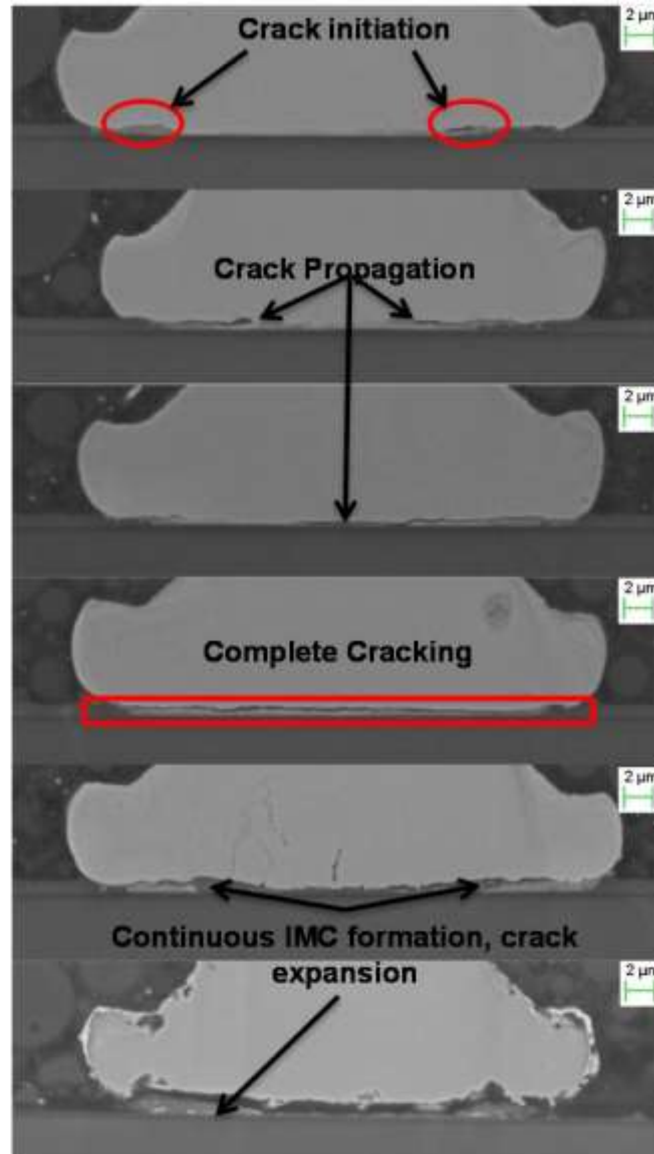

Figure 66: Crack Initiation and Propagation

5.2 Modeling of Cu-Al Wire Bond IMCs De-bonding

Generation of Geometrical Representation of IMC Grains

Intermetallic compound such as CuAl2, CuAl and Cu_9Al_4 are polycrystalline quasi-brittle materials. Those types of materials are composed of many grains of varying size and orientation and their thermo-mechanical behaviors are related to their microstructure characteristics. Therefore, precise geometrical representation of IMC is essential to accurately characterize the non-linear fracture process within Cu-Al IMCs.

Voronoi cell finite element model has been widely used in material science to generate microstructure of heterogeneous materials [Ghosh 1995, Faber 1999, Alonso 2011, Ghosh 2004]. For a given set of sites in a domain, Voronoi diagram is defined as a collection of cells each of which contains domain points closer to corresponding site of cell than to any other site. Given a set of sites X= {xi}, i from 1 to n, Voronoi diagram of X can be expressed as n cells {Wi}, i from 1 to n, where

$$\Omega_i = \{x \in R^2 \| \|x - x_i\| \leq \| \|x - x_j\|, \forall j \neq i\} \tag{48}$$

Each cell is the intersection of a set of half spaces, created by bisecting planes of Delaunay edges incident to corresponding site.

Procedures for generating IMC grain structures in Abaqus are shown in Figure 67. Matlab is used to generate the coordinates of Voronoi tessellations and all the connectivity of vertices. Those data information is then read by a Python script to construct and assemble the IMC grain geometry in Abaqus. Cu-Al IMC grains are generated using Voronoi tessellation. Figure 68 shows plots of both regular and irregular hexagon-shaped grain IMC geometries with a 0.1μm average unit length.

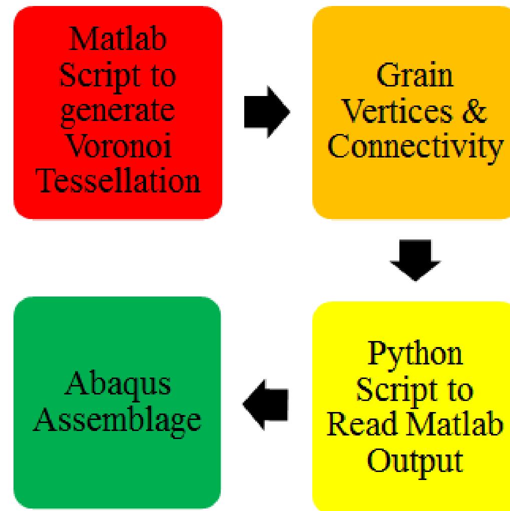

Figure 67: Procedures for Generating IMC Grain-like Structures

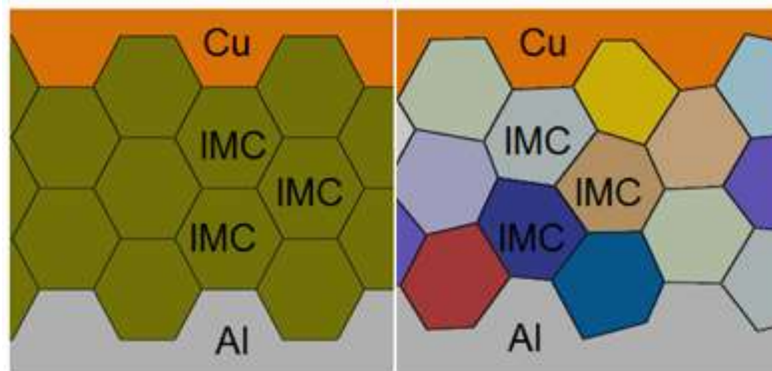

Figure 68: Procedures for Generating IMC Grain-like Structures

Finite Element Formulation of Intrinsic Cohesive Zone Model

The behavior of grain interface element is governed by the intrinsic cohesive zone model [Park 2012]. According to the model, cohesive crack propagation consists of four stages, namely elastic,

initiation, softening and complete failure. The governing equation is obtained from the principle of virtual work,

$$\int_{\Omega} \delta\varepsilon \cdot \sigma dV + \int_{\Gamma_c} \delta\Delta \cdot T_c dS = \int_{\Gamma} \delta u \cdot T_{ext} dS \tag{49}$$

Where δε, δu and δDare virtual strain, displacement and separation, the first term on the left hand side represents the internal force of bulk element and the second term represents the internal cohesive force of cohesive surface elements. The term in the right is related to the external forces.

Discretizing domain W and then interpolating the nodal displacement $\overline{u}$ with shape function N, displacement field u is obtained.

$$u(X) = N\overline{u} \tag{50}$$

Next, in order to obtain the local separation D by using global nodal displacement, global coordinates X are transformed to local coordinates x of a cohesive element using a coordinated transformation matrix Λ

$$x = \Lambda X \tag{51}$$

Likewise, $\overline{u}$ can be transformed to local nodal displacement $\tilde{u}$ by a rotational matrix R

$$\tilde{u} = R\overline{u} \tag{52}$$

The local nodal displacement separation $\tilde{\Delta}$ along the surface normal and tangential directions can be obtained by using a local displacement-separation matrix L

$$\tilde{\Delta} = L\tilde{u} \tag{53}$$

Then, separation of a cohesive element is interpolated

$$\Delta(x) = N\widetilde{\Delta} \tag{54}$$

Substituting equation (53) (54) into equation (55) results in the formation of the global displacement-separation matrix B where B=NLR

$$\Delta(x) = B\widetilde{u} \tag{55}$$

The internal force vector fcoh of a cohesive element is obtained based on B matrix

$$f_{coh} = \int_{\Gamma_c} B^T T_c dS \tag{56}$$

Tangent matrix Kcoh of a cohesive element is given as

$$K_{coh} = \frac{\partial f_{coh}}{\partial \overline{u}} = \int_{\Gamma_c} B^T \frac{\partial T_c}{\partial \Delta} BdS \tag{57}$$

Where Tc and the gradient of Tc are obtained from the potential based cohesive zone model given as

$$\begin{aligned} \psi(\Delta_n, \Delta_t) &= \min(\phi_n, \phi_t) + [\Gamma_n (1 - \frac{\Delta_n}{\delta_n})^{\alpha} (\frac{m}{\alpha} + \frac{\Delta_n}{\delta_n})^m \\ &+ \langle \phi_n - \phi_t \rangle][\Gamma_n (1 - \frac{|\Delta_t|}{\delta_t})^{\beta} (\frac{n}{\beta} + |\Delta_t| \delta_t)^n + \langle \phi_t - \phi_n \rangle] \end{aligned} \tag{58}$$

Where Δ_n and Δ_t are the normal and tangential separations along fracture surface. ϕ_n and ϕ_t are critical energy release rate under pure mode-I and mode- II. Γ_n, Γ_t are energy constants δ_n, δ_t stand for normal and tangential final crack opening widths. α, β are shape parameters and $\langle \cdot \rangle$ is Macaulay bracket.

Detailed description of PPR potential based cohesive zone model, constitutive behavior of a 2D Cohesive Interface element and computational implementation of the model in ABAQUS are provided in an educational research paper by Park.

As shown in Figure 69 and Figure 70, cohesive elements are 2D quadrilateral interface element with four nodes and a single integration point. The initial thicknesses of cohesive interface elements are zero. As the neighboring continuum elements deform, the two surfaces of the cohesive interface elements separate.

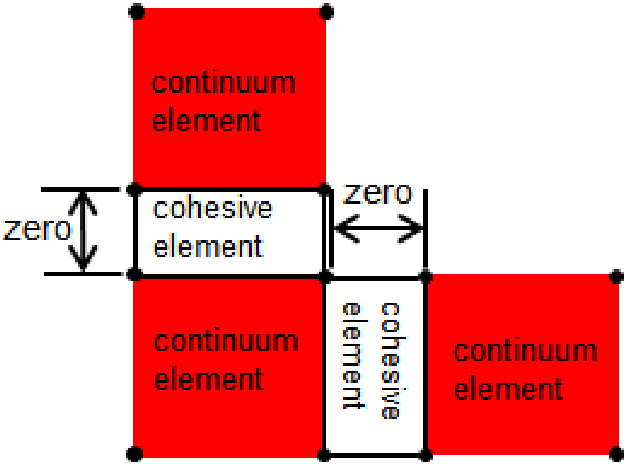

Figure 69: Cohesive Elements at Undeformed State

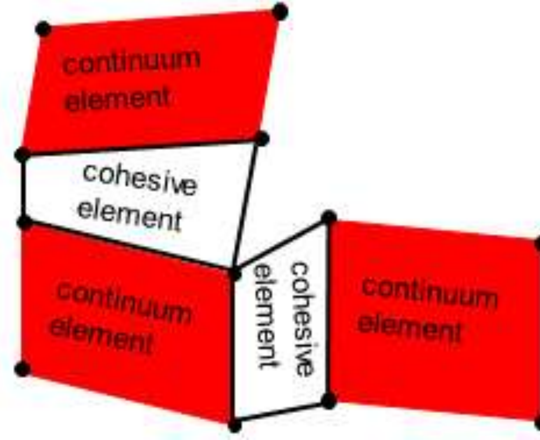

Figure 70: Cohesive Elements at Deformed State

Cohesive Traction-separation Relationship

A typical cohesive traction-separation behavior of a cohesive interface element is depicted in Figure 71 and Figure 72. Normal/tangential tractions increase as opening/tangential displacement increases until maximum traction are reached. After that, it gradually decreases until it becomes zero. Unloading and reloading occurs when external loadings change or internal stresses in the neighboring elements are redistributed. If the loading process does not reach the maximum traction, unloading obeys the same law as loading process. Otherwise, unloading is along an elastic path to the original point as shown in a red solid line in both Figures. The contact condition occurs when the normal separation is negative and this can be prevented by introducing a penalty stiffness αp so that Tn= αpDn

$$\alpha_p = \frac{\partial^2 \psi(\Delta_n, \Delta_t)}{\partial \Delta_n^2}\Big|_{\Delta_n=0, \Delta_t=0} \tag{59}$$

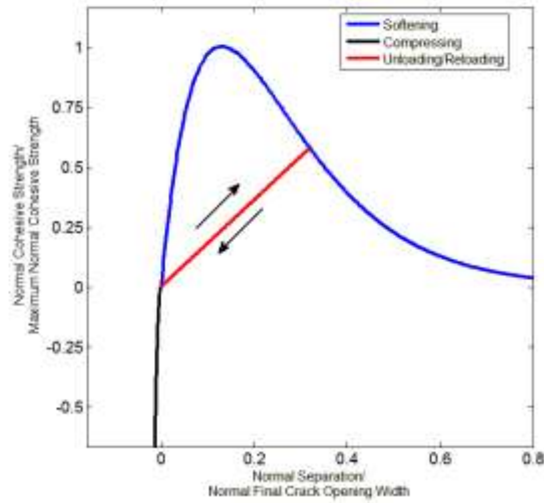

Figure 71: Normal Traction-separation Relationship

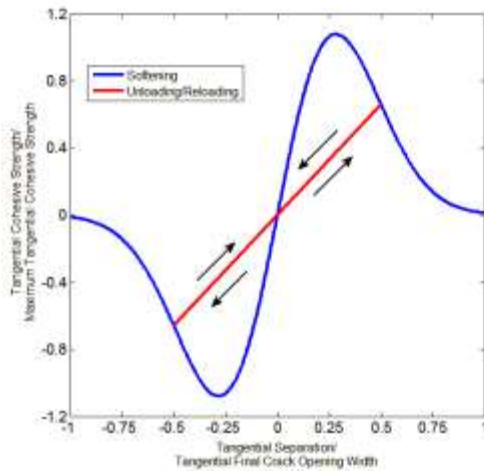

Figure 72: Tangential Traction-separation Relationship

A 2D Cu-Al wire bond geometry is constructed as shown in Figure 73. It is a 10μm by 5μm rectangular with copper to be the majority material on the top representing copper ball bond, a thin layer of aluminum at the bottom representing aluminum pad and a thin grain-shaped layer of Cu-

Al IMC. Similarly, another geometry with irregular grain shaped IMC is constructed as shown in Figure 74. Two geometries are of the same size. The out-of-plane thickness of both models is set to be 50μm.

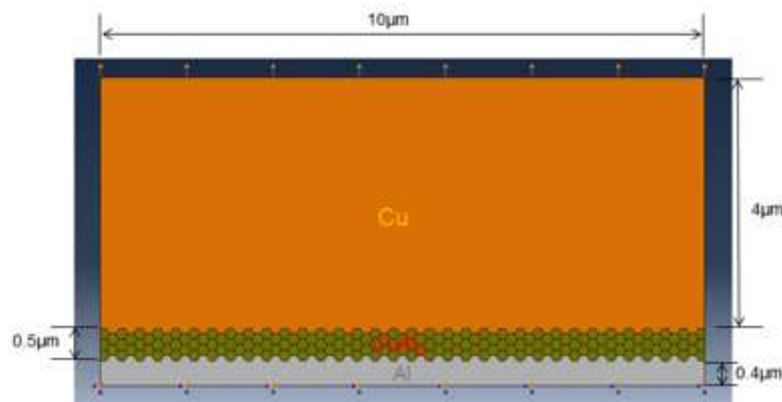

Figure 73: Cu-Al Ball Bond Geometry with Regular Hexagon-shaped IMC grains

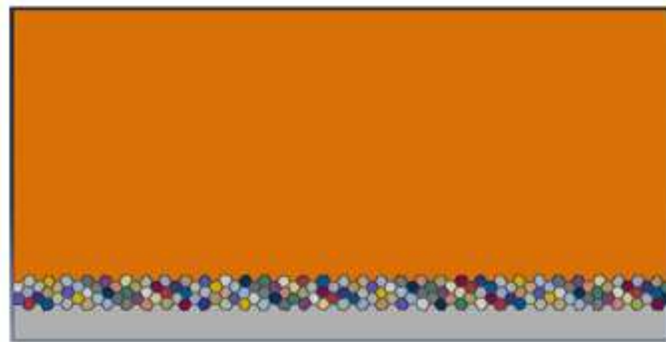

Figure 74: Cu-Al Ball Bond Geometry with Irregular Hexagon-shaped IMC grains

The 3-node plane strain element (CPE3) and 4-node plane strain element (CPE4R) are used to mesh the copper ball bond, aluminum pad and the interior of each IMC grain. All grain boundaries are meshed by using the 4-node cohesive element. For each grain boundary, four cohesive elements are embedded in both geometries as shown in Figure 75 and Figure 76. The total number of element, total number of grain boundary interfaces and total number of cohesive element are

tabulated in Table 3. It can be seen from the Table that the number of grain boundary and cohesive element are identical in both models. The model with irregular grain has slightly more elements than that with regular grain.

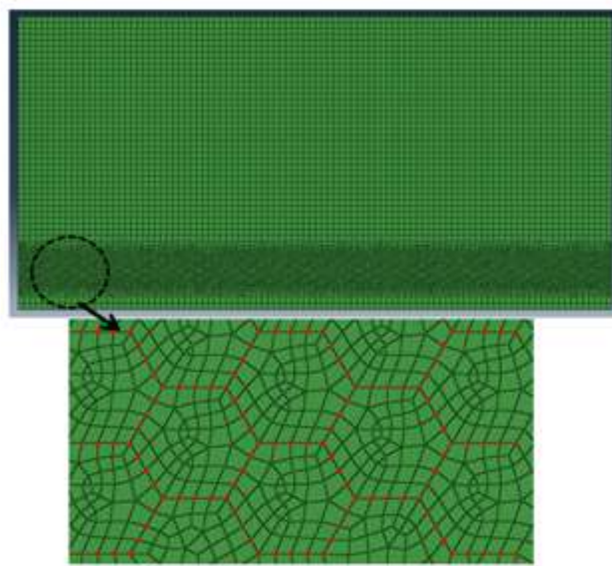

Figure 75: Discretization of Model with Regular Hexagon-Shaped IMC Grains

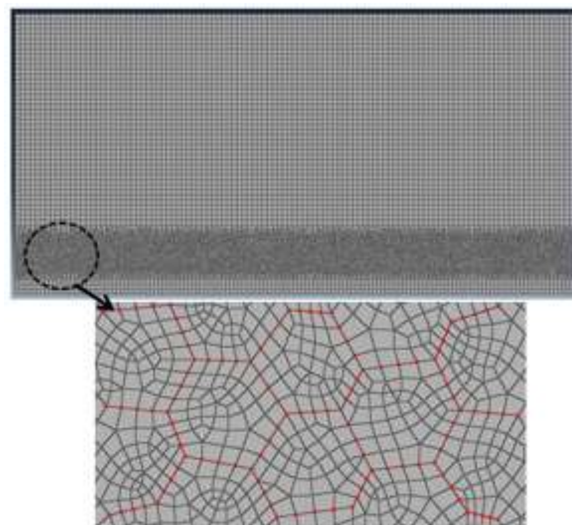

Figure 76: Discretization of Model with Irregular Hexagon-Shaped IMC Grains

Table 3: Comparison between Models with Regular and Irregular Grains

	Regular	Irregular
Number of Element	19156	19368
Number of Grain Interface	631	631
Number of Cohesive Interface Element	2524	2524

The basic mechanical properties of Cu-Al IMCs are provided by Kouters [Kouters 2012] along with stress intensity factors. Normal and tangential critical energy release rate can be calculated by using Equation 13. Maximum normal and tangential cohesive tractions are provided by A. Grams [Grams 2013]. Those values are tabulated in Table 4 and Table 5 respectively.

$$\phi_{n(t)} = \frac{(1-\nu^2)K_I^2}{E} \tag{60}$$

Table 4: Basic Mechanical Properties of Cu-Al IMCs

	Young's Modulus E(Gpa)	Poisson's Ratio ν
Cu	117	0.34
Cu9Al4	186	0.30
CuAl	180	0.30
CuAl2	123	0.35
Al	70	0.30

Table 5: Basic Mechanical Properties of Cu-Al IMCs

	KI(Mpa.m1/2)	Tmax(Mpa)	ϕ(N/m)
Cu9Al4	0.67	30	2.19
CuAl	0.20	30	0.20
CuAl2	0.27	30	0.54

5.3 IMCs De-Bonding Simulation Results and Analysis

Effect of Different Types of Hexagon Grain Shape

To compare the effect of Cu-Al IMCs grain shape on the reliability performance of wire bond, both models are subjected to identical vertical displacement loading on the top side of the models while bottom side of both models is fixed as shown in Figure 73. Since $CuAl_2$ is the main composition of IMC layer after high temperature aging, its properties are used to represent the whole IMC layer in the model. Both models are assigned with uniform grain boundary interfacial strength. The overall bond strength is the average reaction forces at nodes on the top side of the model. The result of reaction force-displacement curve is shown in Figure 77. From the plot, it can be seen that overall mechanical response of Cu-Al wire bond model is sensitive to grain shape. Model with regular grain shape IMC has higher bond strength than model with irregular grain shape (around 20% at peak average reaction force).

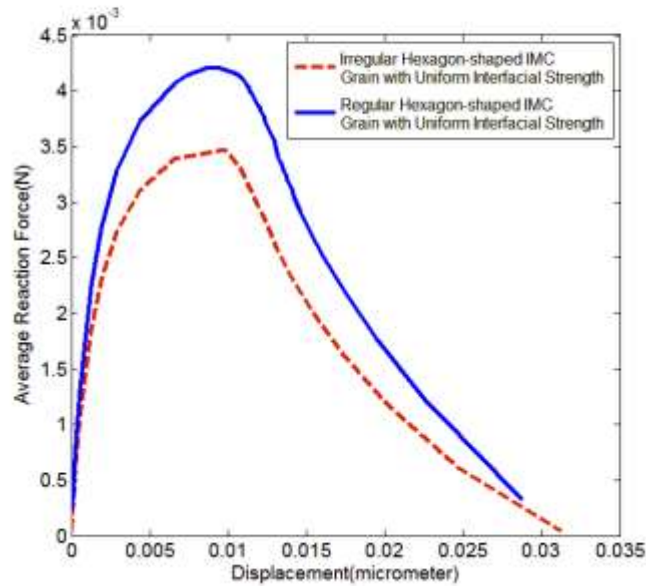

Figure 77: Regular Grain Shape vs. Irregular Grain Shape

The micro-crack pattern of both models are shown in Figure 78 and Figure 79. Crack initiation happened in sync across the IMC layer in model with regular shape IMC as boundaries that are perpendicular to the direction of displacement loading are under same stress. In model with irregular grain shape, crack initiation does not occur simultaneously because some of the grain boundaries are subjected to higher stress than others. Crack propagations in model with regular grain shape is along horizontal axis while crack propagation in model with irregular grain shape follow a zigzag path. Figure 80 shows normal stress in the model with irregular grain shape.

Figure 78: Micro-crack Pattern in Regular Shape IMC

Figure 79: Micro-crack Pattern in Irregular Shape IMC

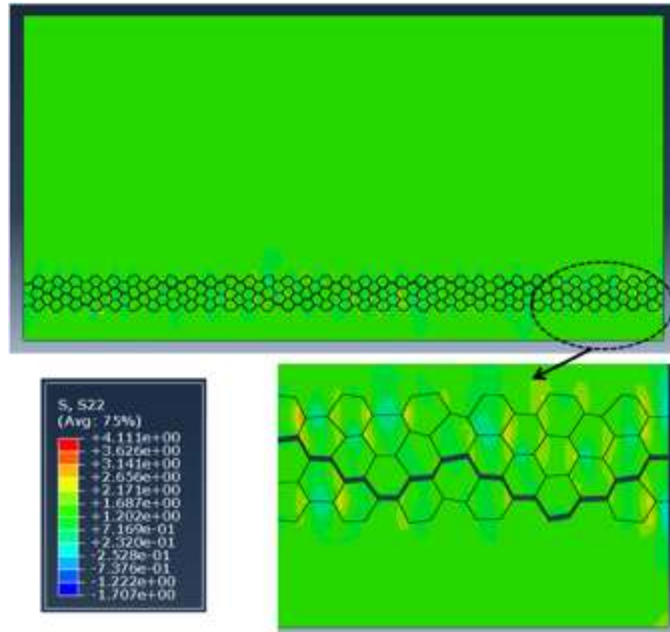

Figure 80: Micro-crack Pattern and σ22 in Model with Irregular Grain Shape

Effect of Different Types of Grain Interfacial Strength

Cu-Al IMCs usually contain various microstructural defects such as voids and preexisting cracks. In order to take those factors into consideration when predicting micro-mechanical behavior of wire bond, An proposed to use Weibull-based grain interfacial strength [An 2013] to account for those defects. In the following simulation, instead of using uniform grain interfacial strength, Weibull distribution [Weibull 1951] is adopted to describe the variability in IMC interfacial strength. 631 sets of maximum normal /tangential energy release rate and maximum normal/tangential cohesive tractions obtained from Weibull distribution are randomly assigned to 631 grain interfaces. Weibull parameters are picked (k=5, l=1.08) so that those 4 cohesive element parameters change from 30% to 170% of the average value used in models with uniform grain

interfacial strength. Also, 50% of those values are above the average values while the other 50% is below the average values as shown in Figure 81.

$$f(x;\lambda,k)=\frac{k}{\lambda}(\frac{x}{\lambda})^{k-1}e^{-(x/\lambda)^k}$$

$$\mathrm{x}:\phi_{\mathrm{n}}^{\mathrm{i}}/\phi_n(\phi_t^i/\phi_t,\sigma_{\max}^i/\sigma_{\max},\tau_{\max}^i/\tau_{\max}) \tag{61}$$

To study the effect of different types of grain interfacial strength on the reliability performance of Cu-Al wire bond. Results of models with uniform grain interfacial strength are compared with Results of models with Weibull distributed grain interfacial strength. The reaction force-displacement curve is plotted in Figure 82. It shows that model with Weibull distributed IMC grain interfacial strength has a lower overall mechanical response in both cases even though half of the grain interfacial strengths in Weibull model are stronger than the interfacial strength in uniform interfacial strength model. This conclusion indicates that pre-existing defects plays an important role in Cu-Al bond strength. Figure 82 also shows that when interfacial strength is Weibull distributed, model with regular grain shape loses less overall mechanical strength (9%) than model with irregular grain shape (23%). The normal displacement field and corresponding normal stress field for a Weibull distributed model with irregular grain shape are plotted in Figure 83.

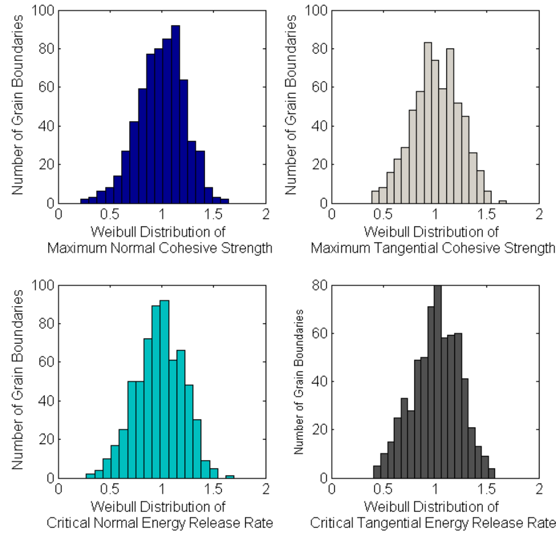

Figure 81: Weibull Distributed Grain Interfacial Strength

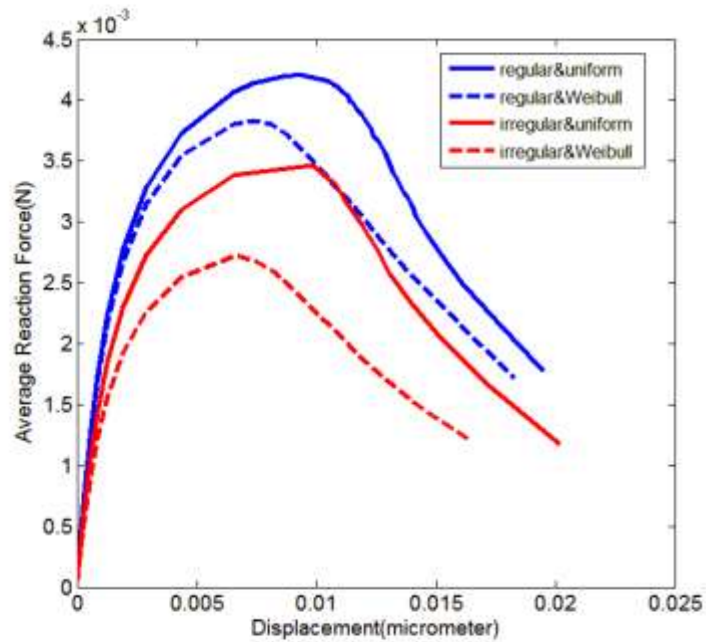

Figure 82: Uniform Grain vs. Weibull Distributed

Effect of Cu-Al IMC Growth

To find out how IMC growth influences the reliability of Cu-Al wire bond, models with three different IMC thicknesses are constructed as shown in Figure 84. They are models with irregular grain shape and Weibull distributed grain interfacial strength. The results of reaction force-displacement curves are plotted in Figure 85. From the plot, it can be seen that as IMC thickness increases, the overall mechanical response of Cu-Al wire bond decreases. This observation is in good agreement with the experimental findings. The reason for the decrease of bond strength can be attributed to the fact that the number of grains with weak interfacial strength (less than half of the average interfacial strength in the model) increase as IMC thickness increases and grains with weak interfacial strength play a key role in determining the bond strength of a Cu-Al wire bond as shown in the paper previously.

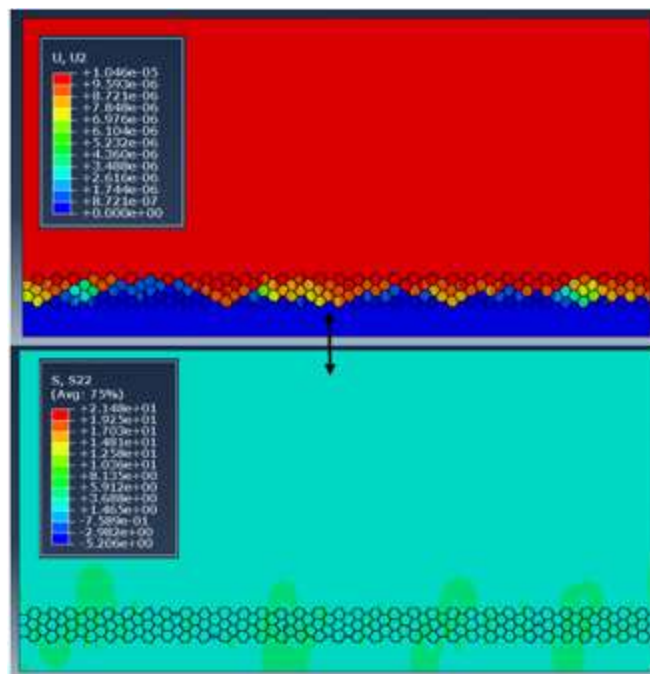

Figure 83: Normal Displacement and Normal Stress Contour

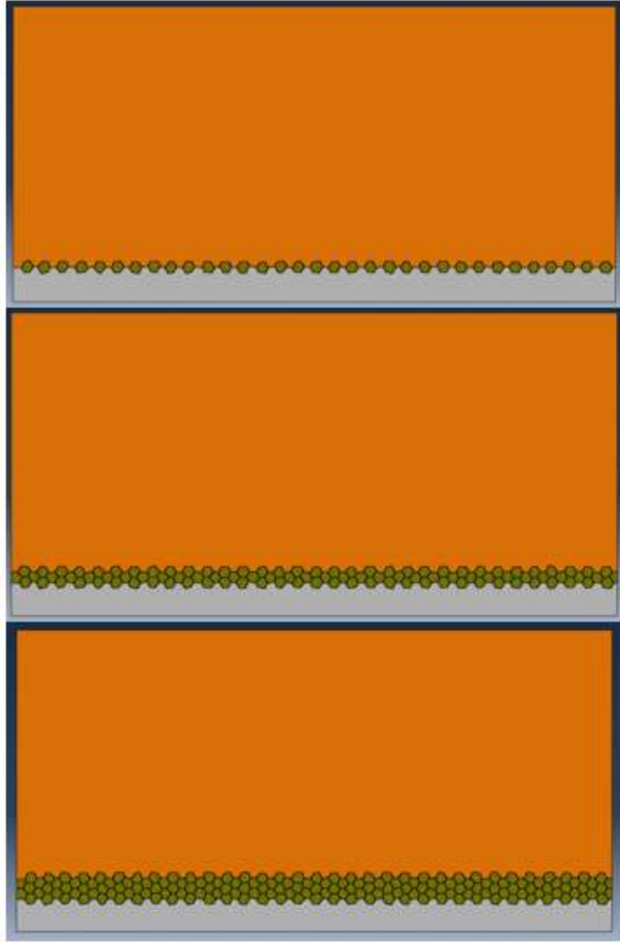

Figure 84: Models with Different IMC Thicknesses

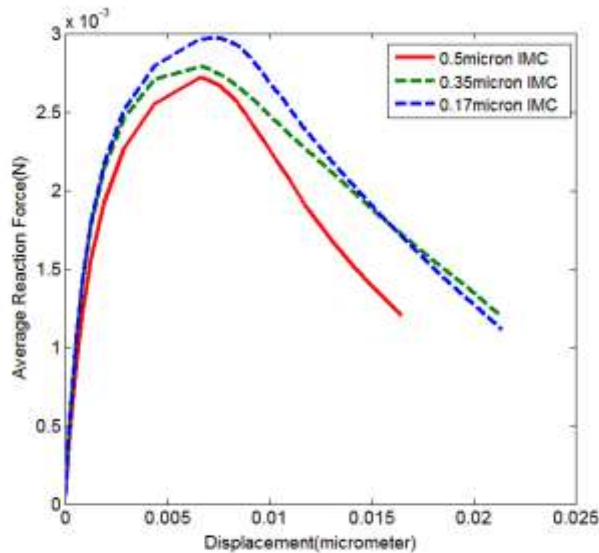

Figure 85: Models with Different IMC Thicknesses

In other word, growth of Cu-Al IMC results in the increasing number of weak IMC grain. Those grains make it easier for crack to initiate and propagate across bond pad interface causing wire bond failure.

Failure Mode under Multiple Cu-Al IMCs

Previous studies have shown that high temperature (175°C-225°C) exposure of Cu-Al wire bond leads to the formation of different intermetallic phases and the primary phases are Cu9Al4, CuAl and $CuAl_2$. To study how this affects the reliability performance of Cu-Al wire bond, a model with multiple IMC layers are constructed as shown in Figure 86. Three layers of IMC labeled with different colors are stacked up in the model with red grain layer being Cu_9Al_4, yellow grain layer being CuAl and dark brown grain layer being $CuAl_2$. The IMCs has irregular grain shape and Weibull distributed grain interfacial strength. Material properties listed in are assigned to the

corresponding layers. The result of micro-crack pattern is shown in Figure 87. Despite the randomly Weibull distributed grain interfacial stress, crack initiation and propagation occurred mostly horizontally within Cu_9Al_4 layer. It implies that crack formation and propagation is not only influenced by grains with weak interfacial strength, but also phase transformation in Cu-Al wire bond. This finding is again in good agreement with experimental findings.

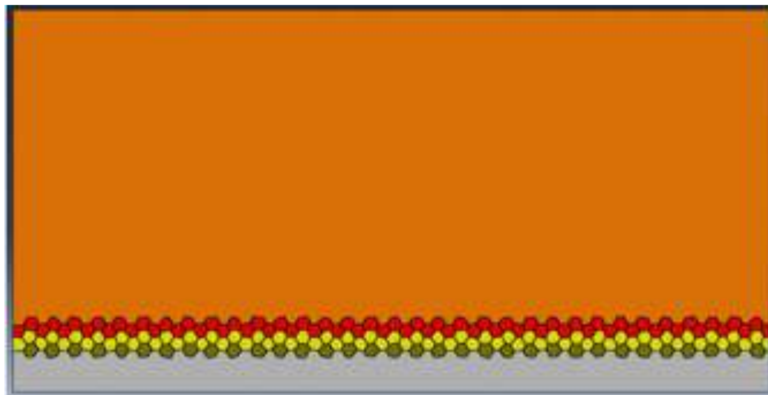

Figure 86: Models with Multiple IMC Layers

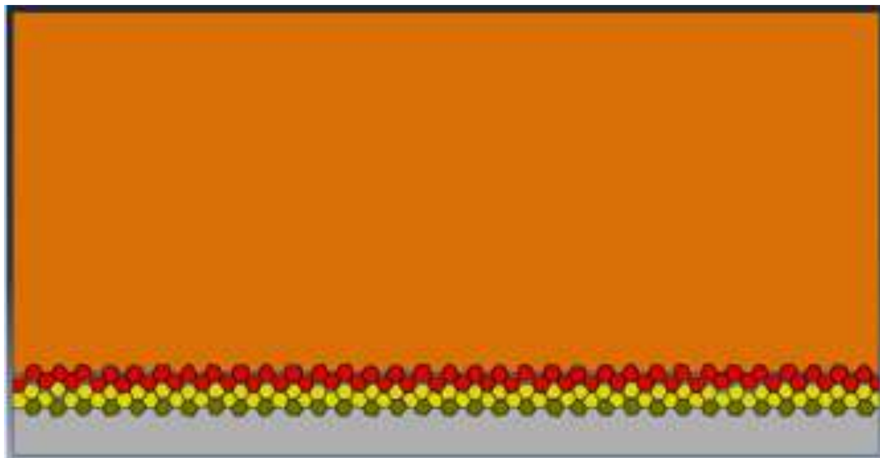

Figure 87: Micro-crack Pattern in Model with Multiple IMCs

This chapter introduces a grain level FEM to simulate the de-bonding process in the Cu-Al wire bond interfacial area. Simulation results shows that:

1. Overall mechanical response of wire bond is sensitive to IMC grain shape. Model with irregular hexagon-shape IMC grains has a stronger bond strength when it comes to wire pulling.

2. Model with Weibull distributed grain interfacial strength has a significant lower bond strength than model with uniformly distribution grain interfacial strength even though half of the grain interfacial strengths in Weibull model are stronger than the interfacial strength in uniform interfacial strength model. This implies that pre-existing defects in IMCs plays an important role in Cu-Al bond strength.

3. Increase of IMC thickness decreases the overall bond strength of Cu-Al wire bond as a result of increasing number of weak grain in IMC during interdiffusion.

4. Phase transformation influences crack propagation as well as grains with weak interfacial strength.

Simulation results are verified as all of them are in consistent with experimental findings of Cu-Al wire bond. Future work will be focusing on relating the methodology with fracture strength and electric resistance of Cu-Al wire bond to build a RUL prediction model for Cu-Al wire bond.

Chapter 6 COMSOL Cu Wire Bond Corrosion Modeling

In this chapter, several approaches to measuring the chloride ion diffusivity are introduced. A series of electrochemical corrosion test has been performed on both aluminum and copper and those test results will be incorporated into a predictive Butler-Volmer equation-based micro-galvanic corrosion model in order to quantitatively analyze the localized corrosion occurring at the bond pad interface.

6.1 Test Vehicle & Experimental Approaches

The test samples used in this study is bulk molding compound samples with a thin square shape. The samples are labeled as A, B, C, D, E and F. Sample thickness ranges from 0.5mm to 1mm. Samples length ranges from 42mm to 45mm as shown in Figure 88.

Figure 88: Molding compound sample F

Molding compound, A is a multi-aromatic epoxy. Molding compound B is an epoxy-phenol with some new resin. Molding compound C is a new non-epoxy resin. Molding compound D is a high temperature epoxy molding compound. Molding compound E is a silicone encapsulation material capable of high electrical resistivity, high thermal and mechanical stability and molding compound F is also a new type of resin providing superior performance with low warpage, low wire sweep, and high moisture reliability.

Approach

(a) Diffusion Cell Measurement

In order to measure the chloride ion diffusion coefficient in the molding compound, the diffusion cell method is adopted. As it can be seen from Figure 89. It is made up of a stopper, two glass chambers, a clamp, two Styrofoam washers and a pedestal. Epoxy molding compound sample is used as a membrane to separate two glass chambers with a 0.2cm^2 orifice, the upper one is the donor chamber which has the volume capacity of 5ml. potassium and contains chloride solution with designed concentration level (1M). The lower chamber is the receptor chamber in which 5ml deionized water is filled through the sampling port. Due to the concentration gradient at the interface, chloride ion is going to diffuse downwards through the molding compound. A clamp and two washers are used to prevent the leakage at the orifice-membrane interface. The stopper is placed on the top of the donor chamber to prevent any vaporization and the sampling port is sealed with parafilm for the same reason. The whole setup is vertically placed upon a pedestal.

Because of the ion diffusion in between solutions in the glass chambers, the concentration of chloride ion at both chambers will change as a function of time and the result of that will be used to calculate the diffusion coefficient of chloride ion in EMCs. As it is mentioned previously, laboratory grade potassium chloride powder is used to make the 1M concentration solutions. Potassium hydroxide and hydrochloric acid will be added to the solution in order to adjust the PH value to a designed level. As temperature and PH value will influence the ionic diffusion rate, experiments are performed at different temperature conditions and different PH conditions. The

thin thickness of the molding compound samples allows fast ionic diffusion. In the experiment, the PH is adjusted by using Cole Parmer PH meter as shown in Figure 90 and the change of ion concentration is monitored by using Q-TOF premier mass spectrometer manufactured by Waters.

Figure 89: Diffusion Cell Setup

Figure 90: PH meter

The Q-TOF Premier is a hybrid orthogonal acceleration Time-of-Flight mass spectrometer that enables automated exact mass measurement of precursor and fragment ions.

Before actually measuring the concentration of chloride ion in solutions, a calibration process is conducted in order to minimize the experiment error. During this process, four tubes of potassium chloride solution with different known concentrations are made. In each of the four test tubes, 1microliter of solution has been moved from the test tube into the testing vial where the solutions are going to be tested. The result of the test gives the chloride ion counts of the corresponding 1microliter solutions. The plot of ion counts as a function of the logarithmic values of the corresponding concentrations is shown is Figure 91. Once this step is done, the subsequent ion counts measurements are converted to the ionic concentrations simply by using this linear regression model.

In this chapter, Fick's law of diffusion is used to describe the ionic diffusion [Belton 1987] and solve for the diffusion coefficient D in m^2/s. The original model can be simplified, resulting in a one-dimensional diffusion model based on the assumption that the ionic diffusion along length and width of EMCs are both negligible because of the comparable small size of the thickness of the samples.

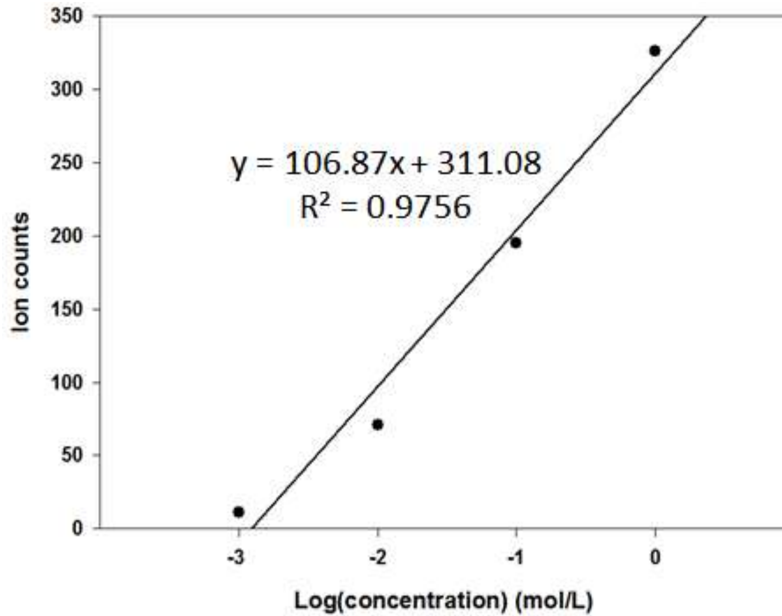

Figure 91: Calibration Plot

Given the Fick's law J=-D (dx/dc) where J stands for the ionic flux in moles/cm^2.s and c is the ionic concentration in moles/L, one is able to calculate the diffusion coefficient by plugging the concentration level of chloride ion in the receptor chamber, the experiment time and the thickness of the sample into the equation above. Figure 92 below shows the calculation steps made at room temperature in molding compound F as an example.

$$J_{cl^-} = -D\frac{dc}{dx}$$

$$\frac{mol}{m^2 * s} = \frac{m^2}{s} * \frac{mol/m^3}{m}$$

$$D_{RT} = -J_{cl^-} / \frac{dc}{dx} =$$

$$\frac{(1.77 \cdot 10^{-3} mol/L) * (5 \cdot 10^{-3} L)}{(2 \cdot 10^{-5} m^2) * (5.18 \cdot 10^5 s)} \Bigg/ \frac{(1 - 1.77 \cdot 10^{-3}) \cdot 10^3 (mol/m^3)}{5.3 \cdot 10^{-4} m} = 4.54 * 10^{-13} m^2/s$$

Figure 92: Calculation of Diffusion Coefficient at RT

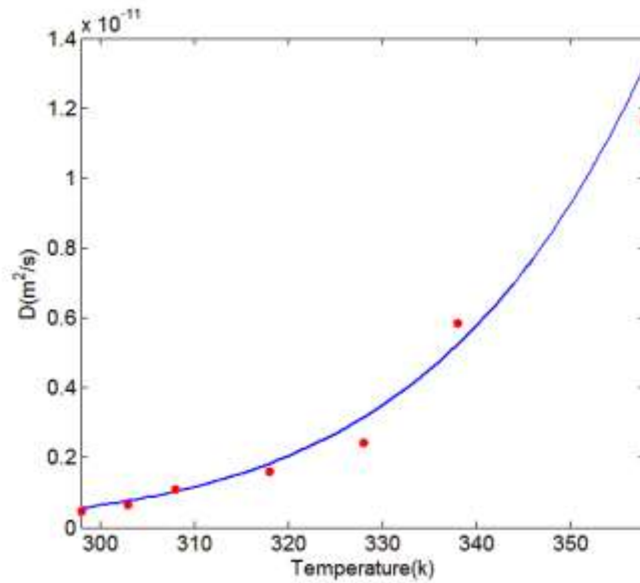

Figure 93: Diffusion Coefficient as a Function of T

As it is shown in Figure 93, the change of the value of diffusion coefficient as a function of temperature can be characterized by using the Arrhenius equation [Lantz 2007]. Fitting the data using Arrhenius equation resulted in an activation energy of 46.8kJ/mol.

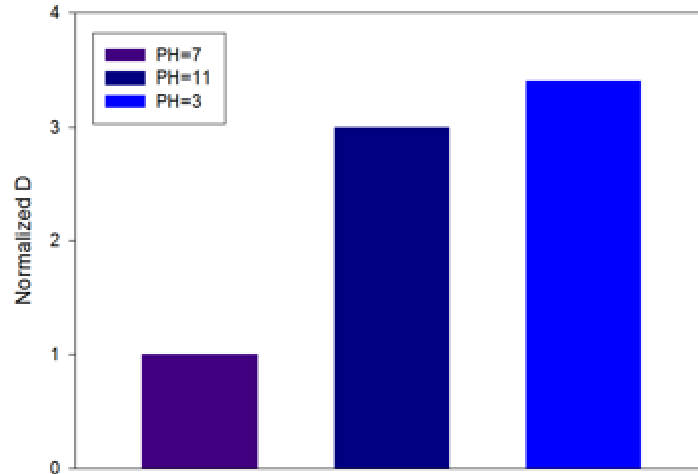

Figure 94: Comparison of Diffusion Coefficient Values under different PH values at room temperature

Figure 94 indicates the influence of acidic and alkaline environmental conditions on the rate of diffusion at room temperature. The value of Ds at pH=3 and pH=11 are 3 times and 3.4 times as much as that of D at pH=7.

(b) ICPMS-Based Diffusion Measurement

As an alternative to the diffusion cell approach, inductively coupled plasma–based approach [Simon 2004] is going to be presented as it helps crosscheck the accuracy of the pervious approach.

Inductively coupled plasma is a powerful tool for the determination of concentration of ionic species in a variety of different sample matrices. With this technique, solid samples are ashed by high temperature and then ashes are dissolved into a specific solution. After that, solution is injected into a radiofrequency (RF)-induced argon plasma using one of a variety of nebulizers. The sample mist reaching the plasma is quickly dried, vaporized, and energized through collisional

excitation at high temperature. The atomic emission emanating from the plasma is viewed in either a radial configuration, collected with a lens or mirror, and imaged onto the entrance slit of a wavelength selection device. Single element measurements can be performed with a simple monochromatic tube combination, simultaneous multielement determinations are performed for up to 70 elements with the combination of a polychromatic and an array detector. The analytical performance of such systems is competitive with most other inorganic analysis techniques, especially with regards to sample throughput and sensitivity.

In this experiment, several pieces of EMC sample F are immersed into a 1M KCl solution beaker at a room temperature with a piece of aluminum foil sheet covered on the top to prevent water from evaporating. Samples are taken out periodically from the beaker. After that, they are rinsed thoroughly with distilled water to remove any leftover KCl solution on the surface and are ground and analyzed immediately using inductively coupled plasma as shown in Figure 95. The results are average chloride ion ingress at different aging hours in the EMC samples.

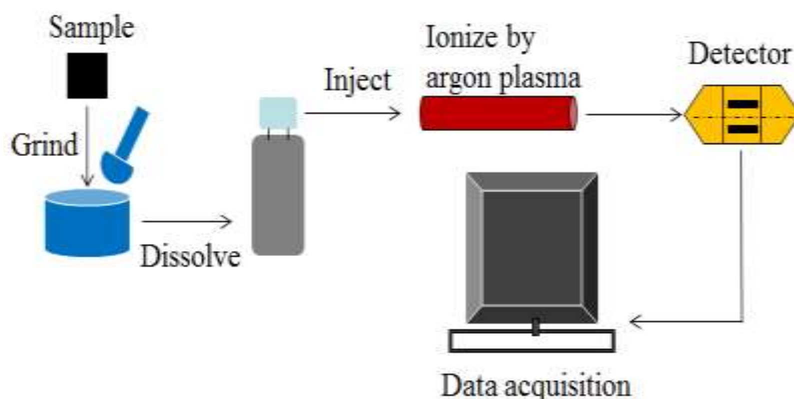

Figure 95: Schematic of ICP-MS main processes

Once the data is acquired, COMSOL simulation is used to calculate the change of concentration with respect to time in EMC samples. Before jump to the calculation, it is of great importance to estimate the maximum local concentration at this EMC sample. Lantz [Lantz 2003] Performed the diffusion cell experiments and found out the maximum diffusion coefficient of chloride ion in several different EMC samples by using TOF-SIMS analysis. The author comes to conclusions that firstly, prior to exposure to NaCl solution, there is a constant Cl ion concentration across the fracture surface of the EMC. Secondly, the maximum concentration is around one order of magnitude of the initial randomly distributed concentration. According to the conclusions above, Figure 96 shows the schematic plot of the ICPMS experiment results.

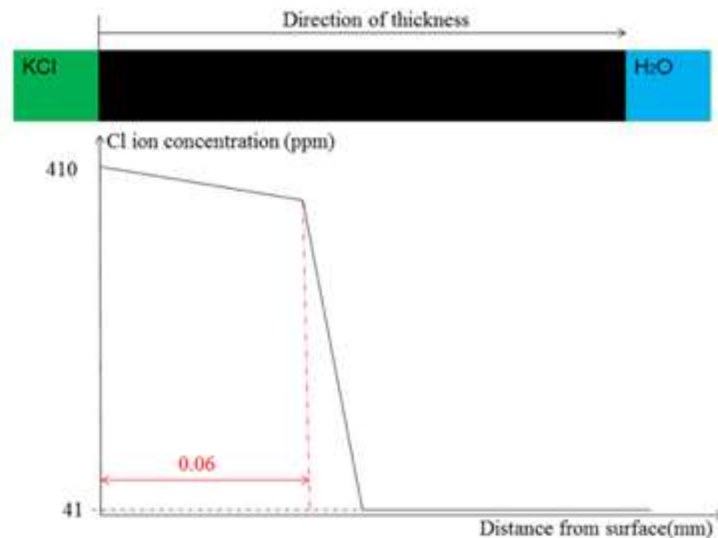

Figure 96: Schematic Picture of Concentration Profile

As provided by ICPMS, the average initial concentration is 41ppm in EMC sample F, thus, the maximum concentration is set to be 410 ppm. In addition, 1D diffusion model has been used because of the length and the width of the samples are considerably greater than the thickness.

Electric potential gradient is set to be zero because the lack of electrical field. Trial and error is used to calculate the diffusion coefficient of the chloride ion at room temperature.

In addition to the steps above, the empirical equations provided by Springer0 is plotted and compared to the results of simulation in order to cross-check value of D.

$$c(t) = c_s \left[1 - \exp\left[-7.3 \left(D \cdot t / h^2 \right)^{3/4} \right] \right]$$

(62)

In this equation, c(t) denotes the concentration at time t, cs stands for the saturation level, h is the thickness of the EMC sample.

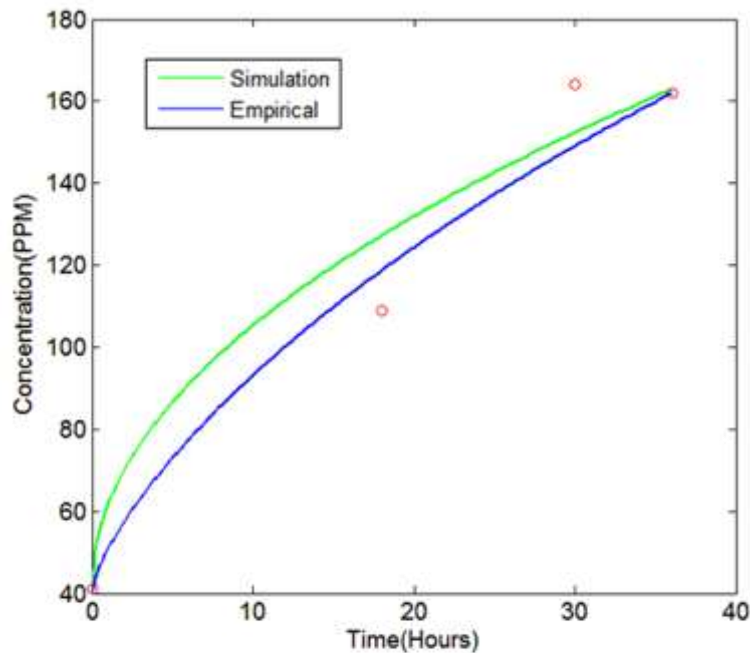

Figure 97: Comparison among Results of Multiphysics Simulation, Empirical Equation and Experiment results

From Figure 97, it can be readily seen that the simulation results not only match the experiment data but also fit the empirical equation, the maximum error between experiment results and simulation results is 16.8%. As a result, diffusion coefficient of chloride ion under room temperature is acquired, which is $1.7*10^{-13}m^2/s$. The result acquired by this approach is approximately 2.5 times small than the D value calculated by the diffusion cell approach. As both results have the same orders of magnitude, the two previous approaches are considered to be suitable approaches to calculating the diffusion coefficient of chloride ion in the molding compound.

(c) Scanning Electron Microscope & Energy-dispersive X-ray spectroscopy Analysis

In this series of experiments, molding compound samples are aged in 1M potassium chloride solutions at different temperatures for different amount of time and the cross-section of samples are investigated by using the scanning electron microscope and energy-dispersive X-ray spectroscopy technologies after they are rinsed thoroughly with DI water. The instrument model used here is Zeiss EVO 50 series along with an Oxford INCA EDS X-ray Microanalysis System. Due to the complex formulation of epoxy molding compounds, ionic diffusion paths inside EMCs are not as simple as that inside homogenous materials. Previously, there are two major assumptions of the ionic diffusion path in EMCs known as bulk ionic diffusion and interfacial ionic diffusion [Crank 1968]. In bulk ionic diffusion, the ionic species travel through the matrix as opposed to the interfacial diffusion in which ionic species travel through the interfaces of the matrix and the filler materials.

Figure 98 shows the microscopic view of EMC sample B after being aged at 1M KCl solution for three weeks at 85^0C. As it can be seen readily from the image, this type of molding compound is filled with fillers that have two different shapes. One of which is round-shape and the other is bar-shape.

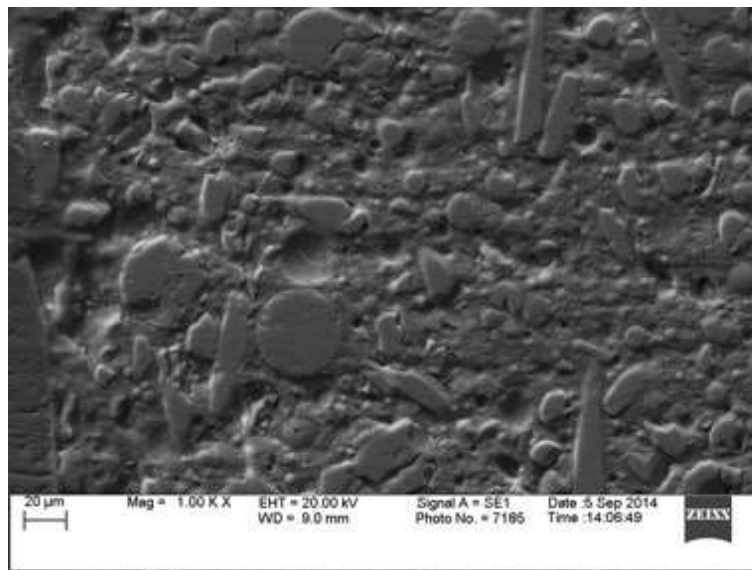

Figure 98: SEM Image of Cross-section of EMC Sample B after a 3-week immersion in 1M KCl Solution at 85^0C

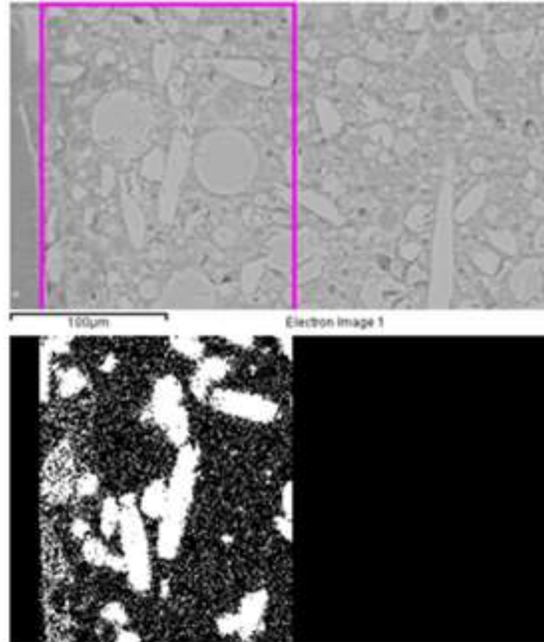

Figure 99: EDS Mapping Image of Figure 98

In order to figure out the number of filler materials in the EMC, EDS mapping image is acquired from the left part of Figure 98. Figure 99 indicates a strong calcium signal at the white-colored part. This part is perfectly aligned with the bar-shaped filler material in the previous image which implies two things, there are two different types of filler materials in EMCs and one of them contains certain amount of element calcium.

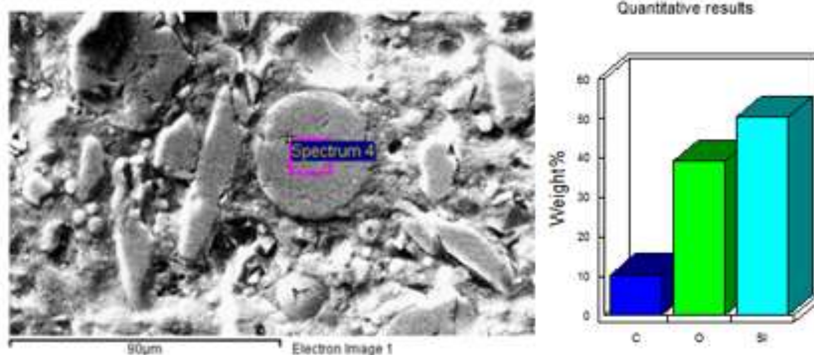

Figure 100: SEM Image and EDS Spot Analysis of Filler Material A

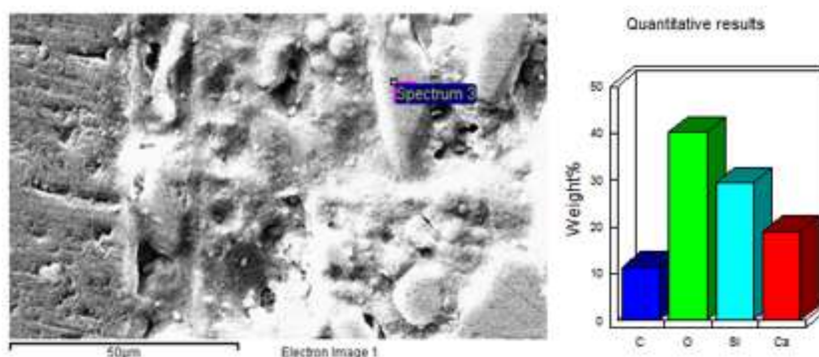

Figure 101: SEM Image and EDS Spot Analysis of Filler Material B

Figure 100 and Figure 101 show the results of EDS spot analysis of both two filler materials. As shown by the bar charts, both of the filler materials contain element carbon, oxygen and silicon. In addition to those aforementioned elements, filler B contains an extra noticeable amount of calcium. Based on the information provided above, filler A is considered to be round fused silica which is widely used in EMCs to impart the desired coefficient of thermal expansion, elastic modulus and fracture toughness properties. Filler B is considered to be calcium carbonate that can enhance the thermal transfer property of the polymer.

In an attempt to find out the diffusion mode of chloride ion, the chloride ion mapping image is obtained from the left part of Figure 100. Before the immersion process, the mapping signal of chloride ion is below the detection limit of the SEM/EDS instrument. After the immersion, the mapping signal image of chloride ion is acquired and is overlapped with the image of Figure 100.

As it has been stated, the left edge of the molding compound has been aged in 1M KCl solution at 850C for 3 weeks. According to Figure 102, signal of chloride ion in the image are strongest in the area closed to the edge and signal intensity decreases as it gets deep into the EMC. This is in consistent with the fact that ionic ingress starts from the solution/EMC interface and proceeds due to the concentration gradient. Further investigation of the image below leads to the conclusions that ionic species tends to diffuse through the interfacial area particularly between the matrix and the calcium carbonate as there is almost no signal detected on the bar-shaped material and chloride signal is relatively stronger at the filler/matrix interface.

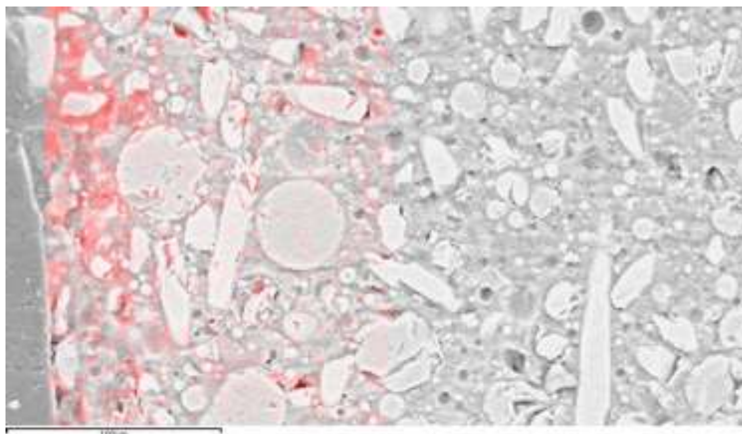

Figure 102: Overlap between Chlorine Mapping & x-section of EMC Sample B

Based on the analysis above, we are confident of making the conclusion that ionic diffusion inside EMC sample B is interfacial diffusion. More specifically, it diffuses around the calcium carbonate. The reason for this interfacial diffusion is probably because of the fact that there are micro-voids at the matrix/filler interface that allows moisture and ionic species to reside and it is easier for ionic species to diffuse through this interfacial path as this path has relatively the lowest

diffusion resistance compared to the rest of the paths. Another set of 1M KCl solution immersion experiments have been performed on the EMC sample F at 1500C for 96 hours.

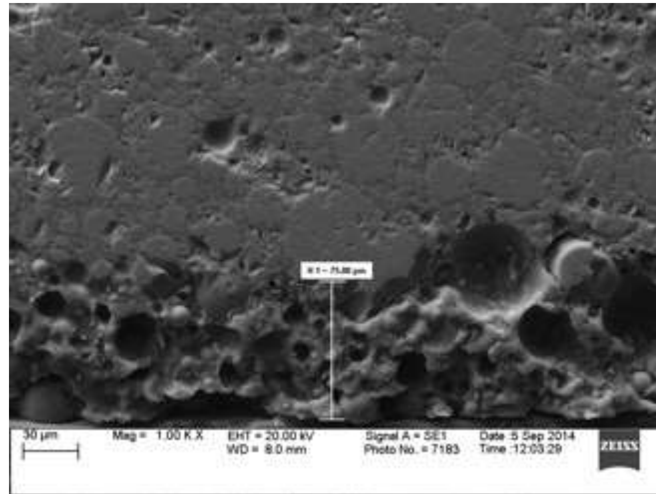

Figure 103: SEM Image of Cross-section of EMC Sample F after a 96-hour immersion in 1M KCl Solution at 150^0C

As it is shown in Figure 102, this type of EMC has only one filler material of round fused silica. The EMC/solution interface degraded towards the center of the cross-section for about 75 micrometers due to the high temperature. From the image, it is obvious that the degraded part looks like a bunch of craters with different sizes, based on this special type of change of morphology and the fact that fused silica has high thermal stability, it can be concluded that the degradation is most likely caused by either the dissolution of epoxy resin or the reaction between epoxy resin and water around the edge at a high temperature. As a result, EMC could no longer hold on to the filler material because the loss of binding material.

(d) Weight Loss Test

Weight loss tests were performed on all of the 6 EMC samples. Before the actual tests, those samples were baked at 130^0C isothermal aging chamber for 72 hours to remove the moisture.

As it shows in Figure 103, long-term exposure to very high temperature results in degradation of the binding material in molding compound which leads to the gradual loss of weight. EMC sample F has the biggest percentage weight loss after 2000 hour thermal aging while sample D has the smallest one among all the six samples. This result is in consistent with the descriptions in EMC technical data sheet in that the only EMC sample that has the property of high thermal stability is sample E. Thus E should be the best for HTSL while F should be avoided using under high temperature. Figure 104 shows the result of weight loss of EMC sample candidates.

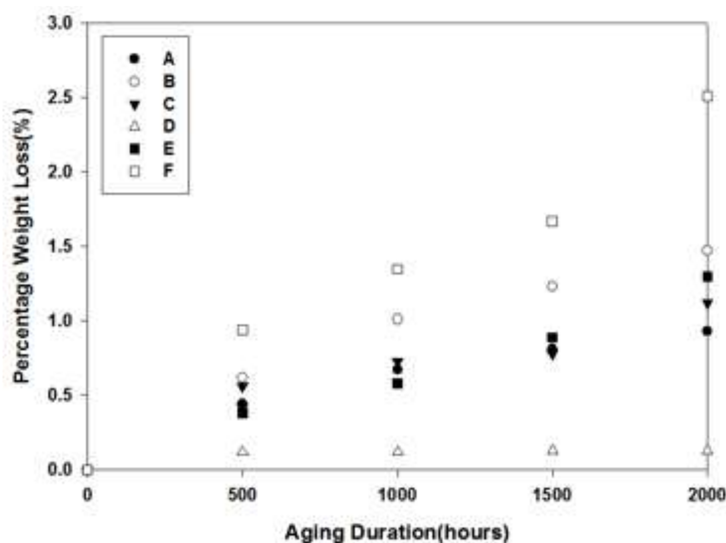

Figure 104: Weight Loss Test under 200^0C

(f)Electrochemical Polarization Test

Electrochemical polarization can provide significant useful information regarding the corrosion rate and susceptibility of specific materials to corrosion in designated environments.

In this paper, copper and aluminum samples were tested in solutions with different PH values and chloride ion concentrations in an attempt to figure out the effect of them on the corrosion behaviour of these two metals.

The types of metal used in this study are 6061 aluminum alloy and 110 copper. The metal rod were cut into small pieces, on which electrical wire are soldered. Then the pieces of samples were cold mounted in epoxy resin to give an exposed area to the solution. The exposed surface areas were hand-polished with BUEHLER grinding paper up to 1200 grit and then degreased with ethanol, cleaned with distilled water and dried by air pump.

Experiments were carried out in a conventional three-electrode electrochemical cell [Szklarska 1986, Zaid 2008] with a sliver chloride reference electrode and a platinum counter electrode immediately after the sample preparation process in order to avoid prolonged exposure to air.

Samples were immersed in solutions for 24-48 hours prior to the tests to attain stable open circuit potentials. During the tests, the scan rate is set to 0.15mV/sec and the initial potential is set to at least 250mV below the OCP. Once the V-I curves were acquired, Tafel extrapolation method is used to fit curves to obtain Tafel parameters.

Table 6: Electrode Potential Difference between Copper and Aluminum in KCl solutions with different pH values and Different Values of Ion Concentration

	pH=3	pH=11
0M	0.52	0.38
0.01M	0.53	0.52

From Table 6, it can be seen that the potential gap between copper and aluminum increases noticeably as the concentration of chloride ion increases in alkaline solution, which indicates an increasing likelihood of galvanic corrosion between two metals. As for acidic conditions, the potential gap stays almost the same and the gap maintains at a relative high value.

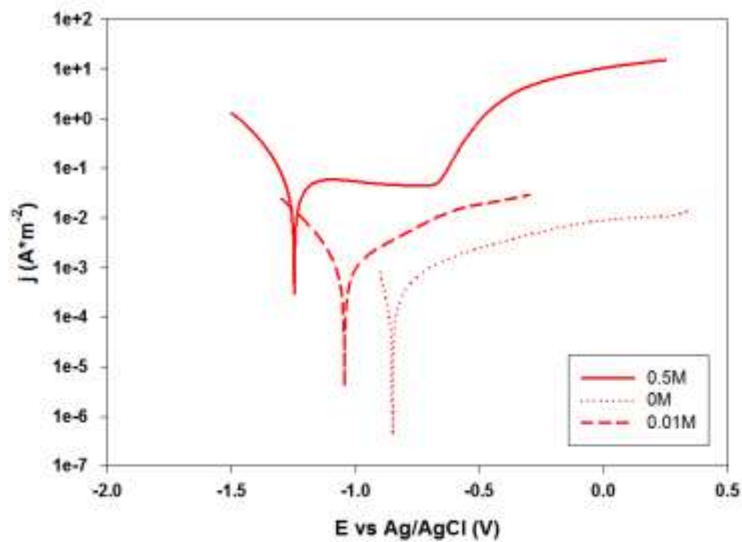

Figure 105: Polarization Curves of Aluminum under Different Values of Chloride Ion Concentration at pH=7

Figure 105 shows that as concentration of chloride ion increases, the open circuit potential of aluminum shifted to more negative values and the exchange current density increase drastically.

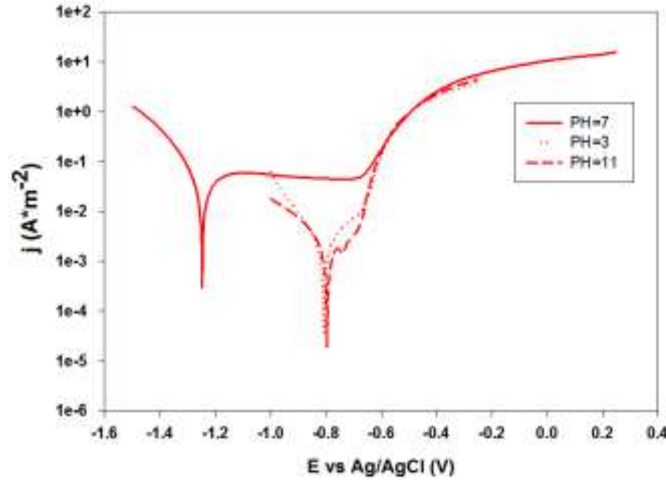

Figure 106: Polarization Curves of Aluminum under Different pH Values at 0.5M Concentration of KCl

According to Figure 106, OCP shifted to more negative when aluminum is immersed in a neutral solution and the current density stays unchanged as overpotential increases from 0.1V to 0.55V at pH=7. The same phenomenal didn't occur at the acidic and alkaline conditions. This is attributed to the fact that aluminum is amphoteric. Under highly oxidizing and high concentration of chloride ion condition, passivation layer will be dissolved very quickly compared to that of neutral condition. In other word, the pitting corrosion potential coincides with the corrosion potential in acidic and alkaline solutions.

Tafel parameters of both copper and aluminum were obtained at neutral condition under different values of KCl concentration and these parameters were used in the Bulter- Volmer equation in the simulation part to help calculate the dissolution rate of the aluminum pad in a copper aluminum wire bond system as shown in Table 7.

Table 7: Tafel Parameters

	j(Al)(A*m^{-2})	j(Cu)	E(Al)(V vs Ag/AgCl)	E(Cu)
Cl-=0(M)	0.0003	0.0001	-0.895	-0.147
CL-=0.01	0.01	0.01	-1.044	-0.102
CL-=0.5	0.05	0.04	-1.246	-0.231

	α(Al)	β(Al)	α(Cu)	β(Cu)
Cl-=0(M)	0.3	0.3	0.25	0.25
CL-=0.01	0.3	0.3	0.2	0.2
CL-=0.5	0.2	0.2	0.18	0.18

6.2 Corrosion at Cu-Al IMC Interface

In the previous publication, the simulation mainly focuses on the transport of impurity in EMCs. Despite giving some insight into the ion-related corrosion, it doesn't provide anything that relates corrosion rate of copper aluminum bond pad with the local concentration of chloride ion. In this part, a Butler-Volmer equation based micro-galvanic corrosion model is introduced in order to give more insight into the ion-related corrosion.

This specific corrosion process initiates when two dissimilar metals (copper and aluminum) are electrically connected, and are in a conductive environment known as electrolyte (EMC). The corrosion is always associated with the presence of halide (chloride ion) as a catalyst [Benedeitit 1995].

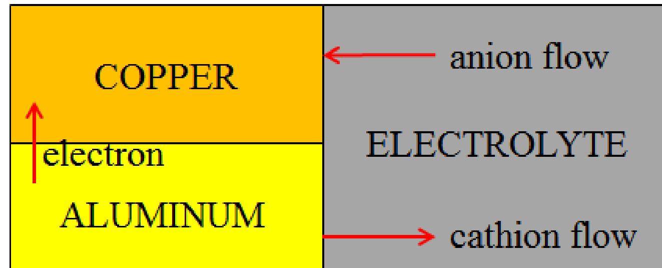

Figure 107: Schematic Plot of Galvanic Corrosion

$$O_2 + 2H_2O + 4e^- \rightarrow 4OH^- \tag{63}$$

$$Al \rightarrow Al^{3+} + 3e^- \tag{64}$$

As shown in Figure 107, the aluminum part acts as anode which undergoes material dissolution while copper part acts as cathode where the oxygen reduction takes place. The electrons produced by the anodic reaction will be used by cathodic reaction. In this simulation, it is assumed that aluminum dissolution is the only anodic reaction and oxygen reduction is the only cathodic reaction [Murer 2010].

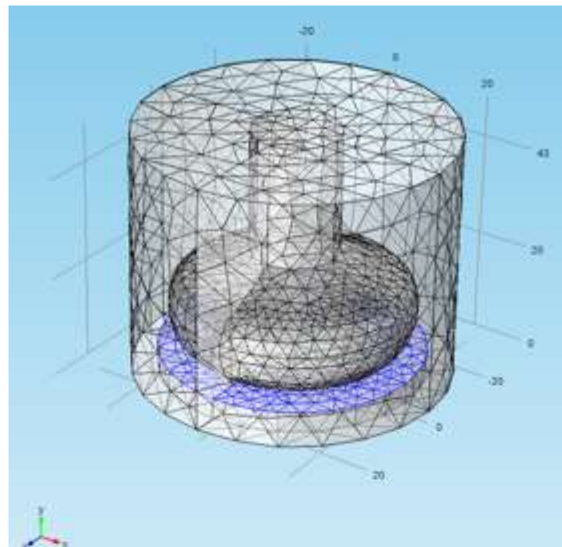

Figure 108: Model Geometry (unit in μm)

Figure 108 shows the simulation geometry, the cylindrical galvanic system is made of copper wire, ball bond and aluminum pad whose top surface is highlighted with blue. The radius of the ball bond is 25 μm and the thickness of aluminum pad is 4 μm. The rest of the space is filled with epoxy molding compound. Governing Equations and Subdomain Conditions

$$\nabla^2 \Phi = 0 \tag{65}$$

Laplace equation is obtained combining the equation of conservation of charge with the constitutive equation relating the electric field distribution to the electrochemical potential gradient. Φ is the potential in the domain (V) in reference to Ag/AgCl. The conductivity of electrolyte is set to 0.045S/m according to the technical data sheet of molding compound F.

$$N_i = -D_i \nabla c_i - z_i \mu_i F c_i \nabla \Phi \tag{66}$$

Nernst-Planck equation is used to describe the transport of ionic species in the EMCs. The driving force of the ionic transport is concentration gradient and electric gradient. In this equation, Ni is the ionic flux (numbers of ions per unit area per unit time), Di is the diffusion coefficient of species i, ci stands for its concentration, zi denotes the charge number of species i. F is the universal gas constant and Φ is the applied electrostatic potential. μ is the mobility of the charged particle i which is given by the Einstein-Smoluchowski relation:

$$\mu_i = D_i \, q / k_B T \tag{67}$$

Where kB is Boltzmann constant. T stands for the temperature; q is the elementary charge. The change of ionic concentration in time is givens by:

$$\frac{\partial c_i}{\partial t} + \nabla \cdot (N_i) = R \tag{68}$$

Where R is the reaction term (mol/m3.s) and it stands for the evolution of hydrogen ion and hydroxide ion due to the oxygen reduction combined with the water autoprotolysis.

$$2H_2O \rightarrow H_3O^+ + OH^- \tag{69}$$

The production rates of both ionic species are calculated by using the chemical reaction equilibrium:

$$R_{H^+} = R_{OH^-} = k_{wf} - k_{wb} * [H^+][OH^-] \tag{70}$$

Where Kwf and Kwb are forward and backward reaction constant. The values of them are set to be 10^{-8} and 1 so that the calculation could actually converge. [H+] and [OH-] are the ionic concentration term.

The use of Laplace equation indicates that the galvanic corrosion is under a kinetic control. As a result, the Butler-Volmer based equations could be applied on the metal/EMC interface to calculate the corrosion current density shown in Figure 109 and Figure 110:

$$j_c = j_{0c}\{(\exp(E_c - \phi)/\alpha_c) - (\exp(E_c - \phi)/-\beta_c)\} \tag{71}$$

$$j_a = j_{0a}\{(\exp(E_a - \phi)/\alpha_a) - (\exp(E_a - \phi)/-\beta_a)\} \tag{72}$$

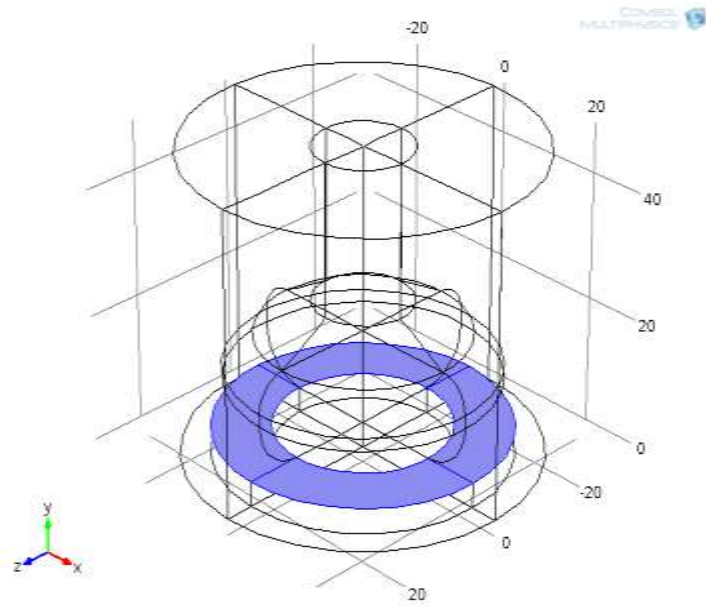

Figure 109: Aluminum Pad/EMC Interface

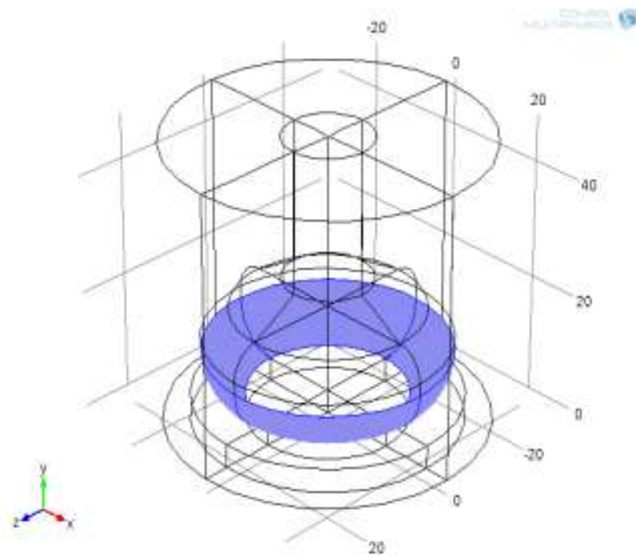

Figure 110: Copper ball bond/EMC Interface

The normal derivatives of the electrode potential Φ at these two highlighted boundaries are given by

$$\partial\phi / \partial n = j_{c(a)} / \sigma \tag{73}$$

The Aluminum pad dissolution and local evolution of hydrogen ion are both related to the Butler-Volmer equations by using

$$j = F\sum_{i=1}^{n} z_i N_i \tag{74}$$

The fluxes of species are proportional to the current densities. For aluminum pad dissolution, the ionic flux is jc/3F. For hydroxide ion evolution, the associated ionic flux is -ja/F.

All the other boundaries are set to be insulating and no flux:

$$\vec{n} \cdot N_i = 0 \tag{75}$$

$$\partial\phi / \partial\vec{n} = 0 \tag{76}$$

Moving Boundary

In order to track the dissolution of aluminum pad and the effect of the dissolution on the corrosion current density, moving boundary condition is imposed on the aluminum pad. The pad dissolution rate is given by:

$$v = N_{Al^{3+}} M / \rho \tag{77}$$

Where v is the dissolution rate in the unit of m/s, M and ρ are molar mass and density of aluminum respectively. It is also assumed that only aluminum pad is subjected to free dissolution and the direction of it is along the negative y-axis.

Table 8: Initial Conditions

	Al^{3+}	H^+	OH^-
D(m^2/s)	$4.54*10^{-13}$	$4.54*10^{-13}$	$4.54*10^{-13}$
C0 (mol/m^3)	0	10^{-4}	10^{-4}

Diffusion coefficient of all the ionic species have been set to be the same as the value of chloride ion which is obtained by performing the diffusion cell measurements previously. The initial concentration of hydrogen ion and hydroxide ion are set shown in Table 8.

The Tafel parameters are used in the simulation to simulate the effect of concentration of chloride ion and pH value on the corrosion current density at aluminum pad/EMC interface and the evolution of hydrogen ion in the neighborhood of copper ball bond.

Simulation Results

Time dependent solver is used to solve the problem. The following corrosion current density (Figure 111) contours are obtained from the simulation under zero concentration of chloride ion and neutral environmental condition.

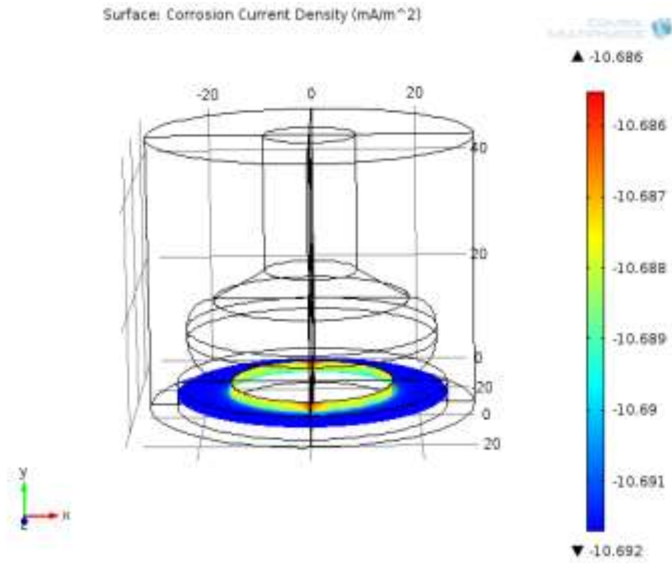

Figure 111: Time=5*10^6(Second)

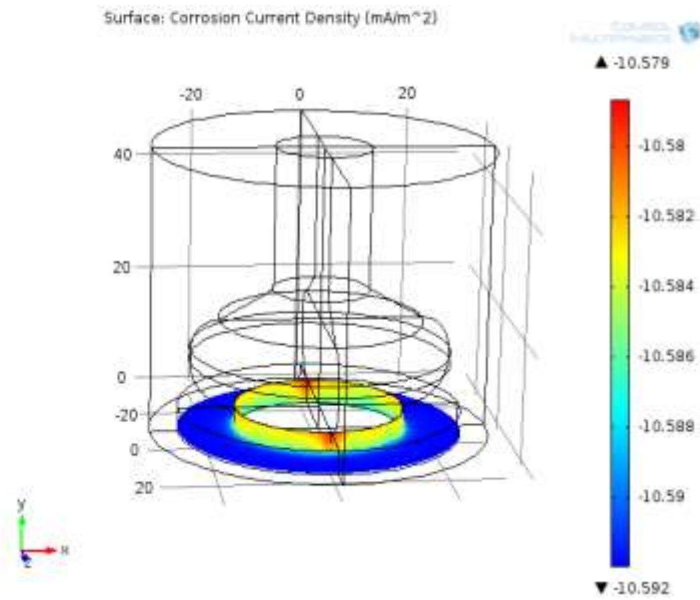

Figure 112: Time=10^7(Second)

As shown in Figure 112, the corrosion current density under initial neutral and zero concentration of chloride ion are approximately 10 milliamps. The corrosion current density at inner part of aluminum pad is slightly smaller than that at the outer part. As time proceeds, the progression of dissolution of the pad can be directly seen from the plot. From Figure 112, it shows that the pad dissolves 1 μm after 2 months under aforementioned condition.

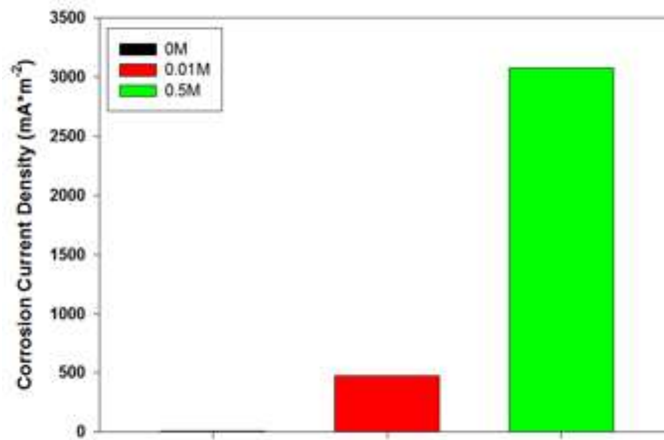

Figure 113: Comparison of Average Corrosion Current Density

The effect of local concentration of chloride ion on the corrosion current density can be seen from Figure 113. When the concentration of chloride ion is 0.01M, the correspond corrosion current density is 500 milliamps and for 0.5M ionic concentration condition, the correspond value reaches 3000 milliamps. The corrosion rate increases drastically as the concentration of chloride ion in the neighborhood of copper aluminum bond pad increases.

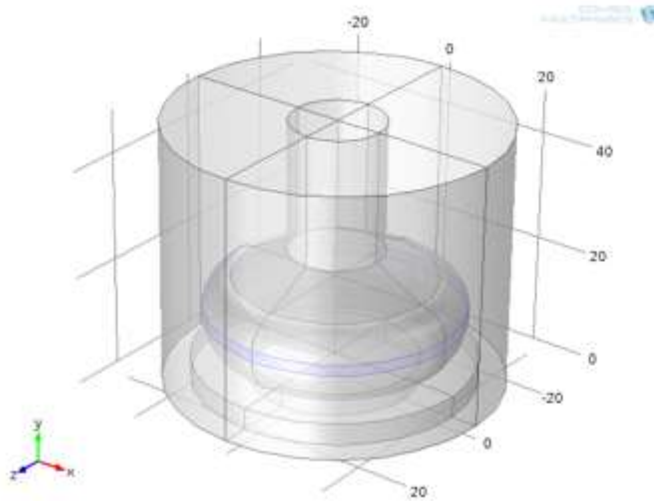

Figure 114: Hydroxide Ion Flux

It is considered that the rate of peripheral matrix dissolution around a cathodic particle is accelerated by alkaline attack due to the ORR or proton reduction occurring at the particle surface. Thus, the pH evolution at the vicinity of copper ball bond is of great interest. In the simulation, evolution of both hydrogen ion and hydroxide ion in the system are taken into account by adding an ionic flux at the copper/EMC interface which is highlighted with blue in Figure 114. As mentioned in the paper, the oxygen reduction occurring at the neighborhood of the interface will cause the evolution of pH of the system over time.

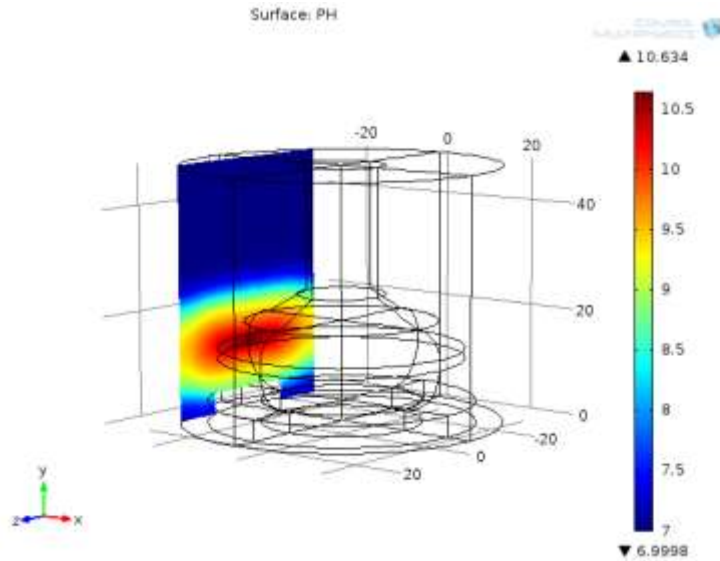

Figure 115: PH contour at time=3(hours)

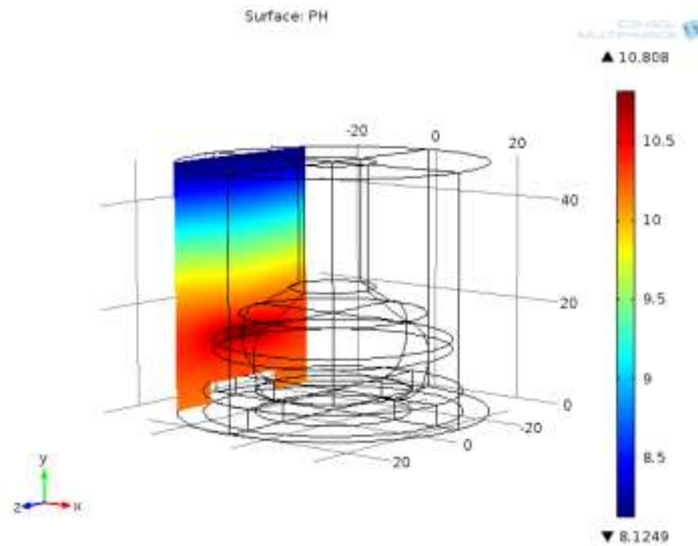

Figure 116: pH contour at time=24(hours)

Figure 115 and Figure 116 shows pH contour on a plane located at the radius of the ball bond. This simulation is also under initial neutral and zero concentration of chloride ion condition. From

the plots, it is obvious that the most alkaline part of the plot is the area in the vicinity of copper bond and as time proceeds, the alkalinity becomes stronger.

Chapter 7 Electrochemical Polarization Based Cu-Al IMC Corrosion Modeling

In this chapter, electrochemical polarizations are performed on copper, aluminum and Cu-Al IMCs. Subsequently, polarization data is used as input in the numerical simulation to investigate effects of different environmental factors on galvanic corrosion rate at Cu-Al bond pad interface. Different boundary condition approaches are introduced and compared to find the most suitable one for the simulation. Results wirebond lifespan simulations are verified by comparing them with experimental results. Acceleration factor model for Cu-Al wire bond application under thermal/humidity conditions is established. Finally, more experiments on BGA377 are performed. Results from experiments are correlated with results obtaining from simulation. Both simulation and experimental results show that the early stage of continuous growth of IMCs mitigates corrosion and increases the reliability of wire bond under high humidity operational conditions.

7.1 Micro-galvanic Corrosion

Metal Corrosion consists of at least two reactions, oxidation reaction and reduction reaction through which electrons are transferred from anode to cathode accompanied by the transport of mass and the reduction of oxygen or hydrogen.

$$M \rightarrow M^{n+} + ne^{-} \tag{78}$$

$$O_2 + 2H_2O + 4e^- \rightarrow 4OH^- \qquad (79)$$

As a result of the exchange of electrons between cathode and anode, current is generated on the metal surfaces. The current rate is influenced by the external applied potential. According to Tafel equation the V-I relation is illustrated as two straight lines where potential is plotted against the log of the reaction rate as shown in Figure 117,

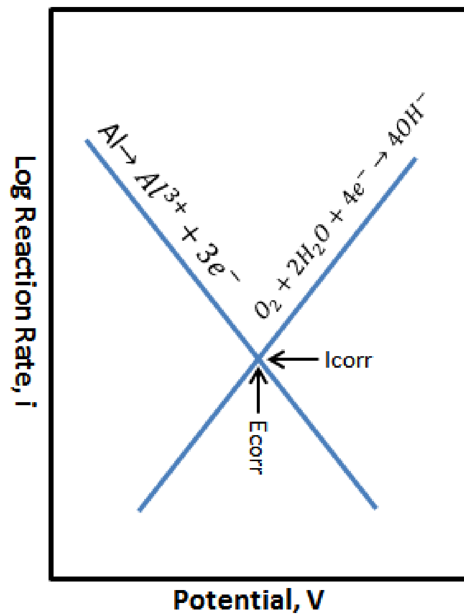

Figure 117: Schematic Plot of V-I Curve

Each metal/environmental combination has its own unique electrode potential. When two metals are in electric contact in that environment, the metal(Al) with more negative electrode potential will have a driving force to lose electrons to the metal (Cu or IMCs) with more positive electrode potential. Electrons are able to flow between them which upsets the individual balances and reestablish the new balance.

According to the mixed potential theory [Bard 2001, Kelly 2001, Hamann 2007], all of the electrons generated by anodic reactions must still be consumed by cathodic reactions, which means that the sum of anodic currents must equal the sum of cathodic currents in a corrosion cell. The schematic plot of Cu-Al galvanic corrosion is shown in Figure 118,

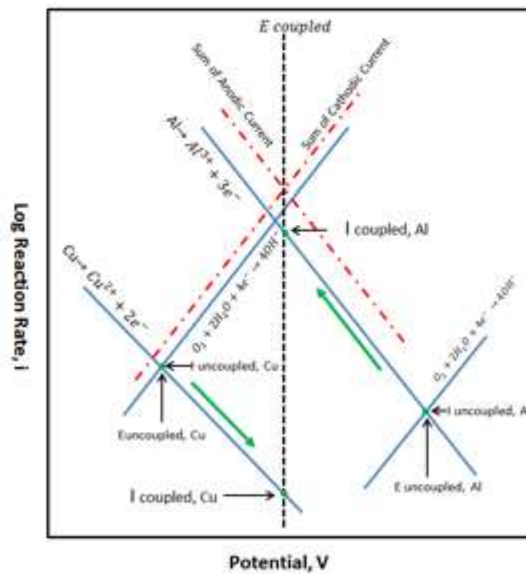

Figure 118: Schematic Plot of Cu-Al Galvanic Corrosion

Red dashed lines are sum of the anodic and cathodic current respectively. The intersection of the red dashed lines is the point where charge balance is reestablished, which is the mixed potential. Points that created by individual reactions crossing the mixed potential line are the new-established reaction rates. The anodic material aluminum, which corrodes at a rate of Icorr_Al when uncoupled with Cu, corrodes at a rate of Icouple_Al when electrically connected to copper. The cathodic material copper, which corrodes at a rate of Icorr_Cu when uncoupled with Al, corrodes at a rate of Icouple_Cu when electrically connected to Al. In sum, in Al-Cu system, Al corrosion rate increases compared to the situation when uncoupled while Cu corrosion rate decreases.

Galvanic Corrosion at Cu-Al bond pad interface

Due to the hydrophilic characteristic of epoxy molding compound, moisture is able to ingress into it especially when the operational environment is humid. It is believed that [Spaan 2010, Liu 2011, Boettcher 2010, Lall 2014, Lall 2015] corrosion occurs at Cu-Al ball bond interface with moisture acting as an electrolyte. Since the edge of the ball bond interface is the only part of interface in direct contact to EMC, galvanic corrosion most likely initiates at this site where Al splash and Cu ball bond forms a small angle as shown in Figure 119 left(as-bonded state). That explains the high humidity failure mode in which crack always initiates at the edge. When wire bonds are annealed at elevated temperature, intermetallic crystal structure grows in between the interfacial area due to phase transformation. If those annealed wire bonds are used under high humidity environmental condition, Cu-IMC-Al then becomes the galvanic corrosion couple as shown in Figure 119right (post thermal-treatment state).

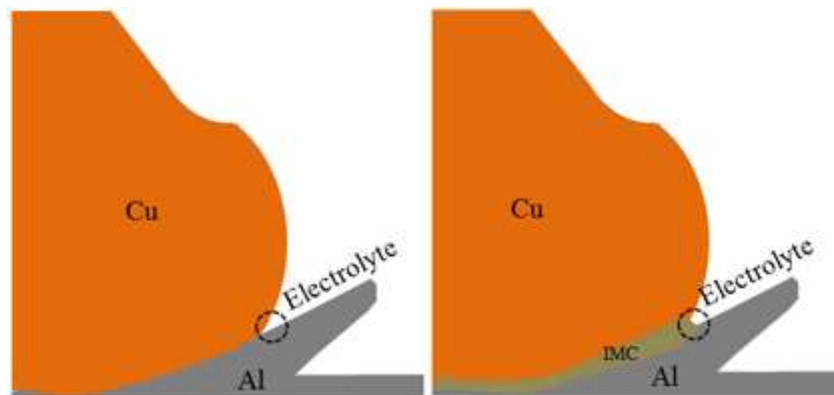

Figure 119: Cu-Al Interfacial Corrosion

7.2 Corrosion Modeling Approach

Numerical Model of Corrosion

Since Cu-Al bond pad interfacial corrosion happens at near nanoscopic level, approaches to quantitatively monitoring the corrosion process is not available yet. In order to overcome this obstacle, numerical corrosion model has been developed to enables the study of corrosion at such a tiny configuration. A predictive model would allow researchers to gain more insight into the corrosion behavior. Prior to the use of the predictive model on bond pad galvanic corrosion, this approach will first be used to simulate large-scale electrochemical corrosion to show its capability.

Assume that the electrolyte surrounding Cu-Al couple is incompressible and electro-neutral. When the system is under steady state conditions, the potential distribution within the electrolyte is governed by the charge conservation equation:

$$\nabla . i = 0 \tag{80}$$

$$i = \sigma E \tag{81}$$

i is the current density. σ is the electric conductivity of the electrolyte and E is the electric field which can be expressed as a function of electric potential:

$$E = -\nabla \phi \tag{82}$$

For constant σ, combining all those equations above results in the equation:

$$\nabla^2 \phi = 0 \tag{83}$$

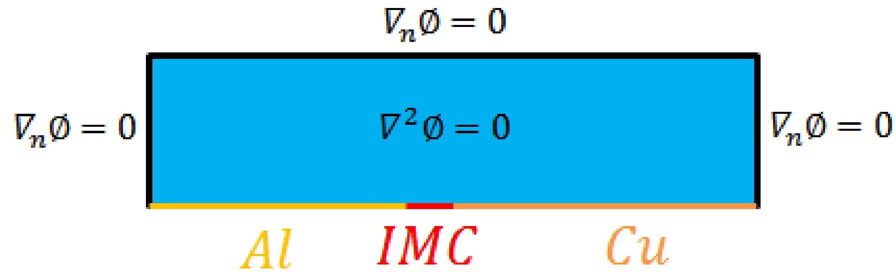

Figure 120: Micro-Galvanic Corrosion Configuration

Figure 120 shows a co-plane Cu-Al micro-galvanic corrosion cell. The metals boundary is 2 micrometers long. The cell has a finite out-of-plane thickness (20μm). All the other boundaries are set to be insulating. On the bottom boundary, the normal derivative of potential at metal electrolyte interface is defined as:

$$\nabla_n \phi = j / \sigma \tag{84}$$

j is the corrosion current density. The potential distribution of metal/electrolyte interface needs to be defined in order to solve the set of equations.

Two main boundary conditions has been developed by researcher over the years to quantify galvanic corrosion [Doig 1979, Murer 2008, Murer 2010, Deshpande 2012, Murer 2012], both will be applied to the model in order to find the more suitable one.

Piecewise Cubic Interpolation Boundary Condition

The local current density at the anode (Al)/electrolyte interface and cathode (IMC, Cu)/electrolyte interface are defined as:

$$\nabla_n \phi = -i_{Al}(\phi)/\sigma$$
$$\nabla_n \phi = -i_{IMC}(\phi)/\sigma$$
$$\nabla_n \phi = -i_{Cu}(\phi)/\sigma \qquad (85)$$

iAl(Φ), iIMC(Φ) and iCu(Φ) are piecewise cubic interpolation functions obtained from lab scale potentiodynamic polarization experiments.

Large-Scale Galvanic Corrosion Experiment

Galvanic corrosion behavior is investigated using electrochemical polarization [Application Note 2010, Enos 1997]. Multipurpose 110 copper and multipurpose 6061 aluminum provided by McMaster-Carr Inc. and Cu-Al intermetallic compounds provided by sophisticated alloys Inc. are used as materials of galvanic couples. Figure 121shows some of the experiment samples. The metal rods are cut into small pieces on which electrical wire are soldered. Those sample pieces are cold mounted in epoxy resin to give an exposed area to the solution they are immersed. Exposed surfaces are polished manually with BUEHLER grinding paper up to 1200 grit followed by degreasing using ethanol. The final procedure of sample preparation is to dry up samples using air pump. Experiments were carried out in a conventional three-electrode electrochemical cell with a sliver chloride reference electrode and a platinum counter electrode immediately after the sample preparation process in order to avoid prolonged sample exposure to air.

Samples were immersed in solutions for 48-72 hours prior to the tests to attain stable open circuit potentials. During the tests, the scan rate is set to 0.15mV/sec and the initial potential is set to at least 250mV below the OCP. Once the V-I curves were acquired, Tafel extrapolation is

performed manually to fit the experimental curve resulting Tafel parameters. In the model verification test, areas of the exposed surfaces are 1.25 inches in diameter and samples are immersed in 0.5M KCl solution with a 7pH.

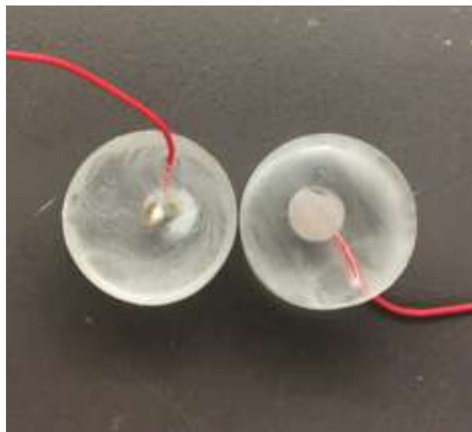

Figure 121: IMC Sample Preparation

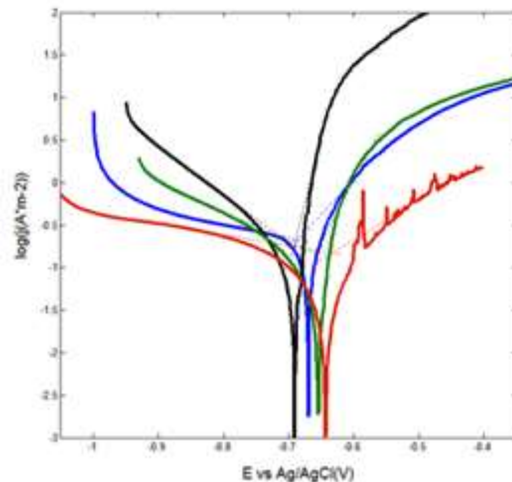

Figure 122: Polarization Curves for Large-scale Cu-Al Corrosion Cell

Figure 122 shows the four polarization curves performed under the same environmental condition as mentioned before. Tafel extrapolation analysis of those curves shows that corrosion

current densities are 0.175 A/m^2, 0.145 A/m^2 0.212 A/m2 and 0.149A/m^2 respectively. Under such environmental condition, a corresponding COMSOL model is built based on the geometry of the samples shown in Figure 123.

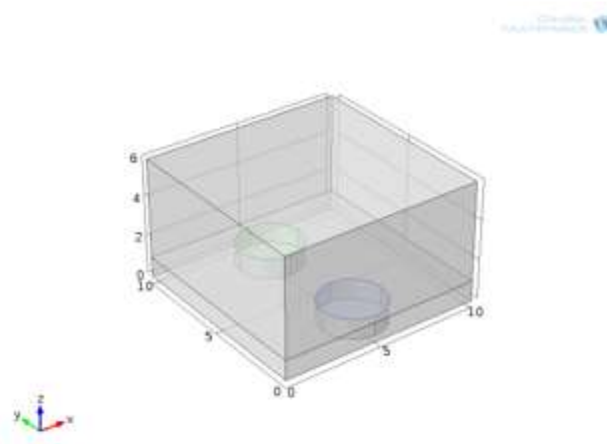

Figure 123: COMSOL 3D Corrosion Model

The green and blue round surfaces represent the exposure surface of both samples with a 10cm by 10cm by 5cm KCl solution surrounding them. The piecewise cubic interpolation functions obtained from polarization are used as boundary conditions for both metal surfaces and the rest of the surfaces are set to be insulating as described in the model introduction. The conductivity of solution is set to be 2.5S/m [Deshpande 2012]. Model is solved using stationary solver and the result is shown in Figure 124.

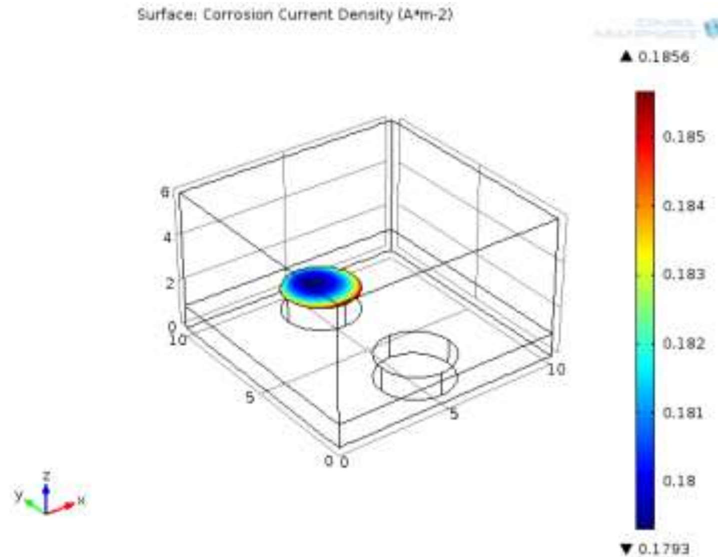

Figure 124: Simulation Result

Simulation result shows that the average current density is 0.182 A/m^2. The difference in rate of corrosion between experiment result and simulation result is around 6%. Thus, the model has shown to be capable of simulating the electrochemical behavior and predict the rate of corrosion.

Butler-Volmer Based Boundary Condition

Another widely-used corrosion boundary condition in is Butler-Volmer based boundary condition. In order to double-check the result of corrosion current density and also to find out which one of them is more appropriate for the microscopic model configuration, it is useful to apply it to the galvanic corrosion model and compare the result of corrosion current density using both boundaries.

Assuming that the electrochemical process is controlled by charge transfer across the metal/electrolyte interface. As a result, the Butler-Volmer based equations could be applied on the metal/EMC interface to calculate the corrosion current density as shown in Equation 71 and Equation 72. This approach requires accurate calculation of linear region from cathodic and anodic polarization parts. The logarithmic nature of current density axis amplifies errors in extrapolation. A poor selection of slopes might cause a huge deviation from the actual corrosion current density. N.M. Noor [Noor 2014] proposes an approach that uses linear regression analysis to locate the linear Tafel region.

According to regression analysis theory, assuming n data pairs (x,y) are linearly related, least square method can be used to fit the dataset in which

$$y_i = \hat{\beta}_0 + \hat{\beta}_1 x_i \tag{86}$$

Where Yi, Xi are the response variable and independent variable, β0 and β1 are population Y-intercept and population slope. The coefficient of determination Rsquare can be used to measure how well data fits the statistic model.

$$\hat{\beta}_0 = \bar{y} - \hat{\beta}_1 \bar{x} \tag{87}$$

Assuming the independence of the error term throughout the polarization dataset and also the fact that there exists a linear region in a polarization curve, let the polarization dataset be divided into k equal intervals, linear regression model can be applied to all k intervals respectively. Each interval will have its own Rsquare and population slope. For a linear region made of several

intervals, high Rsquare region and flat β1 region is expected. Thus, the linear region can be located by observing the variation in these two parameters against the k equal intervals.

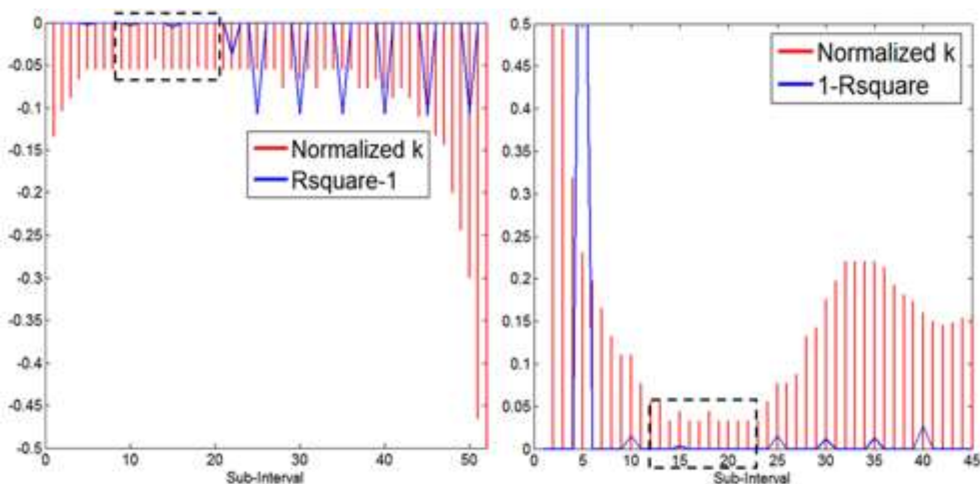

Figure 125: Plots of Locating Linear Regions

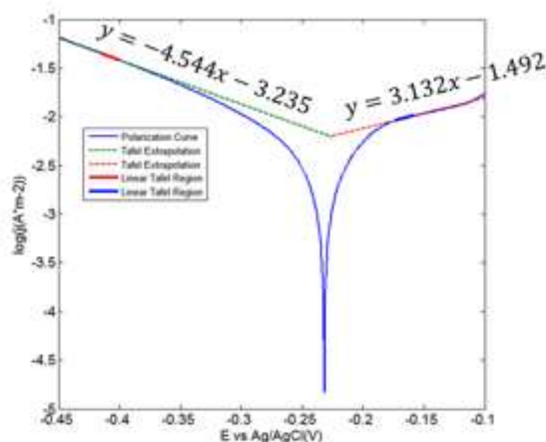

Figure 126: Tafel Extrapolation of Cu under 0.5M Chlorine Concentration and 7pH

As shown in Figure 125, regions with high Rsquare values and relatively flat β1 region has been boxed up to indicate the linear regions within polarization curves. These regions are used to perform Tafel extrapolation from which all the parameters required for the calculation of Butler-

Volmer boundary condition will be obtained as shown in Figure 126 . The same procedures are applied to Al plotted in Figure 127.

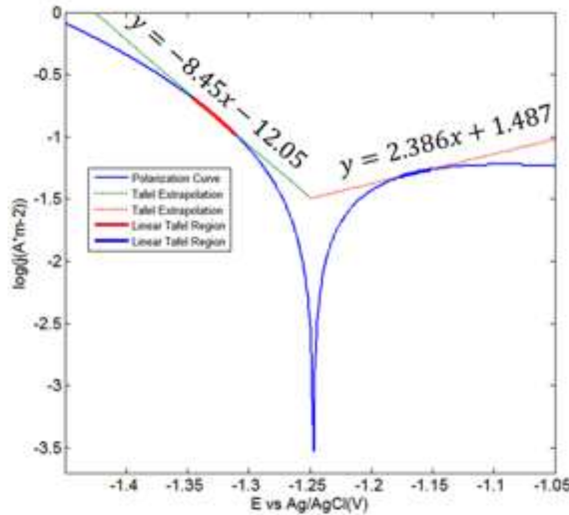

Figure 127: Tafel Extrapolation of Al under 0.5M Chlorine Concentration and 7pH

Table 9: Model Inputs

0.1M/5.2pH	j0(A*m-2)	E(V)	α(V)	β(V)
Cu	0.006	-0.23	0.22	0.32
Al	0.032	-1.25	0.42	0.11

Table 9 sums up the model input and Figure 128 shows simulation results from using both Butler-Volmer B.C. and piecewise B.C. Results of corrosion current density across the Cu-Al galvanic cell are similar except the fact that when handling small geometry configurations (microscopic level), Butler-Volmer based approach tends to average out corrosion current density while piecewise approach gives a clearer picture of the change of corrosion current density across the Al electrode. According the result of Cu-Al bond pad corrosion under uHAST [Boettcher 2010,

Yamada 2010], the part most susceptible to galvanic corrosion is the Cu-Al interfacial part, which is consistent with the findings from the result using piecewise B.C. In the remaining analysis, piecewise approach is utilized.

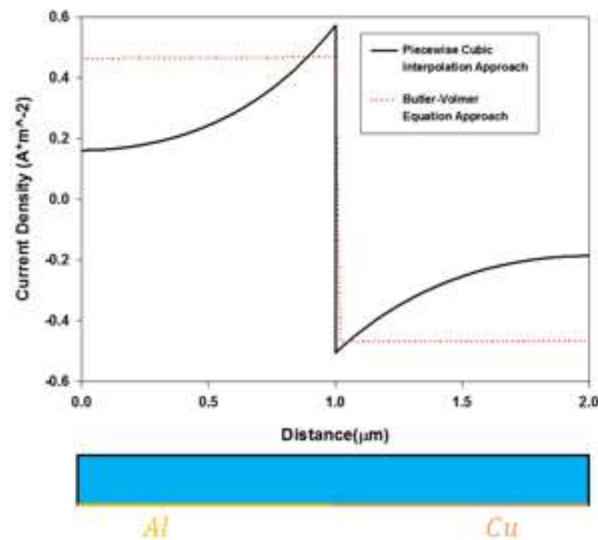

Figure 128: Corrosion under 0.5M Chlorine Concentration and 7pH

7.3 Simulation Results & Analysis

Polarization Experiments

Study of numerical simulation of corrosion behavior at bond pad interfacial area requires polarization curves of copper, aluminum and their IMCs under different environmental conditions. Potentiodynamic polarization experiments have been performed on all of them in KCl solutions with varies chlorine concentration levels and 5.2pH as shown in Figure 129 and Figure 130.

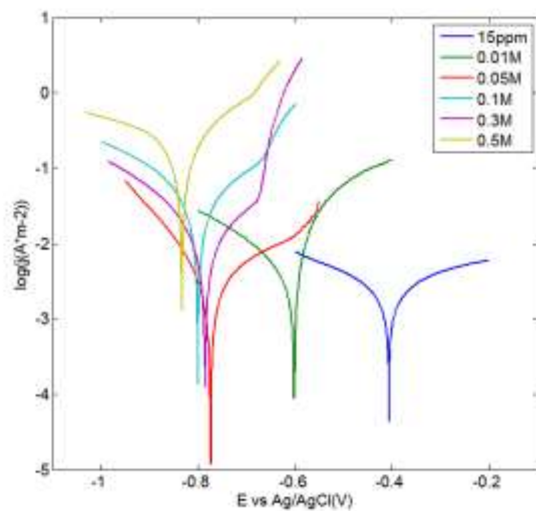

Figure 129: Electrochemical Polarization Curves of Al

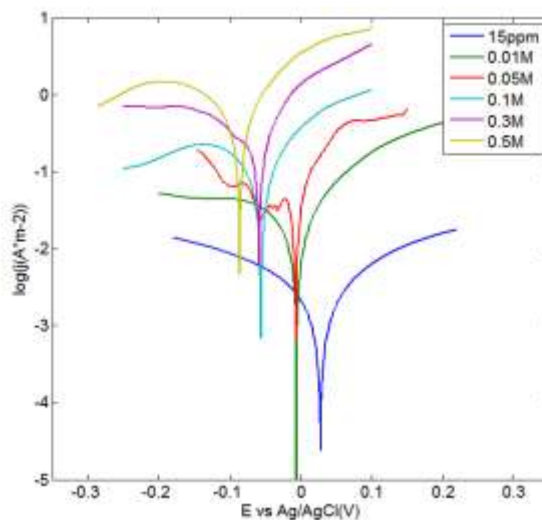

Figure 130: Electrochemical Polarization Curves of Cu

Plots above show that OCP of aluminum and copper shift to a more negative value as chlorine concentration level increases. Also, uncoupled corrosion current density increases as chlorine level increases.

(a) As-bonded state

Effect of Chlorine Concentration Level under 5.2pH Control

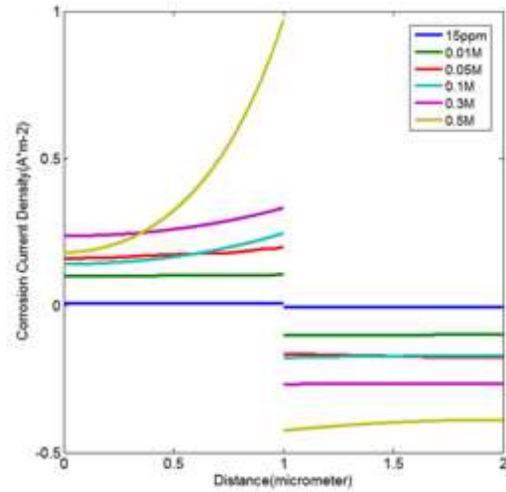

Figure 131: Effect of Chlorine Concentration

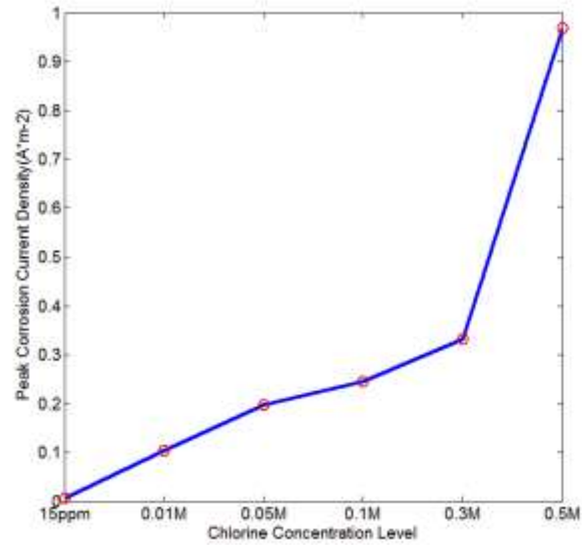

Figure 132: Effect of Chlorine Concentration

As shown in Figure 131 and Figure 132, when corrosion area ratio of copper to aluminum is unity (1μm in length), the region with the highest corrosion rate is the interfacial area towards aluminum pad. Peak current density plot indicates that when chlorine concentration level is very low (15ppm), the corrosion is almost negligible. On the contrary, the corrosion rate is much higher when contaminant level is very high. The difference in corrosion rate between low chlorine level and high chlorine level is more than two orders of magnitude in this case as corrosion reaches a steady state.

Effect of pH Value under 0.1M KCl and Room Temp. Control

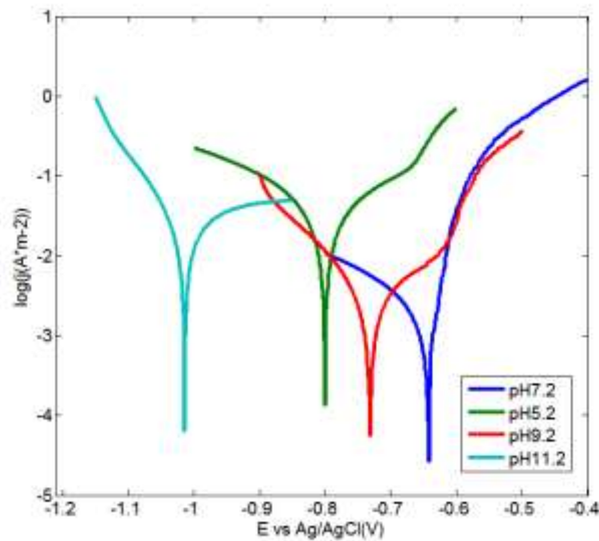

Figure 133: Effect of pH (Al)

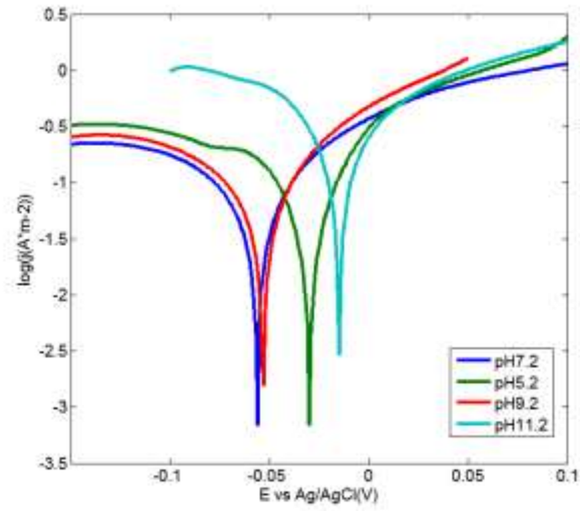

Figure 134: Effect of pH (Cu)

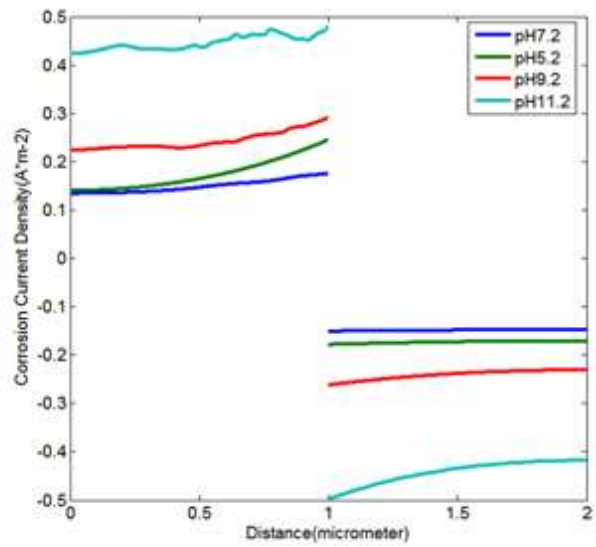

Figure 135: Effect of pH (Cu-Al Corrosion Cell)

It is believed that anodic dissolution is favored by alkaline attack due to the oxygen reduction reaction or proton reduction occurring at the vicinity of corrosion surface [Murer 2012]. Equation

2 shows that as corrosion proceeds, electrons will be transported to the surface of the metal and then react with oxygen and moisture at the surface. This process causes the local alkalization, which facilities the localized corrosion and leads to higher exchange rate of electron that boosts the corrosion rate again. Polarization experiments have been performed in 0.1M KCl solutions with various pH values Figure 133, Figure 134 and Figure 135 show that rate of corrosion increases as the pH value of a solution becomes more alkaline, this conclusion is in consistent with conclusions of previous studies [Zaid 2008] that Cu-Al coupling possesses the highest corrosion resistant when the environmental condition is close to neutral because Al is amphoteric.

Effect of temperature with 0.1M KCl and 5.2pH control

In an attempt to study how change of temperature influences corrosion rate, polarization tests are performed at elevated temperatures by using heated water bath as shown in Figure 136.

Figure 136: Polarization Experiment Setup

Corning digital stirring hotplate is used to heat the solution to designed temperatures and glass thermometer is used to monitor temperatures to make sure that solutions are heated evenly. Experiments are performed at 22ºC, 40ºC and 80ºC. Results are shown in Figure 137, Figure 138 and Figure 139.

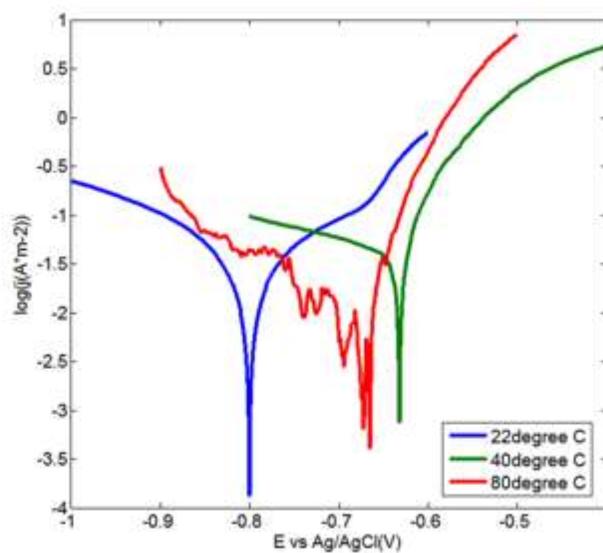

Figure 137: Polarization Curves of Al

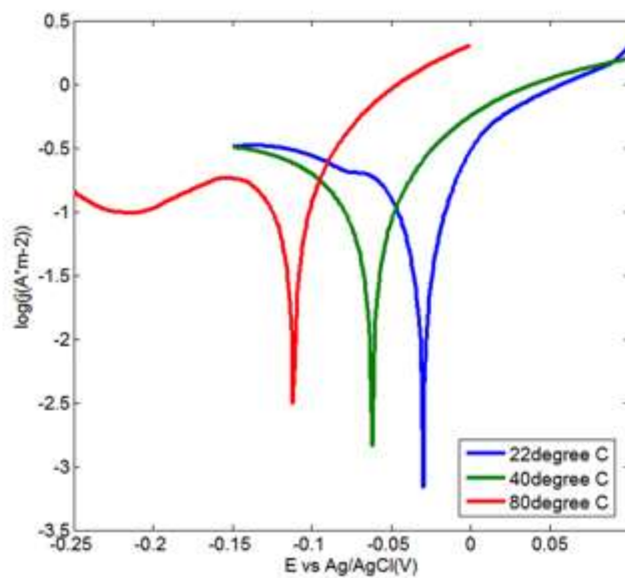

Figure 138: Polarization Curves of Cu

Temperature is considered as one of the major factors which affect chemical reaction rate. As shown in the plot, the rate of corrosion increases by a factor of 10 as operational temperature goes from room temperature to 80ºC as shown in the simulation results.

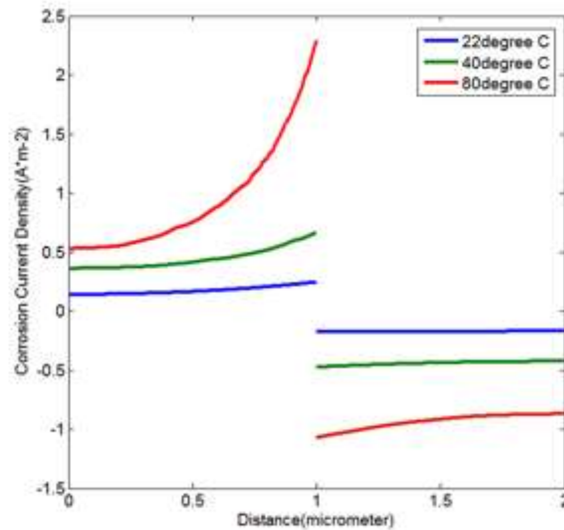

Figure 139: Simulation Results under Different Temperatures

(b) Post Thermal-treatment State

When wire bond has been aged in high temperature before being subjected to high humidity conditions, IMCs becomes part of the corrosion couples. IMC polarization experimental data has been incorporated in the simulation. Figure 140 and Figure 141 show IMCs polarization curves under pH5.2/ 0.5M condition and micro-galvanic corrosion simulation plots with different lengths of CuAl.

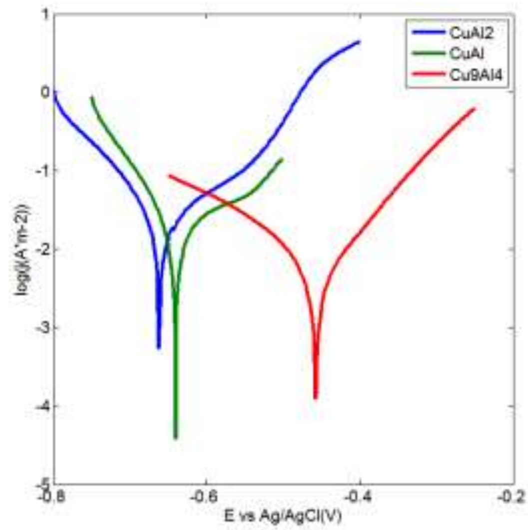

Figure 140: Polarization Curves of Cu-Al IMCs

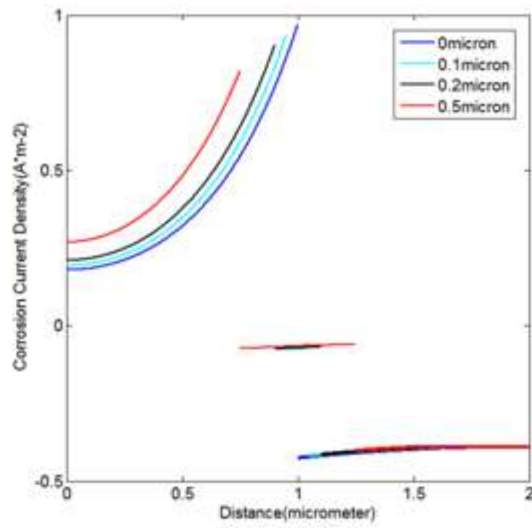

Figure 141: Result with Different CuAl Lengths

Table 10: Corrosion Decrease as IMCs Grow

IMC Type	IMC Thickness(μm)	Corrosion Decrease (%)
CuAl	0.1	4
	0.2	9
	0.5	19
CuAl2	0.1	2
	0.2	12
	0.5	22
Cu9Al4	0.1	3
	0.2	7
	0.5	15

Maximum corrosion rate decreases as the length of CuAl increases. Simulations have been run on the rest of IMCs and the results are similar to that of CuAl. Growth of IMC mitigates the galvanic corrosion in all three cases as shown in Table 10. Peak corrosion rate decreases at different IMC lengths in reference to peak corrosion rate at zero IMC thickness. By comparing those results, it can be concluded that when IMC length is fixed, CuAl2 has the highest corrosion resistance amount those IMCs while Cu9Al4 has the lowest corrosion resistance. When the IMC thickness is 0.5 μm, peak corrosion reduction is around 20% in the case of CuAl and CuAl2.

AF Modeling

(a) Corrosion Rate Calculation

As corrosion proceeds at Cu-Al interface, copper ball bond is going to be detached from Al pad eventually. Assuming that corrosion proceeds in a steady state, corrosion rate can be calculated by using Faraday's law [Tait 1994, ATSM Standard 2014]:

$$v = \frac{M}{zF\rho} j \qquad (88)$$

v is peak corrosion rate (m/s), M is molar mass of aluminum (g/mol), F is Faraday's constant, z is electron number and ρ is density of aluminum (kg/m3).

Typical radius of copper ball bond ranges from 25-50 microns. In the following lifespan prediction (LP), 35 microns is used. Table 11, Table 12 and Table 13shows some of the LPs of Cu-Al wire bond under different aging conditions.

Table 11: Lifespan Prediction as a Function of Cl contamination Level

5.2pH/22ºC/0.1µm IMC Thickness		
Chlorine Concentration(M)	Peak Corrosion Current Density(A/m2)	LP (hours)
0.01	0.11	2558
0.05	0.19	1481
0.1	0.23	1223

Table 12: Lifespan Prediction as a Function of pH Level

0.1M Chlorine Concentration/22ºC /0.1µm IMC Thickness		
pH	Peak Corrosion Current Density(A/m2)	LP (hours)
5.2	0.23	1223
7.2	0.18	1563
9.2	0.28	1005

Table 13: Lifespan Prediction as a Function of Temperature

5.2pH/0.1M Chlorine Concentration/0.1µm IMC Thickness		
Temperature (ºC)	Peak Corrosion Current Density(A/m2)	LP (hours)
22	0.23	1223

40	0.60	469
80	2.33	120

(b) Simulation Verification

Package with built-in contaminant test is performed in order to test the ability of simulation to estimate the lifespan of Cu-Al wirebond in practical cases. High concentration of chlorine is introduced to the chip-scale package with Cu-Al wire bond as a way to accelerate wire bond time to failure process. The test condition, dimensions of package and EMC parameters are tabulated in Table 14 and Table 15. Micro-CT image of the package is shown in Figure 142. Details of this test are described elsewhere [Lall 2015].

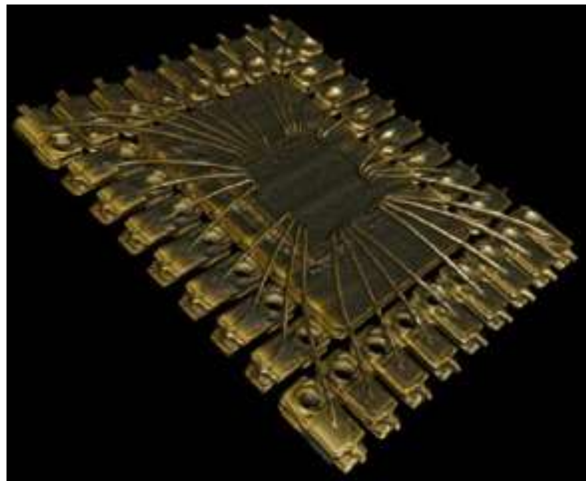

Figure 142: Micro-CT Reconstruction of Package

Table 14: Dimensions of Test Vehicle

Parameter	Dimensions(mm)
Width of Package	4.5
Length of Package	5.5

Height of Package	0.7
Length of Pin	0.45
Width of Pin	0.3
Pitch	0.5
Bond Radius	0.035

Table 15: Built-in Contaminant Test

Temperature	130(120,100) °C
Relative Humidity	100%
pH	5.2
Chlorine Concentration	0.1M

Simulations are run under the same environmental condition as described in Table 15 expect lower temperatures. Since the corrosion simulation is essentially a model that predicts the chemical reaction rate of aluminum with oxygen and moisture, temperature dependence of reaction rate can be well predicted by Arrhenius equation as shown in Equation 89:

$$k = Ae^{-\frac{\Delta Q}{RT}} \tag{89}$$

Where k is reaction rate of aluminum corrosion (μm/s), A is the multiplication factor (μm/s), T is the operational temperature (K), R is the gas constant (1.99cal/mol.K) and DQ is the activation energy (Kcal/mol). Using Equation 13, Reaction rate values from simulation at 22°C, 40°C and 80°C are fitted and plotted against 1/T as shown in Figure 143. The corresponding activation energy is 7.94 Kcal/mol. Table 16 shows the comparison of activation energy for aluminum corrosion previously published in literature [Musa 2011, Foaud 2012, Hassan 2013]. Activation energy obtained in current experiment is in good agreement with those obtained by researches.

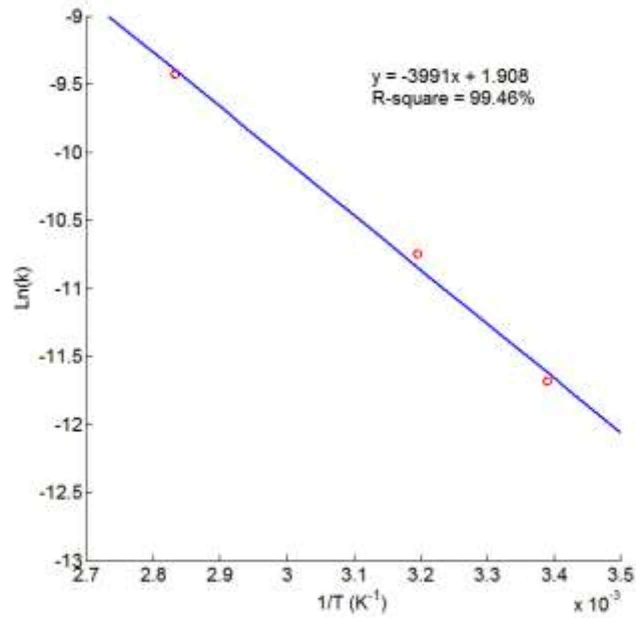

Figure 143: Ln (k) vs 1/T

Table 16: Comparison of Activation Energy for Al Corrosion

Study	Temperature Range(°C)	RH (%)	DQ(Kcal/mol)
Musa 2011	30-60	100	11.1
Foaud 2012	30-70	100	6.0
Hassan 2013	30-40	100	6.4
Current Study	22-80	100	7.9

Those projected corrosion rates are used to calculate the lifespan of 32-pin packages. Comparison of package lifespan between experiment and simulation are displayed in Table 17.

Table 17: Comparison of experimental & simulation results

Temperature(°C)	Experimental Lifespan (hours)	Simulation Lifespan (hours)	Error (%)
100	31	29	6.5
120	48	37	22.9
130	60	64	6.2

Prediction error ranges from 6.2% to 22.9%. Table 17 shows that corrosion simulation is able to predict the lifespan of Cu-Al wire bond in real cases within reasonable error range.

7.4 Acceleration Factor Model

Currently, the acceleration factor model of Cu-Al wire bond operated in harsh environmental conditions is not fully described even though its reliability performance has been a constant research subject for decades. In this section, an AF model is developed based on temperature, humidity and some critical environmental parameters related to EMCs. Then, the AF model is compared with the well-known Peck's corrosion model.

To start with, a time-to-failure model under operating condition is established as shown:

$$TF_o = A_0 \cdot RH_o^{-N} \cdot \exp(\frac{A_1}{T_o}) \cdot C_o^{A_2} \cdot IMC_o^{A_3} \cdot \left|pH-7\right|_o^{A_4} \tag{90}$$

Where the subscripts "o" stands for the operating condition, likewise, the TF model under acceleration conditions can be expressed as,

$$TF_a = A_0 \cdot RH_a^{-N} \cdot \exp(\frac{A_1}{T_a}) \cdot C_a^{A_2} \cdot IMC_a^{A_3} \cdot \left|pH-7\right|_a^{A_4} \tag{91}$$

Subsequently, AF can be derived using Equation 14 and 15 as shown:

$$AF = \frac{TF_o}{TF_a} = \exp\left[A_1(\frac{1}{T_o} - \frac{1}{T_a})\right] \cdot (\frac{RH_o}{RH_a})^{-N}$$
$$\cdot (\frac{C_o}{C_a})^{A_2} \cdot (\frac{IMC_o}{IMC_a})^{A_3} \cdot (\frac{|pH-7|_o}{|pH-7|_a})^{A_4} \quad (92)$$

Equation 16 can be transformed to a linear equation as shown:

$$Ln(AF) = A_1(\frac{1}{T_o} - \frac{1}{T_a}) - N(Ln(\frac{RH_o}{RH_a})) +$$
$$A_2 Ln(\frac{C_o}{C_a}) + A_3 Ln(\frac{IMC_o}{IMC_a}) + A_4 Ln(\frac{|pH-7|_o}{|pH-7|_a}) \quad (93)$$

The dataset consists of 113 experimental observations. The result of regression model is tabulated in Table 18. Low VIF values indicate that there is no multicollinearity issue in the dataset. P-value is tested for null hypothesis of zero respective coefficients. Zero P-values indicate that each one of the predictors has significant effect on the prediction of acceleration factor. The result of ANOVA test and R2 value is shown in Table 19 and Table 20, respectively. Zero P-value from ANOVA test again confirms the adequacy of the regression model. R-square value of the regression model is 96.28%.

Table 18: Result of Multi-linear Regression

Term	Coefficient	SE Coefficient	P-Value	VIF
A1	4393	87.3	0.000	1.04
A2	-0.29	0.03	0.000	1.03
A3	0.16	0.03	0.000	1.00
A4	-0.27	0.02	0.000	1.04
N	2.20	0.14	0.000	1.23

Table 19: Result of ANOVA Test

Source	DF	SS	MS	F	P
Regression	5	72.25	14.45	559.70	0.000
Residual Error	108	2.78	0.02		
Total	113	75.04			

Table 20: Model Summary

Model Summary			
S	R-square	R-square(adj.)	R-square(pred.)
0.16	96.28%	96.11%	95.92%

The result of regression model is written in Equation 18, According to the model, the increase of both temperature and relative humidity increases AF value thus reducing the lifespan of wire bond. Also, because of the amphoteric nature of aluminum, the closer pH value is to 7, the lower AF will become. The contamination level should be limited as small as possible to prolong the lifespan.

$$AF = \exp\left[4393\left(\frac{1}{T_o} - \frac{1}{T_a}\right)\right] \cdot \left(\frac{RH_o}{RH_a}\right)^{-2.20} \cdot \left(\frac{C_o}{C_a}\right)^{-0.29} \cdot \left(\frac{IMC_o}{IMC_a}\right)^{0.16} \cdot \left(\frac{|pH-7|_o}{|pH-7|_a}\right)^{-0.27} \tag{94}$$

As for the effect of IMC growth on the reliability performance of Cu-Al wire bond, regression model predicts that growth of IMC reduces interfacial corrosion rate. This conclusion is based completely on the electrochemical perspective. While it holds true before the growth of IMC reaches a critical point, it fails to represent the effect of IMC growth after the thickness passes that

critical point. According to experimental results on Cu-Al reliability performance, while initial continuous growth of IMC mitigates the interfacial corrosion as it strengthens bond, excessive IMC growth increases the interfacial corrosion rate as excessive IMC thickness increase is accompanied by the increase of the number of defect such as voids or weak grain boundaries within IMC. Corrosion will be likely to accelerate because it tends to attack through those weak IMC grain boundaries, which is also known as intergranular corrosion.

In order to account for the transition point of IMC thickness on the effect of Cu-Al wire bond reliability, the regression model is modified. A parabolic relationship between AF and IMC thickness is postulated as shown in Figure 144. The so-called Critical IMC thickness is proposed so that the effect of IMC growth on Cu-Al wire bond reliability performance reveres once IMC thickness passes the critical thickness. Previous experimental results has shown that IMC critical thickness is related to the Al pad thickness. In this model 0.5 μm is used.

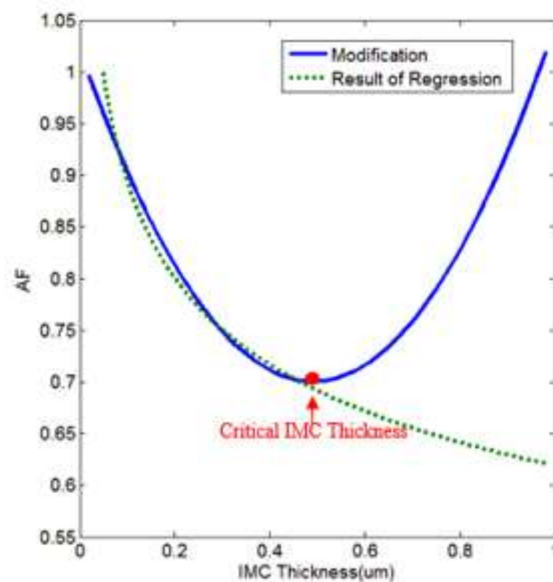

Figure 144: Regression Model Modification

Final regression model is written in Equation 19, Changes of AF with respect to each predictor are plotted in Figure 145.

$$AF = \exp\left[4393\left(\frac{1}{T_o} - \frac{1}{T_a}\right)\right] \cdot \left(\frac{RH_o}{RH_a}\right)^{-2.20} \cdot \left(\frac{C_o}{C_a}\right)^{-0.29}$$
$$\cdot \left(\frac{|pH-7|_o}{|pH-7|_a}\right)^{-0.27} \cdot \left[1.33\left(\frac{IMC_o}{IMC_a}\right)^2 - 1.31\left(\frac{IMC_o}{IMC_a}\right) + 1.02\right] \qquad (95)$$

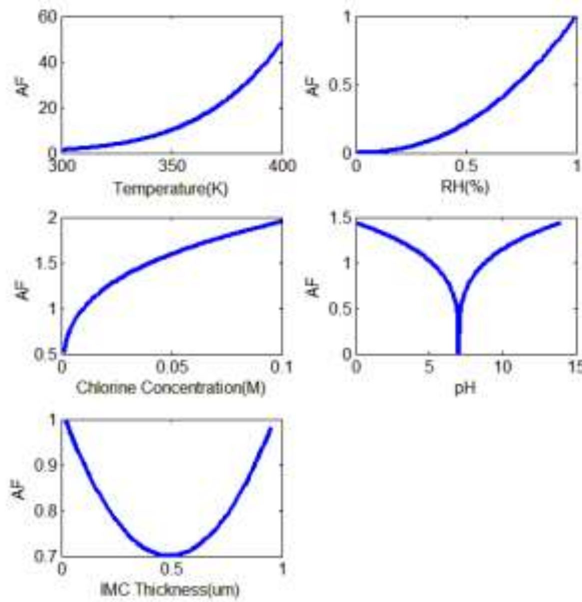

Figure 145: Change of AF with Respect to Each Predictor

Equation 12 is used to predict AF values of Cu-Al wire bond under different acceleration conditions. Figure 146 shows the comparison of AF between experimental results and results from model prediction on a square plot. As shown in the plot, the regression line passes through the origin making a rough angle of 45° with either axis.

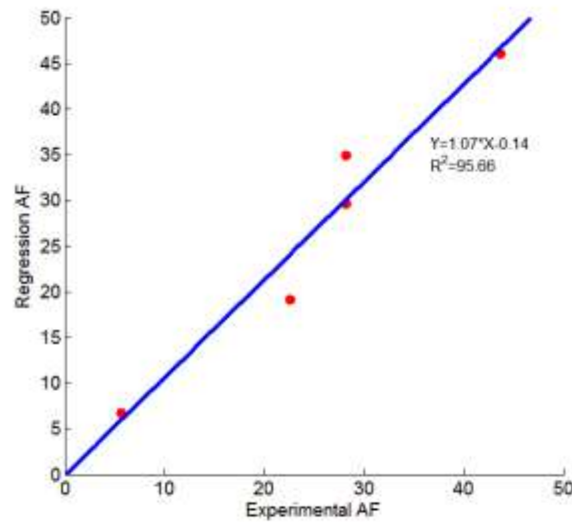

Figure 146: Validation of Regression Model

Table 21 shows the comparison of AF model between current study and study done by Peck [Peck 1986]. Peck's model was developed from a statistical review of time to failure experiments designed to calculate the combined effect of temperature, humidity and voltage bias. The AF model presented in this study is a generalized Peck's model with the inclusion of additional stresses. As shown in Table 21, both study has a similar N value while Ea in the current study is lower than the value obtained by Peck.

Peck's Model

$$AF = \exp\left[\frac{E_a}{R}(\frac{1}{T_o}-\frac{1}{T_a})\right]\cdot(\frac{RH_o}{RH_a})^{-N}\cdot f(V) \tag{96}$$

Current Study

$$AF = \exp\left[\frac{E_a}{R}(\frac{1}{T_o}-\frac{1}{T_a})\right]\cdot(\frac{RH_o}{RH_a})^{-N}\cdot f(\frac{C_o}{C_a})$$
$$\cdot f(\frac{|pH-7|_o}{|pH-7|_a})\cdot f(\frac{IMC_o}{IMC_a}) \tag{97}$$

Table 21: Model Comparison

Parameter	N	Ea(eV)
Peck's Model	2.7	0.7
Current Study	2.2	0.4

Effect of Growth of IMC

In previous section, numerical simulation results have shown that growth of Cu-Al IMCs mitigates corrosion rate at bond pad interface. In this section, experiments on packages BGA337 (Figure 147) with Cu-Al wire bond interconnects have been performed and experimental results are then compared to simulation results.

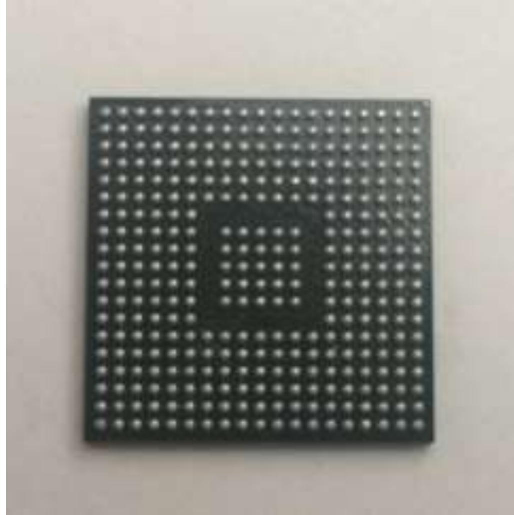

Figure 147: Image of BGA337

Test Procedures

Packages are subjected to 175°C isothermal aging condition up to 810 hours. IMC growth is monitored at different aging durations. Subsequently, aged samples are subjected to temperature/humidity condition of 130ºC/100%RH up to 96 hours. Samples with different aging durations are taken out, decapped and ball shear strengths are measured.

Part of sample packages are cold mounted and then polished after isothermal and/or humidity treatment. Polished surfaces are sputter coated with gold, at 25μA, for 2 minutes.
IMC growth and identification was examined using scanning electron microscopy and energy dispersive spectroscopy. Development of IMC layer is shown in Figure 148.

Results

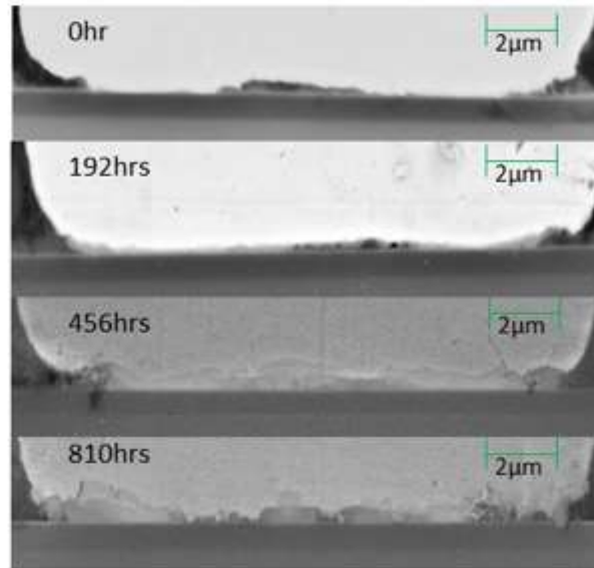

Figure 148: IMC Growth under Isothermal Aging

Figure 148 shows that there is no visible IMC layer at as-bonded state from the SEM image. After 192 hours of high temperature thermal aging, a thin layer of IMC is present at interfacial area. This IMC is confirmed as $CuAl_2$. As aging duration keeps increasing, IMC layer becomes thicker and more than one component is present. CuAl and $CuAl_2$ are the dominant parts after 810 hours of isothermal aging.

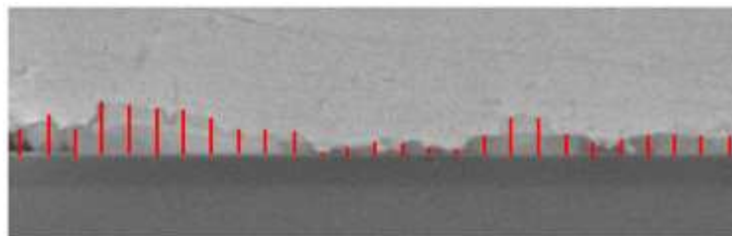

Figure 149: Measurements of IMC Thickness

IMC thickness is calculated by the approach shown in Figure 149. IMC thickness readings are evenly sampled across the interface. The final IMC thicknesses are the average of those readings.

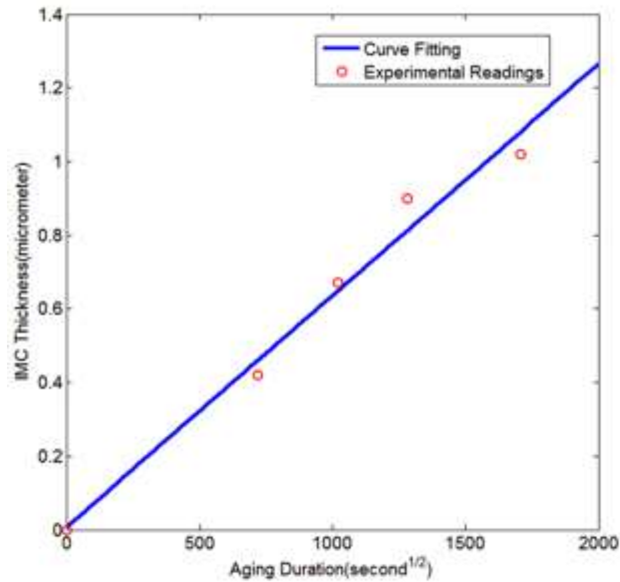

Figure 150: Change of Thickness vs Aging Duration

Figure 150 shows that change of IMC thickness is linearly related to the square root of isothermal aging duration up to 810 hours aging.

Decappsulation process is based on the use of the combination of red fuming nitric acid and concentrated sulfuric acid at elevated temperature [Lall 2015]. This process has been developed and optimized for BGA 337 so that the damage of decapsulation is reduced to minimum. There are two set of samples in this test, one set consists of samples with only isothermal aging process up to 810 hours and the other set consists of samples with isothermal aging and subsequent temperature/humidity aging up to 96 hours. 30 wire bonds are tested in each package. Box plot of ball shear strengths are shown in Figure 151.

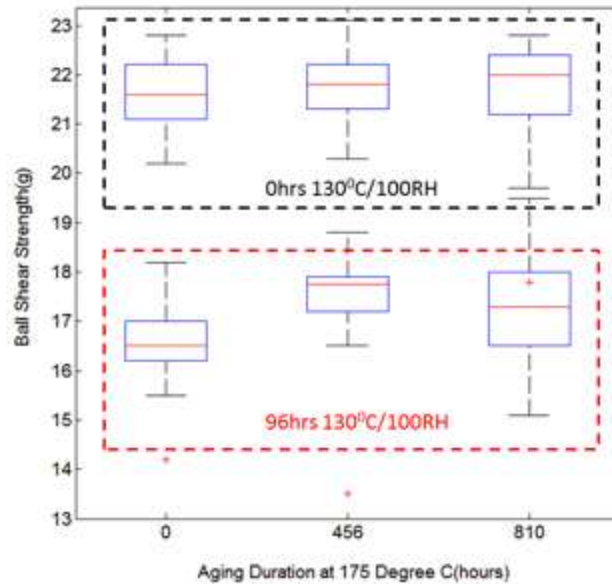

Figure 151: Box Plot of Ball Shear Strengths

Ball shear strength increases slightly after isothermal aging. The increase in ball shear strength is due to fact that the initial growth of IMC creates a stronger bond between copper ball bond and aluminum pad at an early stage of isothermal aging. After subsequent 96 hours of temperature/humidity aging, ball shear strength goes down in all three aging durations, which is caused by galvanic corrosion at bond pad interface due to high humidity. The percentage reduction in ball shear strength is highest in samples with zero isothermal aging and lowest in samples with 456 hours of isothermal aging. The reason for that is because initial growth of continuous IMC layer mitigates the galvanic corrosion at bond pad interface. However, as aging duration increases, the thickness of IMC increases along with the increase of the number of defect such as voids or weak grain boundaries within IMC. At the early stage of growth of IMC, it mitigates rate of corrosion. As aging proceeds to the next stage, the effect of increase of number of defect in IMC

finally overwhelms the positive effect of IMC growth. From then on, further growth of IMC will only provide detrimental effect on interfacial reliability.

Failure Mode Analysis

Cu-Al wire bond interfaces are examined after a long exposure (720 hours) to temperature/humidity environmental condition (130ºC/100RH). As shown in Figure 152, there is a visible crack at Cu-Al interfacial area. In order to prove that the crack is caused by galvanic corrosion, element mapping is performed to find out trace of oxygen. Intensity of red dots indicates concentration of oxygen at that particular location. As expected, the most oxygen-rich region is crack surrounding area, which proves the involvement of corrosion in crack propagation.

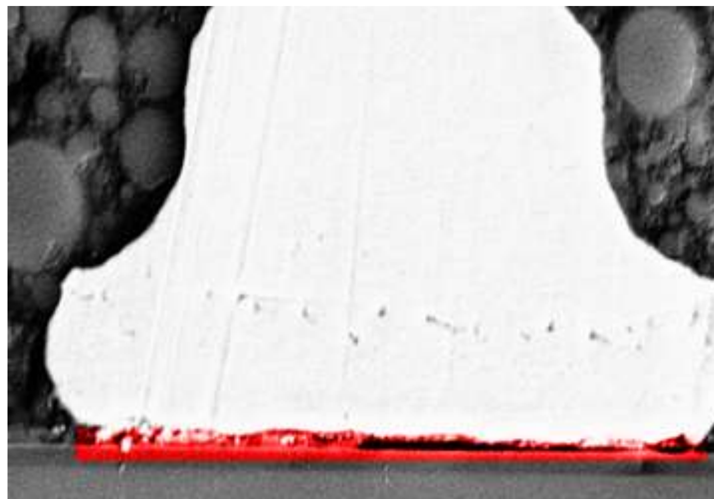

Figure 152: Oxygen Mapping

Chapter 8 Reliability Assessment of Cu-Al WB under High Voltage Bias Application

In this chapter, as the high voltage reliability performance of Cu-Al wire bond is a relatively new topic, there are no existing public literature available. Nevertheless, some relevant studies of Cu-Al wire bond under low biased humidity tests have given their thoughts on the failure mechanism of Cu-Al wire bond under voltage bias [Chiu 2014]. Basically, electrical bias influences Cu-Al wire bond in two distinct ways. The first way is through speeding up the transport of contaminants towards the bond pad interface. It is known that epoxy molding compound contains certain level of contaminant such as chlorine. Those contaminants are initially bonded with large organic chemical compounds known as functional groups [Soestbergen 2007]. Due to degradation of epoxy molding compound (EMC) under high temperature or high humidity aging, chlorine ions are gradually released from functional groups and becomes free to move in EMCs. Under the voltage bias, negatively charged chloride ions are forced to migrate towards the bond pad interface, where Cu-Al IMCs are attacked by chlorine. The whole chlorine attacking IMCs process is the process of micro galvanic corrosion as described in the previous studies [Lall 2015, Lall 2016]. The corrosion rate of wire bond has proven to be directly related to the concentration level of chlorine in the vicinity of Cu-Al wire bond. The second way is through directly altering

the electrochemical potential distribution across the corrosion front of Cu-Al wire bonds, thus accelerates corrosion process and results in premature failure of Cu-Al wire bond.

In order to study how high voltage bias affects reliability performance of Cu-Al wire bond, this paper first presents an experimental setup capable of running high voltage bias tests on Cu-Al wire bond interconnects. After that, a migration-diffusion cell experiment is introduced to quantify the effect of voltage bias on transport of chlorine in EMCs. A Butler-Volmer based corrosion simulation is used to quantify the effect of voltage bias on corrosion rate of Cu-Al wire bond based on results of electrochemical polarization tests on Cu-Al IMCs [Lall 2016].

8.1 Test Setup & Test Procedures

A QFN daisy chain package is used as the test vehicle provided by Taxes Instruments. There are 32 Cu-Al wire bonds in the QFN package. The specification of this package is listed in Table 22. Each test sample is mounted onto a printed circuit board in order to connect all the Cu-Al wire bonds in series so that wire bonds can be tested under high voltage conditions simultaneously. Figure 153 shows how the assembly of test vehicle looks like.

Table 22: Dimensions of QFN Package

Parameter	Dimensions(mm)
Width of Package	5.0
Length of Package	5.0
Height of Package	0.80
Length of Pin	0.60
Weight of Pin	0.35
Pitch	0.50
Bond Radius	0.035

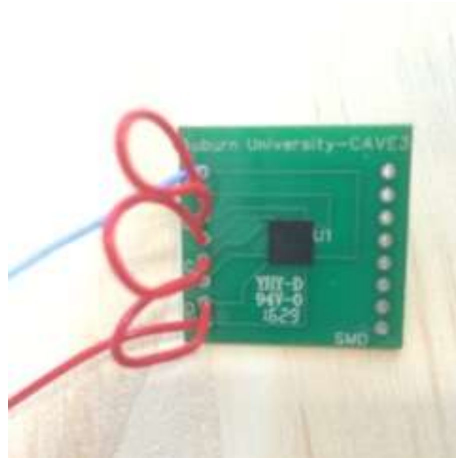

Figure 153: Test Vehicle

A half bridge-based DC high voltage test setup is schematically illustrated in Figure 2. It consists of one pulse width modulation controller UC3825AN, one high voltage (600V), high-side low-side gate driver UCC27714, a pair of power MOSFETs, a power resistor, two DC power supplies and some other electric components such as resistors, diodes and capacitors etc.

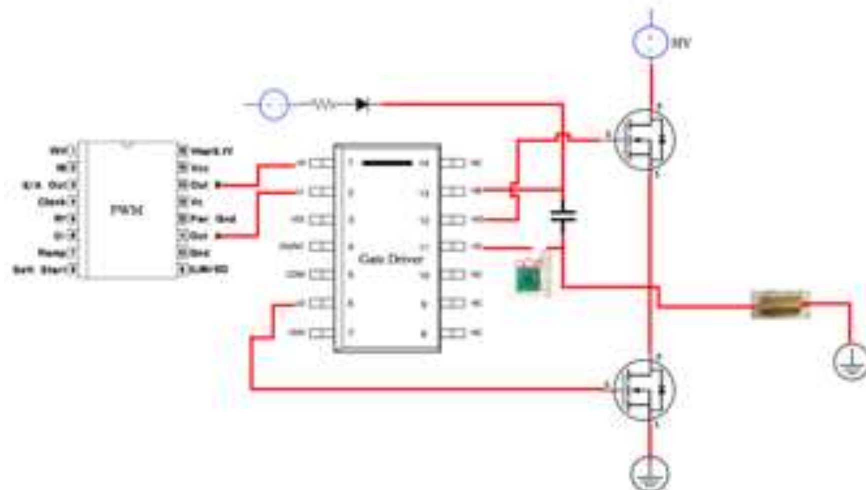

Figure 154: Schematic Plot of High Voltage Test Setup

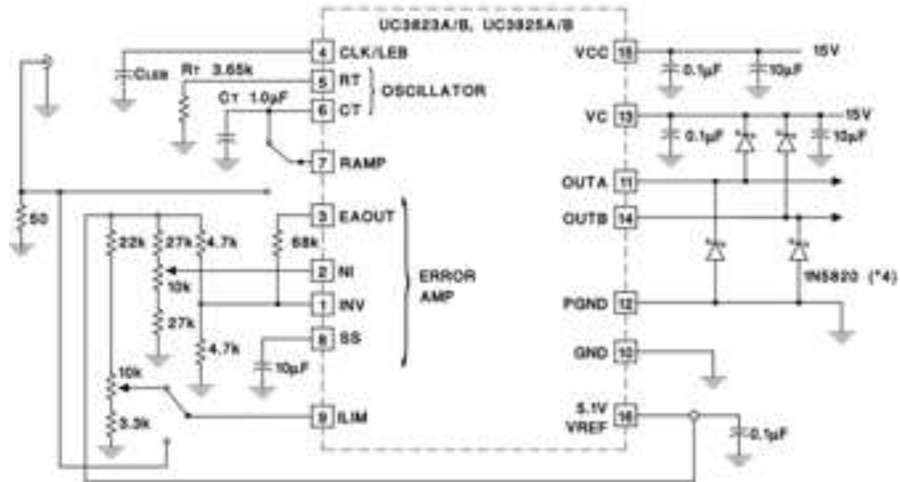

Figure 155: Setup of PWM Controller

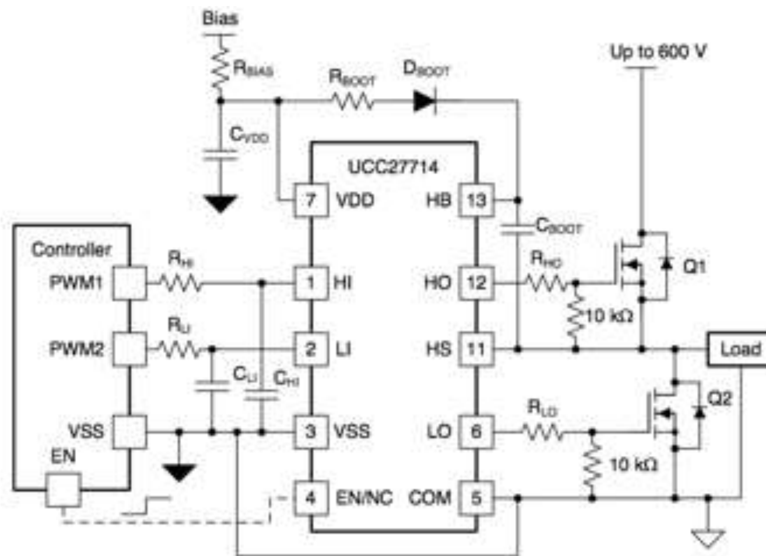

Figure 156: Setup of Gate Driver

The main idea is to design a setup capable of periodically subjecting 16 pairs of Cu-Al wire bonds to high DC Voltage without introducing the effect of current and with adjustable magnitude of voltage and adjustable duty cycle. The PWM controller in Figure 154 is set up as shown in Figure 155 to generate a pair of complementary square wave signal outputs at pin 11 and pin 14. These two output pins are then connected to HI pin and LI pin of gate drive IC as shown in Figure 2. The gate driver circuit is set up as shown in Figure 156. The gate driver is employed between the PWM output and the gates of two power MOSFETs. The level shift circuit is the interface from the high-side and low-side input to the high-side (pin 12) and low-side output (pin 6). As shown in Figure 157, with input signals from PWM, the level shift generates on-pulse based on the rising edge of the input signals and off-pulse based on the falling edge of the input signals.

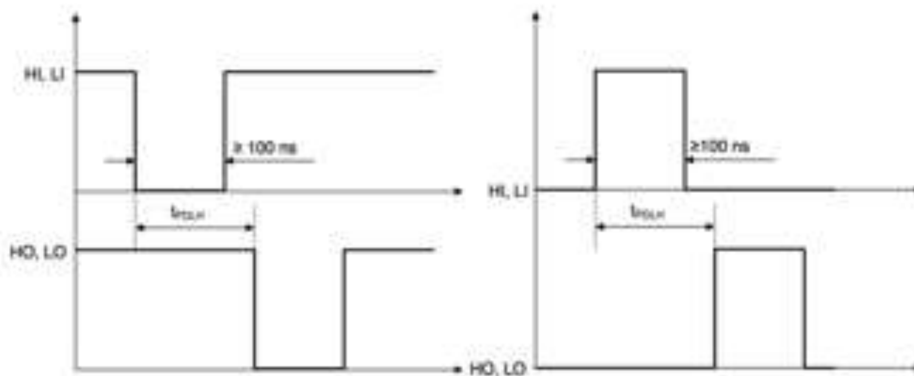

Figure 157: Schematic Plots of the Functionality of Gate Driver

A bootstrapping circuit is employed along with the gate driver and a PWM to help control two power MOSFETs and a power resistor is used to dissipate the energy generated by high voltage source. As shown in Figure 154, this circuit enables users to turn on the upper MOSFET while keep the lower MOSFET off and vice versa. During the on-stage of the lower MOSFET, the upper

MOSFET is off and the bootstrapping capacitor is at its empty state originally. During this stage, this capacitor will be charged to its full stage. During the off-stage of the lower MOSFET, the fully charged bootstrapping capacitor pulls up HO pin above the power supply rail (HS pin) and provides the energy to sustain Vgs above its threshold, which causes the upper MOSFET to be turned on. During this stage, Cu-Al wire bonds and the power resistors are subjected to high voltage stress. The setup is shown is Figure 158. The gate driver is embedded in a socket and then connected to the breadboard from which the circuitry is set up. A pair of heat sinks and fans are used to cool down two power MOSFETs. By adjusting the output amplitude of power source and the duty cycle of PWM controller, this setup is able to implement various high voltage test conditions.

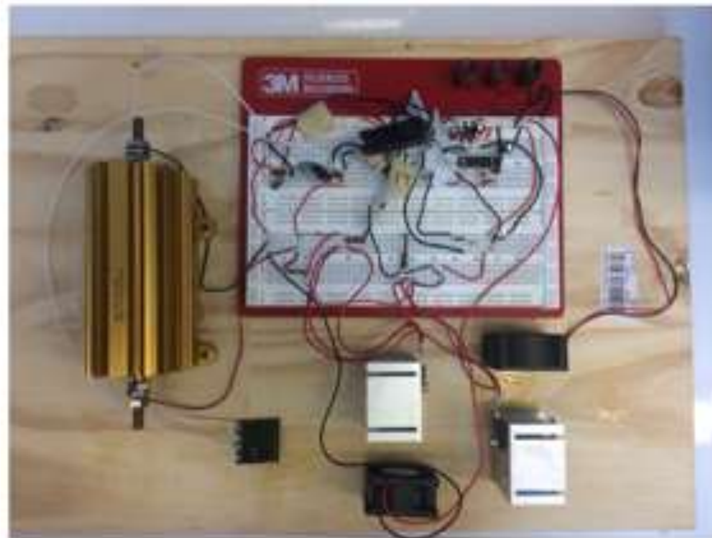

Figure 158: High Voltage Test Setup

An oscilloscope is used to detect the voltage waveform passing through Cu-Al wire bonds as shown in Figure 159. As it can be seen from the plot, a continuous square waveform is observed.

It is 20 volts at the top of waveform and 0 volt at the bottom of waveform. The duty cycle is set to be 0.4 and the frequency of waveform is 5kHz.

Figure 159: Voltage Waveform Passing through Cu-Al WB

High Voltage/Temperature Aging Test

A test matrix is designed to study the effect of high voltage on the reliability performance of Cu-Al wire bonds. Test packages are divided into three groups and subjected to either one of three isothermal conditions. 175°C, 200°C and 225°C. Part of the package samples in 175°C group are subjected to additional high voltage stress using the test setup as shown in Figure 160. It has shown in the previous publications [Lall 2013] that electrical resistance of Cu-Al wire bonds can be used as a leading indicator to monitor the progression of damage in those wire bond interconnects. The industrial standard of wire bond failure is 20 percent resistance increase off the initial resistance of wire bond. In this experiment, resistances of wire bond pairs are measured periodically to record

the damage accumulation in Cu-Al wire bonds in order to compare time-to-failure durations of Cu-Al wire bonds under various stressed conditions.

Figure 160: High Voltage/Temperature Test Setup

Test Results

As shown in Figure 161, when aged under high temperature isothermal conditions without additional high voltage stress, average time-to-failure durations at 175°C, 200°C and 225°C conditions are 1728 hours, 720 hours and 480 hours, respectively. When a voltage stresses 10V (0.4 duty cycle) is added to Cu-Al wire bonds at 175°C, average time-to-failure durations at these two aging conditions become 576 hours. If average time-to-failure duration of Cu-Al wire bonds under sole effect of 175°C isothermal aging is considered as a baseline measurement, the effect of extra voltage stress on Cu-Al wire bond reduces the average time-to-failure durations.

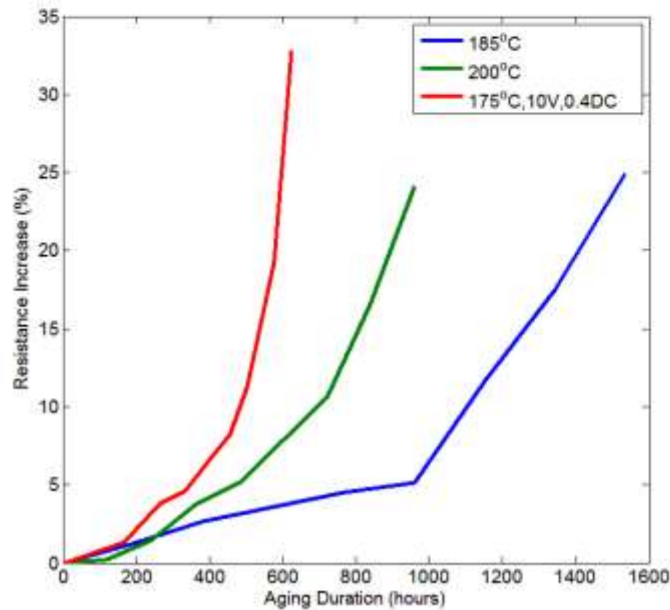

Figure 161: Effect of temperature/voltage bias on Cu-Al WB interconnect

8.2 Diffusion-Migration Cell Experiments

From the result of high voltage/temperature test on Cu-Al wire bond, it can be concluded that voltage bias accelerates time-to-failure durations of wire bonds. In this paragraph, details of the role voltage stress played in the process of Cu-Al wire bond failure will be discussed and two important voltage-bias-related factors will be quantified by using a diffusion-migration cell test setup.

As mentioned briefly in the introduction, chlorine contamination in epoxy molding compounds is one of the most detrimental factors which causes wire bond to fail. The main reason is that it accelerates the rate at which galvanic corrosion occurs at Cu-Al wire bond interface. Since chlorine

initially exists inside certain chemical functional groups in EMCs such as 1,2-Chlorohydrin [Soestbergen 2007], it won't have any effect on wire bond corrosion as it cannot react with any of Cu-Al IMCs. However, high-stress operational environment such as high temperature or high humidity will cause degradation of EMC. During the degradation process, organic chloride ions are released from those functional groups and they become free to move around in EMCs and react with Cu-Al IMCs. In the presence of voltage bias, the negatively charged chloride ion will be forced to move in a direction where electrical potential goes up. As the chlorine migration proceeds in EMCs, soon there will be a substantial chlorine accumulation at the vicinity of Cu-Al wire bonds which have a high electric potential than other wire bonds. The corrosion rate at those wire bond interfacial areas will increase by a lot compared to those wire bonds interfacial area which do not have a substantial chlorine concentration buildup at the vicinity. The transport of ionic species in EMCs can be modeled using Nernst-Planck equation [Lall 2015], the two important parameters that affect transport rate of chlorine are diffusion coefficient of chlorine and ionic mobility of chlorine. In order to study how temperature affects the transport rate of chlorine in EMCs and model the transport behavior of chlorine in EMCs under voltage bias, the diffusion-migration cell test setup is designed and used to obtain both parameters under different operational temperatures.

First, as shown in Figure 162, a diffusion cell [Lall 2015] is designed to measure diffusion coefficient of chlorine in EMCs. It consists of two glass chambers, a metal clamp, two Styrofoam washers, a stopper and a pedestal. A thin flat sample epoxy molding compound is placed in between two glass chambers, both chambers have a 0.2cm2 orifice. The upper chamber is filled with concentrated potassium chloride solution while the lower chamber is filled with DI water.

The concentration gradient across the EMC sample will drive chlorine ion to diffuse to the lower chamber over time. Fick's first law is used to describe the transport behavior of ionic species under concentration gradient.

Figure 162: Diffusion Cell

The sample molding compound used in tests is the molding compound used to encapsulate Cu-Al wire bonds in the test vehicle. Diffusion coefficients of chlorine are estimated at several different operational temperatures.

Based on the description of transport behavior of ionic species by Fick's law, Nernst-Planck equation is derived to account for the effect of additional electric bias on ionic species as another driving force during the process of ionic transport. Equation 3 show the mathematic form of this equation. It can be seen from the Nernst-Planck equation that negatively charged ionic species

tends to move along the direction of increasing electric potential field. Ionic mobility of chlorine differs from one EMC to another and also it is temperature dependent. Estimating ionic mobility of chlorine in the test vehicle will make it possible to model the complex transport behavior of chlorine under both concentration gradient and electric potential gradient.

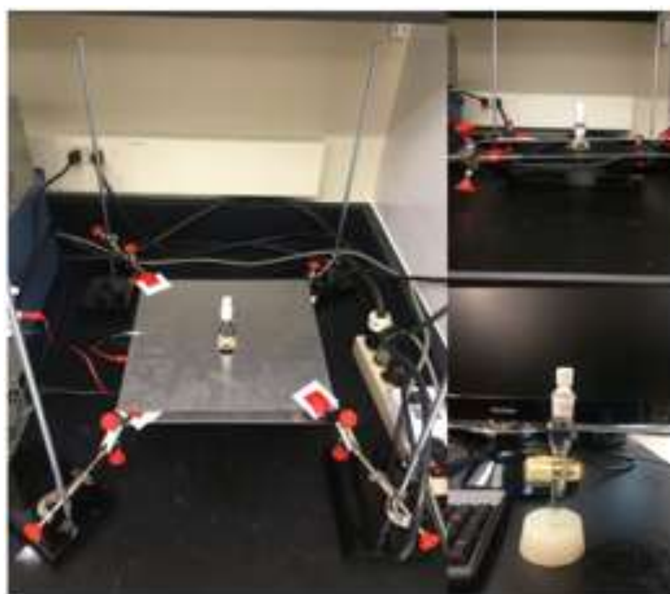

Figure 163: Migration Cell

The migration cell setup is shown in Figure 163. It is designed based on the diffusion cell setup. As it can be seen from Figure 10, two parallel metal plate (30cm by 30cm) is placed on both side of the thin flat epoxy molding compound sample. The distance from EMC sample to either one of metal plates is 1.25cm. Metal plates are subjects to 30V electric bias using a DC power supply to create an electrostatic field which goes through the EMC sample. Insulting pads are used to make sure that there is no electric connection between either metal plates and clamps used to fix them. The metal clamp used previously in the diffusion cell setup is replaced with a polymer clamp

created using a 3D printer to minimize the interference it might causes to the electrostatic field in between the two metal plates. The testing procedures are similar to that of a diffusion cell. The whole setup is place in room temperature environment to examine ionic mobility of chlorine at room temperature. For ionic mobility measurements at elevated temperatures, another fixture is designed to accommodate migration cell setup inside a thermal chamber as shown in Figure 164.

Figure 164: Migration Cell in a Thermal Chamber

There are two unknowns in Nernst-Planck equation which needs to be determined before one can use it to estimate the ionic mobility of chlorine at room temperature. Diffusion coefficient of chlorine at room temperature as one of the input parameters, which can be calculated using the diffusion cell experiment. The other unknown is the electric potential gradient across the sample EMC. Here, COMSOL software is used to model electric field and estimate the electric potential gradient.

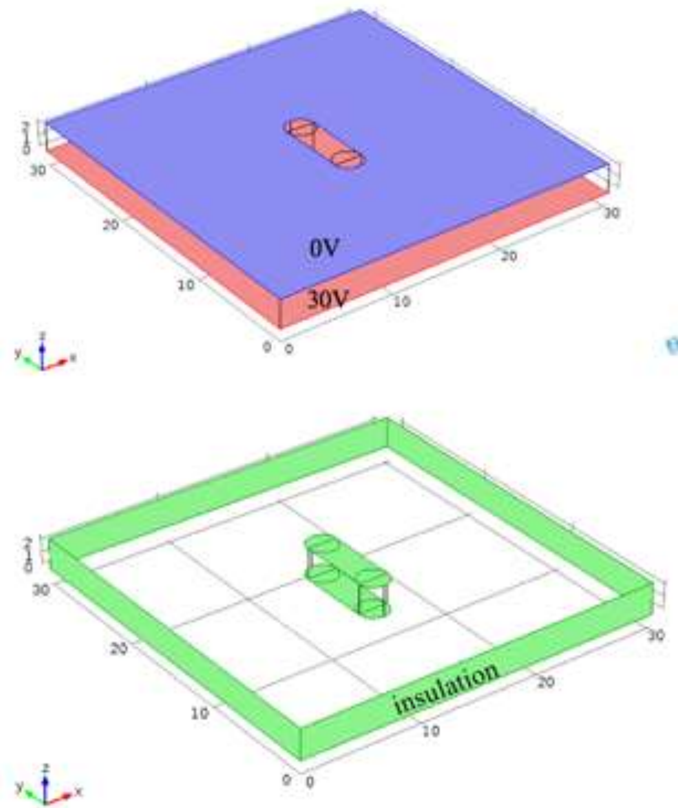

Figure 165: COMSOL Electric Field Modeling

As shown in Figure 165, a 3D geometry has been constructed to resemble the migration cell setup. The purple and red surfaces represent the two metal plates of the migration cell. The distance between two surfaces is 2.5cm as that of the migration cell setup. The upper surface is set to be grounded and the lower surface is set to be subjected to 30V electric potential. Both surfaces have an elliptical shaped opening in the middle which resembles the openings of the migration cell setup. The green surface area is set to be insulating and the relative permittivity of inner side of the model is set to be 1 which corresponds to that of air. The model has been solved and the result

of electric potential gradient across the center of the openings shown in Figure 166 as a red vertical line is extracted and plotted in Figure 167.

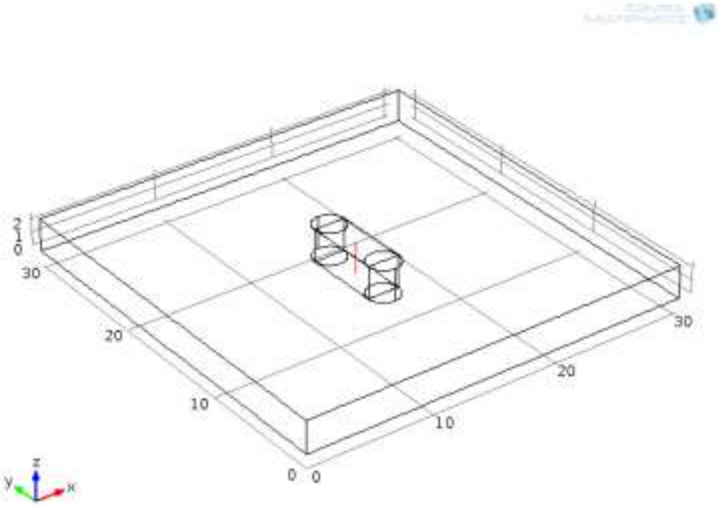

Figure 166: Location Where Electric Potential Gradient is Extracted

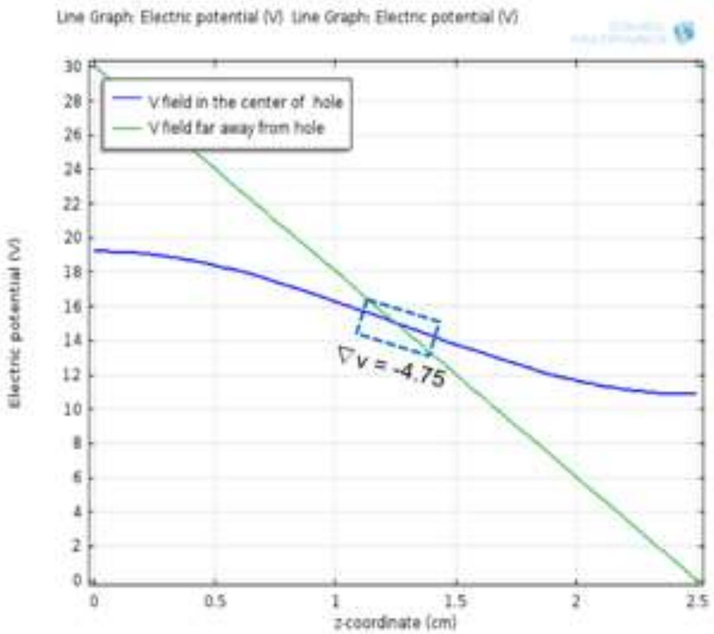

Figure 167: Electric Potential across Z-direction

It can be seen that potential across the center of the openings is quite different from that far away from the two openings. Electric field in the vicinity of the two opening area is altered due to the discontinuity of charged surface. However, voltage across the EMC sample is almost linear, which means that the electric potential across the EMC sample of the migration cell is approximately constant. The result is -4.75V/cm as shown in Figure 167. Once electric potential gradient across the migration cell is obtained, it is used in Equation 3 to estimate ionic migration of chlorine in the targeting EMC sample at room temperature. By using the same methodology, both diffusion coefficient and ionic migration of chlorine can be measured at different operational temperatures. The result of all the measurements are shown in Table 23.

Table 23: Summary of D and μ measurements

Temperature (°C)	Diffusion Coefficient (cm2/s)	Mobility (cm2/(V.s))
25	$1.74*10^{-11}$	$1.55*10^{-9}$
45	$2.66*10^{-11}$	$2.15*10^{-9}$
55	$3.18*10^{-11}$	$3.32*10^{-9}$
85	$6.91*10^{-11}$	$6.42*10^{-9}$

Galvanic Corrosion Simulation

A package-level Cu-Al wire bond corrosion model [Lall 2015, Lall 2016] has been built in COMSOL to simulate to corrosion progression at the bond pad interfacial area as a result of galvanic corrosion of IMCs caused by chlorine attack which is the result of degradation of epoxy molding compound under high temperature/humidity conditions. The model geometry is shown in Figure 168 and Figure 169.

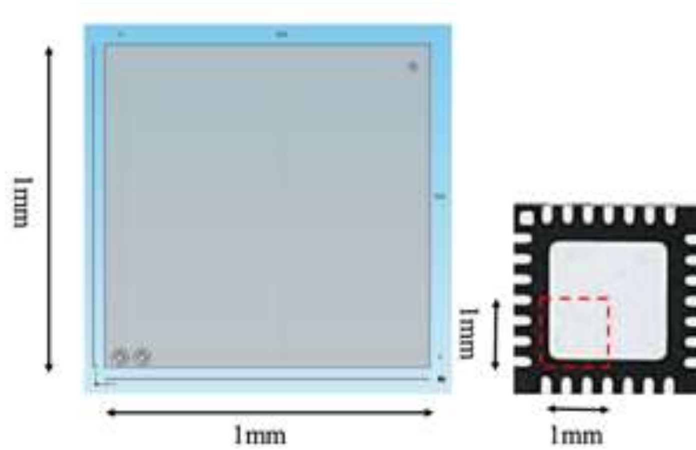

Figure 168: Cu-Al WB Corrosion Model

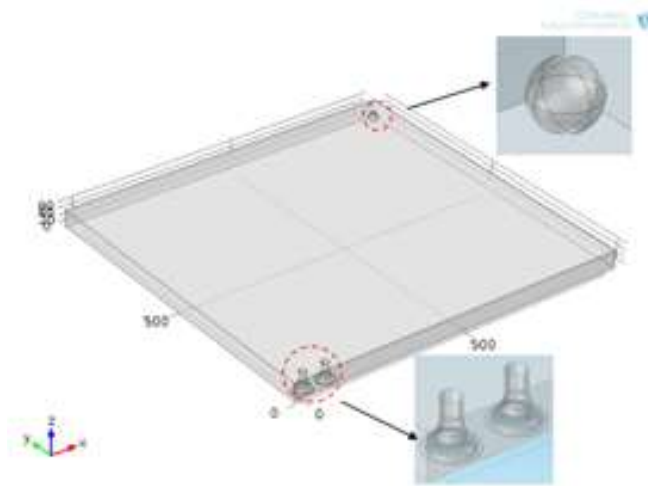

Figure 169: Close-up View of Model Geometry

The model geometry is built based on 1/4 the size of the test vehicle as shown in Figure 168. The height of the model is set to be 50μm. The ball-shaped object in the upper right corner of model is used to represents those impurities source as a whole which are located at the center location of the package. A chlorine influx is set at the ball object to simulate the release of chloride

ion at 130°C/100RH. There are a set of two Cu-Al wire bond constructed on the opposite side of the impurities ball object. The corrosion rate of Cu-Al wire bond is programmed by a user-define function based on the corrosion rate function derived from the AF model [Lall 2016]. Voltage bias is set between these two wire bonds to simulate the effect of voltage on the lifetime of Cu-Al wire bond interconnect. Both diffusion coefficient of chlorine and ionic mobility of chlorine in EMC used in the test vehicle at 130°C are estimated using Arrhenius equation and they are used as model input to simulate the transport behavior of chlorine. The corrosion kinetics of model is based on electrochemical measurements of Cu-Al IMCs [Lall 2016]. Simulation is run with different voltage biases between two Cu-Al wire bond to study the effect of voltage biases on corrosion rate of wire bond over time. The result is plotted in Figure 170.

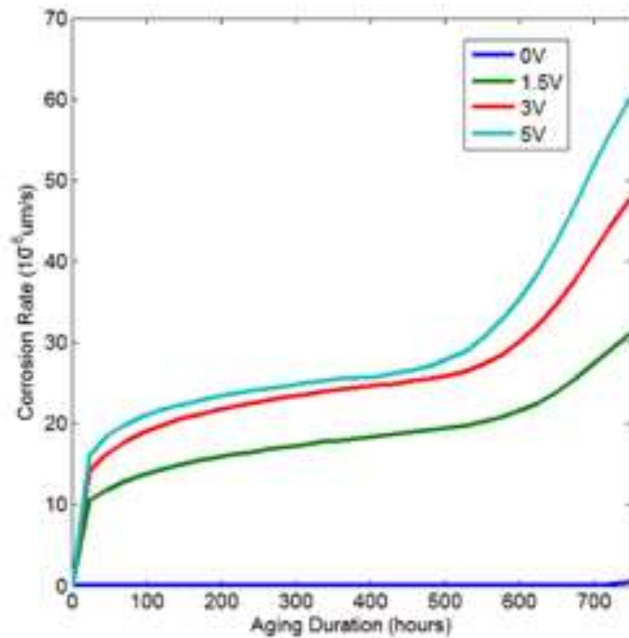

Figure 170: Effect of Voltage Bias on WB Corrosion at 130°C/100RH

As it can be seen from Figure 170, corrosion rate of Cu-Al wire bond increase as voltage bias across two wire bonds increases. The reason for the rise in corrosion rate is that chlorine ion transport towards the vicinity of bond pad interface become faster as the driving force (electric field) become stronger in the vicinity of Cu-Al wire bond. The faster accumulation of local chlorine concentration then accelerates the Cu-IMCs-Al corrosion process and leads to the failure of wire bond.

Chapter 9 MATLAB Multiphysics FE Simulation of Cu-Al WB Corrosion

In this chapter, a finite-element-analysis based novel numerical multiphysics framework is proposed to model the corrosion progression of Cu-Al wire bond interconnect subjected to HAST conditions. The model is characterized by Butler-Volmer equation and Nernst Planck equation. It features corrosion front tracking, a moving meshing-based approach to keep track of the corrosion progression at the Cu-Al bond pad interfacial area. It captures the effect of IMC growth, contaminant transport during the high humidity aging process as well as the electric bias.

The propose of this framework is to help electronic packaging manufacture improve the reliability performance of their design of Cu-Al wire bond system by showing the expected simulated-lifespans without forcing them to commit too much time and money to performing experimental tests. Also, the model can serve as a prognostic health management (PHM) tool to examine the remaining RUL of wire bond (crack length vs aging duration) so that necessary maintenance steps can be taken before catastrophic system failure occurs.

9.1 Overview of Cu-Al WB Corrosion Modeling

Cu-Al wire bond corrosion is described in the flowchart of WB corrosion simulation as shown in Figure 172. Most commercial microelectronics are molded in EMCs which are hydrophilic. When exposed to humidity operational conditions, EMCs absorb moisture [Soestbergen 2007]. In producing epoxy resins based on epichlorohydrin, impurities containing chlorine is formed such as 1,2-Chlorohydrin. High-stress operational environment will also cause the degradation of epoxy molding compound [Paulson 1996]. This process generates organic chlorine as shown in Figure 171.

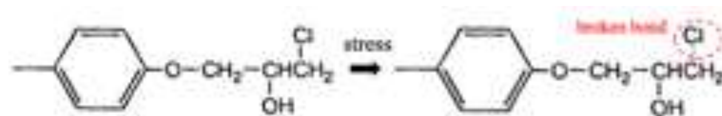

Figure 171: Schematic plot of chlorine release during EMC degradation process

Moisture ingress increases the rate at which chlorine transports, making it easier for ionic contaminant to diffuse towards Cu-Al wire bond interfacial area as a result of concentration

gradient. When voltage bias is applied between different wire bond interconnects, it will create an electrostatic field inside which the wire bond interconnect with higher electric potential will attract the negatively charged ionic species such as chloride ions. The local accumulation of chlorine in the vicinity of Cu-Al bond pad interfacial area acted as a catalyst, causing the corrosion of Cu-rich IMC to corrode. In this galvanic corrosion system, Cu-rich IMC Cu_9Al_4 is the anode and copper ball bond is cathode. Due to the material nature of aluminum, aluminum pad is passivated. As corrosion proceeds, cathode-to-anode ratio of this corrosion system will increase as a result of the continuous consumption of anode layer (Cu_9Al_4). The change of cell geometry leads to the change of corrosion rate. A moving mesh technique is used to account for the continuous change of corrosion cell geometry and thus make it possible to simulate the corrosion progression. The corrosion simulation will keep track the development of corrosion crack until a complete crack is formed at the Cu-Al wire bond interfacial area.

The nature of galvanic corrosion is very complex. There are numerous factors involved in determining the corrosion rate of a galvanic corrosion cell formed in Cu-Al wire bond interfacial area. In order for corrosion to occur, both electron path and ionic path should be present in a galvanic corrosion system. The fundamental of micro-galvanic corrosion and how different factors affect corrosion rate of wire bond are covered in my previous publications [Lall 2016, Lall 2015]. As shown in the upper box of Figure 173, all those factors related to Cu-Al wire bond micro-galvanic corrosion are divided into 3 categories, which are epoxy mold compound (EMC), Cu-Al wire bond and operational environment, respectively.

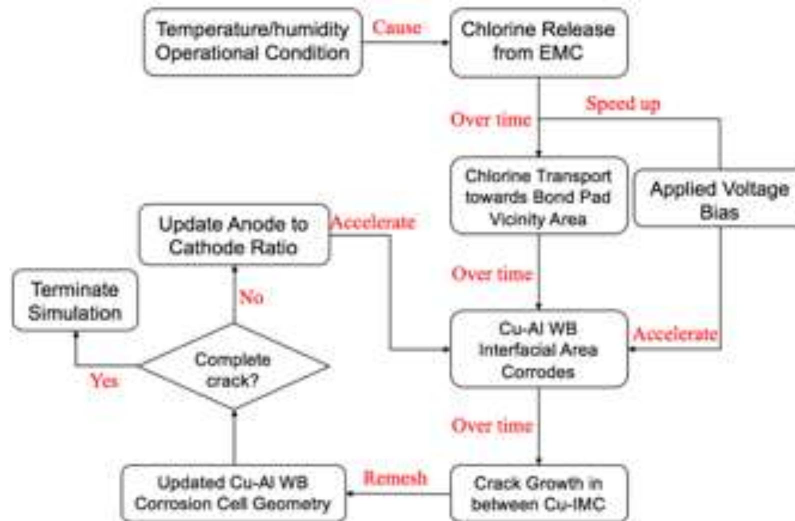

Figure 172: Flowchart of Cu-Al WB Corrosion Simulation

Under each category, there are several sub-factors which belongs to the 3 main categories and those factors need to be quantified and used as input to the multiphysics model. quantification of different factors requires different experimental techniques. For example, migration-diffusion cell experiments are performed to calculate the diffusion coefficient and mobility of different ionic species in different EMCs under different operational temperatures. Electrochemical properties of Cu-Al wire bond and its IMCs are acquired by running polarization experiments using a three-electrode system.

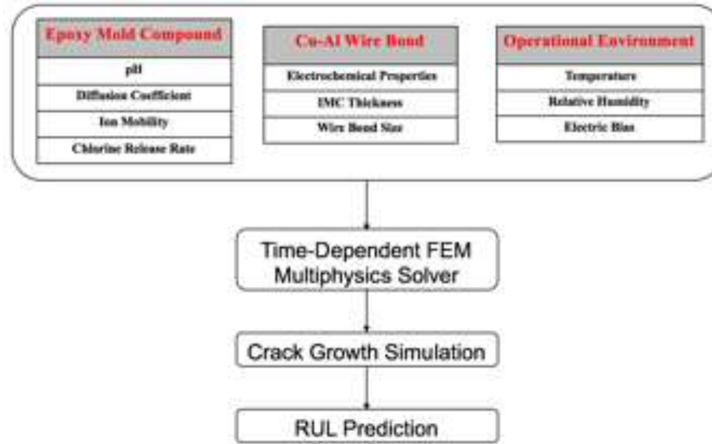

Figure 173: Factors Involved in Cu-Al WB Galvanic Corrosion

The schematic plot of micro-galvanic corrosion cell is shown in SEM image of crack progression are shown in Figure 174 and Figure 175.

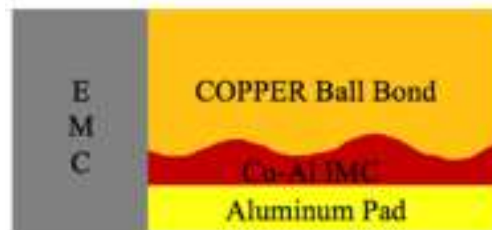

Figure 174: Schematic Plot of Micro-Galvanic Corrosion Cell

Figure 175: SEM Image of Crack Progression at Cu-Al WB interface

It represents the EMC-bond pad interface. There are four components. EMC, copper ball bond, Cu-Al IMCs and aluminum pad. As shown in the Figure 174, the interface of copper ball bond and Cu-rich IMC is represented using a Scallop-like wave. The measured average length and height of a semi-wave interface is 0.94 micrometer and 0.21 micrometer, respectively. The part of anode in contact with EMC is highlighted in green whilst the part of cathode in contact with EMC is highlighted in black. As shown in Figure 176, corrosion initiates at the edge of wire bond and it proceeds towards the center of wire bond. Figure 177 depicts a corrosion model geometry with a partially developed crack from which the cathode-to-anode ratio increases as indicated by the ratio of length of black curve to green curve. The purple curve line is used to represent the interface between IMC and aluminum pad. It is assumed to be insulated as a result of aluminum passivation.

Figure 176: Initial Geometry of Corrosion Model

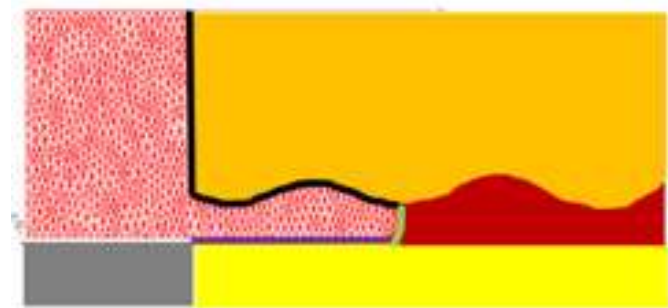

Figure 177: Geometry of Corrosion Model with a Developed Crack

9.2 Mathematic Model for Cu-Al WB Corrosion

Transport of chlorine in EMC can be modeled using Nernst-Planck equation as shown in Equation (98)

$$\frac{\partial c}{\partial t} = \nabla \cdot (D\nabla c) + z\mu\nabla \cdot (c\nabla V) \tag{98}$$

Where z is the electron number of chlorine, μ stands for the ionic mobility of chlorine (m2/(V.s)), V denotes the voltage bias of the system (V). t stands for time (s). In a dilute solution, the transport behavior of ionic species is governed by both concentration gradient and electric potential gradient. The progression of contaminant transport in EMC will eventually induce galvanic corrosion of Cu-Al WB. The corrosion kinetics is well predicted by Butler-Volmer equation [Murer 2010, Robert 2002] as shown in Equation 99 and Equation 100.

$$j_c = j_{0c} * (e^{\frac{E_c - V}{\alpha_c}} - e^{\frac{E_c - V}{-\beta_c}}) \tag{99}$$

$$j_a = j_{0a} * (e^{\frac{E_a - V}{\alpha_a}} - e^{\frac{E_a - V}{-\beta_a}}) \tag{100}$$

where ja, jc are anodic/cathodic corrosion current density (A/m2). j0a and j0c represent anodic/cathodic free corrosion density (A/m2). Ea and Ec denote anodic/cathodic open circuit potential (V). alpha and beta are Tafel parameters [David 1997].

Gauss–Seidel iterative scheme

As shown in Figure 178, in order to model the transport of chlorine in EMCs, both electric field and ionic concentration field need to be calculated. These two fields are coupled together. The change of electric field in EMCs will change the concentration distribution of chlorine in EMCs. On the other hand, the change of concentration of chlorine at the vicinity of Cu-Al wire bond interfacial area will change the kinetics of galvanic corrosion. Therefore, it will consequently alter the electric field. The nonlinear nature of coupled systems of equations make it difficult to solve them. In this paper, Gauss–Seidel iterative [Mats 2010] scheme is utilized to tackle the problem.

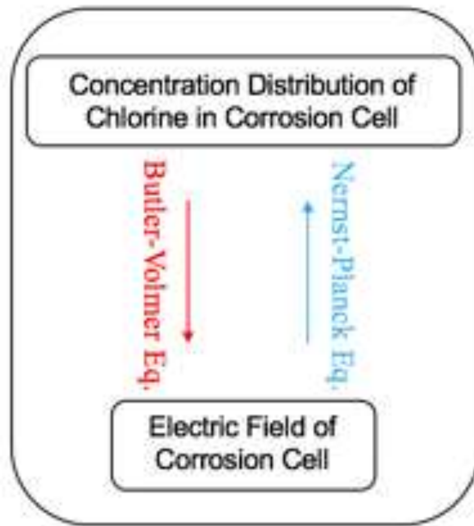

Figure 178: A System of Coupled Non-linear PDEs

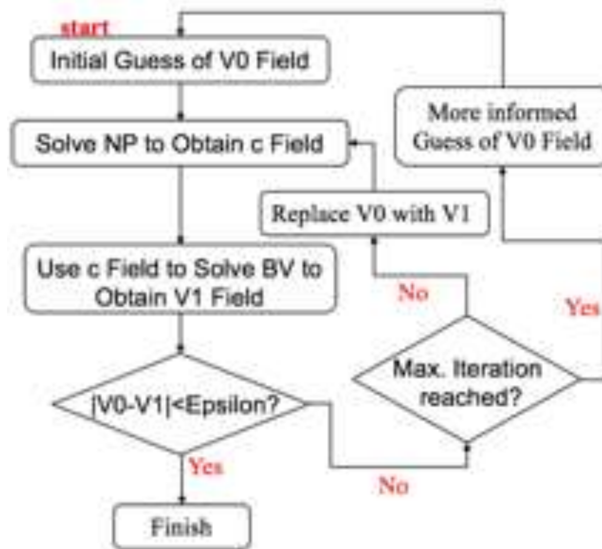

Figure 179: Gauss–Seidel Iterative Scheme

As shown in Figure 179, to start with, an initial guess of the current-time electric field (V0) is used to solve the chlorine concentration field using Nernst-Planck equation. Once the ionic concentration field is determined, Butler-Volmer boundary condition will be used in combine with concentration field to acquire an electric field (V1) for the micro-corrosion system. After that, the difference between V0 and V1 is compared to a predetermined threshold value epsilon. If the difference is smaller threshold, the initial guess is accepted and both fields are obtained at the current-time. If not, first the number of iterations of the solving process is compared to the preset maximum iteration count. If current iteration counts are smaller, the initial guess of electric field V0 will be replaced by derived electric field V1and the process will resume from the beginning until either the difference between V0 and V1 are smaller than epsilon or the iteration counts surpasses the preset maximum iteration count. In latter case, a more informed guess of electric

field (V0) will be used to restart the whole solving process till the difference between V0 and V1is smaller than the threshold.

Scheme to keep track of corrosion front

Due to the complex nature of micro-galvanic corrosion in Cu-Al WB/EMC corrosion system, corrosion rate of Cu-rich IMC layer shifts continuously throughout the entire corrosion process. The accurate calculation of lifetime of Cu-Al wire bond interconnect under different aging environments relies on the accurate capture of the corrosion cell geometry. As pointed out by Sarkar, the transport of chlorine occurs at much higher speed then motion caused by galvanic corrosion of Cu-rich IMC boundary. This poses a problem in terms of computational implementation of the corrosion model [Sarkar 2011, Sarkar 2012]. An assumption is used to circumvent this problem. It states that for a given corrosion cell geometry, a steady-state process can be used to approach the transport of chlorine modeling. Namely, the rate at which chlorine concentration changes becomes constant at the time scale in which corrosion boundary of Cu-rich IMC evolves. The corrosion front tracking scheme is illustrated in Figure 180. On the top of Gauss–Seidel iterative scheme, a time dependent solver is added to the simulation. Starting with the initial time zero, Gauss–Seidel iterative scheme is used to solve systems of equations to obtained both the electric potential field and chlorine concentration field. Then, based on the corrosion rate of Cu-rich IMC derived from Butler-Volmer boundary condition and the preset time increment between the next-time and initial-time, corrosion cell geometry is updated. The entire domain is remeshed and both electric field and ionic concentration field are extrapolated

and estimated based on the result of previous-time simulation. If the preset finial-time is bigger than the current-time and also if a complete crack has not formed in Cu-rich IMC layer, the simulation proceeds to the next-time calculation till one of the two conditions is satisfied.

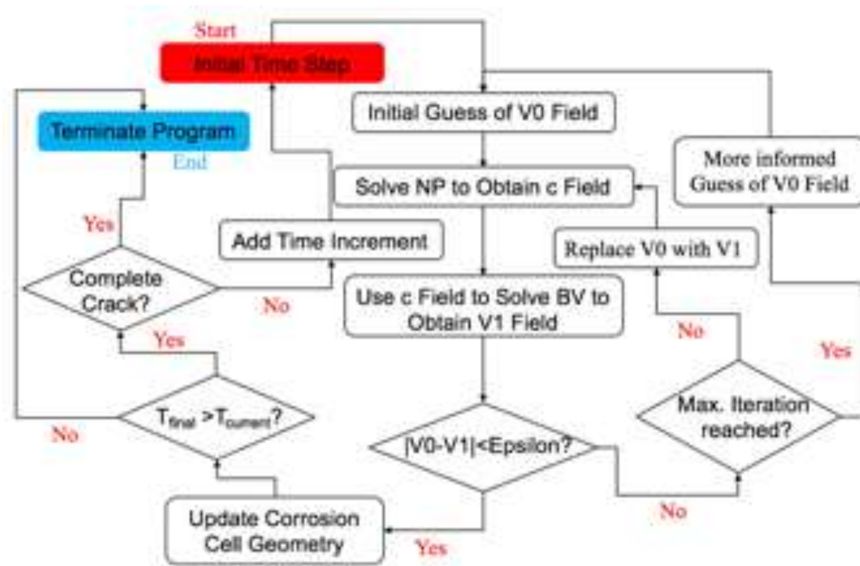

Figure 180: Cu-Al WB Corrosion Front Tracking

9.3 Model Implementation

This paragraph covers the detailed implementation of Nernst-Planck equation and Butler-Volmer boundary condition. Matlab is used as the coding platform. As shown in Figure 181, the initial simulation domain includes only EMC which is represented by color blue and un-corroded EMC/Cu-Al wire bond interface as there is no corrosion happening at time zero. Concentration field c and electric field V are two unknown fields need to be quantified. Ω1 and Ω2 are essentially the same domain. The former is a corrosion cell domain used to calculate corrosion kinetics of Cu-rich IMC. The latter is a transport cell domain used to calculate the transport kinetics of chlorine.

Γc and Γa are cathodic (copper ball bond) /EMC and anodic (Cu-rich IMC)/ EMC interfaces where Butler-Volmer B.C. are imposed. Γin are chlorine source boundary where a chlorine influx is imposed. The rest of the boundary are either electric insulation or concentration insulation B.C.s.

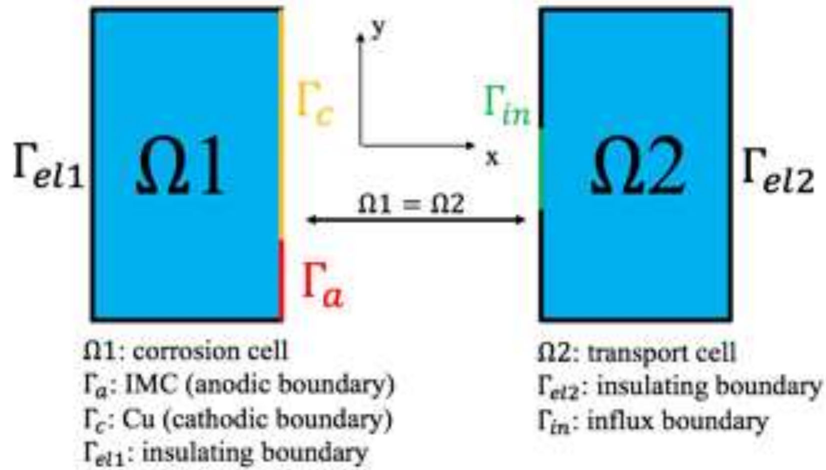

Figure 181: Initial Simulation Domain and Important Boundaries

FEM Approach to Solve PDE Subjected to BV B.C.

Distribution of electric potential within corrosion cell satisfy Laplace's equation as shown in Equation 101,

$$\nabla^2 \mathrm{V} = 0 \tag{101}$$

Anode and cathode boundaries are subjected to Butler-Volmer boundary condition shown in Equation 99 and Equation 100. All the other boundaries are subjected to insulating boundary condition as shown in Equation 102,

$$\nabla_n \mathrm{V} = 0 \tag{102}$$

The corrosion cell domain can be characterized by a generic form of a second-order PDE as shown in Equation 103,

$$\frac{\partial}{\partial x}\left(\alpha_x \frac{\partial V}{\partial x}\right) + \frac{\partial}{\partial y}\left(\alpha_y \frac{\partial V}{\partial y}\right) + \beta u = g \qquad \text{in } \Omega_e \tag{103}$$

The corrosion cell boundaries can be characterized by a generic form of mixed boundary condition as shown in Equation 104,

$$(\alpha_x \frac{\partial V}{\partial x} + \alpha_y \frac{\partial V}{\partial y}) * \hat{a}_n + \gamma V = q \qquad \text{on } \Gamma_a, \Gamma_c \text{ and } \Gamma_{el} \tag{104}$$

The weak formulation of corrosion cell domain can be obtained by constructing the weighted residual of a single element with domain Ωe and this element residual is ideally zero, provided that the numerical solution V is identical to the exact solution. However, this is not the case, which means the element residue re is always nonzero. The objective is to minimize re in a weighted sense. To achieve it, element residue are multiplied with a weighted function w and then the result are integrated over the entire domain Ω. The result of integration is set to zero as shown in Equation 105 and Equation 106,

$$r^e = \frac{\partial}{\partial x}\left(\alpha_x \frac{\partial V}{\partial x}\right) + \frac{\partial}{\partial y}\left(\alpha_y \frac{\partial V}{\partial y}\right) + \beta u - g \tag{105}$$

$$\iint_{\Omega_e} (w * r^e) dxdy = 0 \tag{106}$$

Parameters of generic PDE and generic B.C. can be replaced to represent the galvanic corrosion cell problem as shown in Equation 107,

$\alpha_x = 1,\ \alpha_y = 1,\ \beta = 0,\ \gamma = 0$

$$q = -\frac{j_a(V)}{\sigma} \text{ on } \Gamma_a, \quad q = -\frac{j_c(V)}{\sigma} \text{ on } \Gamma_c \tag{107}$$

The result of integration is shown in Equation 1008

$$-\iint_{\Omega_e} \left[\frac{\partial w}{\partial x}\frac{\partial V}{\partial x} + \frac{\partial w}{\partial y}\frac{\partial V}{\partial y}\right] dxdy = -\oint_{\Gamma_e} w \left(\frac{\partial V}{\partial x} n_x + \frac{\partial V}{\partial y} n_y\right) dl \tag{108}$$

A linear triangular element is used to discretize the entire domain [Mats 2010] and it is mapped to the master triangle which lies on the natural coordinate system (ξη-plane) as shown in Figure 182,

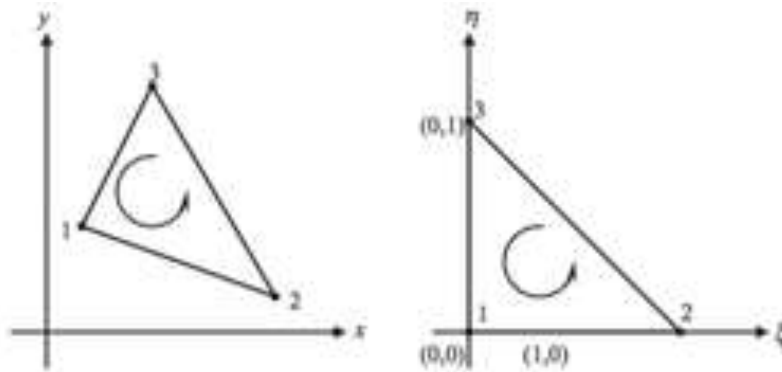

Figure 182: Linear Triangular Element in xy-plane & ξη-plane

The shape function at each node can be expressed as shown in Equation 109,

$$N_1(\xi, \eta) = 1 - \xi - \eta, \quad N_2(\xi, \eta) = \xi, \; N_3(\xi, \eta) = \eta \tag{109}$$

In case of using linear triangular elements to discretize the problem domain, both the primary unknown V and weight w can be expressed as shown in Equation 110,

$$V = \sum_{j=1}^{3} V_j^e N_j, \quad w = N_i \tag{110}$$

Apply Green's theorem to Equation 108 and rearrange it, one can get the simplified governing equation as shown in Equation 111,

$$\{V_i^e\} = p_i^e = -\int_{\Gamma_a} N_i(\frac{j_a}{\sigma})dl - \int_{\Gamma_c} N_i(\frac{j_c}{\sigma})dl$$

$$\text{where,}\ \ M_{ij}^e = -\iint_{\Omega_e}\left[\frac{\partial N_i}{\partial x}\frac{\partial N_j}{\partial x} + \frac{\partial N_i}{\partial y}\frac{\partial N_j}{\partial y}\right]dxdy$$

$$p_i^e = -\oint_{\Gamma_e} N_i\left(\frac{\partial V}{\partial x}n_x + \frac{\partial V}{\partial y}n_y\right)dl = \int_{\Gamma_e} N_i q dl \qquad (111)$$

Equation 111 can be linearized using Newton-Galerkin method. Set f(V)=ja and g(V)=jc and apply Taylor expansion to both f(V) and g(V) around assumed solution V0, the final result is shown in Equation 112 and the solving scheme is schematically shown in Figure 183.

$$f(V_0^e + \delta^e) \simeq f(V_0^e) + f'(V_0^e) * \delta^e, g(V_0^e + \delta^e) \simeq g(V_0^e) + g'(V_0^e) * \delta^e$$

$$K = (M_{ij}^e - \frac{1}{\sigma}\int_{\Gamma_a} N_i f'(V_0^e)dl - \frac{1}{\sigma}\int_{\Gamma_c} N_i g'(V_0^e)dl)$$

$$X = \delta^e$$

$$b = \frac{1}{\sigma}\int_{\Gamma_a} N_i f(V_0^e)dl + \frac{1}{\sigma}\int_{\Gamma_c} N_i g(V_0^e)dl - M_{ij}^e V_0^e$$

$$K\{X\} = b \qquad (112)$$

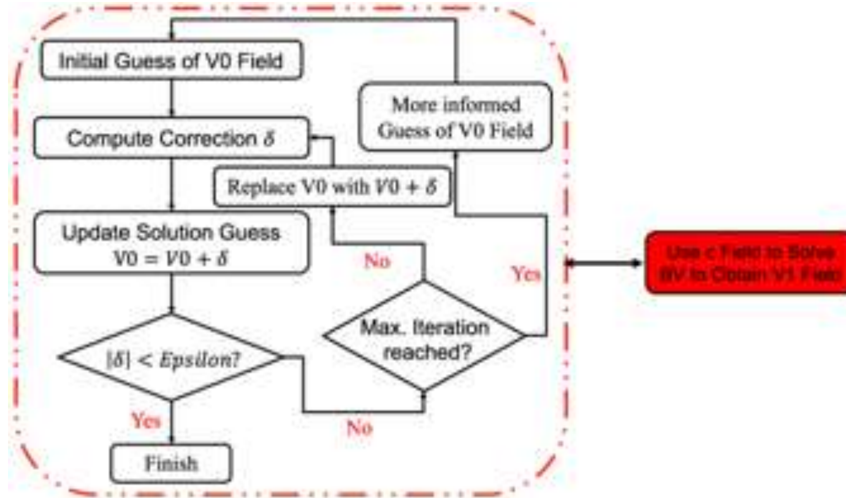

Figure 183: Newton-Galerkin method

A set of Tafel parameters and a set of geometrical parameters for the corrosion cell are listed in Table 24. Previously, these parameters are used to calculate the potential distribution in a corrosion cell using finite difference method and commercial multiphysics software by two researchers [Doig 1997, Turner 2013], respectively. Here, the simulation is performed again in order to verify the model. Figure 184 show the electric potential distribution under both zero polarization and 4.5V polarization. The result V field in both cases are identical to the results obtained by these two researches. Therefore, the accuracy of corrosion cell modeling can be verified.

Table 24: Simulation Parameters for a PDE subjected to Butler-Volmer B.C.

Property	Value
αa, αc anodic reaction of metal A,B	0.05V/dec
βa, βc cathodic reaction of metal A,B	0.05V/dec
j0a, j0c, free corrosion density	1A/m^2
sa, sc, surface length of metal A,B	0.01m
σ conductivity of the electrolyte	10S/m

w thickness of the electrolyte	0.01m
Va free corrosion potential of metal A	0.5V
Vc free corrosion potential of metal B	-0.5V

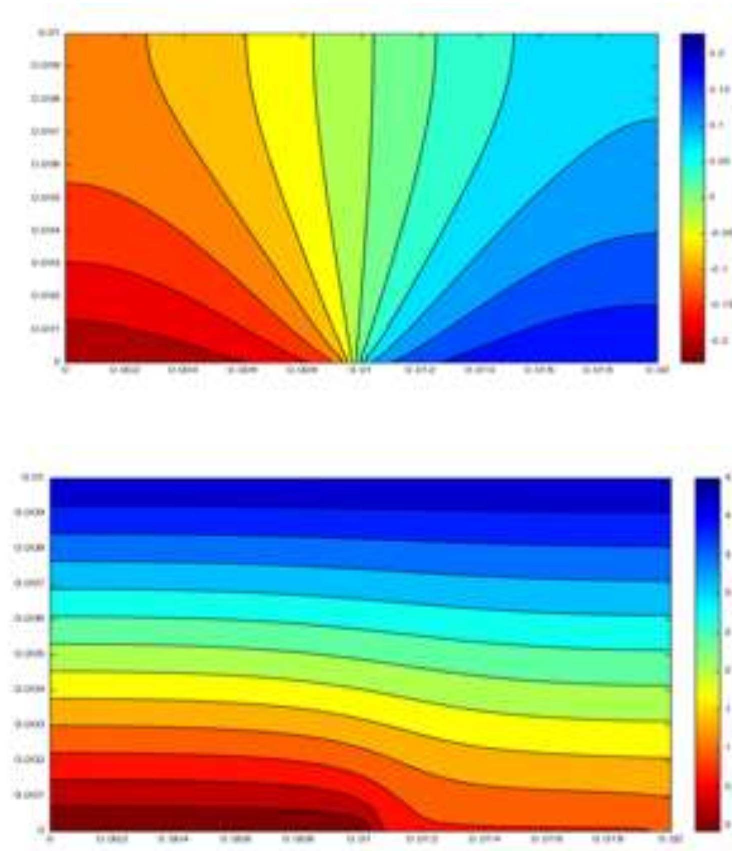

Figure 184: Test Simulation Results (electric field distribution with/without polarization)

FEM Approach to Solve Time-Dependent Diffusion Equation

As expressed in Equation 1, Nernst-Planck equation model the transport behavior of chloride ion in EMCs based on the effect of concentration gradient as well as the effect of electric potential gradient. Using the similar discretization approach shown in solving PDE subjected to Butler-

Volmer equation, the domain-discretized form can be expressed as shown in Equation 113 and Equation 114,

$$\iint_{\Omega_e}[N]^T[N]\{\frac{\partial c}{\partial t}\}dxdy = -\iint_{\Omega_e}[\nabla N]^T D[\nabla N]\{c\}dxdy - \iint_{\Omega_e}[\nabla N]^T z\mu\nabla V[N]\{c\}dxdy \tag{113}$$

$$\text{Set } M_{ij}^e = -D\iint_{\Omega_e}\left[\frac{\partial N_i}{\partial x}\frac{\partial N_j}{\partial x} + \frac{\partial N_i}{\partial y}\frac{\partial N_j}{\partial y}\right]dxdy$$

$$A_{ij}^e = \iint_{\Omega_e} N_i N_j dxdy$$

$$G_{ij}^e = -z\mu\nabla V\iint_{\Omega_e}\left[\frac{\partial N_i}{\partial x}N_j + \frac{\partial N_i}{\partial y}N_j\right]dxdy \tag{114}$$

substitute Equation 114 for Equation 113 and rearrange it, one can get Equation 115,

$$\frac{\partial\{c\}}{\partial t}[A] = [M]\{c\} + [G]\{c\} \tag{115}$$

integrate Equation 18 from time t to time t+1 as shown in Equation 116,

$$\int_{t_l}^{t_{l+1}}\frac{\partial\{c\}}{\partial t}[A]dt = \int_{t_l}^{t_{l+1}}[M]\{c\}dt + \int_{t_l}^{t_{l+1}}[G]\{c\}dt \tag{116}$$

Using backward Euler method to discretize the time domain resulting in the time-discretized form as shown in Equation 117,

$$\left(c_{t_{l+1}} - c_{t_l}\right)[A] = [M]c_{t_{l+1}}(t_{l+1} - t_l) + [G]c_{t_{l+1}}(t_{l+1} - t_l) \tag{117}$$

Given the initial condition of chlorine concentration, Nernst-Planck equation can be solved successively as shown in Equation 118,

$$([A] - [M]\Delta t - [G]\Delta t)c_{t_{l+1}} = [A]c_{t_l} \tag{118}$$

Here, two case studies will be presented to show how NP equation governs the transport of chlorine in epoxy molding compounds. The purpose of the first case is to demonstrate the transport of chlorine without the effect of bias. There is an initial chlorine accumulation at the center of the transport cell as shown in Figure 185, due to the concentration gradient, chlorine will diffuse toward its vicinity. The simulation parameters are listed in Table 25.

Table 25: Simulation Parameters for a transport cell

Property	Value
D, diffusion coefficient of chlorine	$10^{-10}m^{2/}s$
c0, initial concentration at center	$10mol/m^2$
c1, initial concentration elsewhere	$0mol/m^2$
h, height of transport cell	0.01m
w, width of transport cell	0.02m

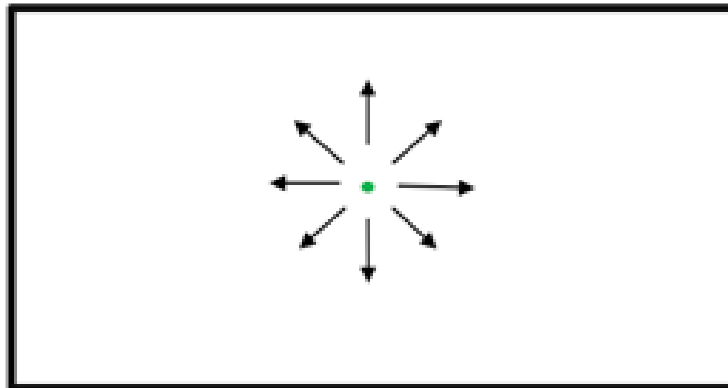

Figure 185: Case Study 1

As shown in Figure 186, under the influence of concentration gradient, chlorine diffuses uniformly outwards in all directions, making several concentric concentration circles around the

center of transport cell. When the upward and downward diffusion process is stopped by insulation boundaries, chlorine begins to diffuse toward left and right in a symmetric fashion.

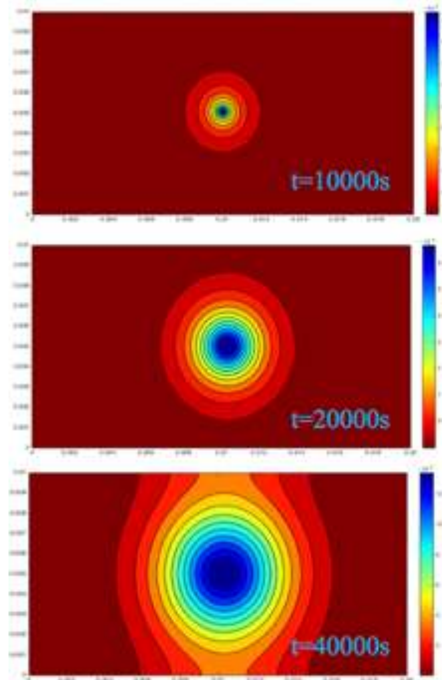

Figure 186: Concentration contour at different durations

The purpose of the second case study is to demonstrate how electric potential gradient affect this transport process. As shown in Figure 187, inside a transport cell with insulating boundaries, there is a chlorine source on the top of the cell. At the bottom of transport cell, there is a couple of electrically connected dissimilar metal surfaces creating an electric field over the entire cell, which affects the transport of negatively charged chlorine. The simulation parameters are listed in Table 26. The resultant electric field is shown in Figure 188. The electric field lines indicate the electric potential drop from the highest to the lowest. At the beginning of the chlorine transport process, since there is barely electric potential difference in the area where chloride ions are present (the

upper middle area in Figure 18 where the uniform pale green indicates a constant electric potential zone), The driving force of chlorine transport is concentration gradient. As shown in the upper plot of Figure 189, The continuous release of chlorine at the source creates a series of concentric concentration semicircle contour. The concentration contour skews to the right as chlorine transport farther away from the source as shown in the bottom part of upper middle plot of Figure 189. There is more chlorine accumulated at bottom right than that of bottom left. This is caused by the electric field in the transport cell. As chlorine transports farther away from the source, the effect of concentration gradient becomes weaker and weaker. On the other hand, electric potential force at those regions are stronger than that at the top of the cell. As a result, negatively charged chlorine migrates along the opposite direction of electric field line. This complex chlorine transport process will reach a point where the effect of diffusive driving force of concentration gradient counteract that of migrational driving force of electric potential gradient at every place in the transport cell as shown in the two lower plots of Figure 189. Those two chlorine concentration contours are similar. This transport process will never reach steady state due to the constant influx of chlorine from the top of the cell. This phenomenon is similar to what happens in a Cu-Al WB corrosion cell. The continuous release of organic chlorine as a result of EMC degradation under harsh environmental conditions will disturb the concentration balance established previously in the corrosion cell under effects of both concentration gradient and electric potential gradient.

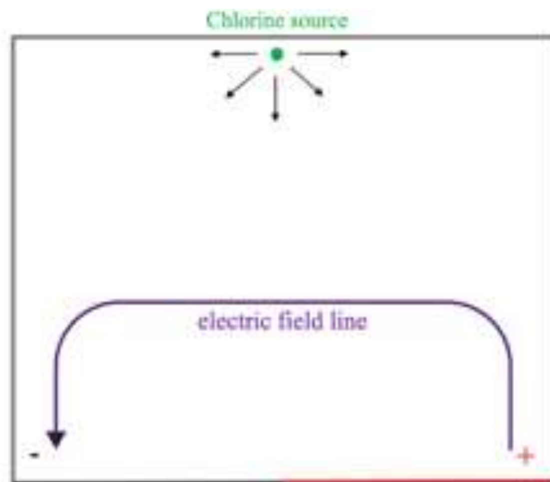

Figure 187: Case study 2

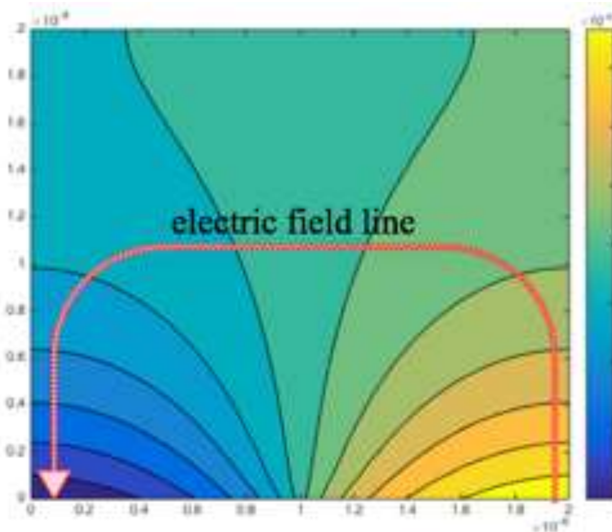

Figure 188: Electric field

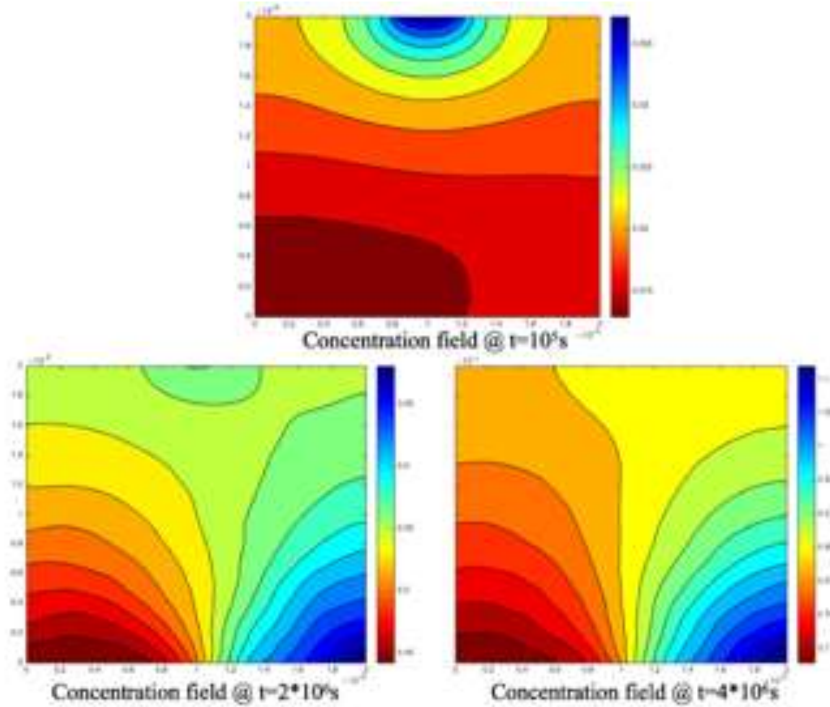

Figure 189: Chlorine concentration field

Table 26: Simulation Parameters for NP equation coupled with BV B.C.

Property	Value
αa, αc anodic reaction of both metals	0.05V/dec
βa, βc cathodic reaction of both metals	0.05V/dec
j0a, j0c, free corrosion density	1A/m2
sa, sc, surface length of metal A,B	2*10-6m
h, height of corrosion cell	2*10-6m
σ conductivity of the electrolyte	10S/m
Va free corrosion potential of metal A	0.5V
Vc free corrosion potential of metal B	-0.5V
D, diffusion coefficient of chlorine	10-17m2/s
μ, mobility of chlorine	10-15m2/(V.s)
Fin, influx of chlorine at source	10-12mol/(m2.s)
c0, initial concentration of chlorine	0mol/m2

Corrosion Front Tracking

In the section of mathematic model for Cu-Al WB corrosion, the scheme to solve time-dependent corrosion simulation is introduced. In this paragraph, details about the implementation of corrosion front tracking will be discussed. The corrosion front is circled up in Figure 190. The EMC/IMC interface will become the corrosion front once the corrosion process is initialized due to the degradation of EMCs. Four sequential general steps are taken successively to track the moving corrosion front as shown in Figure 191. Next-state corrosion boundary is calculated based on current-state corrosion boundary. It then will be utilized to track the next-state simulation geometry. The newly acquired geometry will be remeshed to provide the current-state corrosion boundary, which will again be used to calculate next-state corrosion boundary.

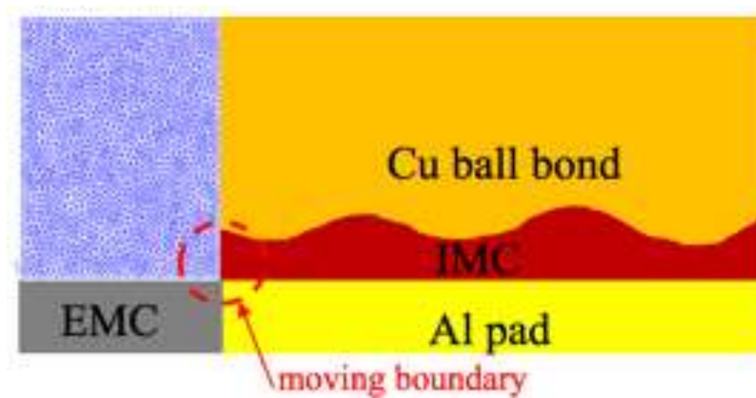

Figure 190: Corrosion front

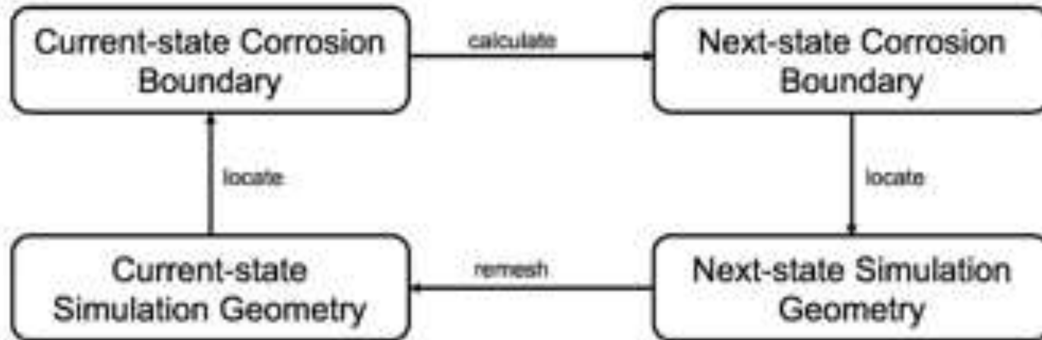

Figure 191: General procedures of corrosion front tracking

Figure 192 and Figure 193 explain how to implement moving corrosion boundary step by step. It starts with calculation of nodal displacements (depicted as blue arrowed lines) of CBNs (corrosion boundary nodes) which are depicted in black dots. Then, next-state CBNs (depicted as grey dots) are projected. The next step is to use the relative location of copper ball bond/IMC interface (depicted as orange wavy line), the relative location of aluminum pad/IMC interface (depicted as yellow straight line) and locations of next-state CBNs to form a new corrosion front. Rank next-state CBNs in a descending order in term of their vertical positions. Locate two CBNs one of which is located at the copper bond region and it is also the node closest to the Cu/IMC interface compared to the rest of CBNs in this region if there exists any. The other node is located at the Cu-rich IMC region and it is also the node closest to the interface compared to the rest of CBNs in the corresponding region. Create a straight line between these two nodes. Then, the upper end point of next-state corrosion boundary (depicted as dashed red curve) can be determined by the intersection of the Cu/IMC curve and the straight line created in the previous step. The lower end point of next-state corrosion boundary can be located in a similar fashion. Once locations of

those two end points are determined, they are used along with locations of the rest of next-state CBNs in Cu-rich IMC region to create a smooth next-state corrosion boundary curve using linear regression. After that, geometry of corrosion cell can be updated and remeshed. Since the remesh process alters the nodal numbers of previously established ones, including nodes inside corrosion cell and nodes on the corrosion cell boundaries, efforts have to be made to relocate those important boundary nodes as well as extrapolate next-state nodal values of electric potential and chlorine concentration from current-state ones. The final step is to replace next-state geometry with current-state geometry so that the process will keep being executed till either a predetermined simulation duration is reached or a complete crack forms in between bond-pad interface.

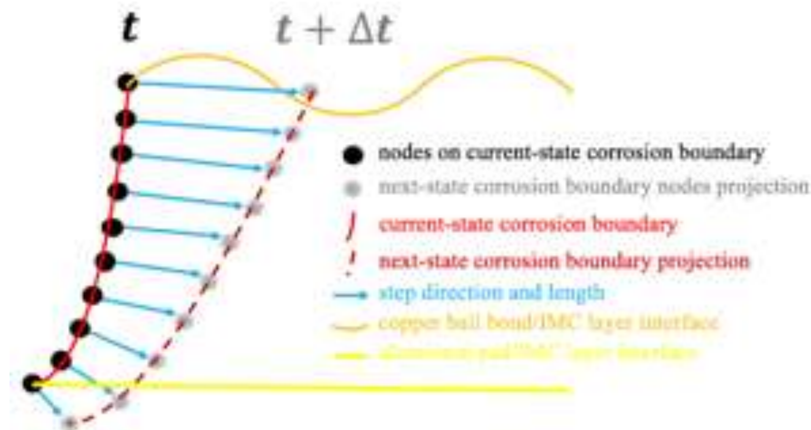

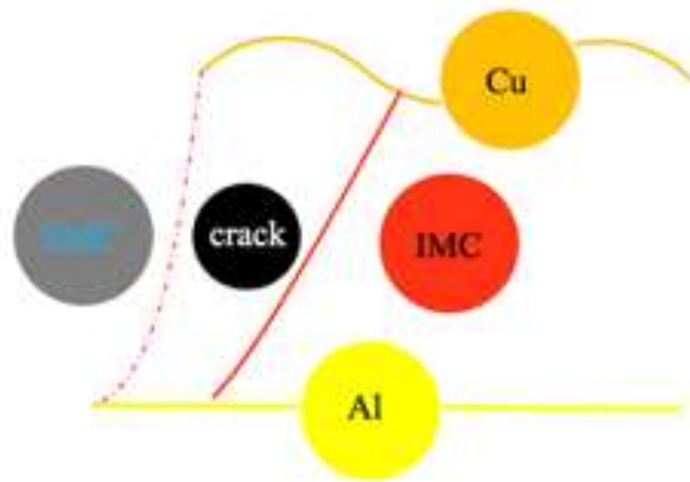

Figure 192: Schematic of corrosion front nodal displacements

The stability issue of using backward Euler scheme to solve this corrosion model is explained in Equation 119, which is derived from Equation 118. Stability is guaranteed if λ is smaller or equal to 1. In practice, the approach of trial and error is employed to find a suitable time-step size so that it is sufficiently small to ensure the stability and sufficiently large to ensure that simulation will terminate within a reasonable amount of time.

$$c_{t+\Delta t} = \left(\frac{[A]}{[A]-([M]+[G])\Delta t}\right) c_t$$

$$c_1 = \left(\frac{[A]}{[A]-([M]+[G])\Delta t}\right) c_0$$

$$c_N = \left(\frac{[A]}{[A]-([M]+[G])\Delta t}\right)^N c_0$$

$$\text{Set } \lambda = \frac{[A]}{[A]-([M]+[G])\Delta t}$$

$$c_N = \lambda^N c_0 \tag{119}$$

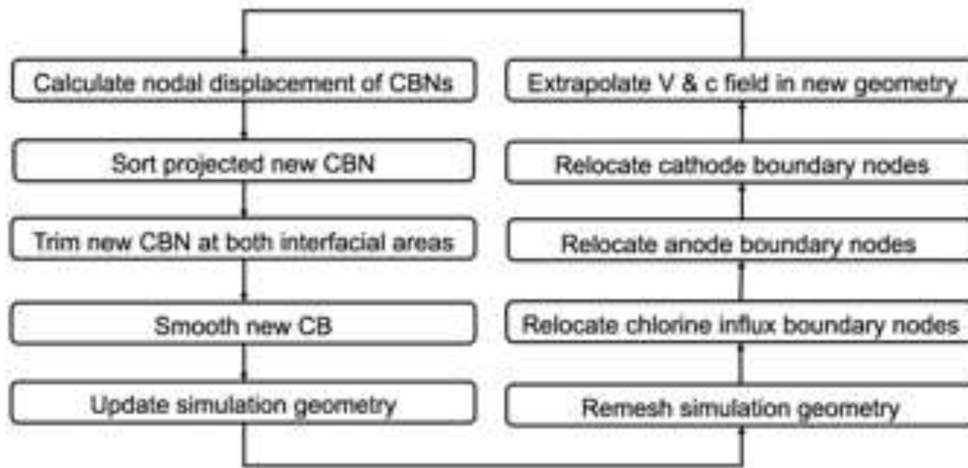

Figure 193: Detailed procedures of corrosion front tracking

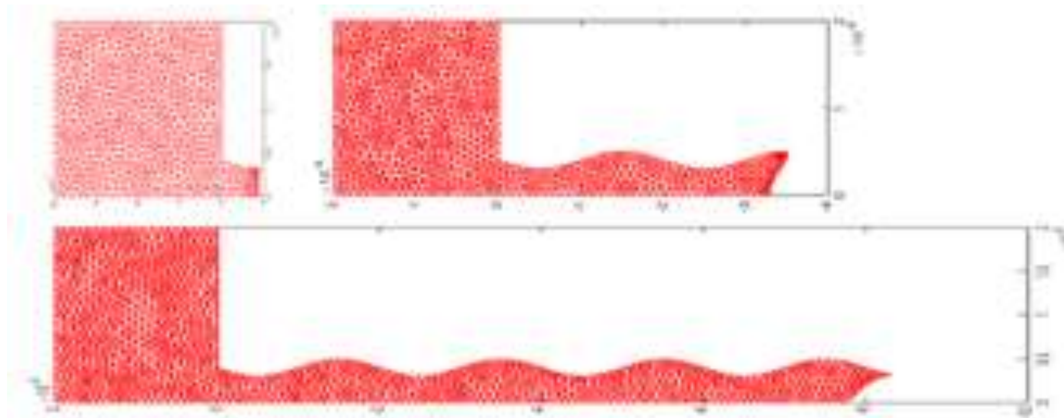

Figure 194: geometrical progression of Cu-Al WB micro-corrosion cell

The geometrical progression of Cu-Al WB corrosion cell is shown in Figure 194. The size of the original cell is 2μm by 2μm. As corrosion proceeds overtime, an interfacial crack initiates and

propagates towards the center of the Cu-Al WB bond pad interface. The height and length of the sinewave-shape interface is set to be 0.2μm and 1μm, respectively to match with those measurements of a real crack as previously shown in Figure 175.

9.4 Construction of Model Inputs

Epoxy Molding Compound Chlorine Release Test

Chlorine contaminant release rate can be experimentally measured using the schematic approach as shown Figure 195. EMC samples are thin (around 0.6 mm) square pieces received from Texas Instruments. Test samples are crushed and ground into very fine EMC sample powders manually using mortar and pestle. In the next step, fine sample powder is dissolved into deionized water under 120 degrees Celsius for 4 hours with a magnetic stirrer stirring the mixture continuously on the top of a hot plate. Then, the mixture is transferred into a Parr bomb test equipment in which various high temperature and humidity stressed conditions can be created. After aging of the mixture, filter is used to separate the power from the deionized water. In the final step, Mohr's titration is utilized to measure the amount of chlorine present in the water. This approach enables the calculation of chlorine release of different type of EMCs under different stressed operational conditions.

Figure 195: Schematic Approach to Calculating Chlorine Release Rate of Different EMCs

Table 27 shows measurements of chlorine release rate of a particular type of EMC under three different temperature and humidity set points. As one can see, EMC degradation rate increases as operational temperature increases.

Table 27: Chlorine Release Rate Measurements

Temperature(0C)	Mean Cl Release rate (ppm/day)
110	2.21
120	2.45
130	2.86

Diffusion-Migration Cell Tests

Both diffusivity and ionic mobility of chlorine are measured at different operational temperatures repeatedly.

Table 28 gives average experimental results.

Table 28: Summary of D and μ measurements

Temperature (°C)	Diffusion Coefficient (cm2/s)	Mobility (cm2/(V.s))
25	$1.86*10^{-11}$	$1.55*10^{-9}$
45	$2.90*10^{-11}$	$2.15*10^{-9}$
55	$3.23*10^{-11}$	$3.32*10^{-9}$
85	6.36*10-11	$6.42*10^{-9}$

Electrochemical Polarization Tests

The experimental setup is shown in Figure 197. Tafel curve has been used for the determination of the open-circuit potential, corrosion potential, or rest potential, E0. The slope of the Tafel curve provides the coefficient of charge transfer, g. The data measured include the current-potential curve and the Tafel Curve [log10 (current) vs potential]. The current-potential curve follows the Butler-Volmer Equation for kinetic-controlled reaction [Bard 2001, McCafferty 2010]. Figure 198 shows the schematic plot of Tafel extrapolation.

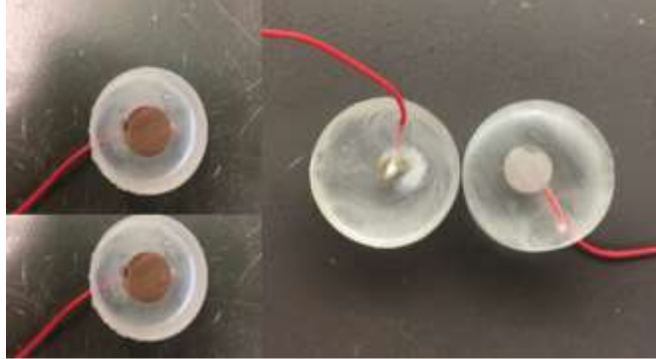

Figure 196: Electrochemical Polarization Test Samples

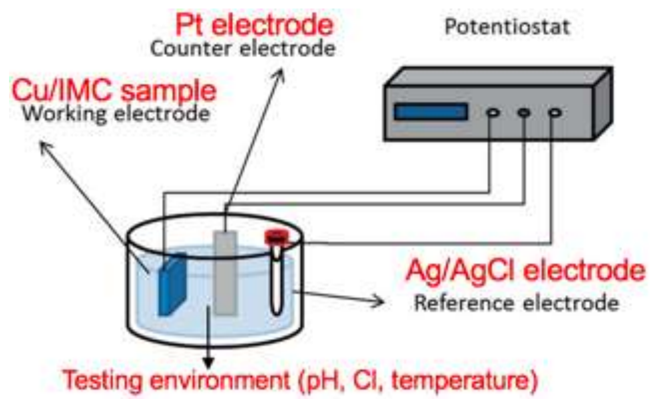

Figure 197: Electrochemical Polarization Test Setup

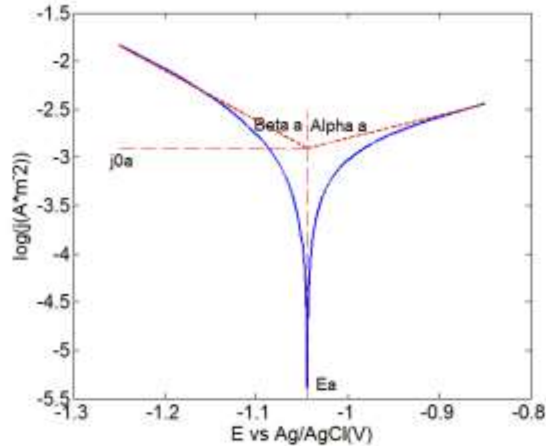

Figure 198: Schematic Plot of Measuring Tafel Parameters

Polarization test matrix is shown in Table 29. Four different temperature/humidity set points are used along with six different chlorine concentration levels. The pH value of the test solution is 6.2, which is the same as that of testing EMC sample given by manufacturer. There are totally 24 unique test conditions for both copper and Cu-Al IMC sample. For each test condition, experiments are performed repeatedly 6 times in order to obtain mean values of Tafel parameters. Figure 199 display a typical polarization test results and Table 30 shows the corresponding Tafel Parameters estimation under one of test conditions. Polarization tests are performed for all the 24 unique test conditions on both Cu-Al IMC and Cu samples. The average value of measured Tafel parameters and standard deviation of test measurements are shown in the last two columns. The mean value of Tafel parameters are then used to help construct regression models which predicts the change of Tafel parameter under different temperatures and chlorine concentration levels.

Table 29: Polarization Test Matrix

Temperature(0C)	Concentration (M)

25	4.2E-4
45	0.01
65	0.05
85	0.1
/	0.3
/	0.5

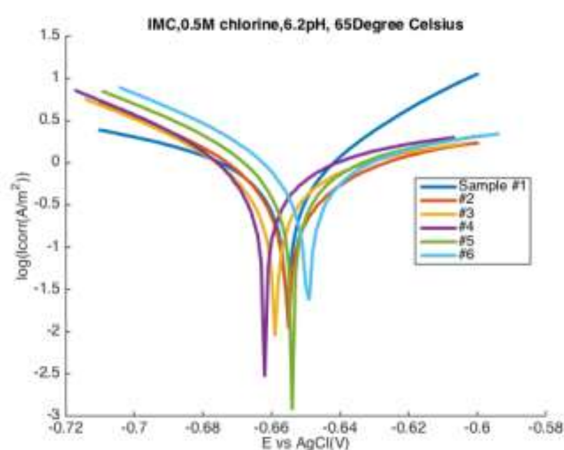

Figure 199: Repeated Measurement at one of the 24 test conditions for Cu-Al IMC

Table 30: Tafel Parameters Estimation of Polarization Tests

	Alpha (V/decade)	Beta (V/decade)	Ecorr (V)	Icorr (V)
#1	0.047	0.111	-0.655	0.794
#2	0.112	0.059	-0.655	0.602
#3	0.162	0.062	-0.660	0.768
#4	0.172	0.062	-0.664	0.934
#5	0.141	0.061	-0.654	0.867
#6	0.053	0.115	-0.651	0.796
AVG	0.115	0.078	-0.656	0.793
SDV	0.054	0.027	0.005	0.112

Summary of Experimental Results

Electrochemical Polarization Tests for Copper

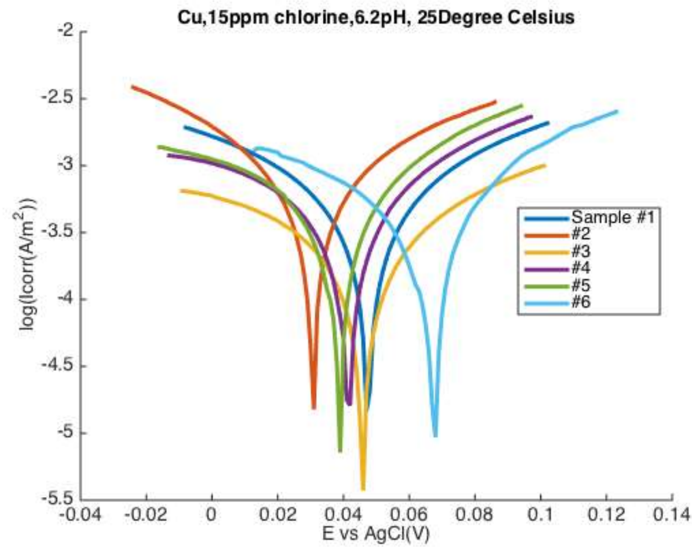

Figure 200: Electrochemical Polarization Test Results of Cu at 6.2pH, 15ppm and 25^{0}C

Table 31: Tafel Extrapolation of Cu at 6.2pH, 15ppm and 25^{0}C

	Alpha_a (V/decade)	Alpha_c (V/decade)	Ecorr (V)	Icorr (A/m2)
#1	0.107	0.117	0.048	0.0006
#2	0.109	0.087	0.031	0.0009
#3	0.111	0.201	0.049	0.0003
#4	0.091	0.155	0.040	0.0006
#5	0.092	0.166	0.036	0.0007
#6	0.101	0.108	0.056	0.0006
AVG	0.102	0.139	0.043	0.0006
SDV	0.009	0.042	0.009	0.0002

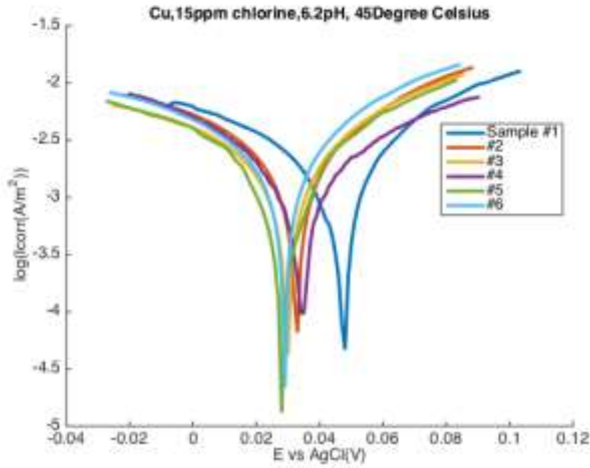

Figure 201: Electrochemical Polarization Test Results of Cu at 6.2pH, 15ppm and 45^{0}C

Table 32: Tafel Extrapolation of Cu at 6.2pH, 15ppm and 45^{0}C

	Alpha_a (V/decade)	Alpha_c (V/decade)	Ecorr (V)	Icorr (A/m2)
#1	0.100	0.108	0.037	0.0028
#2	0.058	0.080	0.033	0.0020
#3	0.102	0.073	0.028	0.0022
#4	0.105	0.104	0.036	0.0024
#5	0.084	0.113	0.027	0.0023
#6	0.109	0.148	0.022	0.0039
AVG	0.093	0.104	0.031	0.0026
SDV	0.019	0.027	0.006	0.0007

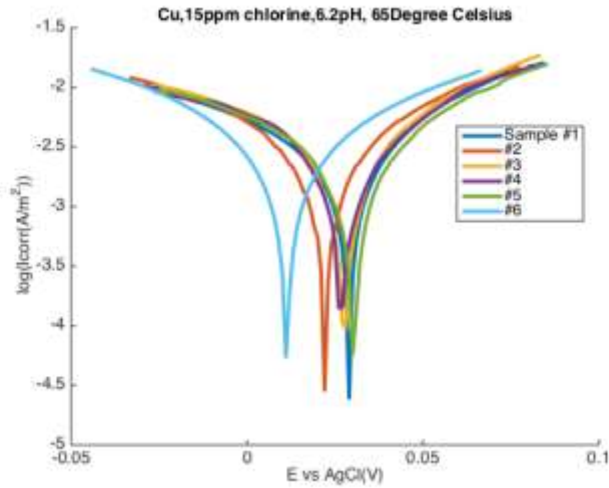

Figure 202: Electrochemical Polarization Test Results of Cu at 6.2pH, 15ppm and 65^0C

Table 33: Tafel Extrapolation of Cu at 6.2pH, 15ppm and 65^0C

	Alpha_a (V/decade)	Alpha_c (V/decade)	Ecorr (V)	Icorr (A/m2)
#1	0.109	0.149	0.022	0.0043
#2	0.096	0.105	0.020	0.0038
#3	0.080	0.116	0.027	0.0038
#4	0.101	0.139	0.023	0.0041
#5	0.084	0.087	0.025	0.0029
#6	0.092	0.098	0.014	0.0037
AVG	0.094	0.116	0.022	0.0038
SDV	0.011	0.024	0.005	0.0005

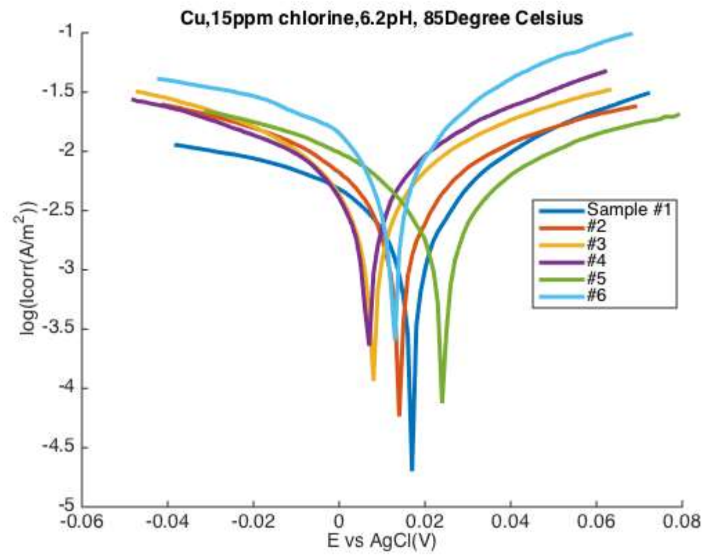

Figure 203: Electrochemical Polarization Test Results of Cu at 6.2pH, 15ppm and 85^0C

Table 34: Tafel Extrapolation of Cu at 6.2pH, 15ppm and 85^0C

	Alpha_a (V/decade)	Alpha_c (V/decade)	Ecorr (V)	Icorr (A/m2)
#1	0.079	0.162	0.013	0.0055
#2	0.088	0.097	0.017	0.0066
#3	0.082	0.086	0.009	0.0078
#4	0.045	0.041	0.006	0.0042
#5	0.116	0.106	0.023	0.0069
#6	0.062	0.036	0.015	0.0085
AVG	0.079	0.088	0.014	0.0066
SDV	0.024	0.047	0.006	0.0016

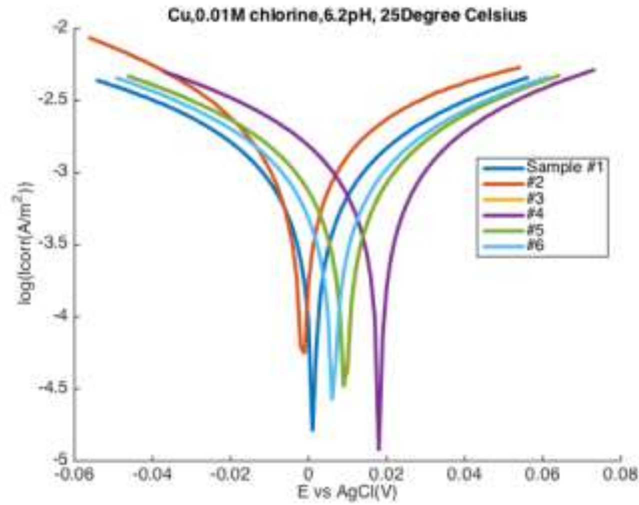

Figure 204: Electrochemical Polarization Test Results of Cu at 6.2pH, 0.01M and 25^{0}C

Table 35: Tafel Extrapolation of Cu at 6.2pH, 0.01M and 25^{0}C

	Alpha_a (V/decade)	Alpha_c (V/decade)	Ecorr (V)	Icorr (A/m2)
#1	0.097	0.103	0.001	0.0013
#2	0.052	0.064	-0.001	0.0011
#3	0.102	0.102	0.009	0.0013
#4	0.104	0.100	0.017	0.0015
#5	0.087	0.087	0.009	0.0011
#6	0.101	0.100	0.006	0.0013
AVG	0.090	0.093	0.007	0.0013
SDV	0.020	0.015	0.006	0.0001

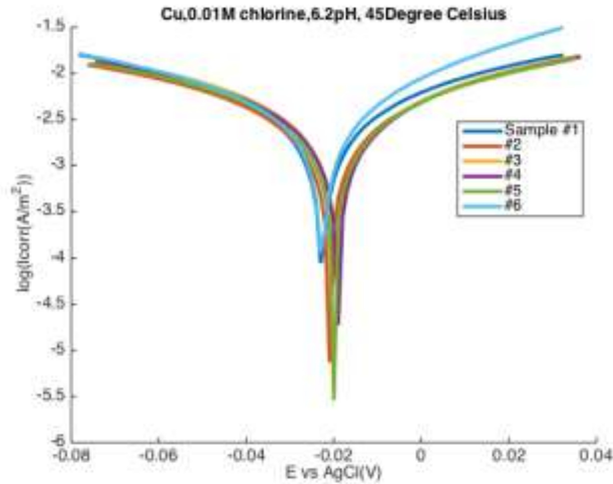

Figure 205: Electrochemical Polarization Test Results of Cu at 6.2pH, 0.01M and 45^0C

Table 36: Tafel Extrapolation of Cu at 6.2pH, 0.01M and 45^0C

	Alpha_a (V/decade)	Alpha_c (V/decade)	Ecorr (V)	Icorr (A/m2)
#1	0.088	0.092	-0.022	0.0040
#2	0.099	0.113	-0.020	0.0040
#3	0.099	0.107	-0.019	0.0044
#4	0.095	0.105	-0.019	0.0040
#5	0.101	0.114	-0.020	0.0042
#6	0.065	0.092	-0.024	0.0043
AVG	0.091	0.104	-0.021	0.0041
SDV	0.014	0.010	0.002	0.0002

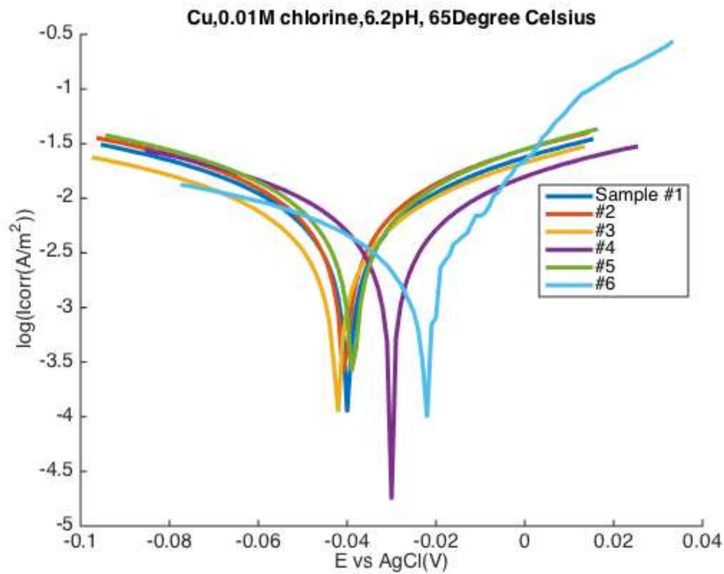

Figure 206: Electrochemical Polarization Test Results of Cu at 6.2pH, 0.01M and 65^0C

Table 37: Tafel Extrapolation of Cu at 6.2pH, 0.01M and 65^0C

	Alpha_a (V/decade)	Alpha_c (V/decade)	Ecorr (V)	Icorr (A/m2)
#1	0.094	0.111	-0.038	0.0095
#2	0.090	0.105	-0.039	0.0103
#3	0.090	0.115	-0.040	0.0076
#4	0.096	0.099	-0.031	0.0079
#5	0.090	0.107	-0.037	0.0110
#6	0.041	0.103	-0.036	0.0055
AVG	0.083	0.106	-0.037	0.0086
SDV	0.021	0.006	0.003	0.0020

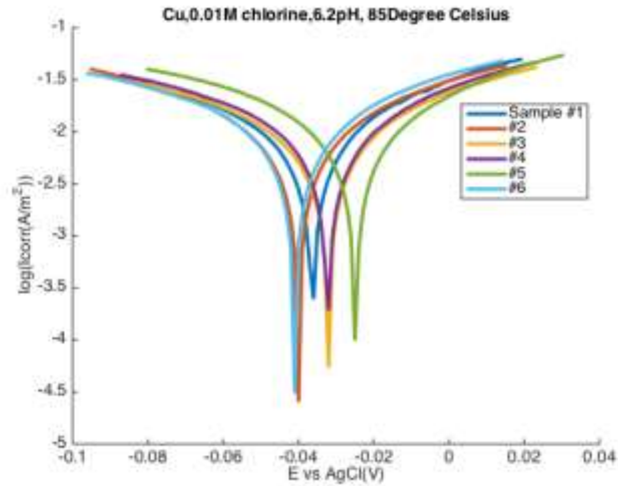

Figure 207: Electrochemical Polarization Test Results of Cu at 6.2pH, 0.01M and 85^{0}C

Table 38: Tafel Extrapolation of Cu at 6.2pH, 0.01M and 85^{0}C

	Alpha_a (V/decade)	Alpha_c (V/decade)	Ecorr (V)	Icorr (A/m2)
#1	0.078	0.109	-0.035	0.0109
#2	0.086	0.091	-0.040	0.0104
#3	0.093	0.116	-0.032	0.0108
#4	0.095	0.111	-0.034	0.0119
#5	0.068	0.084	-0.024	0.0101
#6	0.080	0.093	-0.042	0.0105
AVG	0.083	0.101	-0.035	0.0108
SDV	0.010	0.013	0.006	0.0006

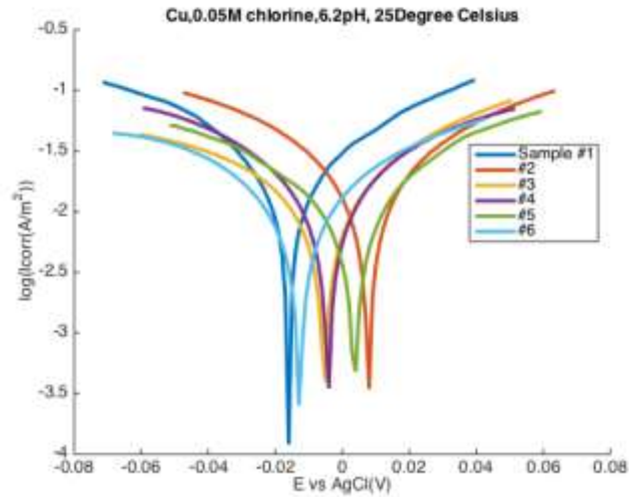

Figure 208: Electrochemical Polarization Test Results of Cu at 6.2pH, 0.05M and 25^0C

Table 39: Tafel Extrapolation of Cu at 6.2pH, 0.05M and 25^0C

	Alpha_a (V/decade)	Alpha_c (V/decade)	Ecorr (V)	Icorr (A/m2)
#1	0.063	0.077	-0.011	0.0230
#2	0.065	0.066	0.008	0.0177
#3	0.083	0.125	-0.008	0.0173
#4	0.096	0.089	-0.005	0.0196
#5	0.125	0.114	-0.005	0.0205
#6	0.102	0.189	-0.004	0.0208
AVG	0.089	0.110	-0.004	0.0198
SDV	0.024	0.045	0.006	0.0021

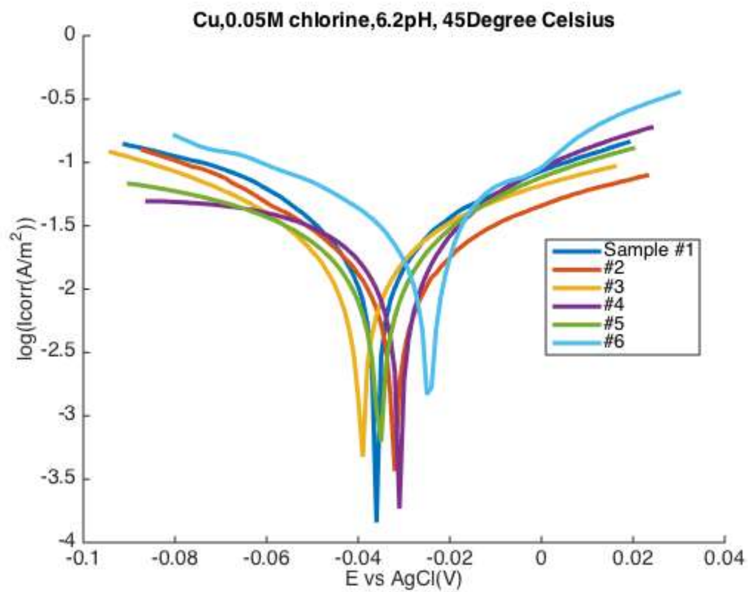

Figure 209: Electrochemical Polarization Test Results of Cu at 6.2pH, 0.05M and 45^{0}C

Table 40: Tafel Extrapolation of Cu at 6.2pH, 0.05M and 45^{0}C

	Alpha_a (V/decade)	Alpha_c (V/decade)	Ecorr (V)	Icorr (A/m2)
#1	0.066	0.081	-0.031	0.0293
#2	0.112	0.083	-0.031	0.0264
#3	0.105	0.085	-0.039	0.0281
#4	0.150	0.060	-0.032	0.0261
#5	0.083	0.126	-0.038	0.0273
#6	0.039	0.053	-0.031	0.0251
AVG	0.093	0.081	-0.033	0.0270
SDV	0.039	0.025	0.004	0.0015

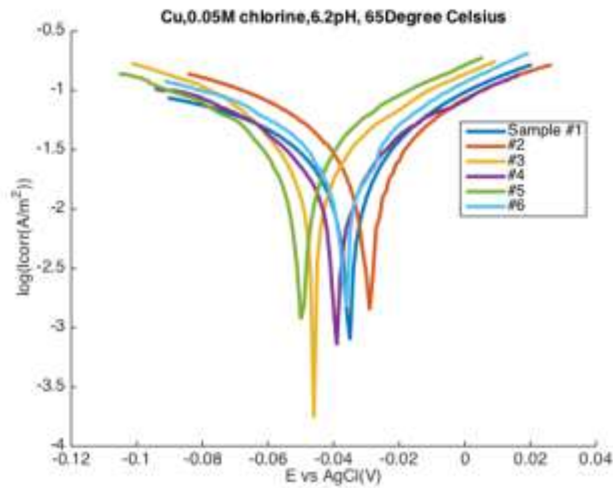

Figure 210: Electrochemical Polarization Test Results of Cu at 6.2pH, 0.05M and 65^0C

Table 41: Tafel Extrapolation of Cu at 6.2pH, 0.05M and 65^0C

	Alpha_a (V/decade)	Alpha_c (V/decade)	Ecorr (V)	Icorr (A/m2)
#1	0.098	0.160	-0.038	0.0412
#2	0.093	0.105	-0.029	0.0432
#3	0.085	0.111	-0.039	0.0470
#4	0.084	0.153	-0.028	0.0398
#5	0.085	0.112	-0.049	0.0428
#6	0.078	0.137	-0.033	0.0446
AVG	0.087	0.130	-0.036	0.0431
SDV	0.007	0.024	0.008	0.0025

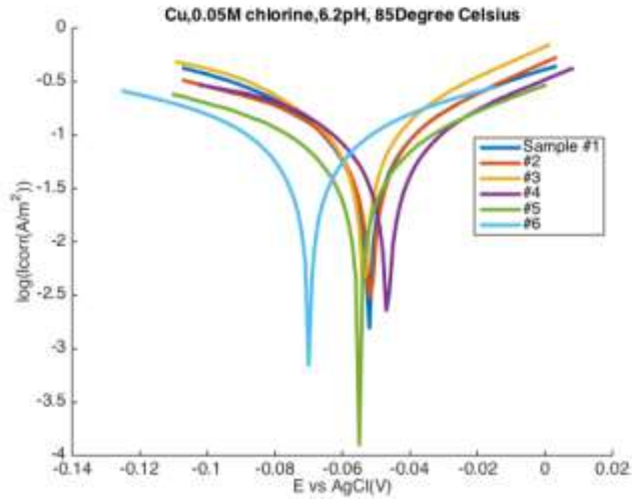

Figure 211: Electrochemical Polarization Test Results of Cu at 6.2pH, 0.05M and 85^{0}C

Table 42: Tafel Extrapolation of Cu at 6.2pH, 0.05M and 85^{0}C

	Alpha_a (V/decade)	Alpha_c (V/decade)	Ecorr (V)	Icorr (A/m2)
#1	0.068	0.068	-0.052	0.0819
#2	0.070	0.124	-0.046	0.1047
#3	0.045	0.048	-0.054	0.0695
#4	0.075	0.123	-0.040	0.0977
#5	0.084	0.119	-0.050	0.0749
#6	0.097	0.084	-0.068	0.0729
AVG	0.073	0.094	-0.052	0.0836
SDV	0.017	0.032	0.009	0.0144

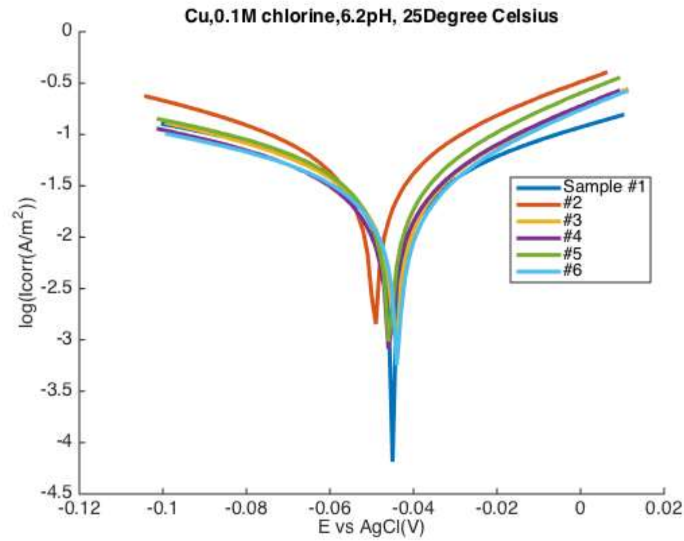

Figure 212: Electrochemical Polarization Test Results of Cu at 6.2pH, 0.1M and 25^{0}C

Table 43: Tafel Extrapolation of Cu at 6.2pH, 0.1M and 25^{0}C

	Alpha_a (V/decade)	Alpha_c (V/decade)	Ecorr (V)	Icorr (A/m2)
#1	0.077	0.107	-0.040	0.0357
#2	0.068	0.053	-0.049	0.0432
#3	0.079	0.053	-0.044	0.0285
#4	0.061	0.107	-0.045	0.0342
#5	0.057	0.103	-0.045	0.0409
#6	0.057	0.109	-0.043	0.0312
AVG	0.066	0.089	-0.044	0.0356
SDV	0.010	0.027	0.003	0.0056

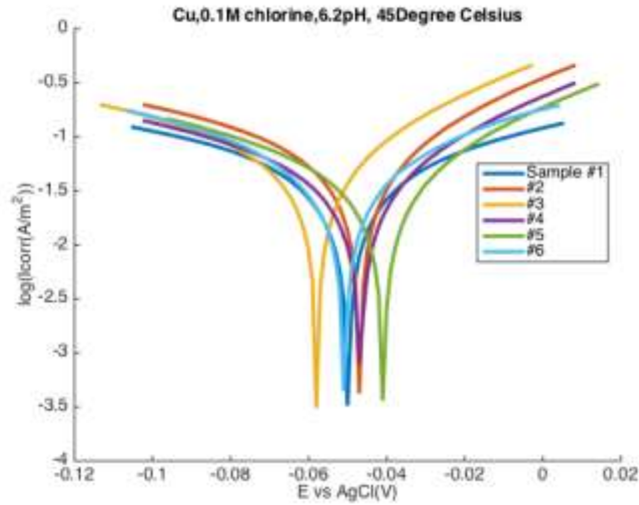

Figure 213: Electrochemical Polarization Test Results of Cu at 6.2pH, 0.1M and 45^{0}C

Table 44: Tafel Extrapolation of Cu at 6.2pH, 0.1M and 45^{0}C

	Alpha_a (V/decade)	Alpha_c (V/decade)	Ecorr (V)	Icorr (A/m2)
#1	0.114	0.133	-0.048	0.0455
#2	0.091	0.055	-0.046	0.0522
#3	0.088	0.056	-0.058	0.0507
#4	0.065	0.110	-0.047	0.0445
#5	0.065	0.102	-0.042	0.0431
#6	0.089	0.096	-0.052	0.0483
AVG	0.085	0.092	-0.049	0.0474
SDV	0.018	0.031	0.006	0.0036

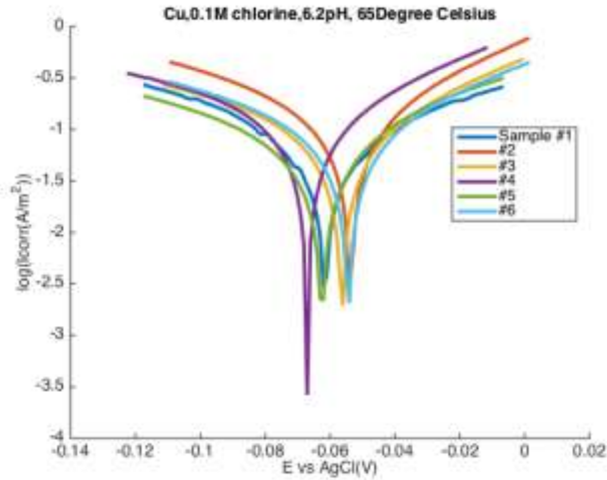

Figure 214: Electrochemical Polarization Test Results of Cu at 6.2pH, 0.1M and 65^{0}C

Table 45: Tafel Extrapolation of Cu at 6.2pH, 0.1M and 65^{0}C

	Alpha_a (V/decade)	Alpha_c (V/decade)	Ecorr (V)	Icorr (A/m2)
#1	0.101	0.110	-0.059	0.0796
#2	0.077	0.057	-0.053	0.0968
#3	0.067	0.101	-0.055	0.0783
#4	0.067	0.050	-0.066	0.0714
#5	0.092	0.108	-0.066	0.0716
#6	0.075	0.102	-0.053	0.0838
AVG	0.080	0.088	-0.059	0.0802
SDV	0.014	0.027	0.006	0.0094

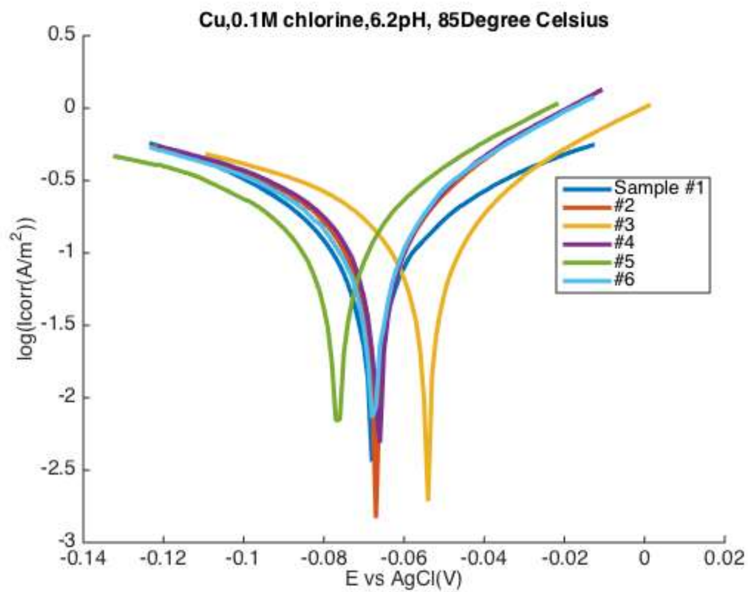

Figure 215: Electrochemical Polarization Test Results of Cu at 6.2pH, 0.1M and 65^{0}C

Table 46: Tafel Extrapolation of Cu at 6.2pH, 0.1M and 85^{0}C

	Alpha_a (V/decade)	Alpha_c (V/decade)	Ecorr (V)	Icorr (A/m2)
#1	0.096	0.104	-0.066	0.1607
#2	0.086	0.051	-0.065	0.1413
#3	0.071	0.129	-0.054	0.1802
#4	0.067	0.125	-0.066	0.2016
#5	0.060	0.093	-0.077	0.1406
#6	0.065	0.119	-0.067	0.1815
AVG	0.074	0.103	-0.066	0.1677
SDV	0.014	0.029	0.007	0.0244

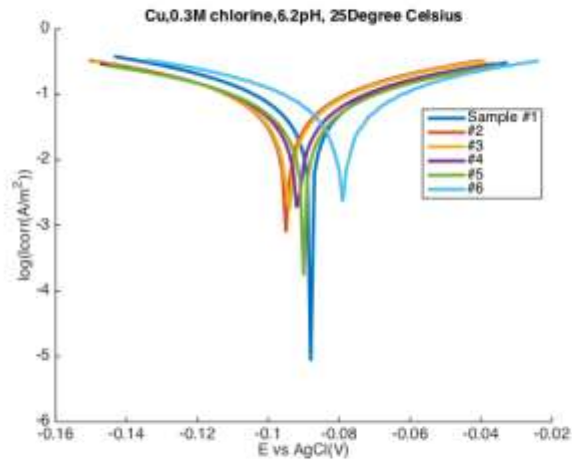

Figure 216: Electrochemical Polarization Test Results of Cu at 6.2pH, 0.1M and 85^{0}C

Table 47: Tafel Extrapolation of Cu at 6.2pH, 0.3M and 25^{0}C

	Alpha_a (V/decade)	Alpha_c (V/decade)	Ecorr (V)	Icorr (A/m2)
#1	0.108	0.092	-0.088	0.0967
#2	0.094	0.097	-0.094	0.0900
#3	0.083	0.086	-0.094	0.0777
#4	0.102	0.108	-0.090	0.0885
#5	0.103	0.105	-0.090	0.0821
#6	0.114	0.111	-0.079	0.1069
AVG	0.101	0.100	-0.089	0.0903
SDV	0.011	0.010	0.006	0.0104

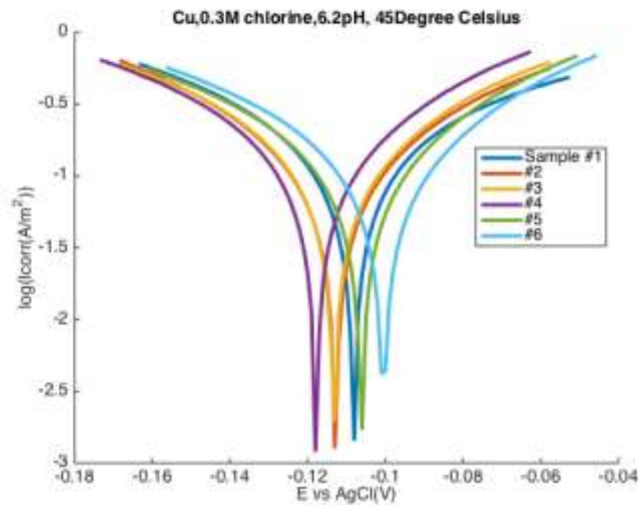

Figure 217: Electrochemical Polarization Test Results of Cu at 6.2pH, 0.3M and 45^{0}C

Table 48: Tafel Extrapolation of Cu at 6.2pH, 0.3M and 45^{0}C

	Alpha_a (V/decade)	Alpha_c (V/decade)	Ecorr (V)	Icorr (A/m2)
#1	0.102	0.089	-0.108	0.1475
#2	0.087	0.083	-0.112	0.1353
#3	0.093	0.099	-0.112	0.1629
#4	0.082	0.093	-0.117	0.1623
#5	0.080	0.093	-0.106	0.1426
#6	0.075	0.089	-0.100	0.1335
AVG	0.086	0.091	-0.109	0.1474
SDV	0.010	0.006	0.006	0.0128

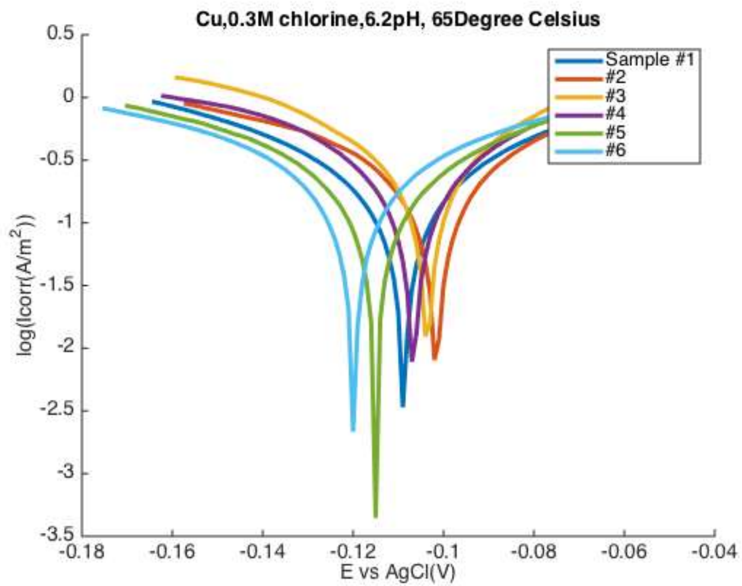

Figure 218: Electrochemical Polarization Test Results of Cu at 6.2pH, 0.3M and 65^{0}C

Table 49: Tafel Extrapolation of Cu at 6.2pH, 0.3M and 65^{0}C

	Alpha_a (V/decade)	Alpha_c (V/decade)	Ecorr (V)	Icorr (A/m2)
#1	0.094	0.099	-0.109	0.2567
#2	0.071	0.126	-0.096	0.2935
#3	0.058	0.056	-0.104	0.2573
#4	0.090	0.066	-0.103	0.2739
#5	0.085	0.120	-0.110	0.2715
#6	0.108	0.129	-0.117	0.2912
AVG	0.084	0.099	-0.106	0.2740
SDV	0.017	0.032	0.007	0.0159

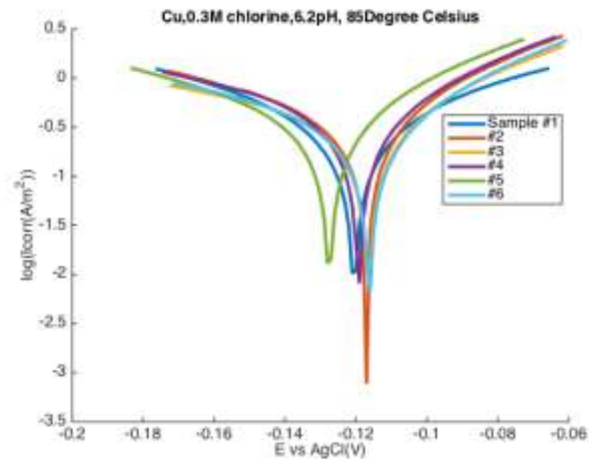

Figure 219: Electrochemical Polarization Test Results of Cu at 6.2pH, 0.3M and 85^{0}C

Table 50: Tafel Extrapolation of Cu at 6.2pH, 0.3M and 85^{0}C

	Alpha_a (V/decade)	Alpha_c (V/decade)	Ecorr (V)	Icorr (A/m2)
#1	0.099	0.100	-0.121	0.3495
#2	0.061	0.113	-0.116	0.3624
#3	0.072	0.136	-0.119	0.3393
#4	0.067	0.117	-0.120	0.3960
#5	0.069	0.097	-0.131	0.3636
#6	0.066	0.129	-0.117	0.3405
AVG	0.072	0.115	-0.121	0.3585
SDV	0.014	0.015	0.005	0.0211

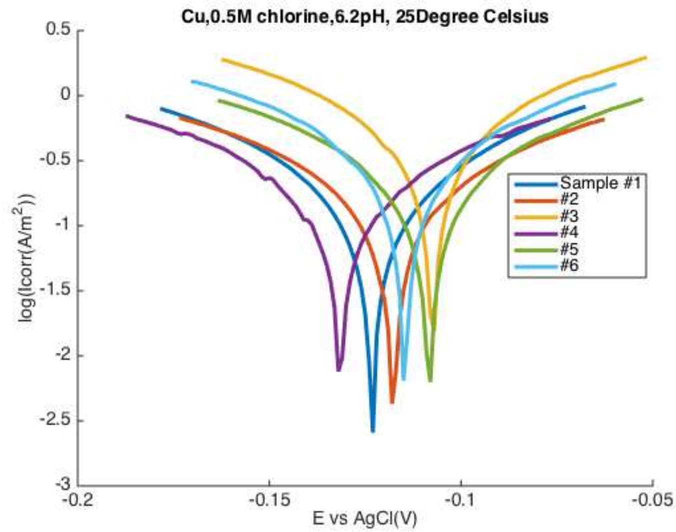

Figure 220: Electrochemical Polarization Test Results of Cu at 6.2pH, 0.5M and 25^0C

Table 51: Tafel Extrapolation of Cu at 6.2pH, 0.5M and 25^0C

	Alpha_a (V/decade)	Alpha_c (V/decade)	Ecorr (V)	Icorr (A/m2)
#1	0.087	0.095	-0.121	0.2012
#2	0.096	0.106	-0.115	0.1914
#3	0.043	0.044	-0.108	0.2350
#4	0.104	0.102	-0.131	0.2001
#5	0.068	0.081	-0.111	0.1911
#6	0.049	0.052	-0.113	0.1788
AVG	0.074	0.080	-0.117	0.1996
SDV	0.025	0.026	0.008	0.0191

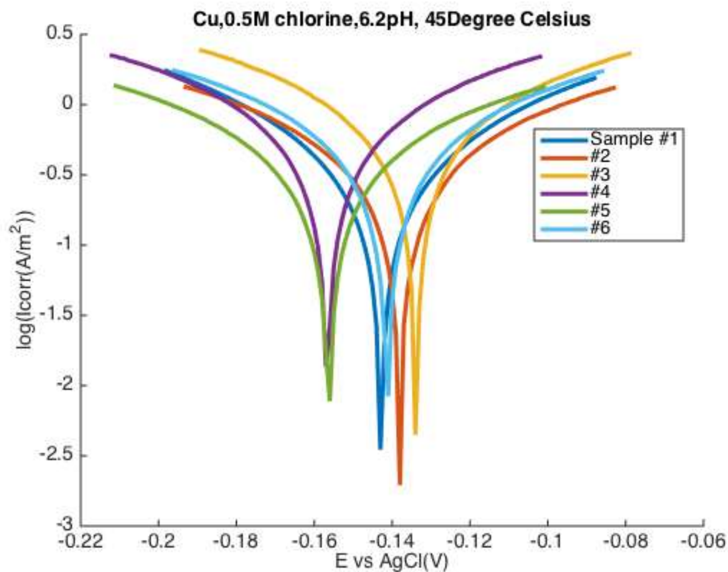

Figure 221: Electrochemical Polarization Test Results of Cu at 6.2pH, 0.5M and 45^{0}C

Table 52: Tafel Extrapolation of Cu at 6.2pH, 0.5M and 45^{0}C

	Alpha_a (V/decade)	Alpha_c (V/decade)	Ecorr (V)	Icorr (A/m2)
#1	0.092	0.086	-0.143	0.3971
#2	0.104	0.103	-0.138	0.3975
#3	0.063	0.063	-0.134	0.4318
#4	0.060	0.054	-0.155	0.3637
#5	0.095	0.091	-0.157	0.3609
#6	0.095	0.090	-0.142	0.4619
AVG	0.085	0.081	-0.145	0.4021
SDV	0.019	0.018	0.009	0.0392

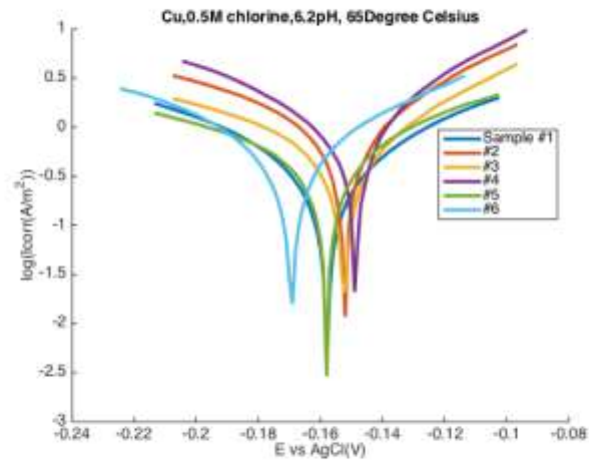

Figure 222: Electrochemical Polarization Test Results of Cu at 6.2pH, 0.5M and 65^{0}C

Table 53: Tafel Extrapolation of Cu at 6.2pH, 0.5M and 65^{0}C

	Alpha_a (V/decade)	Alpha_c (V/decade)	Ecorr (V)	Icorr (A/m2)
#1	0.087	0.098	-0.157	0.4704
#2	0.040	0.032	-0.152	0.4023
#3	0.060	0.103	-0.151	0.5680
#4	0.043	0.034	-0.150	0.5220
#5	0.082	0.109	-0.160	0.4589
#6	0.065	0.061	-0.170	0.4551
AVG	0.063	0.073	-0.156	0.4795
SDV	0.019	0.035	0.008	0.0578

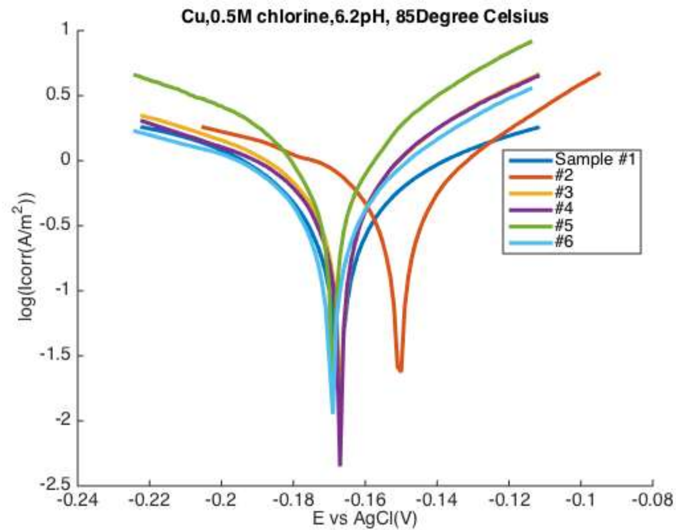

Figure 223: Electrochemical Polarization Test Results of Cu at 6.2pH, 0.5M and 65^{0}C

Table 54: Tafel Extrapolation of Cu at 6.2pH, 0.5M and 85^{0}C

	Alpha_a (V/decade)	Alpha_c (V/decade)	Ecorr (V)	Icorr (A/m2)
#1	0.117	0.139	-0.162	0.6793
#2	0.059	0.152	-0.143	0.7085
#3	0.077	0.124	-0.169	0.8368
#4	0.076	0.112	-0.172	0.7226
#5	0.051	0.038	-0.167	0.6463
#6	0.075	0.134	-0.169	0.6588
AVG	0.076	0.116	-0.164	0.7087
SDV	0.023	0.041	0.011	0.0691

Electrochemical Polarization Tests for Cu-Al IMC

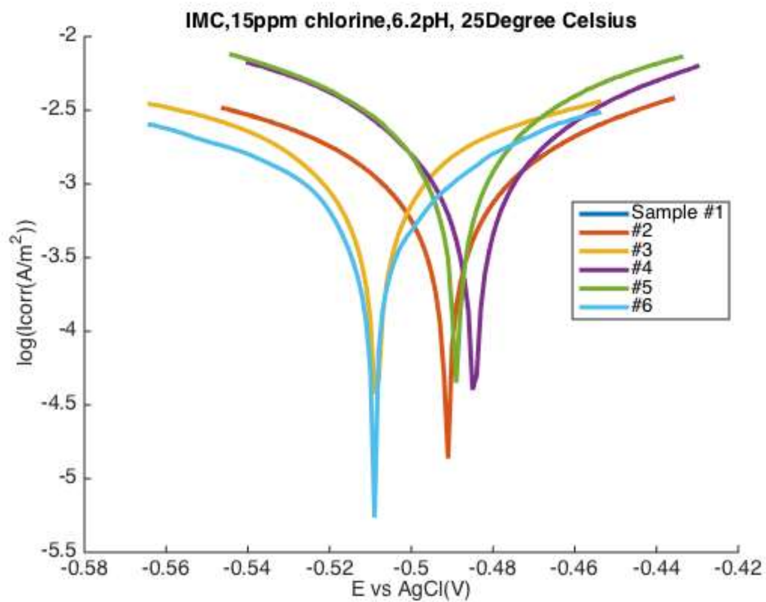

Figure 224: Electrochemical Polarization Test Results of Cu at 6.2pH, 0.5M and 85^0C

Table 55: Tafel Extrapolation of IMC at 6.2pH, 15ppm and 25^0C

	Alpha_a (V/decade)	Alpha_c (V/decade)	Ecorr (V)	Icorr (A/m2)
#1	0.101	0.113	-0.491	0.001
#2	0.090	0.095	-0.492	0.001
#3	0.118	0.116	-0.509	0.001
#4	0.096	0.100	-0.482	0.002
#5	0.102	0.099	-0.489	0.002
#6	0.073	0.091	-0.507	0.001
AVG	0.097	0.103	-0.495	0.001
SDV	0.015	0.010	0.011	0.001

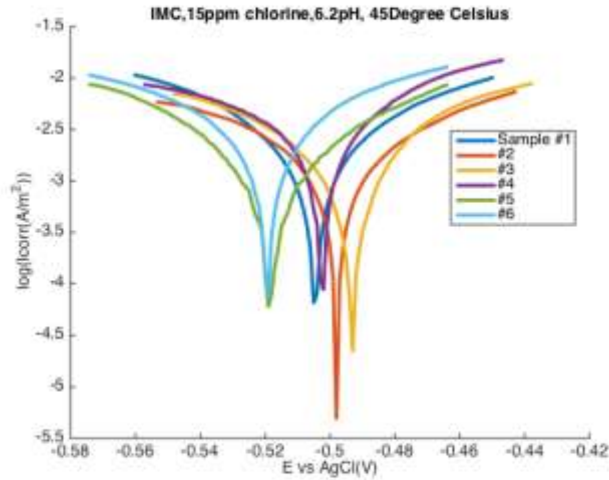

Figure 225: Electrochemical Polarization Test Results of IMC at 6.2pH, 15ppm and 45^{0}C

Table 56: Tafel Extrapolation of IMC at 6.2pH, 15ppm and 45^{0}C

	Alpha_a (V/decade)	Alpha_c (V/decade)	Ecorr (V)	Icorr (A/m2)
#1	0.077	0.071	-0.505	0.002
#2	0.056	0.058	-0.498	0.001
#3	0.128	0.121	-0.500	0.003
#4	0.065	0.050	-0.503	0.002
#5	0.071	0.092	-0.511	0.002
#6	0.110	0.111	-0.523	0.004
AVG	0.085	0.084	-0.507	0.002
SDV	0.028	0.029	0.009	0.001

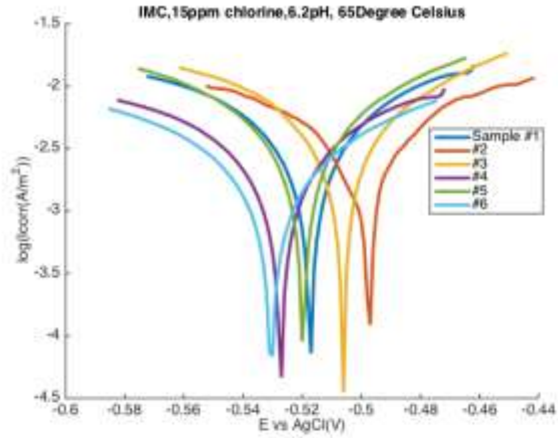

Figure 226: Electrochemical Polarization Test Results of IMC at 6.2pH, 15ppm and 65^0C

Table 57: Tafel Extrapolation of IMC at 6.2pH, 15ppm and 65^0C

	Alpha_a (V/decade)	Alpha_c (V/decade)	Ecorr (V)	Icorr (A/m2)
#1	0.084	0.081	-0.519	0.003
#2	0.133	0.105	-0.506	0.004
#3	0.086	0.119	-0.503	0.005
#4	0.091	0.089	-0.529	0.002
#5	0.070	0.074	-0.521	0.003
#6	0.094	0.108	-0.529	0.002
AVG	0.093	0.096	-0.518	0.003
SDV	0.021	0.017	0.011	0.001

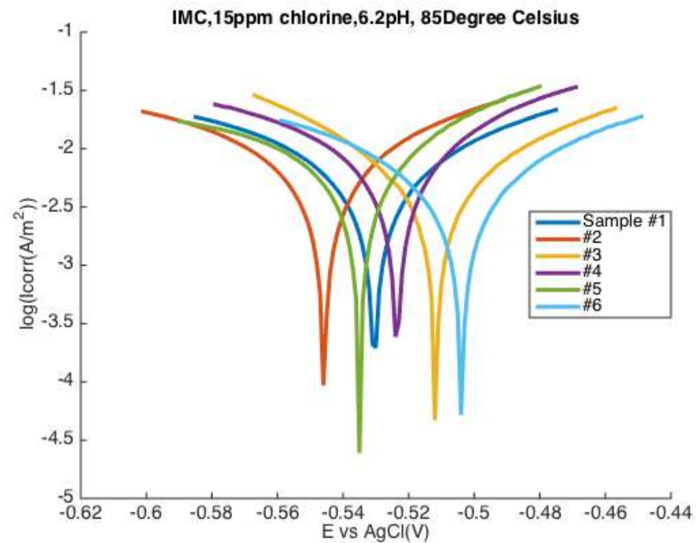

Figure 227: Electrochemical Polarization Test Results of IMC at 6.2pH, 15ppm and 85^0C

Table 58: Tafel Extrapolation of IMC at 6.2pH, 15ppm and 85^0C

	Alpha_a (V/decade)	Alpha_c (V/decade)	Ecorr (V)	Icorr (A/m2)
#1	0.100	0.121	-0.528	0.006
#2	0.091	0.113	-0.545	0.007
#3	0.093	0.082	-0.511	0.006
#4	0.095	0.114	-0.527	0.009
#5	0.101	0.179	-0.539	0.009
#6	0.077	0.081	-0.504	0.004
AVG	0.093	0.115	-0.526	0.007
SDV	0.009	0.036	0.016	0.002

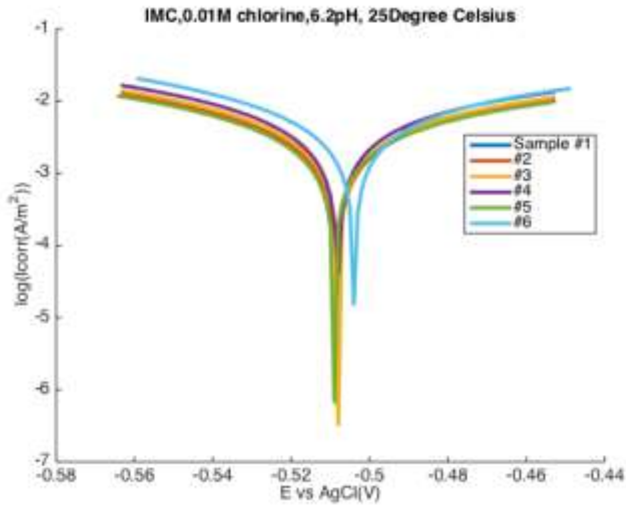

Figure 228: Electrochemical Polarization Test Results of IMC at 6.2pH, 0.01M and 25^{0}C

Table 59: Tafel Extrapolation of IMC at 6.2pH, 0.01M and 25^{0}C

	Alpha_a (V/decade)	Alpha_c (V/decade)	Ecorr (V)	Icorr (A/m2)
#1	0.109	0.094	-0.508	0.004
#2	0.115	0.096	-0.508	0.003
#3	0.079	0.070	-0.508	0.003
#4	0.109	0.093	-0.508	0.004
#5	0.070	0.078	-0.509	0.002
#6	0.112	0.088	-0.504	0.005
AVG	0.099	0.086	-0.507	0.003
SDV	0.019	0.010	0.002	0.001

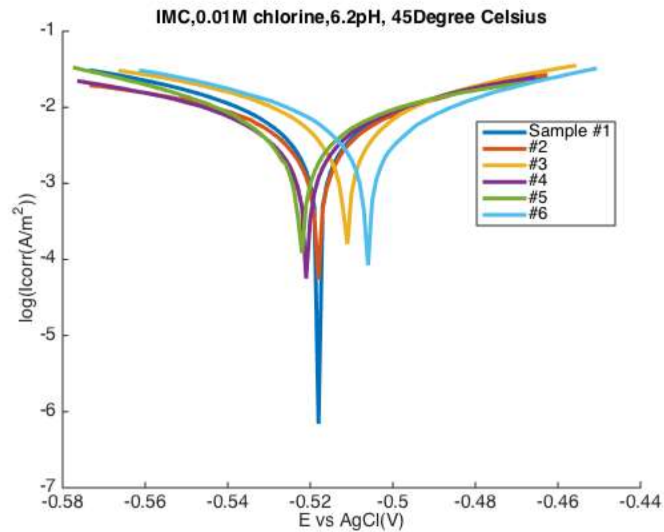

Figure 229: Electrochemical Polarization Test Results of IMC at 6.2pH, 0.01M and 45^0C

Table 60: Tafel Extrapolation of IMC at 6.2pH, 0.01M and 45^0C

	Alpha_a (V/decade)	Alpha_c (V/decade)	Ecorr (V)	Icorr (A/m2)
#1	0.109	0.093	-0.518	0.008
#2	0.100	0.126	-0.519	0.007
#3	0.061	0.059	-0.512	0.006
#4	0.089	0.096	-0.522	0.006
#5	0.113	0.077	-0.524	0.007
#6	0.085	0.094	-0.504	0.008
AVG	0.093	0.091	-0.516	0.007
SDV	0.019	0.022	0.007	0.001

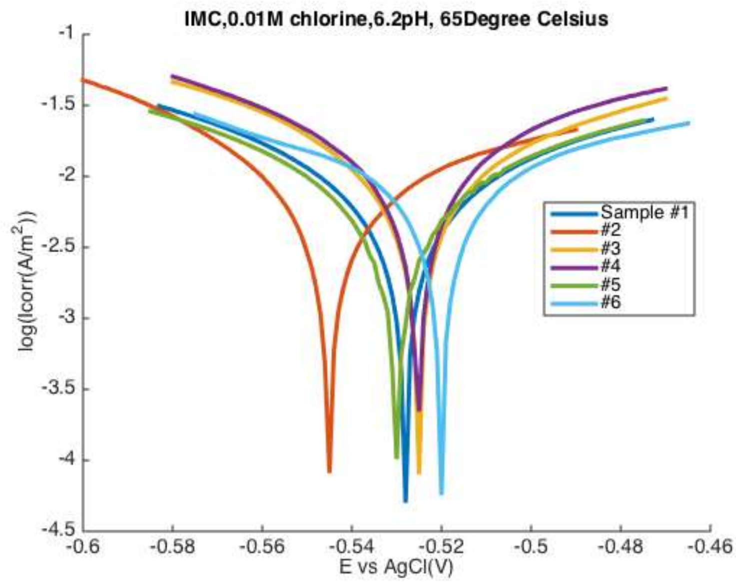

Figure 230: Electrochemical Polarization Test Results of IMC at 6.2pH, 0.01M and 65^{0}C

Table 61: Tafel Extrapolation of IMC at 6.2pH, 0.01M and 65^{0}C

	Alpha_a (V/decade)	Alpha_c (V/decade)	Ecorr (V)	Icorr (A/m2)
#1	0.122	0.100	-0.528	0.009
#2	0.060	0.093	-0.544	0.007
#3	0.075	0.089	-0.524	0.009
#4	0.066	0.077	-0.527	0.010
#5	0.116	0.106	-0.529	0.009
#6	0.155	0.087	-0.532	0.009
AVG	0.099	0.092	-0.531	0.009
SDV	0.038	0.010	0.007	0.001

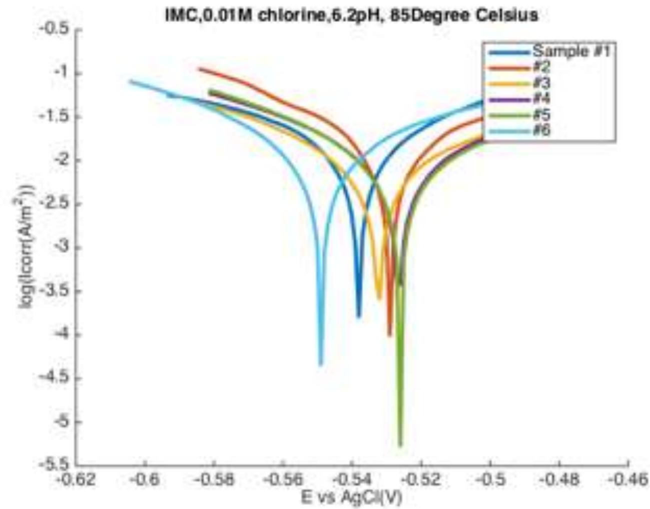

Figure 231: Electrochemical Polarization Test Results of IMC at 6.2pH, 0.01M and 85^0C

Table 62: Tafel Extrapolation of IMC at 6.2pH, 0.01M and 85^0C

	Alpha_a (V/decade)	Alpha_c (V/decade)	Ecorr (V)	Icorr (A/m2)
#1	0.057	0.069	-0.537	0.012
#2	0.076	0.050	-0.531	0.013
#3	0.139	0.094	-0.532	0.013
#4	0.097	0.070	-0.527	0.011
#5	0.119	0.073	-0.526	0.011
#6	0.112	0.080	-0.549	0.017
AVG	0.100	0.073	-0.534	0.013
SDV	0.030	0.014	0.008	0.002

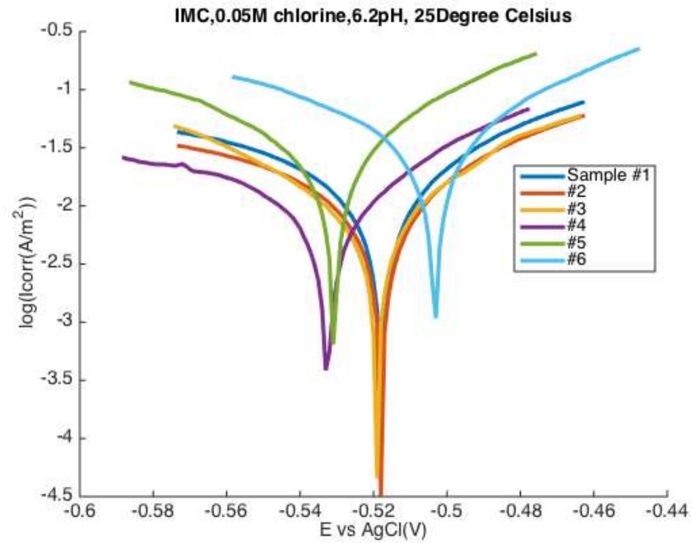

Figure 232: Electrochemical Polarization Test Results of IMC at 6.2pH, 0.05M and 25^{0}C

Table 63: Tafel Extrapolation of IMC at 6.2pH, 0.05M and 25^{0}C

	Alpha_a (V/decade)	Alpha_c (V/decade)	Ecorr (V)	Icorr (A/m2)
#1	0.086	0.139	-0.519	0.018
#2	0.100	0.070	-0.519	0.011
#3	0.095	0.077	-0.528	0.013
#4	0.069	0.167	-0.530	0.012
#5	0.038	0.034	-0.532	0.014
#6	0.040	0.039	-0.505	0.018
AVG	0.071	0.088	-0.522	0.014
SDV	0.027	0.054	0.010	0.003

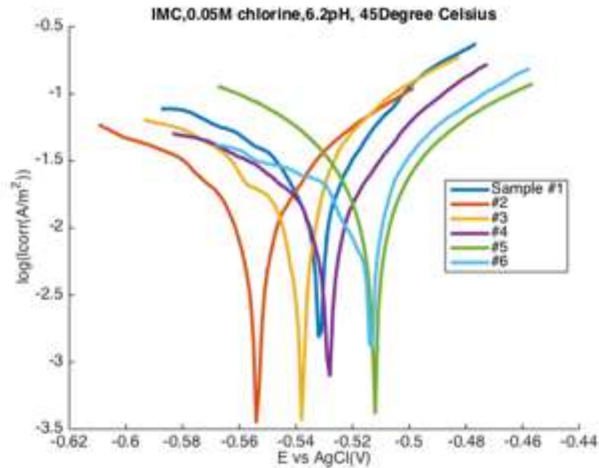

Figure 233: Electrochemical Polarization Test Results of IMC at 6.2pH, 0.05M and 45^{0}C

Table 64: Tafel Extrapolation of IMC at 6.2pH, 0.05M and 45^{0}C

	Alpha_a (V/decade)	Alpha_c (V/decade)	Ecorr (V)	Icorr (A/m2)
#1	0.041	0.080	-0.530	0.021
#2	0.073	0.154	-0.550	0.022
#3	0.081	0.109	-0.550	0.028
#4	0.045	0.087	-0.528	0.015
#5	0.068	0.068	-0.512	0.022
#6	0.083	0.123	-0.530	0.021
AVG	0.065	0.103	-0.533	0.022
SDV	0.018	0.032	0.015	0.004

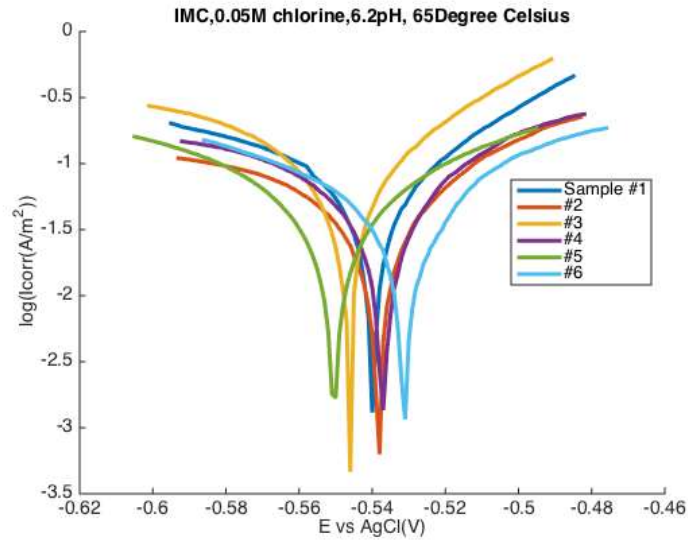

Figure 234: Electrochemical Polarization Test Results of IMC at 6.2pH, 0.05M and 65^{0}C

Table 65: Tafel Extrapolation of IMC at 6.2pH, 0.05M and 65^{0}C

	Alpha_a (V/decade)	Alpha_c (V/decade)	Ecorr (V)	Icorr (A/m2)
#1	0.058	0.107	-0.536	0.063
#2	0.076	0.126	-0.539	0.046
#3	0.056	0.047	-0.547	0.056
#4	0.136	0.219	-0.542	0.087
#5	0.094	0.108	-0.549	0.051
#6	0.134	0.111	-0.542	0.061
AVG	0.092	0.119	-0.542	0.061
SDV	0.036	0.056	0.005	0.014

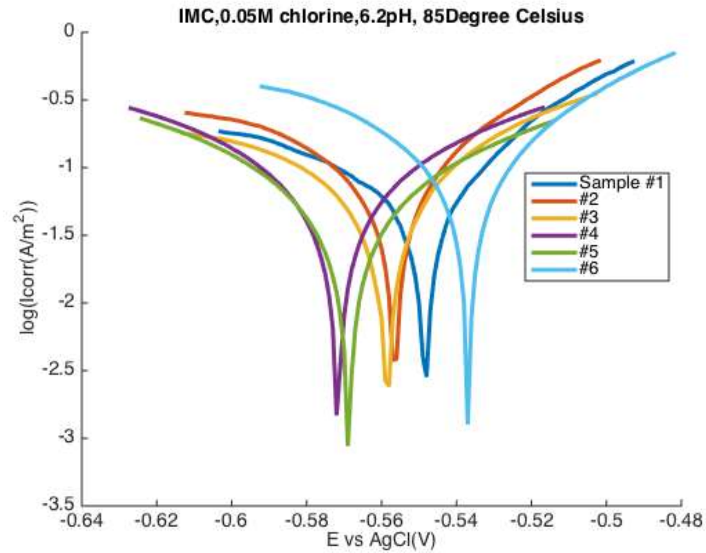

Figure 235: Electrochemical Polarization Test Results of IMC at 6.2pH, 0.05M and 85^{0}C

Table 66: Tafel Extrapolation of IMC at 6.2pH, 0.05M and 85^{0}C

	Alpha_a (V/decade)	Alpha_c (V/decade)	Ecorr (V)	Icorr (A/m2)
#1	0.068	0.138	-0.552	0.084
#2	0.073	0.057	-0.558	0.071
#3	0.092	0.154	-0.560	0.086
#4	0.099	0.111	-0.569	0.083
#5	0.092	0.098	-0.566	0.060
#6	0.072	0.122	-0.534	0.138
AVG	0.083	0.113	-0.556	0.087
SDV	0.013	0.034	0.013	0.027

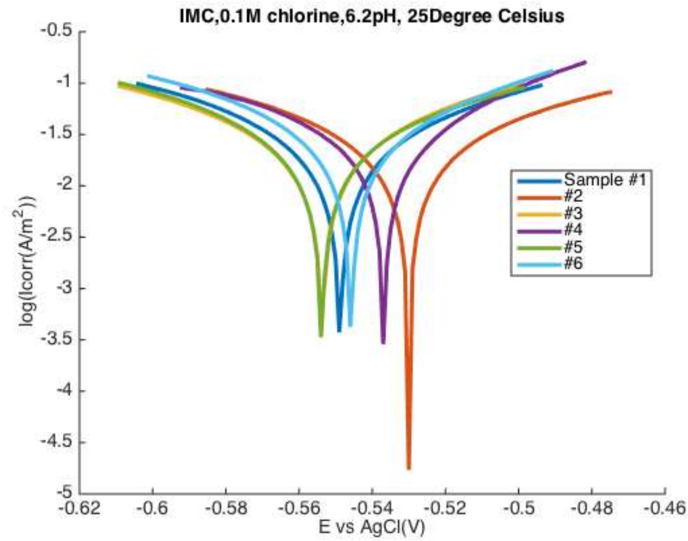

Figure 236: Electrochemical Polarization Test Results of IMC at 6.2pH, 0.1M and 25^{0}C

Table 67: Tafel Extrapolation of IMC at 6.2pH, 0.1M and 25^{0}C

	Alpha_a (V/decade)	Alpha_c (V/decade)	Ecorr (V)	Icorr (A/m2)
#1	0.092	0.098	-0.546	0.026
#2	0.089	0.083	-0.531	0.021
#3	0.087	0.095	-0.553	0.024
#4	0.064	0.094	-0.535	0.025
#5	0.104	0.102	-0.552	0.028
#6	0.081	0.099	-0.542	0.030
AVG	0.086	0.095	-0.543	0.026
SDV	0.013	0.006	0.009	0.003

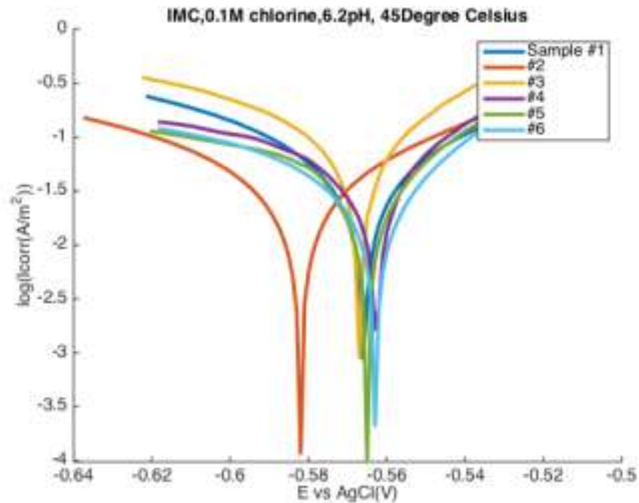

Figure 237: Electrochemical Polarization Test Results of IMC at 6.2pH, 0.1M and 45^0C

Table 68: Tafel Extrapolation of IMC at 6.2pH, 0.1M and 45^0C

	Alpha_a (V/decade)	Alpha_c (V/decade)	Ecorr (V)	Icorr (A/m2)
#1	0.063	0.062	-0.566	0.041
#2	0.066	0.093	-0.578	0.036
#3	0.047	0.037	-0.567	0.053
#4	0.053	0.159	-0.560	0.060
#5	0.058	0.164	-0.563	0.051
#6	0.040	0.079	-0.561	0.028
AVG	0.055	0.099	-0.566	0.045
SDV	0.010	0.052	0.007	0.012

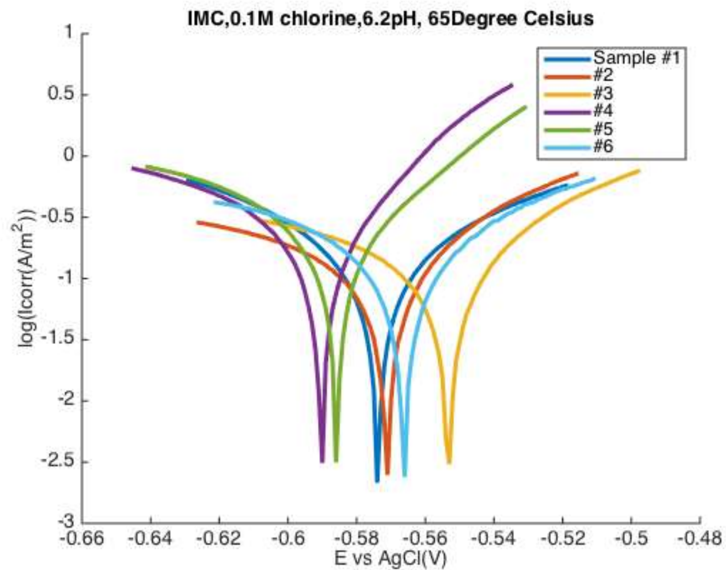

Figure 238: Electrochemical Polarization Test Results of IMC at 6.2pH, 0.1M and 65^{0}C

Table 69: Tafel Extrapolation of IMC at 6.2pH, 0.1M and 65^{0}C

	Alpha_a (V/decade)	Alpha_c (V/decade)	Ecorr (V)	Icorr (A/m2)
#1	0.094	0.089	-0.573	0.157
#2	0.085	0.162	-0.576	0.143
#3	0.088	0.163	-0.559	0.151
#4	0.082	0.034	-0.586	0.183
#5	0.042	0.088	-0.580	0.194
#6	0.085	0.132	-0.564	0.163
AVG	0.079	0.112	-0.573	0.165
SDV	0.019	0.050	0.010	0.020

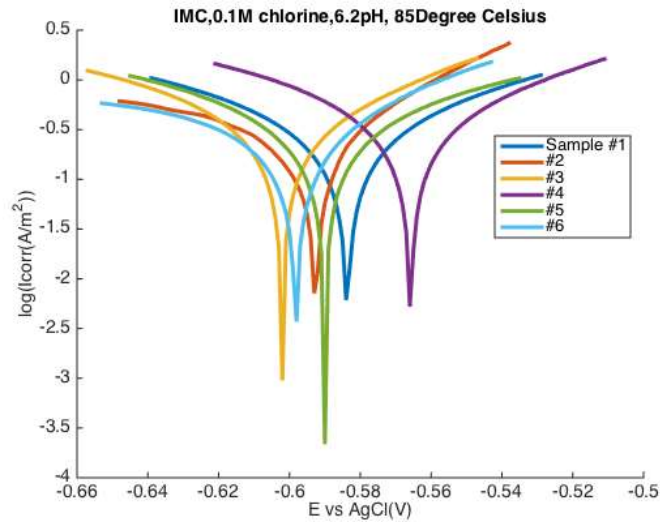

Figure 239: Electrochemical Polarization Test Results of IMC at 6.2pH, 0.1M and 85^{0}C

Table 70: Tafel Extrapolation of IMC at 6.2pH, 0.1M and 85^{0}C

	Alpha_a (V/decade)	Alpha_c (V/decade)	Ecorr (V)	Icorr (A/m2)
#1	0.087	0.095	-0.583	0.272
#2	0.054	0.149	-0.591	0.260
#3	0.067	0.092	-0.598	0.298
#4	0.058	0.056	-0.565	0.226
#5	0.102	0.097	-0.590	0.306
#6	0.070	0.159	-0.597	0.268
AVG	0.073	0.108	-0.587	0.272
SDV	0.018	0.039	0.012	0.029

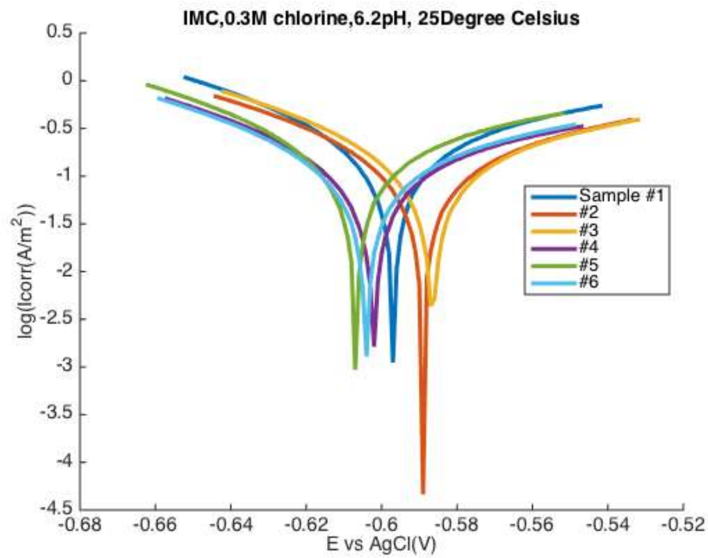

Figure 240: Electrochemical Polarization Test Results of IMC at 6.2pH, 0.3M and 25^{0}C

Table 71: Tafel Extrapolation of IMC at 6.2pH, 0.3M and 25^{0}C

	Alpha_a (V/decade)	Alpha_c (V/decade)	Ecorr (V)	Icorr (A/m2)
#1	0.060	0.088	-0.597	0.147
#2	0.113	0.078	-0.588	0.131
#3	0.115	0.075	-0.585	0.137
#4	0.116	0.072	-0.602	0.114
#5	0.101	0.066	-0.607	0.139
#6	0.101	0.069	-0.603	0.105
AVG	0.101	0.075	-0.597	0.129
SDV	0.021	0.008	0.009	0.016

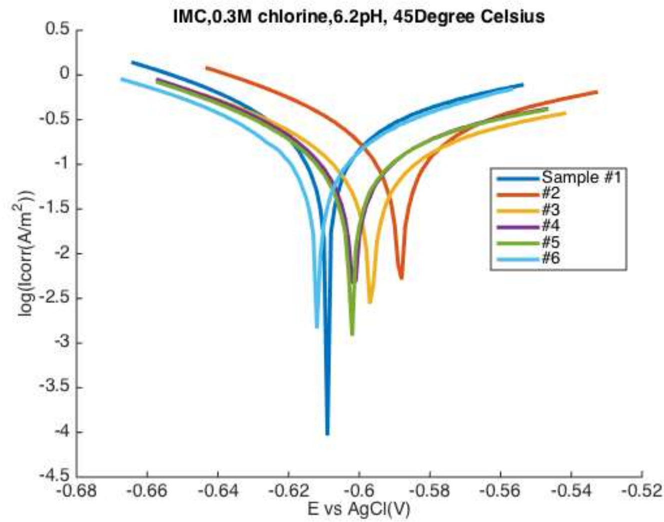

Figure 241: Electrochemical Polarization Test Results of IMC at 6.2pH, 0.3M and 45^{0}C

Table 72: Tafel Extrapolation of IMC at 6.2pH, 0.3M and 45^{0}C

	Alpha_a (V/decade)	Alpha_c (V/decade)	Ecorr (V)	Icorr (A/m2)
#1	0.060	0.088	-0.597	0.147
#2	0.113	0.078	-0.588	0.131
#3	0.115	0.075	-0.585	0.137
#4	0.116	0.072	-0.602	0.114
#5	0.101	0.066	-0.607	0.139
#6	0.101	0.069	-0.603	0.105
AVG	0.101	0.075	-0.597	0.129
SDV	0.021	0.008	0.009	0.016

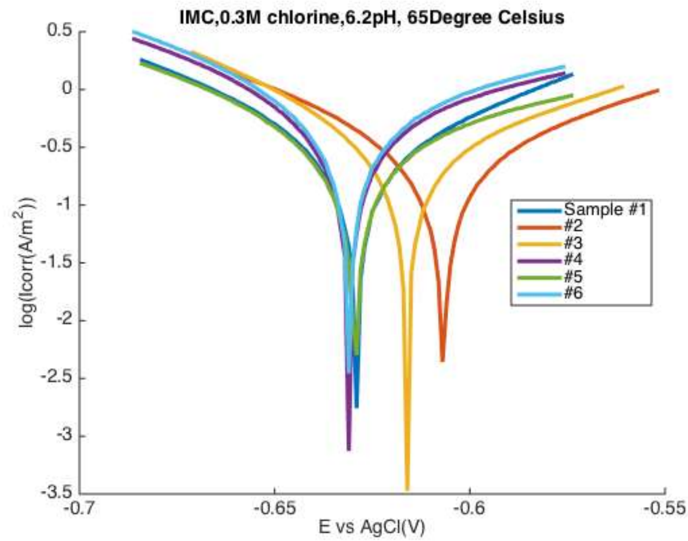

Figure 242: Electrochemical Polarization Test Results of IMC at 6.2pH, 0.3M and 65^0C

Table 73: Tafel Extrapolation of IMC at 6.2pH, 0.3M and 65^0C

	Alpha_a (V/decade)	Alpha_c (V/decade)	Ecorr (V)	Icorr (A/m2)
#1	0.075	0.075	-0.624	0.287
#2	0.093	0.079	-0.604	0.267
#3	0.057	0.080	-0.615	0.235
#4	0.050	0.069	-0.631	0.304
#5	0.103	0.068	-0.629	0.272
#6	0.048	0.062	-0.630	0.318
AVG	0.071	0.072	-0.622	0.281
SDV	0.023	0.007	0.011	0.029

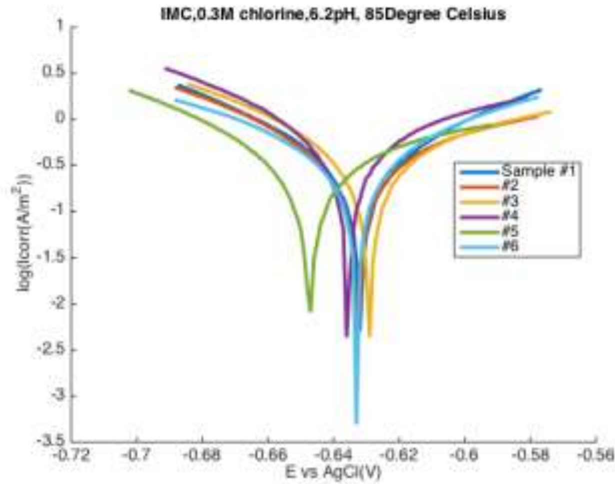

Figure 243: Electrochemical Polarization Test Results of IMC at 6.2pH, 0.3M and 85^{0}C

Table 74: Tafel Extrapolation of IMC at 6.2pH, 0.3M and 85^{0}C

	Alpha_a (V/decade)	Alpha_c (V/decade)	Ecorr (V)	Icorr (A/m2)
#1	0.070	0.068	-0.631	0.355
#2	0.131	0.079	-0.631	0.419
#3	0.107	0.066	-0.629	0.381
#4	0.052	0.069	-0.635	0.388
#5	0.138	0.071	-0.647	0.350
#6	0.092	0.095	-0.634	0.434
AVG	0.098	0.075	-0.635	0.388
SDV	0.034	0.011	0.007	0.034

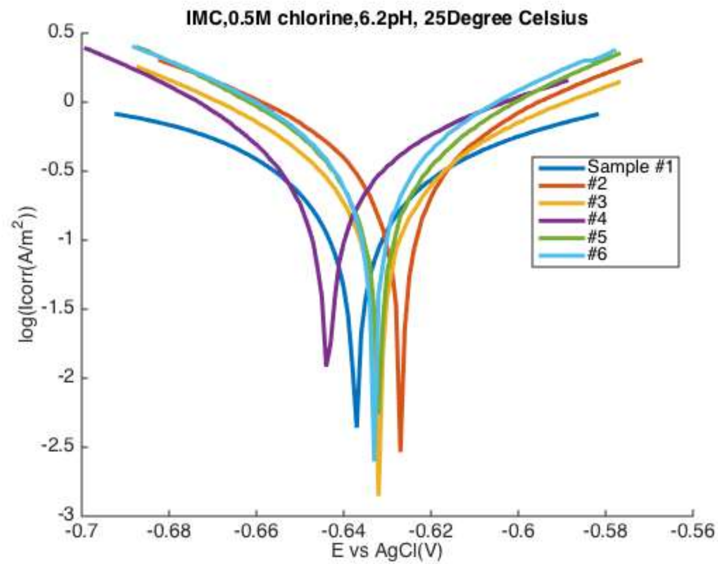

Figure 244: Electrochemical Polarization Test Results of IMC at 6.2pH, 0.5M and 25^0C

Table 75: Tafel Extrapolation of IMC at 6.2pH, 0.5M and 25^0C

	Alpha_a (V/decade)	Alpha_c (V/decade)	Ecorr (V)	Icorr (A/m2)
#1	0.114	0.135	-0.632	0.301
#2	0.077	0.079	-0.626	0.403
#3	0.082	0.075	-0.630	0.314
#4	0.050	0.059	-0.642	0.240
#5	0.053	0.049	-0.630	0.254
#6	0.055	0.055	-0.632	0.314
AVG	0.072	0.075	-0.632	0.305
SDV	0.025	0.031	0.005	0.058

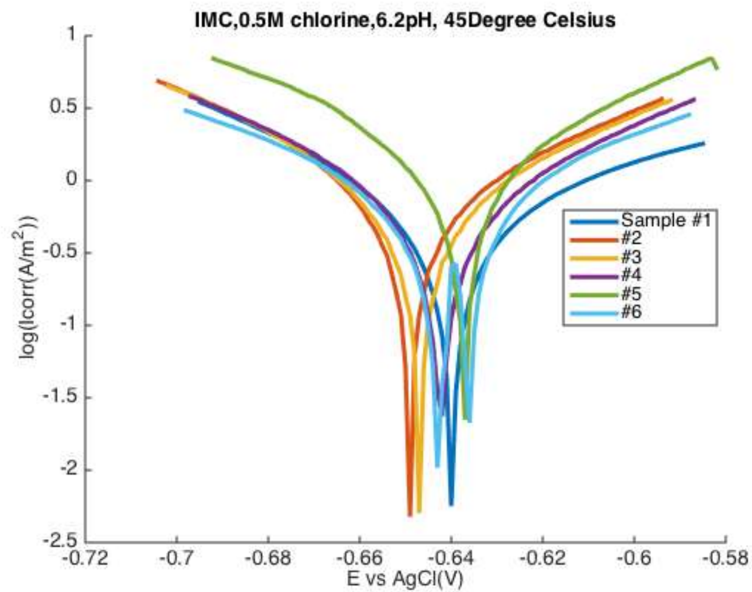

Figure 245: Electrochemical Polarization Test Results of IMC at 6.2pH, 0.5M and 45^{0}C

Table 76: Tafel Extrapolation of IMC at 6.2pH, 0.5M and 45^{0}C

	Alpha_a (V/decade)	Alpha_c (V/decade)	Ecorr (V)	Icorr (A/m2)
#1	0.111	0.070	-0.641	0.579
#2	0.072	0.068	-0.646	0.698
#3	0.073	0.074	-0.643	0.724
#4	0.065	0.063	-0.642	0.552
#5	0.037	0.040	-0.638	0.607
#6	0.087	0.091	-0.641	0.708
AVG	0.074	0.068	-0.642	0.645
SDV	0.024	0.016	0.003	0.074

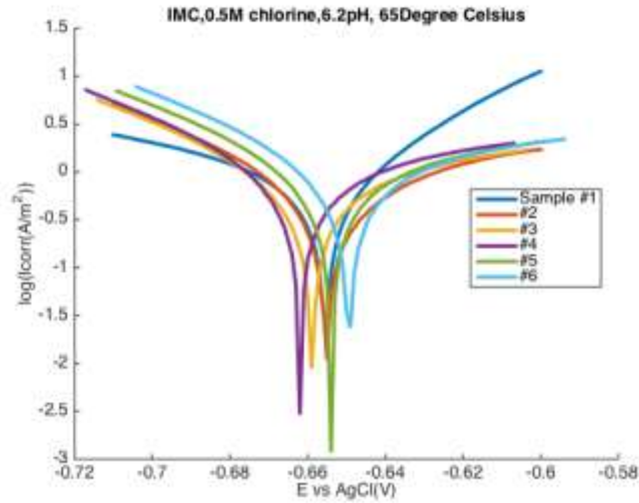

Figure 246: Electrochemical Polarization Test Results of IMC at 6.2pH, 0.5M and 65^0C

Table 77: Tafel Extrapolation of IMC at 6.2pH, 0.5M and 65^0C

	Alpha_a (V/decade)	Alpha_c (V/decade)	Ecorr (V)	Icorr (A/m2)
#1	0.047	0.111	-0.655	0.794
#2	0.112	0.059	-0.655	0.602
#3	0.162	0.062	-0.660	0.768
#4	0.172	0.060	-0.664	0.934
#5	0.141	0.061	-0.654	0.867
#6	0.053	0.115	-0.650	0.796
AVG	0.115	0.078	-0.656	0.793
SDV	0.054	0.027	0.005	0.112

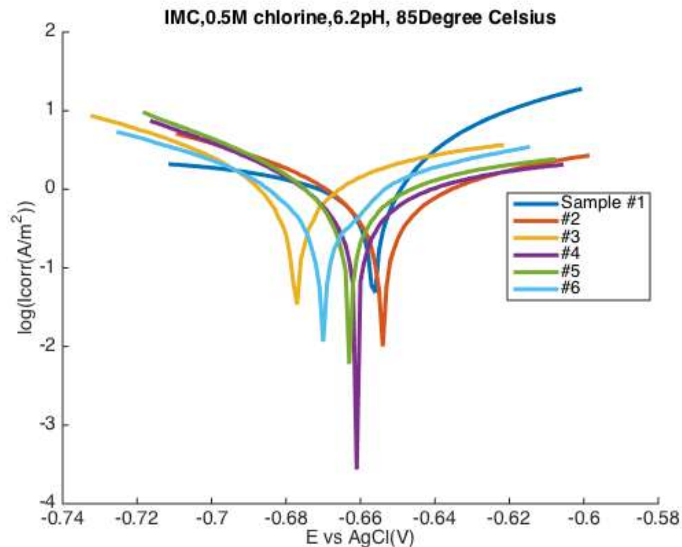

Figure 247: Electrochemical Polarization Test Results of IMC at 6.2pH, 0.5M and 85^0C

Table 78: Tafel Extrapolation of IMC at 6.2pH, 0.5M and 85^0C

	Alpha_a (V/decade)	Alpha_c (V/decade)	Ecorr (V)	Icorr (A/m2)
#1	0.099	0.042	-0.665	0.931
#2	0.108	0.071	-0.653	0.863
#3	0.047	0.066	-0.677	0.827
#4	0.132	0.057	-0.662	0.818
#5	0.159	0.057	-0.665	1.074
#6	0.105	0.070	-0.673	0.976
AVG	0.108	0.061	-0.666	0.915
SDV	0.037	0.011	0.008	0.099

Regression models are construct to help predict and extrapolate Alpha, Beta, OCP and Icorr for both Cu-Al IMC and Cu under various temperature and chlorine concentration inputs. As it can be seen from those plots, both Alpha and Beta value of Cu-Al IMC and Cu are nearly independent of temperature and chlorine concentration variation. For OCP of both metal, it decreases as chlorine concentration increases or as temperature increases. For Icorr, it increases as chlorine

concentration increases or as temperature increases. Regression models are then used in Cu wire bond corrosion simulation to predict Tafel parameter of both metals at each time step.

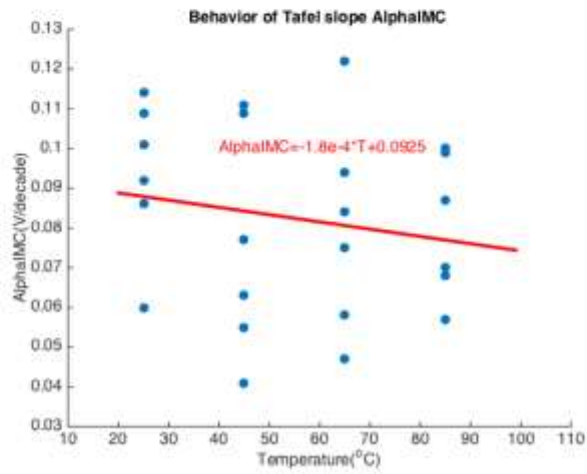

Figure 248: Cu-Al IMC Alpha as a Function of Temperature

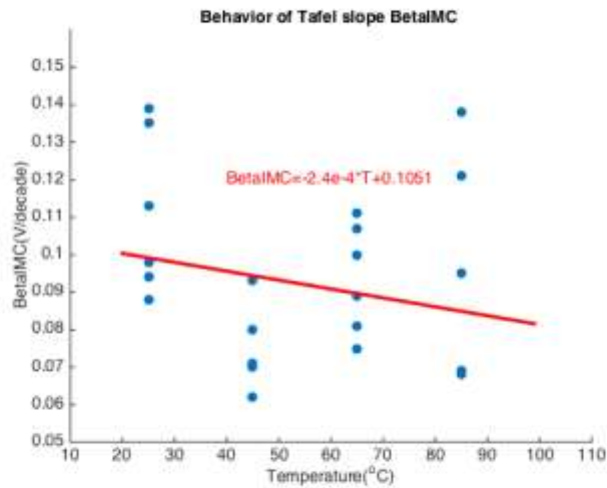

Figure 249: Cu-Al IMC Beta as a Function of Temperature

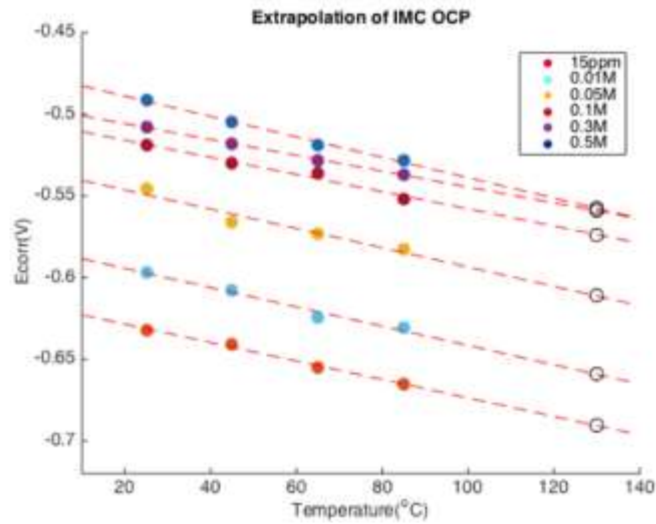

Figure 250: Cu-Al IMC OCP as a Function of Temperature

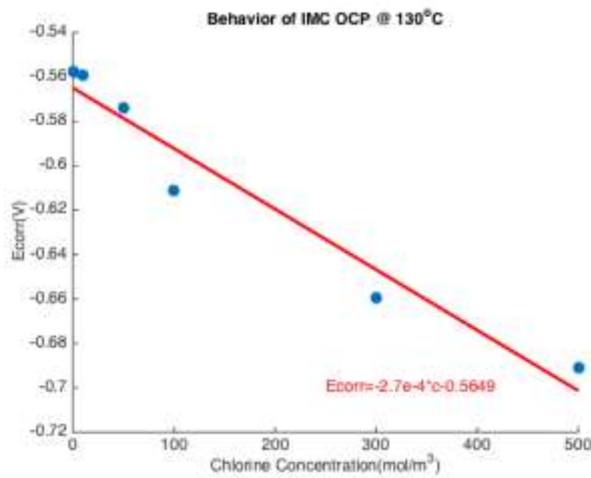

Figure 251: Cu-Al IMC OCP as a Function of Concentration

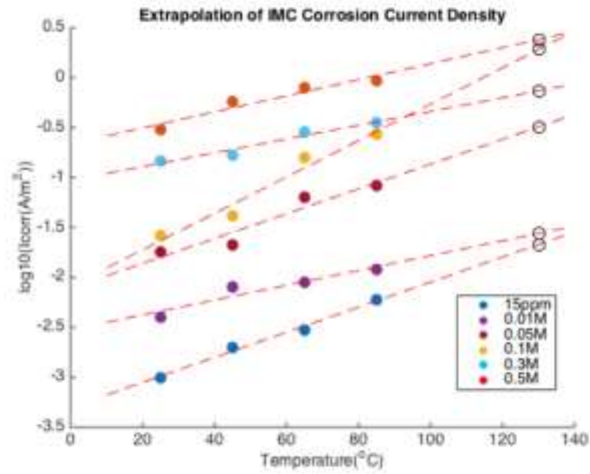

Figure 252: Cu-Al IMC Icorr as a Function of Temperature

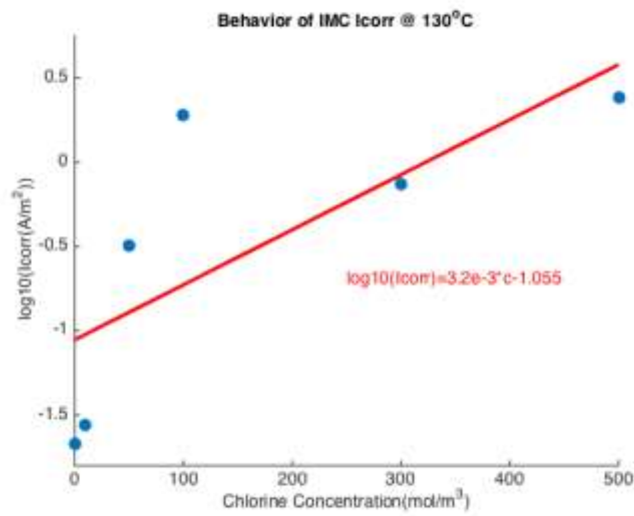

Figure 253: Cu-Al IMC Icorr as a Function of Concentration

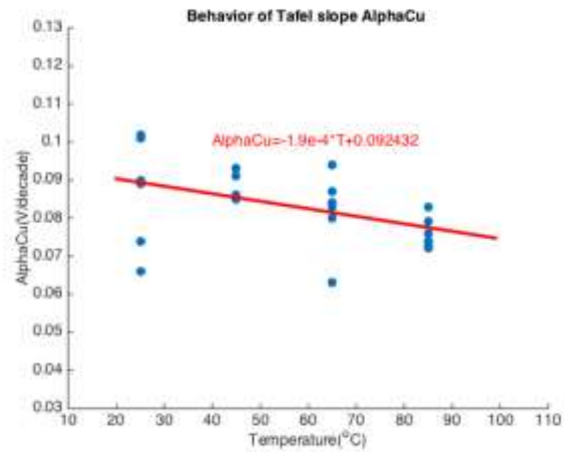

Figure 254: Cu Alpha as a Function of Temperature

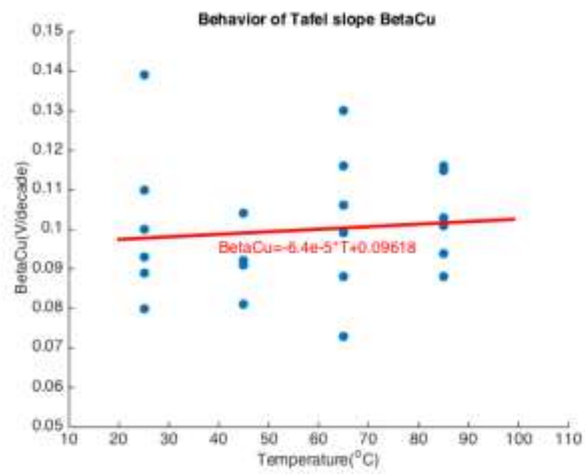

Figure 255: Cu Beta as a Function of Temperature

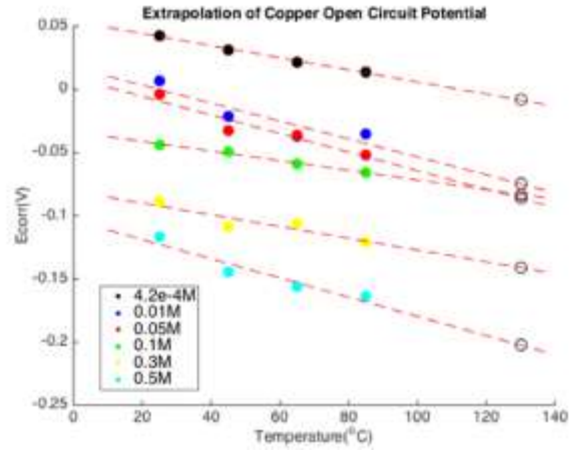

Figure 256: Cu OCP as a Function of Temperature

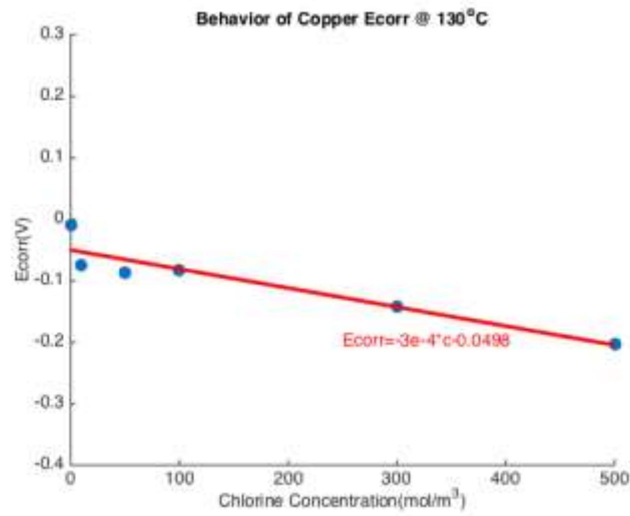

Figure 257: Cu OCP as a Function of Concentration

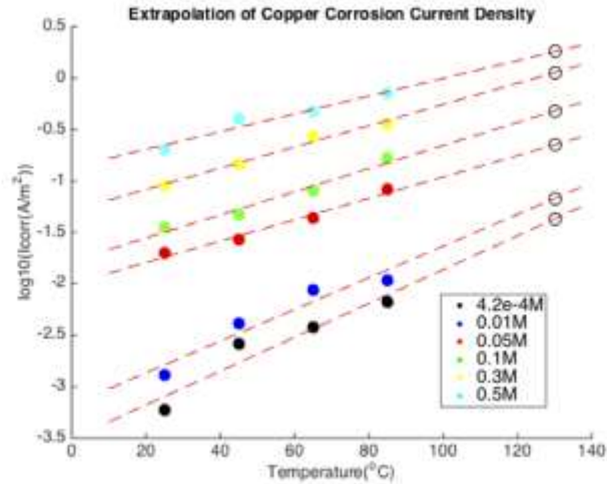

Figure 258: Cu Icorr as a Function of Temperature

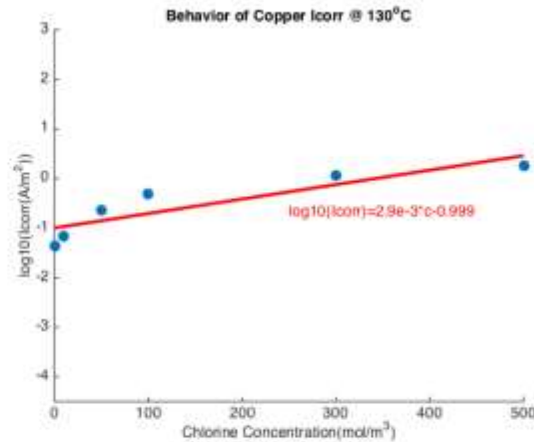

Figure 259: Cu Icorr as a Function of Concentration

9.5 Corrosion Simulation

A Cu wire bond corrosion simulation under biased HAST (1300C/100RH/1V) is performed. Regression data analysis is used to construct regression model of chlorine diffusivity, mobility and release rate under different testing temperatures as shown in Figure 260, Figure 261 and Figure

262, respectively. At each time step, the model inputs are shown in Table 79. Figure 263 gives 4 snapshots of corrosion simulation at different time steps. As it can be seen from the plot, simulation starts with no crack at Cu-Al IMC layer. As time proceeds, crack is visible after one hour of aging at 1300C/100RH/1V condition. After that, crack keeps growing from the edge of wire bond toward the center of the wire bond. At 240-hour time step, the length of the crack becomes 4.5 microns. Figure 264 shows the growth of crack length as a function of aging duration. Using this plot, one can predict the remaining useful life of a Cu wire bond interconnect used under 1300C/100RH/1V test condition and estimate the reliability performance of Cu wire bond without actually performing time-to-failure reliability tests on multiple electronic packages with Cu wire bond used as first level interconnect.

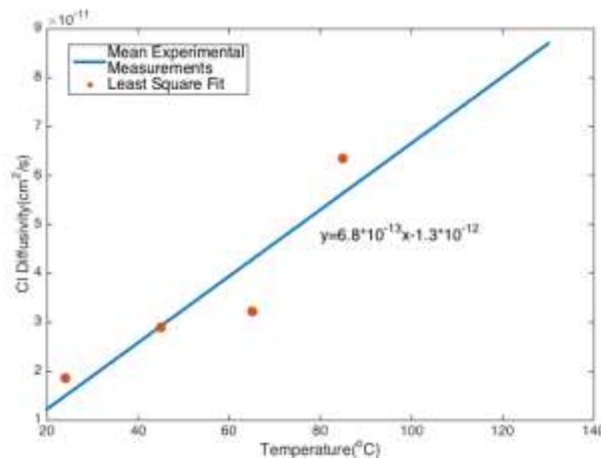

Figure 260: Cl Diffusivity as a Function of Temperature

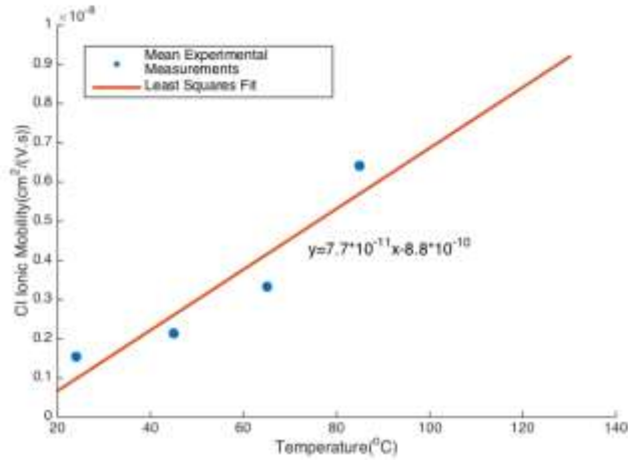

Figure 261: Cl Ionic Mobility as a Function of Temperature

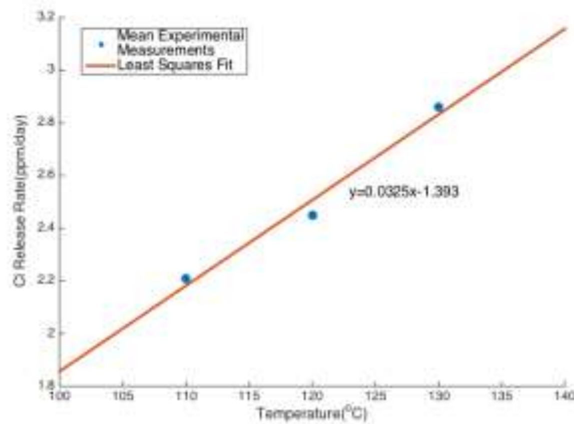

Figure 262: Cl Release Rate as a Function of Temperature

Table 79: Simulation Inputs

Diffusivity of Cl (cm2/s)	Temp. dependent
Mobility of Cl cm2/(V.s)	Temp. dependent
Cl release rate (ppm/day)	Temp. dependent
Cu OCP (vs Ag/AgCl)	Temp. & Cl level dependent
Cu-Al OCP (vs Ag/AgCl)	Temp. & Cl level dependent
Cu Icorr (A/cm2)	Temp. & Cl level dependent
Cu-Al Icorr (A/cm2)	Temp. & Cl level dependent

Cu Alpha	Temp. dependent
Cu-Al Alpha	Temp. dependent
Cu Beta	Temp. dependent
Cu-Al Beta	Temp. dependent
Wire bond radius (micron)	35
IMC thickness (micron)	0.2
Voltage bias (V)	1.0

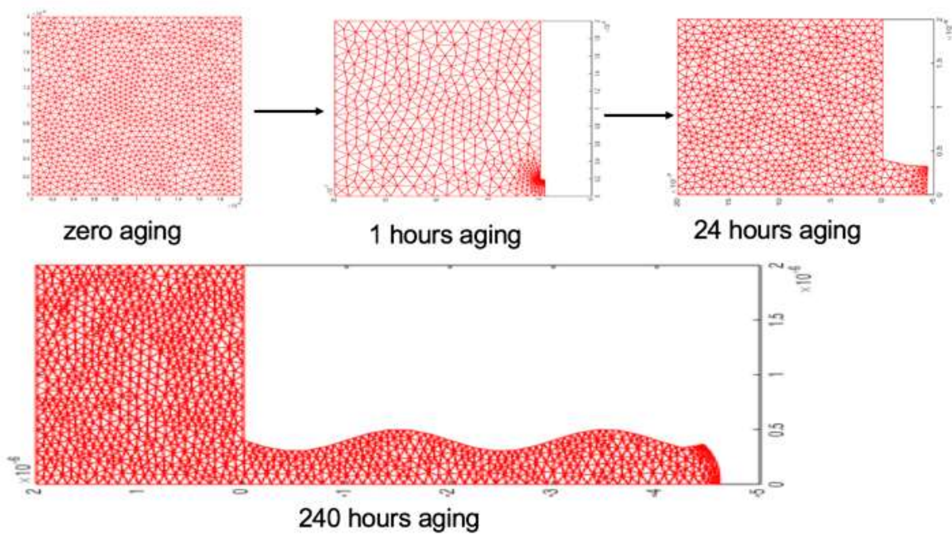

Figure 263: Crack Initiation and Crack Propagation

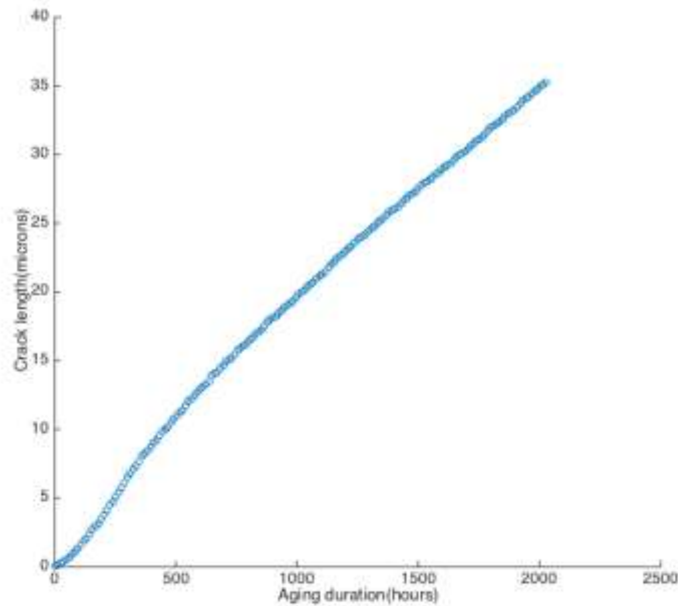

Figure 264: Cu-Al IMC Crack Length vs Aging Duration at 1300C/100RH/1V Simulation Conditions

Chapter 10 Summary and Conclusions

Since the year 2008, Cu wire bond has been used increasingly in the electronic packaging industry. corrosion-related Cu wire bond failure is one of the major concerns that prevent the mass production of copper wire bond. Studies and researches that have been done in this dissertation helps with the fundamental understanding of wire bond failure mechanisms and modes under different types of accelerated harsh environmental conditions. Methodologies and techniques

developed in this Ph.D. work provide detailed and thorough tools that could be used to assess the damage progression of Cu-Al wire bond and predict the failure of Cu-Al wire bond in advance so that proper maintenance work can be done before catastrophic failure of microelectronics occurs. Several finite element-based predictive multiphysics corrosion frameworks are introduced to help provide more insight into the Cu-Al wire bond corrosion problems and at the same time offer RUL estimations based on the inputs obtained from the operational environment, the Cu-Al wire bond and the epoxy molding compound.

Reference

Alonso L., Levy B., “Computing 2D periodic Centroidal Voronoi tessellation”, 8th ISVD, 2011

An T., Qin F., “Intergranular cracking simulation of the intermetallic compound layer in solder joints”, Computational Materials Science 79(2013) pp.1-14

Application Note CORR-4, “Electrochemistry an corrosion: overview and techniques”, Princeton Applied Research 2010

ASTM Standard G102-89, Annual Book of ASTM Standards, 2014 ASTM International, Philadelphia

Bard A., “Electrochemical methods: fundamentals and applications” 2nd Edition, 2001, John Wiley Sons, Inc.

Barrie A., “In diffusion in polymers”, London, 1968

Bazant Z., Ajdari A., Phys. Rev. E75 (2007) 021502

Belton D. J., “Moisture sorption and its effect upon the microstructure of epoxy molding compounds,” in Proc. IEEE/CHMT Int. Electron. Manufact. Technol. Symp., 1987, pp 158–169

Benedeitit A., Sumodjo P., “Electrochemical Studies of Copper, Copper Aluminum and Copper Aluminum Silver Alloys: Impedance in 0.5M NaCl”, Electrochemical Acta. Vol. 40, 1995 pp. 2657-2668

Bogatin E., Potter D., “Roadmaps of packaging technology”, Chapter 9, 1997

Boettcher T., Rother M., “On the intermetallic corrosion of Cu-Al wire bonds”, 2010 12th EPTC pp.585-590

Chiu Y., “The corrosion performance of Cu alloy wire bond on Al pad in molding compound of various chlorine contents under biased-HAST”, ECTC 2014 pp.419-426

Crank J., Park G., “Diffusion in Polymers. London”, UK: Academic,1968

Deshpande K., “Effect of aluminum spacer on galvanic corrosion between magnesium and mild steel using numerical model and SVET experiments”, Corrosion Science 62 (2012), pp. 184-191

Doig P., Flewitt P., “A finite difference numerical analysis of galvanic corrosion for semi-infinite linear coplanar electrode”, J. Electrochem. Soc, 1979, pp. 2057-2063

Drozodov M., G. Gur, “Detailed investigation of ultrasonic Al-Cu wire-bonds I”, J Mater Sci (2008), pp. 6029-6037

Drozodov M., W. Kaplan, “Detailed investigation of ultrasonic Al-Cu wire-bonds II”, J Mater Sci (2009), pp. 6038-6048

Enos D., “The potentiodynamic polarization scan technical report 33”, 1997, Issue 2.0 pp. 5-15

Faber V., Gunzburger M., “Centroidal Voronoi Tessellations: Applications and Algorithms”, Society for Industrial and Applied Mathematics, 1999, pp.637-676

Foaud N., Ali A., “Inhibition of aluminum corrosion in hydrochloric acid solution using black mulberry extract”, J. Mater. Environ. Sci. 2012, pp.917-924

Grams A., Prewitz T., “Simulation of an aluminum thick wire bond fatigue crack by means of the cohesive zone method”, EuroSimE 2013 pp.1736-1744

Ghosh S., Liu Y., “Voronoi cell finite element model based on micro-polar theory of thermoelasticity for heterogeneous materials”, International Journal for Numerical Methods in Engineering, 1995, pp.1361-1398

Ghosh S., Moorthy S., “Three dimensional Voronoi cell finite element model for microstructures with ellipsoidal heterogeneities”, Computational Mechanics 34(2004), pp.510-531

Ginsberg G., “Surface mount and related technologies”, Volume 57, 1989

Halloran G., “Planar analysis of Cu-Al Intermetallics”, ISTFA, San Jose 2013, pp.297-300

Hamann C., Hamnett A., Wolf Vielstich, “Electrochemistry”, 2nd Edition, 2007, Wiley-VCH

Hang C., Wang Q., Mayer M., “Growth behavior of Cu/Al intermetallic compounds and cracks in copper ball bonds during isothermal aging”, Microelectronics Reliability (48) 2008, pp. 416-424

Hassan R., Zaafarany I., “Kinetic of corrosion inhibition of aluminum in acidic media by water-soluble natural polymeric pectates as anionic polyelectrolyte inhibitors”, Materials 2013, pp.2436-2451

Jung J., Zhou H., “Bonding mechanism in ultrasonic gold ball bonds on copper substrates. Adhesive Science Technology, 2003, pp.435-451

Kelly R., “Electrochemical techniques in corrosion science and engineering”, 2002, Marcel Dekker, Inc.

Kim H., Lee J., “Effect of Cu/Al IMC on copper wire and aluminum pad bondability”, TCPT, 2003, pp.367-374

Kouters M., Gubbels G., “Characterization of intermetallic compounds in Cu-Al ball bonds”, EuroSimE 2012, pp.978-986

Lall P., Deshpande S., “Fuming acid based decapsulation process for Cu-Al wire bond system molded with different EMCs”, 2015 ASME pp. 1-15

Lall P., Deshpande S., “Prognostication of Cu-Al wire bond reliability under high temperature storage and temperature-humidity”, 2014, ECTC pp.1973-1985

Lall P., Luo Y., “Degradation mechanisms in electronic mold compounds subjected to high temperature in neighborhood of 200°C, ECTC 2014, pp. 242-254

Lall P., Luo Y., "Multiphysics modeling of corrosion in Cu-Al wire bond interconnects in high humidity environments", ECTC 2015, pp. 1045-1056

Lall P., Luo Y., "Multiphysics life-prediction model based on measurement of polarization curves for Cu-Al Intermetallics", ECTC 2016, pp. 1027-1037

Lall P. Luo Y., "resistance spectroscopy based Assessment of Degradation in Cu-Al wire bond interconnects" ASME 2013 International Technical conference pp. V001T05A017

Lantz L., Pecht M., "Ion Transport in Encapsulants Used in Microcircuit Packaging" IEEE transactions on components and packaging technologies, Vol. 26, No.1, March 2003 p199-205

Lantz L., Pecht M., "Ion transport in encapsulants used in microcircuit packaging", 2003 TCPT pp.199-205

Lantz L., Pecht M., "The measurement of Ion diffusion in epoxy molding compounds by dynamic secondary ion mass spectroscopy", 2008, TCPT Vol.31 pp.527-535

Lee A., "Electrochemical studies of CuAl interfaces for reliability performance of wire bonding packages", 2012, SRC Task#2285.001

Lee A., Wu Y., "Electrochemical studies of Cu-X/Al interfaces for service reliability of wire bonding packages", 2014 SRC Task#2285.001

Liu H., Zhou J., "Reliability of copper wire bonding in humidity environment," EPTC, 2011, pp. 53–58

Lu G., Shim M., "Effects of moisture on properties of epoxy molding compounds", Journal of applied polymer science, 2001, Volume 81, pp.2253-2259

Lu Y., Wang Y., "Growth of CuAl intermetallic compounds in Cu and Cu(Pd) wire bonding", 2011 ECTC, pp.1481-1488

Murali S., Srikanth N., "An analysis of Intermetallics formation of gold and copper ball bonding on thermal aging", Mater Res Bull 2003 pp.637-650

Murer N., Missert N., "Finite element modeling of galvanic corrosion of aluminum at engineered copper particle", Journal of the Electrochemical Society, 2012, pp. 265-276

Murer N., Missert N., "Towards the modeling of microgalvanic coupling in aluminum alloys: the choice of boundary conditions", COMSOL conference BOSTON, 2008

Murer N., Oltra R., "A Discussion on the Application of Local Probe Techniques", Corrosion Science 52, 2010 pp 130-139

Murer N., Oltra R., "Numerical modelling of the galvanic coupling in aluminum alloys", Corrosion Science 52 (2010), pp. 130-139

Musa A., Mohamad A., "Galvanic corrosion of aluminum alloy and copper in 1.0 M nitric acid" Int. J. Electrochemistry Sci. 2011, pp.5052-5065

Noor M., Othman R., "Determination of linear Tafel region from piecewise linear regression analysis", Int. J. Electroactive Mater, 2014, pp. 22-27

Reinoso J., "Damage features in polycrystalline quasi-brittle materials: Application to silicon wafers", 2013, 1st International Workshop: Impact of mechanical and thermal loads on the long term stability of PV modules

Park K., Paulino G., "Computational implementation of the PPR potential-based cohesive model in ABAQUS", Engineering Fracture Mechanics 93(2012) pp.239-262

Pecht M., Nguyen L., “Plastic-encapsulated microelectronics”, New York: Wiley, 1995

Pecht M., Preeti S. Chauhan, Zhaowei Zhong “Copper Wire Bonding”, Springer, 2014

Peck D., “Comprehensive model for humidity testing correlation”, IEEE/IRPS, 1986, pp.44-50

Ribeiro M., “Kalman and extended Kalman filters: concept, derivation and properties”, 2004

Rongen R., Goumans L., “Lifetime Prediction of Cu-Al wire bonded contacts for different mould compounds”, 2014, ECTC pp.411-418

Seki H., Ping C., “Study of EMC for Cu bonding wire application”, 2010 IEEE

Simon E. Jackson, Norman J., Pearson L., “The application of laser ablation-inductively coupled plasma mass spectrometry to in situ U-PB zircon geochronology” Volume 211, Issues 1–2, 8 November 2004, Pages 47–69

Shen C. Springer G., “Moisture absorption and desorption of composite materials”, Journal of composite materials, Vol.10, (1976) pp.2-20

Soestbergen M., Biesheuvel P., “Modified Poisson-Nernst-Planck theory for ion transport in polymeric electrolytes”, Journal of Electrostatics 2008

Soestbergen M., Ernst L., “Transport of corrosive constituents in epoxy molding compounds”, IEEE EuroSimE pp.42-47 2007

Soestbergen M., Ernst L., “Transport of Corrosive Constituents in Epoxy Molding Compounds” 8th. Int. Conf. on Thermal, Mechanical and Multiphysics Simulation and Experiments in Micro-Electronics and Micro-Systems, EuroSimE 2007 pp. 42-47

Stephan, H. M. Goh, “High temperature storage performance of copper ball bonding wires”, IEEE Electronics Packaging Technology Conference, 2005, pp. 602-607

Spaan E., Ooms E., “Wire bonding the future: a combined experimental and numerical approach to improve the Cu-wire bonding quality,” EuroSimE, 2010, pp. 1-4

Springer S., Chen H., “Moisture absorption and desorption of composite materials”, Journal of composite materials, Vol.10, (1976) pp.2-20

Suhling J., “Mechanics of electronic packaging”, chip-level interconnections”, 2013

Schueller R., “Copper wire bond failure mechanisms”, 2013

Sylvester J., “Comparing Au, Ag and Cu wire bonding”, 2013

Szklarska., Pitting Corrosion of Metals, NACE, Houston, TX, 1986

Tait S., “An Introduction to Electrochemical Corrosion Testing for Practicing Engineers and Scientist” 1994, Racine, WI

Teverovsky A., “Effect of environments on degradation of molding compound and wire bonds in PEMs”, 2006 ECTC, pp.1415-1424

Weibull W., Sweden S., “A statistical distribution function of wide applicability”, Journal of Applied Mechanics 1951, pp.293-296

Wolff F., Breach C., “Characterization of intermetallic growth in copper and gold ball bonds on aluminum metallization”, Proc. EPTC, pp.348-353, 2004

Workley J., Kvech S., “Fundamental aspects of ion extraction in inductively coupled plasma mass spectrometry” Atomic Spectroscopy, Vol. 51 Issue 8, pp. 779-815 1996

Yamada T., Uno T., “Improving humidity bond reliability of copper bonding wires,” ECTC, 2010, pp. 1725–1732

Zaid B., Saidi D., “Effect of PH and Chloride Concentration on Pitting Corrosion of AA6061 Aluminum Alloy”, Corrosion SCIENCE 50(2008) pp 1841-1847

Zarchan P., “Fundamentals of Kalman Filtering: a practical approach”, 2000